AMERICAN UNIVERSITY OF BEIRUT

Optimal Experiment Design for Modeling and Estimation of Intra-Cortical Neuronal Activity from EEG Recordings: A Kalman Filtering Approach

by
Mahmoud Kassem Madi

A dissertation
submitted in partial fulfillment of the requirements
for the degree of Doctor of Philosophy
to the Department of Electrical and Computer Engineering
of the Faculty of Engineering and Architecture
at the American University of Beirut
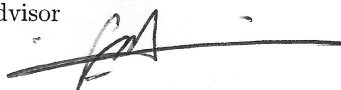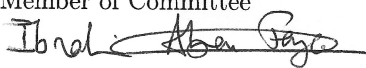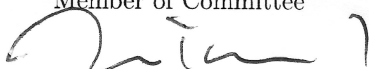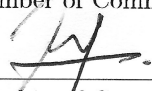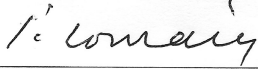
Beirut, Lebanon
November 2016
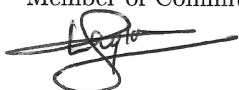
AMERICAN UNIVERSITY OF BEIRUT

Optimal Experiment Design for Modeling and Estimation of Intra-Cortical Neuronal Activity from EEG Recordings: A Kalman Filtering Approach

by
Mahmoud Kassem Madi

Approved by:

Dr. Nassir Sabah, Professor Electrical and Computer Engineering	Chair of Committee
Dr. Fadi Karameh, Associate Professor Electrical and Computer Engineering	Advisor
Dr. Ibrahim Abou-Faycal, Associate Professor Electrical and Computer Engineering	Member of Committee
Dr. George Saad, Assistant Professor Civil and Environmental Engineering	Member of Committee
Dr. Ziad Nahas, Professor Psychiatry	Member of Committee
Dr. Victor Araman, Associate Professor Olayan School of Business	Member of Committee
Dr. Youssef Comair, Professor Lebanese American University	Member of Committee
Dr. Leila Issa, Assistant Professor Lebanese American University	Member of Committee

Date of thesis defense: November 25, 2016

AMERICAN UNIVERSITY OF BEIRUT

THESIS, DISSERTATION, PROJECT RELEASE FORM

Student Name: __Madi_____Mahmoud_____Kassem___
Last   First   Middle

○ Master's Thesis ○ Master's Project ☑ Doctoral Dissertation

☐ I authorize the American University of Beirut to: (a) reproduce hard or electronic copies of my thesis, dissertation, or project; (b) include such copies in the archives and digital repositories of the University; and (c) make freely available such copies to third parties for research or educational purposes.

☑ I authorize the American University of Beirut, to: (a) reproduce hard or electronic copies of it; (b) include such copies in the archives and digital repositories of the University; and (c) make freely available such copies to third parties for research or educational purposes after: **One ___ year from the date of submission of my thesis, dissertation or project.**
      Two ___ years from the date of submission of my thesis , dissertation or project.
      Three ☑ years from the date of submission of my thesis , dissertation or project.

_____   Sep. 14 - 2017
Signature   Date

This form is signed when submitting the thesis, dissertation, or project to the University Libraries

Acknowledgements

First and foremost, my deepest gratitude goes towards my parents, for whom I owe this achievement, for their endless support and dedication through these years.

My greatest appreciation goes to my advisor Prof. Fadi Karameh. His persisting support and invaluable guidance made achieving this work possible. He is an interesting, creative, and remarkable advisor, and it has been a great pleasure working with him.

I would like to acknowledge my thesis committee members, especially Prof. Ibrahim Abou-Faycal, Prof. Victor Araman, and Prof. George Saad for their dedicated time and constructive comments.

An Abstract of the Dissertation of

Mahmoud Kassem Madi   for   Doctor of Philosophy
                               Major: Electrical and Computer Engineering

Title: Optimal Experiment Design for Modeling and Estimation of Intra-Cortical Neuronal Activity from EEG Recordings: A Kalman Filtering Approach

Kalman filtering methods have long been regarded as efficient adaptive Bayesian techniques for estimating hidden states in models of linear dynamical systems under Gaussian uncertainty. Recent advent of the nonlinear Cubature Kalman Filter (CKF) allows for stable parametric estimation in inherently nonlinear systems driven by random inputs of Gaussian nature. Employing CKF techniques, therefore, carries high promise for modeling many biological phenomena where the underlying processes exhibit inherently nonlinear, continuous, and noisy dynamics and the associated measurements are uncertain and time-sampled. As with any estimation technique, the solution accuracy remains dependent on the quality of the input/output data sets over finite recording horizon. To improve accuracy, an Adaptive Design Optimization (ADO) can be employed for intelligently choosing inputs whose corresponding outputs are maximally informative about unknown parameters and/or hidden states.

In this dissertation, we address improving model fitting (states and parameters estimation) and model assessment (model selection) procedures in a Kalman-based framework and by integrating techniques from Adaptive Design Optimization (ADO). We proposed efficient identification algorithms that select in single experimental trials those system inputs that cause the output trajectory to be maximally informative about the nonlinear system model parameters. We demonstrated the performance of these algorithms in several simulated scenarios that are derived from benchmark nonlinear problems (Double-well and Van der Pol oscillators), as well as from nonlinear stochastic neuronal models of electric

potential generation (conductance-based neuronal models and the Jansen model) and metabolic activity signals (hemodynamic model). Such algorithms include OID-SCKF algorithm which is an adaptive approach for joint input design and parametric identification of nonlinear system models. When compared to estimation with Kalman filter with inputs being randomly selected, the proposed method in combining Kalman filtering with optimally designed inputs showed that, in principle, better convergence and higher estimation accuracy can be attained for a set of simulated scenarios that are derived from benchmark nonlinear problems as well as from nonlinear stochastic neuronal models. Yet, these gains in estimation accuracy posed heavy computational load making this procedure intractable for on-line applications. Moreover, we introduced a method based on Dual Kalman filters to circumvent solving the optimization problem associated with the OID-SCKF method and hence drastically reduced the computational needs to design informative input/output data. Investigation of the Dual Kalman method for a set of simulated models demonstrated the immense gain in computational power against the OID-SCKF method in designing informative inputs while maintaining the out-performance in estimation accuracy over those cased where the inputs are randomly selected.

The proposed Dual Kalman method was extended to be applied for on-line applications in which the underlying model structure along with a set of model parameters are considered unknown. The proposed on-line single-phase procedure in which model fitting (parameters estimation) and model assessment (model selection) were carried out simultaneously using Bayesian approaches to model selection and by designing experiments that produce informative outcomes about model unknowns. This procedure demonstrated to accurately identify the true underlying model structure (and its unknown parameters) from a pool of model candidates having different levels of complexity.

For off-line model fitting (states and parameters estimation) problems, we proposed a procedure to optimally design the tuning parameters of the Kalman filter based on sensitivity analysis of the model. The proposed approach is demonstrated on input deconvolution problem and showed to produce more confident estimates and better convergence without the need of an iterative tuning process from the designer.

Finally, we addressed the accuracy of state and parameter estimation using CKF and CD-CKF techniques in the context of neural state estimation from EEG and fMRI recordings as specific examples of physiological dynamical system modeling. Starting with nonlinear state-space simulation models, we elaborate estimation performance while varying conditions related to (i) the observation sampling frequency, (ii) the observation signal-to-noise ratio and (iii) the structure of the additive noise process underlying the state dynamics. In particular, we aim to highlight those situations where an added benefit can be obtained by explicitly

employing a hybrid filtering (CD-CKF). Our results showed that the explicit consideration of the continuous nature of the underlying biological process can (1) provide a significant improvement in the accuracy of the estimates and (2) allow for a wider range of noise processes that are commonly thought to adversely affect the applicability of Gaussian-based techniques such as the Kalman filter.

Contents

List of Figures

xv

List of Tables

Chapter 1

Introduction

Physiological signal recordings have long played a central role in probing and deciphering the functional state of the underlying biological process. Towards this goal, dynamical system modeling aims principally to develop a causal link between the observed signals and the predicted process outputs. In brain sciences, modeling is generally intended to provide a link between the ongoing activity of a neuronal system and a host of associated aggregate recordings including directly related electrical measurements (such as the electroencephalogram EEG, electrical corticogram ECoG, Local Field Potentials LFP) and indirectly related metabolic measurements (such as fMRI). For a vast majority of these models, the computational and identification complexity of these models quickly increases with the inclusion of realistic assumptions on both the process and its measurement conditions.

First, at the process level, realistic descriptions often result in continuous-time, nonlinear, stochastic and possibly time-varying dynamics. Starting with a set of ordinary differential equations, models commonly include (i) nonlinear relationships among several variables (e.g. voltage-dependent ionic conductances), (ii) uncertainty or randomness in describing the process response to its environment (e.g. *in vivo* synaptic noise), and (iii) modulation of the process itself by external inputs or factors (e.g. effect of neuromodulators ACh). Second, at the measurement level, observation of the process is attained indirectly through one or more continuous-time variables that relate to the neuronal activity and are limited by spatial smearing (e.g. extracellular currents) or temporal filtering (e.g. blood oxygenation levels). These observation variables are subsequently recorded over regular intervals in time to produce a sequence of noisy discrete-time physiological recordings.

Along with the increase in model complexity, the correct identification of the model parameters and the accurate estimation of its hidden internal states be-

come key challenges, particularly since the efficiency and performance of available estimation tools depends on a set of assumptions on the process dynamics (linearity, time-invariance) and its operating conditions (process and measurement noise structure) that become clearly violated in these models.

The temporal dynamics for a wide array of physical and biological systems can be described by a set of nonlinear ordinary differential equations relating the system outputs to several internal (or intermediate) states and to the system inputs. These equations, furthermore, often contain sets of parameters that reflect the topology of the system, its operating conditions, as well as other exogenous environmental factors acting on it. The development of input/output predictive models for such systems, therefore, hinges upon the ability to obtain accurate estimates of both the internal states and the parameters of the system model based on experimental recordings. Major challenges to performing such model identification include (a) the limited flexibility in performing repeated experimental manipulations, (b) the noisy character of the measured output in vivo, and/or (c) the availability of auxiliary output measurements rather than the direct process output.

From a system theoretic viewpoint, state-space formulations constitute a flexible framework whereby both the modeling and estimation problems can be combined for a wide range of realistic physiological modeling assumptions. In the context of modeling, state-space allows for separate descriptions of the dynamic processes and their uncertainties (continuous-time dynamics and noise impact in both the hidden states and observation variables) from the method of observation and its imperfections (discrete time noisy multiple channel recordings) [2]. State-space formulations of dynamical systems allow for describing the system response to both controlled and random inputs ($\mathbf{u}_t$) in terms of a measurement function $\mathbf{g}$ of the output $\mathbf{y}_t$ (the static observation equation (1.2)) and a dynamic evolution function $\mathbf{f}$ on the internal system states $\mathbf{x}_t$ (the process equation (1.1)) as determined by a set of model parameters θ:

$$\dot{\mathbf{x}}_t = \mathbf{f}_\theta\left(\mathbf{x}_t, \mathbf{u}_t\right) + \mathbf{w}_t \tag{1.1}$$

$$\mathbf{y}_t = \mathbf{g}_\theta\left(\mathbf{x}_t, \mathbf{u}_t\right) + \mathbf{e}_t \tag{1.2}$$

Moreover, it is noted that this approach allows for a distinct, more natural treatment of the uncertainty in the dynamics (the process noise $\mathbf{w}_t$) and the recording imperfections and noise (the measurement noise $\mathbf{e}_t$).

In the context of estimation, state-space summarizes the system history in a set of first order dynamics memory elements (or states) whereby knowledge of their current value and future inputs completely characterizes the system evolution into the future (first order Markov chain), thereby allowing for efficient time-recursive estimation.

2

This type of state estimation problems is usually solved with Bayesian filters whereby the posterior probability density function (pdf) of the states is constructed, based on all available information up to current time, to provide a complete statistical description of the states at current time [3]. Subsequently, new information that becomes available from new measurements is combined with the old information to modify the posterior pdf using Bayes theorem.

Arguably, the Kalman filter is the most widely used type of Bayesian filters available to solve the state estimation problem. In the Kalman setup, it is assumed that both the state noise and the measurement disturbance are samples of an additive, zero mean random processes that admit Gaussian probability distributions [4].

The Kalman Filter (KF) was originally formulated for linear time-varying systems but has recently received increased attention with the introduction of techniques for estimating nonlinear time varying dynamical systems. Such filters are the Extended Kalman filter (EKF) [5], the Unscented Kalman filter (UKF) [6, 7, 8], and the most recently introduced filter the Cubature Kalman filter (CKF) [9, 3].

Kalman filter extensions (EKF, UKF, and CKF) that deal with nonlinear systems have also found their way to numerous applications in a wide variety of areas in Biology [10, 11, 12, 13, 14, 15, 16]. In the neural sciences, Kalman filter applications include neural activity modeling and estimation [11, 17, 18, 19], Seizure prediction and control [20, 21, 22, 23, 24], Sleep and EEG modeling [25, 26, 27, 28], and particularly brain connectivity estimation in psychology and cognition [29, 30, 31, 32, 33]. The time-varying adaptive nature of Kalman filtering continues to place it among other popular estimation techniques, particularly those based on Dynamic Causal Modelling (DCM) [34]. DCM is based on generative models that are compared within a Bayesian framework in order to infer the functional connectivity between neuronal populations or brain regions from observed data (EEG, MEG, or fMRI) [35, 36, 37, 38].

From a system identification perspective, finding the correct set of unknown system parameters θ assumes that (a) the parameters are identifiable, i.e., unique parameter estimates are produced for a given data set and a given fitting criterion, and (b) the input data is sufficiently rich to excite the dynamics of the system. In a Kalman filter setting, the model parameters are commonly treated as additional hidden states of the overall system, and are thus estimated at a discrete time step θ_k as part of an augmented state vector $\mathbf{x}_k^{\text{aug}}$ based on the available input/output data. When both identifiability and input richness conditions are satisfied, the ability of a Kalman filter to estimate the system parameters as hidden states is constrained by the sensitivity of the output measurements to changes in these parameters, which in turn might vary with changes in the system operating point. Accordingly, and for a given set of experimental input/output data, the accuracy of the parameter estimates is contingent upon the parameters' correlation to the

output measurements. It is therefore highly advantageous to choose those "correct" data sets that are highly informative about the model parameters. Upon constraining with the limited flexibility of performing lengthly, repeatable and controlled practical experiments (as presented earlier), it becomes crucial to design an efficient single-experiment input profile that maximizes the observability of the parameters from the measured outputs.

In systems biology, the actual circuitry of the underlying systems are usually unknown, and expert knowledge has to be converted into a suitable model structure that represents the interaction of model components. This is achieved through the proposition of model candidates $\mathcal{M}_m, m = 1, \ldots, M$ which represent competing hypotheses of the underlying circuitry. Moreover, each model candidate $\mathcal{M}_m, m = 1, \ldots, M$ has p_m unknown parameters $\boldsymbol{\theta}(\mathcal{M}_m)$ representing system's underlying unknown interactions and mechanisms. Typically, assessment and validation procedures are carried out in order to identify the most plausible model candidate $\mathcal{M}_m$, that most likely to represent the actual circuitry of the underlying system. In validating candidate models, first, they are fitted to a given experimental input/output data set and, second, their generality is tested against novel data recordings. A winning model is one that achieves high accuracy-generality score. Again, as in system identification problems, the distinguishably between model candidates depends on the quality of available input/output data. Therefore, it is convenient to choose those suitable operation conditions (maximally informative data sets) to ensure proper discrimination between model candidates.

Adaptive design optimization (ADO) refers to a large set of techniques that are often used to select, from a set of possible experimental scenarios, those scenarios that can maximally reduce the parametric uncertainty in a predetermined model or choose the highest evidence model from a set of potential candidates. Optimal experiment design has been employed for parameter estimation in systems biology [39, 40, 41, 42, 43, 44, 45], Bio-chemical systems [46, 47, 48, 49], and cognitive neuroscience [50, 51, 52]. Optimal experiments are also designed in order to select the most plausible model from a pool of candidate models in systems biology [53, 42, 54], and in cognitive neuroscience [50, 55, 56].

In the present work, we address improving model fitting (states and parameters estimation) and model assessment (model selection) procedures in a Kalman-based framework and by integrating techniques from Adaptive Design Optimization (ADO). We aim to introduce efficient identification algorithms that select in single experimental trials those system inputs that cause the output trajectory to be maximally informative about the nonlinear system model parameters. We will demonstrate the performance of these algorithms in several simulated scenarios that are derived from benchmark nonlinear problems (Double-well and Van der Pol oscillators), as well as from nonlinear stochastic neuronal models of electric potential generation (conductance-based neuronal models and the Jansen model)

and metabolic activity signals (hemodynamic model).

This dissertation is organized as follows.

Chapter two presents a comprehensive literature review on the neuronal structure of the human brain and the means of monitoring the electrical activity of these structure with imaging techniques such as the electroencephalography (EEG). As well as a mathematical description of the Cubature Kalman Filter (CKF) along with its derivatives (the square-root CKF and the square-root Cubature Kalman Smoother), and its most recent extension, the Continuous-Discrete Cubature Kalman Filter (CD-CKF) and its derivative (the square-root CD-CKF). Finally, a highlight on existing approaches of designing experiments to improve parametric estimation and model inference.

Chapter three presents the mathematical description of various simulation nonlinear models used to demonstrate the performance of the proposed techniques and algorithms aimed to improve the performance of Kalman filter techniques in model fitting (hidden states and parameters estimation) and model selection in the context of neural state estimation from EEG and fMRI (functional magnetic resonance imaging) recordings as specific examples of physiological dynamical system modeling.

Chapter four introduces an adaptive approach for joint input design and parametric identification of nonlinear system models. By integrating techniques from Adaptive Design Optimization (ADO) and square-root Cubature Kalman filtering (SCKF). Along with a demonstration of the algorithm performance in several simulated scenarios that are derived from benchmark nonlinear problems as well as from nonlinear stochastic neuronal models of electric potential generation.

Chapter five proposes an approach whereby the tuning parameters of the Kalman filter are optimally designed based on sensitivity analysis of the underlying system. The method of designing the tuning parameters is demonstrated on a hemodynamic model against manual iterative tuning.

Chapter six presents a new on-line adaptive approach for joint input design and parametric identification of nonlinear system models based on a dual Kalman filters setup which will circumvent the computational demands exerted by the introduced method in chapter four. A demonstration of the algorithm performance is carried out with benchmark nonlinear problems as well as from nonlinear neuronal models.

Chapter seven addresses the problem where the model structure of the underlying system is unknown. Given a pool of model candidates $\mathcal{M}_m, m = 1, \ldots, M$ each with p_m unknown parameters $\boldsymbol{\theta}(\mathcal{M}_m)$, a single-phase on-line procedure which include simultaneous model fitting (parameter estimation using Kalman filter techniques) and model selection (identifying most plausible model structure using

Bayesian approaches) is proposed in which input design is included to improve parametric estimation. A demonstration of the proposed method is conducted by simulating a multi-neuronal-area model based on Jansen model for cortical activity.

Chapter eight presents Kalman-based estimation of effective connectivity between cortical areas from experimental data collected from human subjects while performing a cognitive task (i.e. Picture-Naming task). A comprehensive description of data collection and data processing procedures are introduced. For our application, the cortical areas of interest were chosen from the visual cortex, namely the primary visual cortex (V1) and the secondary visual cortex (V2) from both left and right hemispheres. The cortical areas were modeled with the multi-neuronal-area Jansen model for cortical activity. Parameters estimation and model assessment results for two suggested model candidates of the effective connectivity between these areas based on Cubature Kalamn filter and Cubature Kalman smoother are presented.

Chapter nine addresses those situations where an added benefit (improved estimation accuracy) can be obtained by explicitly employing a hybrid filtering (i.e. CD-CKF). The accuracy of state and parameter estimation is addressed using CKF and CD-CKF techniques in the context of neural state estimation from EEG and fMRI recordings as specific examples of physiological dynamical system modeling. Estimation performance is evaluated while varying conditions related to (i) the observation sampling frequency, (ii) the observation signal-to-noise ratio and (iii) the structure of the additive noise process underlying the state dynamics.

Finally, implications and future directions are included in chapter ten.

Chapter 2

Literature Review

In this chapter, we will present a brief biological review about the human brain and its underlying neuronal structure, an introduction about a medical imaging technique, the electroencephalography (EEG), which is used to monitor the brain electrical activity. In addition, we will describe the mathematical formulation of the Cubature Kalman Filter (CKF) and its derivatives, namely the square-root CKF and the square-root Cubature Kalman Smoother. As well as its most recent extension, the Continuous-Discrete Cubature Kalman Filter (CD-CKF) which was introduced to deal with state-space models of the continuous-discrete kind (continuous-time processes with discrete-time measurements) and its derivative (the square-root CD-CKF). Finally, we will introduce the Adaptive Design Optimization method which refers to a large set of techniques that are often used to select, from a set of possible experimental scenarios, those scenarios that can maximally reduce the parametric uncertainty in a predetermined model or choose the highest evidence model from a set of potential candidates.

2.1   Neuron

The human brain is estimated to have 10^{11} interconnected neurons. The neurons are the basic functioning unit in the central nervous system (CNS). They are specialized to process motor and sensory information coming from peripheral receptors, and are responsible for cognitive processes such as planning, learning, attention and memory.
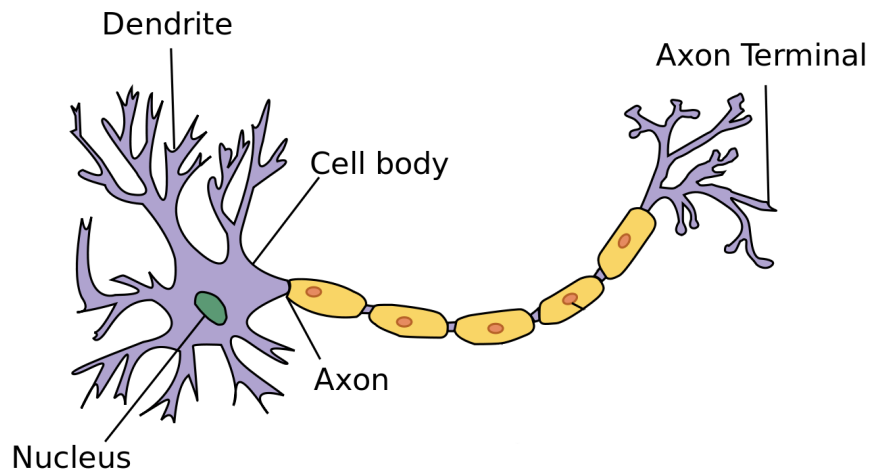
Figure 2.1: Structure of the Neuron.

2.1.1 Neuron Structure

Although there are many types of neurons, they all typically have the following common characteristics (Fig. 2.1):

- Cell body or Soma: it is involved in the main metabolic functions of the cell, and contains the nucleus and all of the other structures that are essential for cell functioning.

- Axon: it represents the conduction component of the neuron over which information (the action potential) is transmitted from one part of the neuron (e.g. the cell body) to the terminal regions of the neuron.

- Dendrites: they are tree-like structures that extend away from the Soma and serve as the input part to the neurons where they receive action potentials from other neurons at specialized junctions called synapses.

- Synapses: These are the terminal regions located at the very end of an axon, at which one neuron forms a connection with another neurons dendrites.

2.1.2 Action Potential

Action potentials (AP) represent the fundamental means of communication in the nervous system. They are electrical signals by which neurons transmit information to one another. They can either cause excitation or inhibition in the post-synaptic neuron. Neurons in a resting state normally have a membrane potential around -70 mV. This means that the voltage difference between the inside of the cell relative to the outside of the cell is negative (Fig. 2.2). When
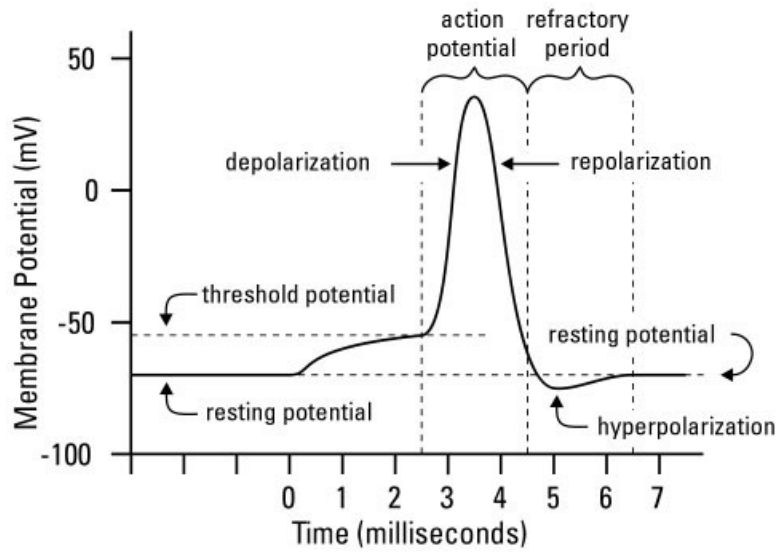
Figure 2.2: Neuron's action potential.

a neuron sends an AP to a post-synaptic neuron, then this AP will be added to all other APs targeting that post-synaptic neuron. If it increases the membrane potential then it is exciting the post-synaptic neuron, and if it decreases the membrane potential it is inhibiting the neuron. If all APs cause the membrane potential to pass the firing threshold then the post-synaptic neuron will fire an action potential.

2.1.3 Neocortex

The neocortex is the seat of the highest forms of biological intelligence in all sensory and cognitive modalities. It is responsible for cognitive processes such as analysis and conscious perception of sensory stimuli, planning and regulation of goal-directed movements, learning, attention and memory [1]. The mammalian sensory neocortex is characterized by its laminar architecture in which neocortical neuronal populations can be horizontally segregated into six different lamina or layers that lie parallel to the cortical surface (Fig. 2.3). These layers fall into three categories:

- Superficial layers: these are layer I, layer II and layer III.

- Middle layer: Layer IV.

- Deep layers: Layer V and layer VI.

Each layer is characterized by the anatomical and electrophysiological properties of its constituent neurons. Another feature of the sensory neocortex is its vertical
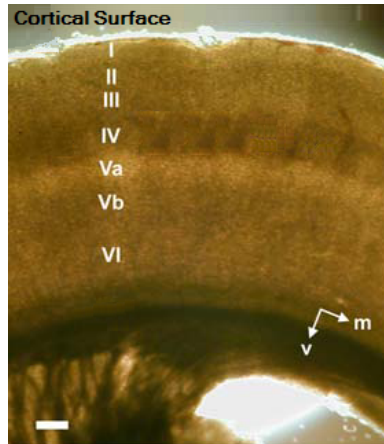
Figure 2.3: Acute coronal slice through the cortex of a rat. All cortical layers are indicated by the Roman numerals. Scale bar 200 μm; m: medial, v: ventral [1].

organization in which neurons stacked on top of each other through the depth of the cortex tend to be connected and have similar response properties despite residing in different layers [57]. This type of vertical structure is called a cortical column or functional column, and has been hypothesized to represent a basic functional unit of sensory information processing [57].

2.1.4 Neurons Types

Based on the segregation of the neocortex into six layers, each layer is characterized by the anatomical and electrophysiological properties of its constituent neurons.

Layer I contains a few neurons. These neurons are all inhibitory neurons and synapse mainly to dendrites of neurons from the deeper layers. Dendrites in layer I not belonging to the population of layer I inhibitory cells are apical dendrites from deep layer pyramidal cells [58]. Layer II/III contains a mix of small pyramidal cells and inhibitory neurons mainly bipolar cells and double bouquet cells. It also contains apical dendrites of layer pyramidal cells [58].

Layer IV contains excitatory spiny stellate cells and a variety of inhibitory cells [58]. The spiny stellate cells are exclusively located in layer IV. Layer V contains large pyramidal cells and a smaller population of inhibitory cells. Axons and basal dendrites of bipolar cells (which are inhibitory and located in layer II/III) are also found in layer V [58].

Layer VI contains large pyramidal cells that project their axons back to the thalamus. Layer VI also contains a class of inhibitory neurons called Martinotti cells

whose axonal outputs make long projections across all layers of the neocortex [58].

2.2 Electroencephalography

Electroencephalography (EEG) is a medical imaging technique that records electrical activity of the brain by means of electrodes placed on the scalp. Brain electrical activity includes action potentials that produce circumscribed electrical fields, and slower, more widespread, post-synaptic potentials [59]. The activity of a single neuron can be recorded by an adjacent microelectrode, but it is too small to be detected by distant scalp electrode. Synchronous activity in a horizontal laminar aggregate of neurons with parallel orientation may, however, be detectable on the scalp [59]. Thus the EEG is a spatio-temporal average of synchronous activity arising in thousands of neurons that have similar spatial orientation.

Cortical pyramidal neurons are considered to be main source of EEG signal because they are well-aligned and fire together [59]. Because voltage fields fall off with the square of distance, activity from deep sources is more difficult to be detected than activity near the skull.

EEG recordings show oscillations that represent synchronized neuronal activity at a variety of frequencies. Several of these oscillations have characteristic frequency ranges, and are associated with different brain states during resting and cognitive tasks.

These characteristic frequencies or rhythms have distinct spatio-temporal. There are five classical brain rhythms (Fig. 2.4):

- Delta rhythm: This is a slow rhythm that ranges between 0.5 and 4 Hz, which is mainly observed in adults during a deep sleep.

- Theta rhythm: Has a frequency band 4-8 Hz. It is observed mainly during drowsiness and idling states.

- Alpha rhythm: Oscillations in the alpha rhythm range between 8-13 Hz band, which appear mainly in the posterior regions of the head (occipital lobe) relaxation states with the eyes closed.

- Beta rhythm: This is a relatively fast rhythm having a band of 13-30 Hz in frequency. It is observed in awaken and conscious states, active thinking, focus, anxiety and stress.

- Gamma rhythm: This rhythm is defined for fast oscillations having frequencies above 30 Hz. It is observed during short-term memory matching of recognized objects, sounds, or tactile sensations.
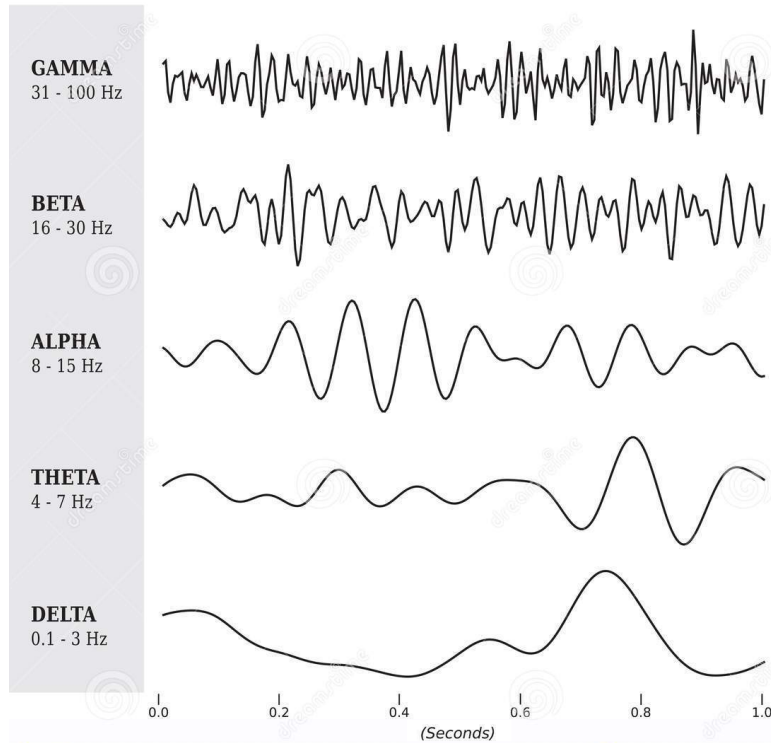
Figure 2.4: Examples of EEG rhythms.

EEG signals measurements are performed using 1 to 256 electrodes. Electrodes are generally placed and named according to a standard model, namely, the 10-20 international system (Fig. 2.5).

2.3 Cubature Kalman Filter

Cubature Kalman filter is a nonlinear filter designed for hidden state estimation from nonlinear dynamic system with additive noise. The nonlinear dynamic system is described by a state-space model comprising a process and measurement equation described in discrete-time domain. The state-space model is defined by the pair of difference equations in discrete-time:

Process Equation: $$\mathbf{x}_k = \mathbf{f}_d(\mathbf{x}_{k-1}, I_{k-1}) + \mathbf{v}_{k-1} \tag{2.1}$$

Measurement Equation: $$z_k = h(\mathbf{x}_k) + w_k \tag{2.2}$$

Where $\mathbf{x}_k \in \mathbb{R}^n$ is the state vector of the dynamic system at discrete time time k, $z_k \in \mathbb{R}^d$ is the measurement at discrete time instance k, $\mathbf{f}_d : \mathbb{R}^n \times \mathbb{R} \to \mathbb{R}^n$ is the process function, $h : \mathbb{R}^n \times \mathbb{R} \to \mathbb{R}^d$ is the measurement function, $v_{k-1} \in \mathbb{R}^n$ is a vector of random Gaussian noise with zero mean and covariance V_{k-1}, $w_k \in \mathbb{R}^d$ is a vector of random Gaussian noise with zero mean and covariance R_k.
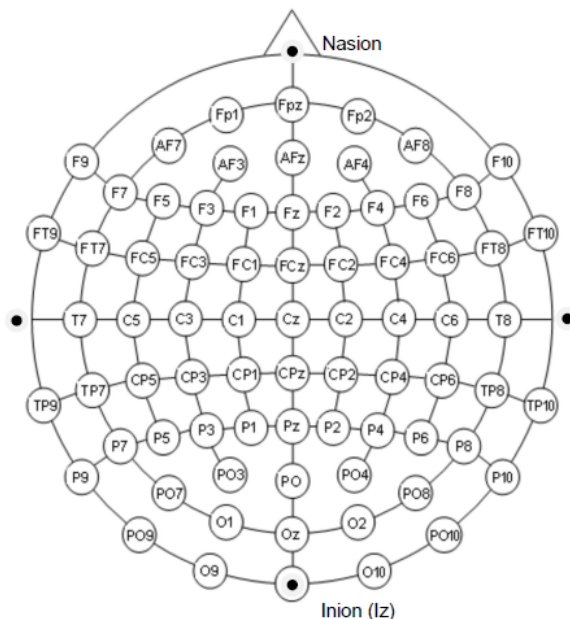
Figure 2.5: Location and nomenclature of a 74-Channel electrodes arrangement.

Typically, The process equation describing a given system has continuous-time dynamics and it is expressed by a continuous stochastic differential equation (SDE):

Process Equation: $\qquad d\mathbf{x}(t) = \mathbf{f}(\mathbf{x}(t), t)dt + \sqrt{\mathbf{Q}}d\boldsymbol{\beta}(t)$ \hfill (2.3)

Where $\mathbf{x}(t) \in \mathbb{R}^n$ is the state of the dynamic system at time t, $\mathbf{f} : \mathbb{R}^n \times \mathbb{R} \to \mathbb{R}^n$ is the drift coefficient, $\beta(t) \in \mathbb{R}^n$ is a standard Wiener process assumed to be independent of states and measurement noise, and $Q \in \mathbb{R}^{n \times n}$ is the diffusion coefficient.

In order to deal with the continuous process equation, we can discretize the SDE using Local Linearization (LL) method as proposed in [30]; this will transform the process equation into a stochastic difference equation.

Local Linearization method consists of transforming a nonlinear SDE to a linear SDE by applying the truncated Itô-Taylor expansion to the drift coefficient $f(\mathbf{x}(t), t)$, then evaluate the analytical solution of the resulting linear SDE and finally approximate the Itôs integral in the obtained solution by means of the composite Trapezoidal rule [60]. The resultant discrete difference equation will be as follows:

$$\mathbf{x}_k = \mathbf{f}_d(\mathbf{x}_{k-1}, k-1) + \mathbf{v}_{k-1} \qquad (2.4)$$

13

Where

$$\mathbf{f}_d(\mathbf{x}_{k-1}, k-1) \approx \mathbf{x}_{k-1} + \mathcal{J}_{k-1}^{-1}[\exp(\mathcal{J}_{k-1}\Delta t) - I_e]\mathbf{f}(\mathbf{x}_{k-1}, k-1) \qquad (2.5)$$

$\mathcal{J}_k$ is the Jacobian of $\mathbf{f}$ at discrete time k and Δt is the time interval between samples, and I_e is the identity matrix.

The state-space model in discrete time description becomes:

Process Equation: $\qquad\qquad\qquad\qquad \mathbf{x}_k = \mathbf{f}_d(\mathbf{x}_{k-1}, I_{k-1}) + \mathbf{v}_{k-1} \qquad\qquad (2.6)$

Measurement Equation: $\qquad\qquad\qquad z_k = h(\mathbf{x}_k) + w_k \qquad\qquad\qquad (2.7)$

Where $v_{k-1} \in \mathbb{R}^n$ is a vector of random Gaussian noise with zero mean and covariance V_{k-1}, $w_k \in \mathbb{R}^d$ is a vector of random Gaussian noise with zero mean and covariance R_k.

The CKF is based on Bayesian filtering paradigm under Gaussian domain, in which the posterior density of the state provides a complete statistical description of the state at that time [9]. This filter includes two steps:

- Time update: compute the predicted density $p(\mathbf{x}_k|z_{1:k-1}) \sim \mathcal{N}(\hat{\mathbf{x}}_{k|k-1}, P_{k|k-1})$. Where:

$$\begin{aligned}
\hat{\mathbf{x}}_{k|k-1} &= E[\mathbf{x}_k|z_{1:k-1}] \\
&= E[f_d(\mathbf{x}_{k-1}, k-1)|z_{1:k-1}] \\
&= \int f_d(\mathbf{x}_{k-1}, k-1)p(\mathbf{x}_{k-1}|z_{1:k-1})d\mathbf{x}_{k-1} \\
&= \int f_d(\mathbf{x}_{k-1}, k-1) \times \mathcal{N}(\mathbf{x}_{k-1}; \hat{\mathbf{x}}_{k-1|k-1}, P_{k-1|k-1})d\mathbf{x}_{k-1} \qquad (2.8)
\end{aligned}$$

$$\begin{aligned}
P_{k|k-1} &= E\big[(\mathbf{x}_k - \hat{\mathbf{x}}_{k|k-1})(\mathbf{x}_k - \hat{\mathbf{x}}_{k|k-1})^T|z_{1:k-1}\big] \\
&= \int f_d(\mathbf{x}_{k-1}, k-1)f_d(\mathbf{x}_{k-1}, k-1)^T \times \mathcal{N}(\mathbf{x}_{k-1}; \hat{\mathbf{x}}_{k-1|k-1}, P_{k-1|k-1})d\mathbf{x}_{k-1} \\
&\quad - \hat{\mathbf{x}}_{k|k-1}\hat{\mathbf{x}}_{k|k-1}^T + V_{k-1} \qquad\qquad\qquad\qquad\qquad\qquad\qquad\qquad (2.9)
\end{aligned}$$

- Measurement update: compute the posterior density $p(\mathbf{x}_k|z_{1:k}) \sim \mathcal{N}(\hat{\mathbf{x}}_{k|k}, P_{k|k})$. The filter likelihood density is assumed to be Gaussian:

$$p(z_k|z_{1:k}) \sim \mathcal{N}(z_k; \hat{z}_{k|k-1}, P_{zz,k|k-1})$$

Where the predicted measurement:

$$\hat{z}_{k|k-1} = \int h(\mathbf{x}_k, k) \times \mathcal{N}(\mathbf{x}_k; \hat{\mathbf{x}}_{k|k-1}, P_{k|k-1})d\mathbf{x}_k \qquad (2.10)$$

and the associated covariance

$$P_{zz,k|k-1} = \int h(\mathbf{x}_k, k)h(\mathbf{x}_k, k)^T \times \mathcal{N}(\mathbf{x}_k; \hat{\mathbf{x}}_{k|k-1}, P_{k|k-1})d\mathbf{x}_k$$
$$- \hat{z}_{k|k-1}\hat{z}_{k|k-1}^T + R_k \tag{2.11}$$

The cross-covariance between the state and the measurement is given by:

$$P_{xz,k|k-1} = \int \mathbf{x}_k h(\mathbf{x}_k, k)^T \times \mathcal{N}(\mathbf{x}_k; \hat{\mathbf{x}}_{k|k-1}, P_{k|k-1})d\mathbf{x}_k - \hat{\mathbf{x}}_{k|k-1}\hat{z}_{k|k-1}^T \tag{2.12}$$

Thus, the conditional Gaussian density of the joint state and the measurement can be written as:

$$p\left(\begin{bmatrix} \mathbf{x}_k^T & z_k^T \end{bmatrix} | z_{1:k}\right) \sim \mathcal{N}\left(\begin{bmatrix} \hat{\mathbf{x}}_{k|k-1} \\ \hat{z}_{k|k-1} \end{bmatrix}, \begin{bmatrix} P_{k|k-1} & P_{xz,k|k-1} \\ P_{xz,k|k-1}^T & P_{zz,k|k-1} \end{bmatrix}\right)$$

From which the posterior density $p(\mathbf{x}_k|z_{1:k}) \sim \mathcal{N}(\hat{\mathbf{x}}_{k|k}, P_{k|k})$ is computed on the receipt of a new measurement z_k through the computation of the so-called Kalman gain K_k:

$$\hat{\mathbf{x}}_{k|k} = \hat{\mathbf{x}}_{k|k-1} + K_k(z_k - \hat{z}_{k|k-1})$$
$$P_{k|k} = P_{k|k-1} - K_k P_{zz,k|k-1} K_k^T$$
$$K_k = P_{xz,k|k-1} P_{zz,k|k-1}^{-1}$$

2.3.1 Third-Degree Cubature Rule

The Bayesian filter in the Gaussian domain reduces to the problem of how to compute integrals of the following form [3]:

$$I(f) = \int f(x) \times \mathcal{N}(x; ., .)dx \tag{2.13}$$

Where $f(x)$ is some nonlinear function.

The heart of Cubature Kalman Filter is to numerically approximate this type of integrals by third-degree spherical-radial rule using an even set of $2n$ equally weighted symmetric cubature points $\{\xi_i, \omega_i\}_{i=1}^{2n}$ (where n is the dimension of the state vector):

$$I(f) = \int f(x) \times \mathcal{N}(x; \mu, \Sigma)dx \approx \sum_{i=1}^{2n} \omega_i f\left(\mu + \sqrt{\Sigma}\xi_i\right) \tag{2.14}$$

Where:

$$\Sigma = \sqrt{\Sigma}\sqrt{\Sigma}^T$$

$$\omega_i = \frac{1}{2n}$$

$$\xi_i = \begin{cases} \sqrt{n}e_i & i = 1, \ldots, n \\ -\sqrt{n}e_i & i = n+1, \ldots, 2n \end{cases}$$

Using this numerical approximation of integrals, the time update of the CKF becomes:

$$\hat{\mathbf{x}}_{k|k-1} = \int f_d(\mathbf{x}_{k-1}, k-1) \times \mathcal{N}(\mathbf{x}_{k-1}; \hat{\mathbf{x}}_{k-1|k-1}, P_{k-1|k-1}) d\mathbf{x}_{k-1}$$

$$= \frac{1}{2n} \sum_{i=1}^{2n} \mathcal{X}_{i,k|k-1}^* \tag{2.15}$$

Where

$$\mathcal{X}_{i,k|k-1}^* = f_d(\hat{\mathbf{x}}_{k-1|k-1} + \sqrt{P_{k-1|k-1}}\xi_i, k-1) \tag{2.16}$$

And the corresponding error covariance:

$$P_{k|k-1} = \int f_d(\mathbf{x}_{k-1}, k-1) f_d(\mathbf{x}_{k-1}, k-1)^T \times \mathcal{N}(\mathbf{x}_{k-1}; \hat{\mathbf{x}}_{k-1|k-1}, P_{k-1|k-1}) d\mathbf{x}_{k-1}$$

$$- \hat{\mathbf{x}}_{k|k-1}\hat{\mathbf{x}}_{k|k-1}^T + V_{k-1}$$

$$= \frac{1}{2n} \sum_{i=1}^{2n} \left(\mathcal{X}_{i,k|k-1}^* \mathcal{X}_{i,k|k-1}^{*T} \right) - \hat{\mathbf{x}}_{k|k-1}\hat{\mathbf{x}}_{k|k-1}^T + V_{k-1} \tag{2.17}$$

And the measurement update equations are approximated as:

$$\hat{z}_{k|k-1} = \int h(\mathbf{x}_k, k) \times \mathcal{N}(\mathbf{x}_k; \hat{\mathbf{x}}_{k|k-1}, P_{k|k-1}) d\mathbf{x}_k$$

$$= \frac{1}{2n} \sum_{i=1}^{2n} \mathcal{Z}_{i,k|k-1} \tag{2.18}$$

Where

$$\mathcal{Z}_{i,k|k-1} = h(\hat{\mathbf{x}}_{k|k-1} + \sqrt{P_{k|k-1}}\xi_i, k-1) \tag{2.19}$$

and the associated covariance:

$$P_{zz,k|k-1} = \int h(\mathbf{x}_k, k) h(\mathbf{x}_k, k)^T \times \mathcal{N}(\mathbf{x}_k; \hat{\mathbf{x}}_{k|k-1}, P_{k|k-1}) d\mathbf{x}_k$$

$$- \hat{z}_{k|k-1}\hat{z}_{k|k-1}^T + R_k$$

$$= \frac{1}{2n} \sum_{i=1}^{2n} \left(\mathcal{Z}_{i,k|k-1}\mathcal{Z}_{i,k|k-1}^T \right) - \hat{z}_{k|k-1}\hat{z}_{k|k-1}^T + R_k \tag{2.20}$$

The cross-covariance between the state and the measurement is given by:

$$P_{xz,k|k-1} = \int \mathbf{x}_k h(\mathbf{x}_k, k)^T \times \mathcal{N}(\mathbf{x}_k; \hat{\mathbf{x}}_{k|k-1}, P_{k|k-1}) d\mathbf{x}_k - \hat{\mathbf{x}}_{k|k-1} \hat{z}_{k|k-1}^T$$

$$= \frac{1}{2n} \sum_{i=1}^{2n} \left(\mathcal{X}_{i,k|k-1} \mathcal{Z}_{i,k|k-1}^T \right) - \hat{\mathbf{x}}_{k|k-1} \hat{z}_{k|k-1}^T \tag{2.21}$$

Where:

$$\mathcal{X}_{i,k|k-1} = \hat{\mathbf{x}}_{k|k-1} + \sqrt{P_{k|k-1}} \xi_i \tag{2.22}$$

2.3.2 CKF Algorithm

A. Time update:

1) Assume at time k that the posterior density function $p(\mathbf{x}_{k-1}|z_{1:k-1}) \sim \mathcal{N}(\hat{\mathbf{x}}_{k-1|k-1}, P_{k-1|k-1})$ is known. Factorize

$$P_{k-1|k-1} = S_{k-1|k-1} S_{k-1|k-1}^T \tag{2.23}$$

2) Evaluate the cubature points $(i = 1, 2, \ldots, 2n)$

$$\mathcal{X}_{i,k-1|k-1} = \hat{x}_{k-1|k-1} + S_{k-1|k-1} \xi_i \tag{2.24}$$

Where the cubature-point set ξ is defined as:

$$\xi_i = \begin{cases} \sqrt{n} e_i & \text{for } i = 1, \ldots, n \\ -\sqrt{n} e_i & \text{for } i = n+1, \ldots, 2n \end{cases}$$

3) Evaluate the propagated cubature points $(i = 1, 2, \ldots, 2n)$

$$\mathcal{X}_{i,k|k-1}^* = f_d(\mathcal{X}_{i,k-1|k-1}, k-1) \tag{2.25}$$

4) Estimate the predicted state

$$\hat{x}_{k|k-1} = \frac{1}{2n} \sum_{i=1}^{2n} \mathcal{X}_{i,k|k-1}^* \tag{2.26}$$

5) Estimate the predicted error covariance

$$P_{k|k-1} = \frac{1}{2n} \sum_{i=1}^{2n} \left(\mathcal{X}_{i,k|k-1}^* \mathcal{X}_{i,k|k-1}^{*T} \right) - \hat{\mathbf{x}}_{k|k-1} \hat{\mathbf{x}}_{k|k-1}^T + V_{k-1} \tag{2.27}$$

17

B. Measurement update:

1) Factorize

$$P_{k|k-1} = S_{k|k-1}S_{k|k-1}^T \tag{2.28}$$

2) Evaluate the cubature points $(i = 1, 2, \ldots, 2n)$

$$\mathcal{X}_{i,k|k-1} = \hat{x}_{k|k-1} + S_{k|k-1}\xi_i \tag{2.29}$$

3) Evaluate the propagated cubature points $(i = 1, 2, \ldots, 2n)$

$$\mathcal{Z}_{i,k|k-1} = h(\mathcal{X}_{i,k|k-1}, k) \tag{2.30}$$

4) Estimate the predicted measurement

$$\hat{z}_{k|k-1} = \frac{1}{2n}\sum_{i=1}^{2n}\mathcal{Z}_{i,k|k-1} \tag{2.31}$$

5) Estimate the innovation covariance matrix

$$P_{zz,k|k-1} = \frac{1}{2n}\sum_{i=1}^{2n}\left(\mathcal{Z}_{i,k|k-1}\mathcal{Z}_{i,k|k-1}^T\right) - \hat{z}_{k|k-1}\hat{z}_{k|k-1}^T + R_k \tag{2.32}$$

6) Estimate the cross-covariance matrix

$$P_{xz,k|k-1} = \frac{1}{2n}\sum_{i=1}^{2n}\left(\mathcal{X}_{i,k|k-1}\mathcal{Z}_{i,k|k-1}^T\right) - \hat{\mathbf{x}}_{k|k-1}\hat{z}_{k|k-1}^T \tag{2.33}$$

7) Estimate the Kalman gain

$$\mathbf{K}_k = P_{xz,k|k-1}P_{zz,k|k-1}^{-1} \tag{2.34}$$

8) Estimate the updated state

$$\hat{x}_{k|k} = \hat{x}_{k|k-1} + \mathbf{K}_k(z_k - \hat{z}_{k|k-1}) \tag{2.35}$$

9) Estimate the corresponding error covariance

$$P_{k|k} = P_{k|k-1} - \mathbf{K}_k P_{zz,k|k-1}\mathbf{K}_k^T \tag{2.36}$$

2.3.3 Square-root Cubature Kalman Filter

The CKF algorithm requires the error covariance matrix ($P_{k|k}$) to be symmetric and positive definite. This condition is often lost by the numerical factorization of $P_{k|k}$ during the time and measurement updates of the CKF, and hence cause the estimation scheme to become unstable. The solution is to use the square-root Cubature Kalman Filter (SCKF) which essentially propagates square-root factor of $P_{k|k}$ ($S_{k|k}$) avoiding matrix square-rooting operations while preserving the symmetry and positive definiteness of the covariance matrix and improving numerical accuracy.

In SCKF, matrix triangular factorizations or triangularizations (e.g., the QR decomposition) is used for covariance updates. The triangularization essentially computes a triangular square-root factor of the covariance without square-rooting a squared-matrix form of the covariance. The triangularization algorithm (e.g., the QR decomposition) is denoted as $S = Tria(A)$ where S is a lower triangular matrix. The matrices A and S are related as follows: Let R be an upper triangular matrix obtained from the QR decomposition on A^T ; then $S = R^T$ [9].

SCKF Algorithm

A. Time update:

1) $S_{k-1|k-1}$ is available.

2) Evaluate the cubature points $(i = 1, 2, \ldots, 2n)$

$$\mathcal{X}_{i,k-1|k-1} = \hat{x}_{k-1|k-1} + S_{k-1|k-1}\xi_i \tag{2.37}$$

Where the cubature-point set ξ is defined as:

$$\xi_i = \begin{cases} \sqrt{n}e_i & \text{for } i = 1, \ldots, n \\ -\sqrt{n}e_i & \text{for } i = n+1, \ldots, 2n \end{cases}$$

3) Evaluate the propagated cubature points $(i = 1, 2, \ldots, 2n)$

$$\mathcal{X}_{i,k|k-1}^* = f_d(\mathcal{X}_{i,k-1|k-1}, I) \tag{2.38}$$

4) Estimate the predicted state

$$\hat{x}_{k|k-1} = \frac{1}{2n} \sum_{i=1}^{2n} \mathcal{X}_{i,k|k-1}^* \tag{2.39}$$

19

5) Estimate the square-root factor of the predicted error covariance

$$S_{k|k-1} = Tria\left(\left[\mathcal{X}_{k|k-1} \quad S_{V,k-1}\right]\right) \tag{2.40}$$

Where $S_{V,k-1}$ denotes the square-root of V_{k-1} such that $V_{k-1} = S_{V,k-1}S_{V,k-1}^T$, and the weighted centered matrix:

$$\mathcal{X}_{k|k-1} = \frac{1}{\sqrt{2n}}\left[\mathcal{X}^*_{1,k|k-1}-\hat{x}_{k|k-1} \quad \mathcal{X}^*_{2,k|k-1}-\hat{x}_{k|k-1} \quad \cdots \quad \mathcal{X}^*_{2n,k|k-1}-\hat{x}_{k|k-1}\right]$$

B. Measurement update:

1) Evaluate the cubature points $(i = 1, 2, \ldots, 2n)$

$$\mathcal{X}_{i,k|k-1} = \hat{x}_{k|k-1} + S_{k|k-1}\xi_i \tag{2.41}$$

2) Evaluate the propagated cubature points $(i = 1, 2, \ldots, 2n)$

$$\mathcal{Z}_{i,k|k-1} = h(\mathcal{X}_{i,k|k-1}) \tag{2.42}$$

3) Estimate the predicted measurement

$$\hat{z}_{k|k-1} = \frac{1}{2n}\sum_{i=1}^{2n} \mathcal{Z}_{i,k|k-1} \tag{2.43}$$

4) Estimate the square-root factor of the innovation covariance matrix

$$S_{\mathcal{ZZ},k|k-1} = Tria\left(\left[\mathcal{Z}^*_{k|k-1} \quad S_{R,k}\right]\right) \tag{2.44}$$

Where $S_{R,k}$ denotes the square-root of R_k such that $R_k = S_{R,k}S_{R,k}^T$, and the weighted centered matrix:

$$\mathcal{Z}^*_{k|k-1} = \frac{1}{\sqrt{2n}}\left[\mathcal{Z}_{1,k|k-1}-\hat{z}_{k|k-1} \quad \mathcal{Z}_{2,k|k-1}-\hat{z}_{k|k-1} \quad \cdots \quad \mathcal{Z}_{2n,k|k-1}-\hat{z}_{k|k-1}\right]$$

5) Estimate the cross-covariance matrix

$$P_{\mathcal{XZ},k|k-1} = \mathcal{X}_{k|k-1}\mathcal{Z}^{*T}_{k|k-1} \tag{2.45}$$

Where the weighted centered matrix:

$$\mathcal{X}_{k|k-1} = \frac{1}{\sqrt{2n}}\left[\mathcal{X}_{1,k|k-1}-\hat{x}_{k|k-1} \quad \mathcal{X}_{2,k|k-1}-\hat{x}_{k|k-1} \quad \cdots \quad \mathcal{X}i_{2n,k|k-1}-\hat{x}_{k|k-1}\right]$$

6) Estimate the Kalman gain

$$\mathbf{K}_k = (P_{\mathcal{XZ},k|k-1}/S_{\mathcal{ZZ},k|k-1}^T)S_{\mathcal{ZZ},k|k-1} \qquad (2.46)$$

7) Estimate the updated state

$$\hat{x}_{k|k} = \hat{x}_{k|k-1} + \mathbf{K}_k(z_k - \hat{z}_{k|k-1}) \qquad (2.47)$$

8) Estimate the square-root factor of the corresponding error covariance

$$S_{k|k} = Tria\left(\left[\mathcal{X}_{k|k-1} - \mathbf{K}_k\mathcal{Z}_{k|k-1}^* \qquad \mathbf{K}_k S_{R,k}\right]\right) \qquad (2.48)$$

2.3.4   Square-root Cubature Kalman Smoother

The square-root Cubature Kalman smoother (SCKS) is a backward pass procedure that follows the forward Kalman filter pass (SCKF) for rolling backwards from $p(\mathbf{x}_N|z_{1:N})$ to $p(\mathbf{x}_1|z_{1:N})$ (where N is the total number data points) in order to compute suitable corrections to the forward filtering results [61]. This procedure is used for computing smoothed estimates of time step k from estimates of time step $k+1$ by starting from the last step $k = N$ and proceeding backward to the initial step $k = 1$. In other words, starting from $\hat{x}_{N|N}$ and $S_{N|N}$ at the end of SCKF forward pass, the algorithm computes the smoothed state estimates $\hat{x}_{k|N}$ and the corresponding error covariance $S_{k|N}$ of time step k given the already smoothed state estimates $\hat{x}_{k+1|N}$ and the corresponding error covariance $S_{k+1|N}$ of time step $k+1$ [61].

SCKS Algorithm

1) Evaluate the cubature points $(i = 1, 2, \ldots, 2n)$

$$\mathcal{X}_{i,k|k} = \hat{x}_{k|k} + S_{k|k}\xi_i \qquad (2.49)$$

Where the cubature-point set ξ is defined as:

$$\xi_i = \begin{cases} \sqrt{n}e_i & \text{for } i = 1, \ldots, n \\ -\sqrt{n}e_i & \text{for } i = n+1, \ldots, 2n \end{cases}$$

2) Evaluate the propagated cubature points $(i = 1, 2, \ldots, 2n)$

$$\mathcal{X}_{i,k+1|k}^* = f_d(\mathcal{X}_{i,k|k}, I) \qquad (2.50)$$

3) Estimate the predicted state

$$\hat{x}_{k+1|k} = \frac{1}{2n} \sum_{i=1}^{2n} \mathcal{X}^*_{i,k+1|k} \tag{2.51}$$

4) Estimate the square-root factor of the predicted error covariance

$$S_{k+1|k} = Tria\left(\begin{bmatrix} \mathscr{X}_{k+1|k} & S_{V,k} \end{bmatrix}\right) \tag{2.52}$$

Where $S_{V,k}$ denotes the square-root of V_k such that $V_k = S_{V,k}S_{V,k}^T$, and the weighted centered matrix:

$$\mathscr{X}_{k+1|k} = \frac{1}{\sqrt{2n}}\begin{bmatrix} \mathcal{X}^*_{1,k+1|k} - \hat{x}_{k+1|k} & \mathcal{X}^*_{2,k+1|k} - \hat{x}_{k+1|k} & \cdots & \mathcal{X}^*_{2n,k+1|k} - \hat{x}_{k+1|k} \end{bmatrix}$$

5) Compute the matrices $\mathbf{U}_{11}, \mathbf{U}_{21}, \mathbf{U}_{22}$ using the triangularization algorithm:

$$\begin{pmatrix} \mathbf{U}_{11} & \mathbf{0} \\ \mathbf{U}_{21} & \mathbf{U}_{22} \end{pmatrix} = Tria\begin{pmatrix} \mathscr{X}_{k+1|k} & S_{V,k+1} \\ \mathscr{X}_{k|k} & \mathbf{0} \end{pmatrix}$$

Where:

$$\mathscr{X}_{k|k} = \frac{1}{\sqrt{2n}}\begin{bmatrix} \mathcal{X}_{1,k|k} - \hat{x}_{k|k} & \mathcal{X}_{2,k|k} - \hat{x}_{k|k} & \cdots & \mathcal{X}_{2n,k|k} - \hat{x}_{k|k} \end{bmatrix}$$

$$\mathscr{X}_{k+1|k} = \frac{1}{\sqrt{2n}}\begin{bmatrix} \mathcal{X}^*_{1,k+1|k} - \hat{x}_{k+1|k} & \mathcal{X}^*_{2,k+1|k} - \hat{x}_{k+1|k} & \cdots & \mathcal{X}^*_{2n,k+1|k} - \hat{x}_{k+1|k} \end{bmatrix}$$

6) Compute the smoother gain:

$$\mathbf{G}_k = \mathbf{U}_{21}/\mathbf{U}_{11} \tag{2.53}$$

7) Compute the smoothed state:

$$\hat{x}_{k|N} = \hat{x}_{k|k} + \mathbf{G}_k(\hat{x}_{k+1|N} - \hat{x}_{k+1|k}) \tag{2.54}$$

8) Compute the square-root of the smoothed state error covariance:

$$S_{k|N} = Tria\left(\begin{bmatrix} \mathbf{U}_{22} & \mathbf{G}_k S_{k+1|N} \end{bmatrix}\right) \tag{2.55}$$

2.4   Continuous-Discrete Cubature Kalman Filter

The presented derivation of CKF in section 2.3 was originally limited to discrete-time domain, where the process and measurement equations are both described by

stochastic difference equations. In order to apply the CKF for continuous-time dynamical systems, we had to discretize the continuous-time process equation using the LL method to transform it to stochastic difference equation.

The motivation behind Continuous-Discrete Cubature Kalman Filter (CD-CKF) is to extend the CKF to deal with state-space models of the continuous-discrete kind. In CD-CKF formulation, the Itô-Taylor expansion of order 1.5 is used to transform the process equation in the stochastic differential equation (SDE) form into a stochastic difference equation. Once more, the behavior of the dynamic system is observed through noisy measurements acquired at discrete time points and it is described by a discrete difference equation. The state-space model is given by:

Process Equation: $\qquad\qquad d\mathbf{x}(t) = \mathbf{f}(\mathbf{x}(t), t)dt + \sqrt{\mathbf{Q}}d\boldsymbol{\beta}(t)$ $\qquad$ (2.56)

Measurement Equation: $\qquad\qquad z_k = h(x_k, k) + w_k$ $\qquad\qquad$ (2.57)

Where $\mathbf{x}(t) \in \mathbb{R}^n$ is the state of the dynamic system at time t, $z_k \in \mathbb{R}^d$ is the measurement at discrete time instance k, $\mathbf{f} : \mathbb{R}^n \times \mathbb{R} \to \mathbb{R}^n$ is the drift coefficient, $h : \mathbb{R}^n \times \mathbb{R} \to \mathbb{R}^d$ is the measurement function, $\beta(t) \in \mathbb{R}^n$ is a standard Wiener process assumed to be independent of states and measurement noise, $Q \in \mathbb{R}^{n \times n}$ is the diffusion coefficient, $w_k \in \mathbb{R}^d$ is a vector of random Gaussian measurement noise with zero mean and covariance R_k.

Applying the Itô-Taylor expansion of order 1.5 to the process equation over the time interval $(t, t + \delta)$ yields [3]:

$$\mathbf{x}_{k+1} = \mathbf{f}_d(\mathbf{x}_k, k) + \sqrt{\mathbf{Q}}\mathbf{w} + (\mathbb{L}f(\mathbf{x}_k, k))\mathbf{y} \qquad (2.58)$$

Where:

$$\mathbf{f}_d(\mathbf{x}_k, k) = \mathbf{x}_k + \delta\mathbf{f}(\mathbf{x}_k, k) + \frac{1}{2}\delta^2 \mathbb{L}_0 \mathbf{f}(\mathbf{x}_k, k) \qquad (2.59)$$

$\mathbb{L}_0$ and $\mathbb{L}$ are two differential operators defined as:

$$\mathbb{L}_0 = \frac{\partial}{\partial t} + \sum_{i=1}^{n} f_i \frac{\partial}{\partial x_i} + \frac{1}{2}\sum_{j=1}^{n}\sum_{p=1}^{n}\sum_{q=1}^{n} \sqrt{Q}_{pj}\sqrt{Q}_{qj} \frac{\partial^2}{\partial x_p \partial x_q}$$

Where f_i denotes the ith element of function vector $\mathbf{f}$.

And the term $\mathbb{L}\mathbf{f}$ denotes a square matrix with its $(i, j)^{\text{th}}$ element being $\mathbb{L}_j f_i$, $(i, j = 1, \ldots, n)$:

$$\mathbb{L}_j f_i = \sum_{p=1}^{n} \sqrt{Q}_{pj} \frac{\partial f_i}{\partial x_p}$$

$(\mathbf{w}, \mathbf{y})$ is a pair of correlated n-dimensional Gaussian random variables, which can be generated from a pair of independent n-dimensional standard Gaussian random variables $(\mathbf{u}_1, \mathbf{u}_2)$ as follows:

$$\mathbf{w} = \sqrt{\delta}\mathbf{u}_1$$

$$\mathbf{y} = \frac{1}{2}\delta^{3/2}(\mathbf{u}_1 + \frac{\mathbf{u}_2}{\sqrt{3}})$$

Accordingly, the correlated Gaussian random variables $(\mathbf{w}, \mathbf{y})$ have the following three covariance matrices (with $\mathbf{I}_n$ being the identity matrix of size $n \times n$):

$$E[\mathbf{w}\mathbf{w}^T] = \delta \mathbf{I}_n$$

$$E[\mathbf{w}\mathbf{y}^T] = \frac{1}{2}\delta^2 \mathbf{I}_n$$

$$E[\mathbf{y}\mathbf{y}^T] = \frac{1}{3}\delta^3 \mathbf{I}_n$$

This CD-CKF filter includes two steps:

- Time update: compute the predicted density $p(\mathbf{x}_k|z_{1:k-1}) \sim \mathcal{N}(\hat{\mathbf{x}}_{k|k-1}, P_{k|k-1})$. Where:

$$\begin{aligned}
\hat{\mathbf{x}}_{k|k-1} &= E[\mathbf{x}_k|z_{1:k-1}] \\
&= E[f_d(\mathbf{x}_{k-1}, k-1)|z_{1:k-1}] \\
&= \int f_d(\mathbf{x}_{k-1}, k-1)p(\mathbf{x}_{k-1}|z_{1:k-1})d\mathbf{x}_{k-1} \\
&= \int f_d(\mathbf{x}_{k-1}, k-1) \times \mathcal{N}(\mathbf{x}_{k-1}; \hat{\mathbf{x}}_{k-1|k-1}, P_{k-1|k-1})d\mathbf{x}_{k-1} \quad (2.60)
\end{aligned}$$

$$\begin{aligned}
P_{k|k-1} &= E\left[(\mathbf{x}_k - \hat{\mathbf{x}}_{k|k-1})(\mathbf{x}_k - \hat{\mathbf{x}}_{k|k-1})^T|z_{1:k-1}\right] \\
&= \int f_d(\mathbf{x}_{k-1}, k-1)f_d(\mathbf{x}_{k-1}, k-1)^T \times \mathcal{N}(\mathbf{x}_{k-1}; \hat{\mathbf{x}}_{k-1|k-1}, P_{k-1|k-1})d\mathbf{x}_{k-1} \\
&+ \frac{\delta^3}{3}\int (\mathbb{L}f(\mathbf{x}_k, k))(\mathbb{L}f(\mathbf{x}_k, k))^T \times \mathcal{N}(\mathbf{x}_{k-1}; \hat{\mathbf{x}}_{k-1|k-1}, P_{k-1|k-1})d\mathbf{x}_{k-1} \\
&+ \frac{\delta^2}{2}\sqrt{\mathbf{Q}}\left(\int (\mathbb{L}f(\mathbf{x}_k, k)) \times \mathcal{N}(\mathbf{x}_{k-1}; \hat{\mathbf{x}}_{k-1|k-1}, P_{k-1|k-1})d\mathbf{x}_{k-1}\right)^T \\
&+ \frac{\delta^2}{2}\int (\mathbb{L}f(\mathbf{x}_k, k)) \times \mathcal{N}(\mathbf{x}_{k-1}; \hat{\mathbf{x}}_{k-1|k-1}, P_{k-1|k-1})d\mathbf{x}_{k-1}\left(\sqrt{\mathbf{Q}}\right)^T \\
&- \hat{\mathbf{x}}_{k|k-1}\hat{\mathbf{x}}_{k|k-1}^T + \delta\mathbf{Q} \quad (2.61)
\end{aligned}$$

To compute the predicted state and its error covariance more accurately at time k given $z_{1:k-1}$, the sampling interval $dt = t_k - t_{k-1}$ (t_k and t_{k-1} are

the discrete-time instances at k and $k-1$ respectively) is divided into m steps of length δ, where $\delta = dt/m$.

Let $\mathbf{x}_k^j$ denotes $\mathbf{x}$ at time $k + j\delta, (1 \le j \le m)$, the statistics of $\mathbf{x}_k^{j+1}$ are given by:

$$
\begin{aligned}
\hat{\mathbf{x}}_{k|k}^{j+1} &= \int f_d(\mathbf{x}_k^j, k + j\delta) \times \mathcal{N}(\mathbf{x}_k^j; \hat{\mathbf{x}}_{k|k}^j, P_{k|k}^j) d\mathbf{x}_k^j \\
&= \frac{1}{2n} \sum_{i=1}^{2n} \mathcal{X}_{i,k|k}^{*(j+1)} \quad \text{(by applying third-degree cubature rule)} \quad (2.62)
\end{aligned}
$$

Where

$$
\mathcal{X}_{i,k|k}^{*(j+1)} = f_d \left(\hat{\mathbf{x}}_{k|k}^j + \sqrt{P_{k|k}^j} \xi_i, k + j\delta \right) \tag{2.63}
$$

And the corresponding error covariance:

$$
\begin{aligned}
P_{k|k}^{j+1} &\approx \int f_d(\mathbf{x}_k^j, k + j\delta) f_d(\mathbf{x}_k^j, k + j\delta)^T \mathcal{N}(\mathbf{x}_k^j; \hat{\mathbf{x}}_{k|k}^j, P_{k|k}^j) d\mathbf{x}_k^j \\
&\quad + \frac{\delta^3}{3}(\mathbb{L}f(\mathbf{x}_k^j, k + j\delta))(\mathbb{L}f(\mathbf{x}_k^j, k + j\delta))^T \\
&\quad + \frac{\delta^2}{2}\sqrt{\mathbf{Q}} \left(\mathbb{L}f(\mathbf{x}_k^j, k + j\delta) \right)^T \\
&\quad + \frac{\delta^2}{2}\mathbb{L}f(\mathbf{x}_k^j, k + j\delta) \left(\sqrt{\mathbf{Q}} \right)^T \\
&\quad - \hat{\mathbf{x}}_{k|k}^j (\hat{\mathbf{x}}_{k|k}^j)^T + \delta\mathbf{Q} \\
&\approx \frac{1}{2n} \sum_{i=1}^{2n} \left(\mathcal{X}_{i,k|k}^{*(j+1)} \mathcal{X}_{i,k|k}^{*(j+1)T} \right) + \frac{\delta^3}{3}(\mathbb{L}f(\mathbf{x}_k^j, k + j\delta))(\mathbb{L}f(\mathbf{x}_k^j, k + j\delta))^T \\
&\quad + \frac{\delta^2}{2}\sqrt{\mathbf{Q}} \left(\mathbb{L}f(\mathbf{x}_k^j, k + j\delta) \right)^T + \frac{\delta^2}{2}\mathbb{L}f(\mathbf{x}_k^j, k + j\delta) \left(\sqrt{\mathbf{Q}} \right)^T \\
&\quad - \hat{\mathbf{x}}_{k|k}^{j+1} (\hat{\mathbf{x}}_{k|k}^{j+1})^T + \delta\mathbf{Q} \quad \text{(by applying third-degree cubature rule)}
\end{aligned}
$$
$$\tag{2.64}$$

- Measurement update (exactly the same as CKF measurement update): compute the posterior density $p(\mathbf{x}_k|z_{1:k}) \sim \mathcal{N}(\hat{\mathbf{x}}_{k|k}, P_{k|k})$. The filter likelihood density is assumed to be Gaussian:

$$
p(z_k|z_{1:k}) \sim \mathcal{N}(z_k; \hat{z}_{k|k-1}, P_{zz,k|k-1})
$$

Where the predicted measurement:

$$\hat{z}_{k|k-1} = \int h(\mathbf{x}_k, k) \times \mathcal{N}(\mathbf{x}_k; \hat{\mathbf{x}}_{k|k-1}, P_{k|k-1}) d\mathbf{x}_k$$

$$= \frac{1}{2n} \sum_{i=1}^{2n} \mathcal{Z}_{i,k|k-1} \quad \text{(by applying third-degree cubature rule)} \quad (2.65)$$

Where

$$\mathcal{Z}_{i,k|k-1} = h(\hat{\mathbf{x}}_{k|k-1} + \sqrt{P_{k|k-1}}\xi_i, k-1) \qquad (2.66)$$

and the associated covariance:

$$P_{zz,k|k-1} = \int h(\mathbf{x}_k, k) h(\mathbf{x}_k, k)^T \times \mathcal{N}(\mathbf{x}_k; \hat{\mathbf{x}}_{k|k-1}, P_{k|k-1}) d\mathbf{x}_k$$

$$- \hat{z}_{k|k-1} \hat{z}_{k|k-1}^T + R_k$$

$$= \frac{1}{2n} \sum_{i=1}^{2n} \left(\mathcal{Z}_{i,k|k-1} \mathcal{Z}_{i,k|k-1}^T \right) - \hat{z}_{k|k-1} \hat{z}_{k|k-1}^T + R_k \qquad (2.67)$$

The cross-covariance between the state and the measurement is given by:

$$P_{xz,k|k-1} = \int \mathbf{x}_k h(\mathbf{x}_k, k)^T \times \mathcal{N}(\mathbf{x}_k; \hat{\mathbf{x}}_{k|k-1}, P_{k|k-1}) d\mathbf{x}_k - \hat{\mathbf{x}}_{k|k-1} \hat{z}_{k|k-1}^T$$

$$= \frac{1}{2n} \sum_{i=1}^{2n} \left(\mathcal{X}_{i,k|k-1} \mathcal{Z}_{i,k|k-1}^T \right) - \hat{\mathbf{x}}_{k|k-1} \hat{z}_{k|k-1}^T \qquad (2.68)$$

Where:

$$\mathcal{X}_{i,k|k-1} = \hat{\mathbf{x}}_{k|k-1} + \sqrt{P_{k|k-1}}\xi_i \qquad (2.69)$$

Thus, the conditional Gaussian density of the joint state and the measurement can be written as:

$$p\left(\begin{bmatrix} \mathbf{x}_k^T & z_k^T \end{bmatrix} | z_{1:k} \right) \sim \mathcal{N} \left(\begin{bmatrix} \hat{\mathbf{x}}_{k|k-1} \\ \hat{z}_{k|k-1} \end{bmatrix}, \begin{bmatrix} P_{k|k-1} & P_{xz,k|k-1} \\ P_{xz,k|k-1}^T & P_{zz,k|k-1} \end{bmatrix} \right)$$

From which the posterior density $p(\mathbf{x}_k|z_{1:k}) \sim \mathcal{N}(\hat{\mathbf{x}}_{k|k}, P_{k|k})$ is computed on the receipt of a new measurement z_k through the computation of the so-called Kalman gain K_k:

$$\hat{\mathbf{x}}_{k|k} = \hat{\mathbf{x}}_{k|k-1} + K_k(z_k - \hat{z}_{k|k-1})$$
$$P_{k|k} = P_{k|k-1} - K_k P_{zz,k|k-1} K_k^T$$
$$K_k = P_{xz,k|k-1} P_{zz,k|k-1}^{-1}$$

2.4.1 CD-CKF Algorithm

A. m-steps Time update: The sampling interval dt is divided into m steps of length δ, where $\delta = dt/m$. For $k + j\delta, j = 1, \ldots, m$

  1) Factorize

$$P_{k|k}^{j} = S_{k|k}^{j} S_{k|k}^{jT} \qquad (2.70)$$

  2) Evaluate the cubature points $(i = 1, 2, \ldots, 2n)$

$$\mathcal{X}_{i,k|k}^{j} = \hat{x}_{k|k}^{j} + S_{k|k}^{j} \xi_i \qquad (2.71)$$

  Where the cubature-point set ξ is defined as:

$$\xi_i = \begin{cases} \sqrt{n}e_i & \text{for } i = 1, \ldots, n \\ -\sqrt{n}e_i & \text{for } i = n+1, \ldots, 2n \end{cases}$$

  3) Evaluate the propagated cubature points $(i = 1, 2, \ldots, 2n)$

$$\mathcal{X}_{i,k|k}^{*(j+1)} = f_d\left(\mathcal{X}_{i,k|k}^{j}, k + j\delta\right) \qquad (2.72)$$

  4) Estimate the predicted state

$$\hat{x}_{k|k}^{j+1} = \frac{1}{2n} \sum_{i=1}^{2n} \mathcal{X}_{i,k|k}^{*(j+1)} \qquad (2.73)$$

  5) Estimate the predicted error covariance

$$\begin{aligned}
P_{k|k}^{j+1} = {} & \frac{1}{2n} \sum_{i=1}^{2n} \left(\mathcal{X}_{i,k|k}^{*(j+1)} \mathcal{X}_{i,k|k}^{*(j+1)T}\right) \\
& + \frac{\delta^3}{3}(\mathbb{L}f(\hat{\mathbf{x}}_k^j, k + j\delta))(\mathbb{L}f(\hat{\mathbf{x}}_k^j, k + j\delta))^T \\
& + \frac{\delta^2}{2}\sqrt{\mathbf{Q}}\left(\mathbb{L}f(\hat{\mathbf{x}}_k^j, k + j\delta)\right)^T + \frac{\delta^2}{2}\mathbb{L}f(\hat{\mathbf{x}}_k^j, k + j\delta)\left(\sqrt{\mathbf{Q}}\right)^T \\
& - \hat{\mathbf{x}}_{k|k}^{j+1}(\hat{\mathbf{x}}_{k|k}^{j+1})^T + \delta\mathbf{Q}
\end{aligned} \qquad (2.74)$$

  6) Increase j by one and repeat the steps (2.70)–(2.74) until j reaches m.

B. Measurement update:

  1) Factorize

$$P_{k+1|k} = S_{k+1|k} S_{k+1|k}^{T} \qquad (2.75)$$

2) Evaluate the cubature points $(i = 1, 2, \ldots, 2n)$

$$\mathcal{X}_{i,k+1|k} = \hat{x}_{k+1|k} + S_{k+1|k}\xi_i \qquad (2.76)$$

3) Evaluate the propagated cubature points $(i = 1, 2, \ldots, 2n)$

$$\mathcal{Z}_{i,k+1|k} = h(\mathcal{X}_{i,k+1|k}, k+1) \qquad (2.77)$$

4) Estimate the predicted measurement

$$\hat{z}_{k+1|k} = \frac{1}{2n} \sum_{i=1}^{2n} \mathcal{Z}_{i,k+1|k} \qquad (2.78)$$

5) Estimate the innovation covariance matrix

$$P_{zz,k+1|k} = \frac{1}{2n} \sum_{i=1}^{2n} \left(\mathcal{Z}_{i,k+1|k} \mathcal{Z}_{i,k+1|k}^T \right) - \hat{z}_{k+1|k}\hat{z}_{k+1|k}^T + R_{k+1} \qquad (2.79)$$

6) Estimate the cross-covariance matrix

$$P_{xz,k+1|k} = \frac{1}{2n} \sum_{i=1}^{2n} \left(\mathcal{X}_{i,k+1|k} \mathcal{Z}_{i,k+1|k}^T \right) - \hat{\mathbf{x}}_{k+1|k}\hat{z}_{k+1|k}^T \qquad (2.80)$$

7) Estimate the Kalman gain

$$\mathbf{K}_{k+1} = P_{xz,k+1|k} P_{zz,k+1|k}^{-1} \qquad (2.81)$$

8) Estimate the updated state

$$\hat{x}_{k+1|k+1} = \hat{x}_{k+1|k} + \mathbf{K}_{k+1}(z_{k+1} - \hat{z}_{k+1|k}) \qquad (2.82)$$

9) Estimate the corresponding error covariance

$$P_{k+1|k+1} = P_{k+1|k} - \mathbf{K}_{k+1} P_{zz,k+1|k} \mathbf{K}_{k+1}^T \qquad (2.83)$$

2.4.2 Square-root Continuous-Discrete Cubature Kalman Filter

The square-root Continuous-Discrete Cubature Kalman Filter essentially propagates square-root factor of $P_{k|k}$ $(S_{k|k})$ avoiding matrix square-rooting operations

while preserving the symmetry and positive definiteness of the covariance matrix and improving numerical accuracy. Matrix triangular factorizations or triangularizations (e.g., the QR decomposition) is used for covariance updates. The triangularization essentially computes a triangular square-root factor of the covariance without square-rooting a squared-matrix form of the covariance. The triangularization algorithm (e.g., the QR decomposition) is denoted as $S = Tria(A)$ where S is a lower triangular matrix. The matrices A and S are related as follows: Let R be an upper triangular matrix obtained from the QR decomposition on A^T ; then $S = R^T$ [3].

Square-root CD-CKF Algorithm

A. m-steps Time update: The sampling interval dt is divided into m steps of length δ, where $\delta = dt/m$. For $k + j\delta, j = 1, \ldots, m$

1) $S^j_{k|k}$ is available.

2) Evaluate the cubature points $(i = 1, 2, \ldots, 2n)$

$$\mathcal{X}^j_{i,k|k} = \hat{x}^j_{k|k} + S^j_{k|k}\xi_i \tag{2.84}$$

Where the cubature-point set ξ is defined as:

$$\xi_i = \begin{cases} \sqrt{n}e_i & \text{for } i = 1, \ldots, n \\ -\sqrt{n}e_i & \text{for } i = n + 1, \ldots, 2n \end{cases}$$

3) Evaluate the propagated cubature points $(i = 1, 2, \ldots, 2n)$

$$\mathcal{X}^{*(j+1)}_{i,k|k} = f_d\left(\mathcal{X}^j_{i,k|k}, k + j\delta\right) \tag{2.85}$$

4) Estimate the predicted state

$$\hat{x}^{j+1}_{k|k} = \frac{1}{2n}\sum_{i=1}^{2n}\mathcal{X}^{*(j+1)}_{i,k|k} \tag{2.86}$$

5) Estimate the square-root factor of the predicted error covariance

$$S^{j+1}_{k|k} = Tria\left(\left[\mathscr{X}^{*(j+1)}_{k|k} \quad \sqrt{\delta}(\frac{\delta}{2}\sqrt{\mathbf{Q}}\mathbb{L}f(\hat{\mathbf{x}}^j_k, k + j\delta)\right.\right.$$
$$\left.\left.\sqrt{\frac{\delta^3}{12}}\mathbb{L}f(\hat{\mathbf{x}}^j_k, k + j\delta))\right]\right) \tag{2.87}$$

Where the weighted centered matrix:

$$\mathscr{X}^{*(j+1)}_{k|k} = \frac{1}{\sqrt{2n}}\left[\mathcal{X}^{*(j+1)}_{1,k|k} - \hat{x}^{j+1}_{k|k} \quad \mathcal{X}^{*(j+1)}_{2,k|k} - \hat{x}^{j+1}_{k|k} \quad \cdots \quad \mathcal{X}^{*(j+1)}_{2n,k|k} - \hat{x}^{j+1}_{k|k}\right]$$

29

B. Measurement update:

1) Evaluate the cubature points $(i = 1, 2, \ldots, 2n)$

$$\mathcal{X}_{i,k+1|k} = \hat{x}_{k+1|k} + S_{k+1|k}\xi_i \qquad (2.88)$$

2) Evaluate the propagated cubature points $(i = 1, 2, \ldots, 2n)$

$$\mathcal{Z}_{i,k+1|k} = h(\mathcal{X}_{i,k+1|k}) \qquad (2.89)$$

3) Estimate the predicted measurement

$$\hat{z}_{k+1|k} = \frac{1}{2n} \sum_{i=1}^{2n} \mathcal{Z}_{i,k+1|k} \qquad (2.90)$$

4) Compute the matrices $\mathbf{T}_{11}, \mathbf{T}_{21}, \mathbf{T}_{22}$ using the triangularization algorithm:

$$\begin{pmatrix} \mathbf{T}_{11} & \mathbf{0} \\ \mathbf{T}_{21} & \mathbf{T}_{22} \end{pmatrix} = Tria \begin{pmatrix} \mathscr{Z}_{k+1|k} & S_{R,k+1} \\ \mathscr{X}_{k+1|k} & \mathbf{0} \end{pmatrix}$$

Where:

$$\mathscr{X}_{k+1|k} = \frac{1}{\sqrt{2n}}\left[\mathcal{X}_{1,k+1|k} - \hat{x}_{k+1|k} \quad \ldots \quad \mathcal{X}_{2n,k+1|k} - \hat{x}_{k+1|k}\right]$$

$$\mathscr{Z}_{k+1|k} = \frac{1}{\sqrt{2n}}\left[\mathcal{Z}_{1,k+1|k} - \hat{z}_{k+1|k} \quad \ldots \quad \mathcal{Z}_{2n,k+1|k} - \hat{z}_{k+1|k}\right]$$

5) Estimate the Kalman gain

$$\mathbf{K}_{k+1} = \frac{\mathbf{T}_{21}}{\mathbf{T}_{11}} \qquad (2.91)$$

6) Estimate the updated state

$$\hat{x}_{k+1|k+1} = \hat{x}_{k+1|k} + \mathbf{K}_{k+1}(z_{k+1} - \hat{z}_{k+1|k}) \qquad (2.92)$$

7) The square-root factor of the corresponding error covariance is given by:

$$S_{k+1|k+1} = \mathbf{T}_{22} \qquad (2.93)$$

30

2.5 Adaptive Design Optimization

Collecting informative measurements is essential in order to ensure proper model inference and/or unknown parameter estimation. Such measurements can also be critical when experiments are costly, time-consuming, or offer a limited quantity of observables.

Optimal design or optimal experiment design refers to a statistical technique that finds the best experiment that produces the most informative measurements and experimental outcome about the underlying model and/or its unknown parameters.

Given the mathematical description of a model and the design space which consists of all possible values of design variables that are controlled by the experimenter, each potential design is treated as a gamble whose payoff is determined by the outcome of an experiment conducted with that design [62]. The payoff represents some measure of the goodness or the utility of the design [62]. The idea is to estimate the utilities of hypothetical experiments carried out with each design so that an "expected utility" of each design can be computed. The expected utility of a given design is computed as the average payoffs across all possible outcomes that could be observed in an experiment carried out with the chosen design [62]. Finally, the optimal design is identified as the design with highest expected utility.

Adaptive design optimization (ADO) is an integrative approach to experimentation that leverages the complementary strengths of design optimization and data modeling [62]. The result is an efficient and informative method of scientific inference [62].

ADO is formulated as a Bayesian sequential optimization algorithm that is executed over the course of an experiment, where the optimal experimental design is updated at intervals (referred as "stages") during the experiment. The algorithm is essentially a Bayesian decision problem where, at each stage, the most informative design is chosen based on the observations of the previous experiments [55]. Specifically, on each stage, given the current knowledge (prior) about statistical model of data, the optimal design with the highest expected utility is identified. Then an experiment is conducted with the optimal design, and measured outcomes are observed and recorded. The observations are used to update the priors of current stage to the posteriors using Bayes theorem. The updated posteriors of current stage will serve as priors for the next stage of the experiment. This iterative process continues until a suitable stopping criterion is met.

The criterion that identifies a design as informative often depends on the objectives of the experimenter. The experiment that yields the most precise parameter

estimates may not be the most effective at discriminating among competing models [55].

Solving for the optimal design at each stage is in general a nontrivial optimization problem since the computation entails simultaneous optimization and high-dimensional integration, which can be analytically intractable for the complex, nonlinear models as often used in many real-world problems [55].

At each stage, the objective of ADO is to find the best design d^* by solving the following optimization problem:

$$d^* = \operatorname*{argmax}_{d \in \mathbb{D}} U(d) \tag{2.94}$$

Where $\mathbb{D}$ is the design space and $U(d)$ is a real-valued function called the global utility function that is a metric of goodness or utility of design d.

2.5.1   ADO for parameter estimation

Suppose that we have a model that mathematically describes our system, but it has some unknown parameters θ that we need to estimate. An experimental design d specifies the choice of the external input to our system. The task is to find the best design (or input) that will give the most informative observations about the unknown parameters.

The global utility function is defined as:

$$U(d) = \iint u(d, \theta, y) p(y|\theta, d) p(\theta) dy d\theta \tag{2.95}$$

Where θ is the unknown parameter vector of the model, y is the outcome vector resulting from a hypothetical imaginary experiment conducted with design d, and $u(d, \theta, y)$ is referred to as the local utility function of design d. It measures the utility of a hypothetical experiment carried out with design d when the parameters of the model take the value θ, and the outcome y is observed.

Thus, $U(d)$ represents the expected value of the local utility function $u(d, \theta, y)$ averaged over the full parameter space, and all possible observations, taken with respect to parameter prior $p(\theta)$ and the probability distribution $p(y|\theta, d)$, respectively [62].

To evaluate the global utility $U(d)$, one must provide explicit specifications for three functions: the parameter prior $p(\theta)$; the probability distribution given parameter θ and design d, $p(y|\theta, d)$; and the local utility function $u(d, \theta, y)$ [62].

2.5.2 ADO for model discrimination

In the case when we do not have an exact model description of our system. Thus we propose a set of models and the task consists of finding the best design (or input) that will give the most informative observations about the most plausible model from a pool of $\mathcal{M}$ potential model candidates.

The global utility function is defined as:

$$U(d) = \sum_{m=1}^{\mathcal{M}} p(m) \iint u(d, \theta_m, y_m) p(y_m | \theta_m, d) p(\theta_m) dy_m d\theta_m \tag{2.96}$$

Where $m = \{1, 2, \ldots, \mathcal{M}\}$ is one of a set of $\mathcal{M}$ models being considered, d is a design, y_m is the outcome of a hypothetical imaginary experiment with design d under model m, and θ_m is a parameterization of model m.

Thus, $U(d)$ represents the expected value of the local utility function $u(d, \theta_m, y_m)$ averaged over all models, the full parameter space, and all possible hypothetical observations, taken with respect to the model prior $p(m)$, parameter prior $p(\theta_m)$ and the probability distribution $p(y_m \theta_m, d)$, respectively [62].

Again, we must provide explicit specifications for the model and parameter priors $p(m)$ and $p(\theta_m)$; the probability distribution given parameter θ_m and design d, $p(y_m \theta_m, d)$; and the local utility function $u(d, \theta_m, y_m)$ [62].

2.5.3 Bayesian Updating of the Optimal Design

The above formulations of ADO for both parameter estimation and model discrimination are presented for finding the optimal design for a single stage. To extend this framework for sequential ADO, let us introduce the subscript symbol $s = \{1, 2, 3, \ldots\}$ to denote an ADO stage. Suppose that at stage s the optimal design d_s^* was obtained by maximizing $U(d)$ on the basis of:

- A set of parameter prior, $p_s(\theta)$ for the case of parameter estimation.

- A set of model and parameter priors, $p_s(m)$ and $p_s(\theta_m)$ with $m = \{1, 2, \ldots, \mathcal{M}\}$, respectively, for the case of model discrimination.

Suppose that an experiment was subsequently carried out with design d_s^*, and an outcome vector z_s was observed. The observed data are used to update the priors to the posteriors by Bayes rule:

- For parameter estimation:

$$p_{s+1}(\theta) = \frac{p(z_s | \theta, d_s^*) p_s(\theta)}{\int p(z_s | \theta, d_s^*) p_s(\theta) d\theta}$$
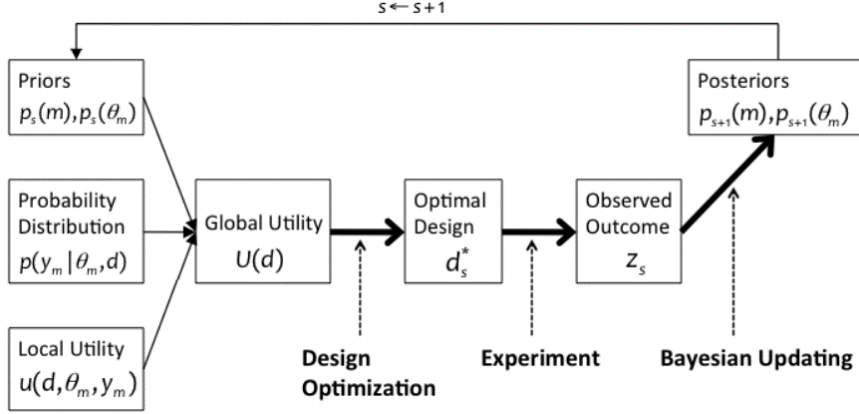
Figure 2.6: Schematic illustration of the steps involved in ADO.

- For model discrimination:

$$p_{s+1}(\theta_m) = \frac{p(z_s|\theta_m, d_s^*)p_s(\theta_m)}{\int p(z_s|\theta_m, d_s^*)p_s(\theta_m)d\theta_m}$$

$$p_{s+1}(m) = \frac{p_0(m)}{\sum_{i=1}^{\mathcal{M}} p_0(i)BF_{i,m}(z_s|d_s^*)}$$

Where $m = \{1, 2, \ldots, \mathcal{M}\}$, and $BF_{i,m}(z_s|d_s^*)$ denotes the Bayes factor defined as the ratio of the marginal likelihood of model i to that of model m,

$$BF_{i,m}(z_s|d_s^*) = \frac{\int p(z_s|\theta_i, d_s^*)p_s(\theta_i)d\theta_i}{\int p(z_s|\theta_m, d_s^*)p_s(\theta_m)d\theta_m}$$

Fig. 2.6 shows a diagram of basic elements and processes of the ADO algorithm.

2.5.4 Local utility function

The choice of the local utility function depends on whether we want to design an experiment for parameter estimation or for model selection. In designing optimal experiments for parameter estimation, different proposed local utility functions are based some metrics of the Fisher information matrix (FIM) which is defined as the expectation of the second derivative of the log-likelihood of the system output function with respect to the change in the parameters:

- A-optimality: seeks to minimize the trace of the inverse of the information matrix.

$$u(d, \theta, y) = -\text{trace}(FIM^{-1})$$

- D-optimality: seeks to maximize the determinant of the Fisher information matrix.

$$u(d, \theta, y) = \det(FIM)$$

- E-optimality: maximizes the minimum eigenvalue of the Fisher information matrix.

$$u(d, \theta, y) = \lambda_{\min}(FIM)$$

- T-optimality: This criterion maximizes the trace of the information matrix.

$$u(d, \theta, y) = \text{trace}(FIM)$$

In designing optimal experiments for model discrimination, one can formulate local utility function motivated from information theory. The local utility of a design for a given model and experiment outcome is the log ratio of the posterior probability to the prior probability of that model [55]:

$$u(d, \theta_m, y_m) = \frac{p(m|y, d)}{p(m)}$$

Chapter 3

Simulation Models

In this chapter, we will introduce the mathematical description of various simulation non-linear models used to demonstrate the performance of the proposed techniques and algorithms aimed to improve the performance of Kalman filter techniques in model fitting (hidden states and parameters estimation) and model selection in the context of neural state estimation from EEG and fMRI (functional magnetic resonance imaging) recordings as specific examples of physiological dynamical system modeling. The presented models herein are examples of EEG generation models based on non-linear stochastic neuronal models of electric potential generation, and fMRI models based on non-linear stochastic models of BOLD (Blood-oxygen-level dependent) signals. Moreover, we will demonstrate the proposed algorithms performance in several simulated scenarios that are derived from benchmark nonlinear problems.

We will present the simulation dynamical models and derive their state-space representations. State-space formulations of dynamical systems provide a particularly flexible framework for predictive models since they allow for describing the system response to both controlled and random inputs in terms of a measurement function $\mathbf{h}$ of the output $\mathbf{z}_t$ (the static observation equation (3.2)) and a dynamic evolution function $\mathbf{f}$ on the internal system states $\mathbf{x}_t$ (the process equation (3.1)) as determined by a set of model parameters θ

$$\dot{\mathbf{x}}_t = \mathbf{f}_\theta\left(\mathbf{x}_t, \mathbf{I}_t\right) + \mathbf{w}_t \tag{3.1}$$

$$\mathbf{z}_t = \mathbf{h}_\theta\left(\mathbf{x}_t, \mathbf{I}_t\right) + \mathbf{e}_t \tag{3.2}$$

Moreover, it is noted that this approach allows for a distinct, more natural treatment of the uncertainty in the dynamics (the process noise $\mathbf{w}_t$) and the recording imperfections and noise (the measurement noise $\mathbf{e}_t$).

A discretized form of the state-space equations can be used to provide future predictions of the states $\mathbf{x}_k$ using the knowledge on its current value (Marko-

vian property), thereby simplifying computations in a Bayesian Framework. The celebrated Kalman filtering approach is an efficient recursive Bayesian estimator that has long been applied to state prediction and (joint) parameter identification problems under Gaussian-distributed noise in linear systems. Kalman filtering extensions, such as the Unscented Kalman Filter and more recently the Cubature Kalman Filter, allow for efficient state estimation under nonlinearities in both the process and observation equations, thus significantly increasing the utility of the Kalman framework in modeling of biophysical phenomena.

We will describe the benchmark nonlinear models, namely the Van der Pol oscillators and Double well. We then introduce simplified models of continuous neural activity (NA) dynamics and associated electric potentials (EP) recordings based on simplified anatomical and physiological properties of the sensory neocortex. Two types of neuronal models will be presented (a) conductance-based neuronal models: a simplified Morris–Lecar model to a describe the neuronal dynamics of different layers of a cortical column, and (b) Jansen neuronal model which is a model for cortical column aimed to emulate the EEG activity of a cortical area. Finally, we will present the hemodynamic model for BOLD signal generation which relates input neural activity (NA) to measured BOLD signals.

3.1   Van der Pol Oscillator

The Van der Pol is a non-conservative oscillator with non-linear damping. It is mathematically represented by the following second-order differential equation:

$$\ddot{x} - \mu(1 - x^2)\dot{x} + x = 0 \tag{3.3}$$

where x is the oscillator position and μ is a constant indicating the strength of damping. The second-order differential equation can be transformed to first order system using the transformation $x_2 = \dot{x}_1$:

$$\begin{cases} \dot{x}_1 = x_2 \\ \dot{x}_2 = \mu(1 - x_1^2)x_2 - x_1 \end{cases} \tag{3.4}$$

where x_1 is the oscillator position and the state vector $\mathbf{x} = [x_1 \ x_2]^T$. For estimation purposes we consider the following two cases.

- Single forced oscillator: A Van der Pol oscillator can be driven by an external input here assumed periodic of the form $I(t) = A\sin(wt)$, as follows

$$\begin{cases} \dot{x}_1 = x_2 \\ \dot{x}_2 = \mu(1 - x_1^2)x_2 - x_1 - I(t) \end{cases} \tag{3.5}$$

- Heterogeneous network of oscillators: We consider a set of N non-identical oscillators connected in a ring configuration (each oscillator coupled to its two nearest neighbors) is considered [63, 64]. Each oscillator i is represented by the following second-order differential equation:

$$\ddot{x}^{(i)} - \mu^{(i)}\big(1 - (x^{(i)})^2\big)\dot{x}^{(i)} + x^{(i)} = K\big(x^{(i-1)} - 2x^{(i)} + x^{(i+1)}\big)$$
$$i = 1, \ldots, N \tag{3.6}$$

where K is the coupling parameter, and it is assumed that only the first oscillator $(i = 1)$ is driven by an external input $I(t)$.

$$\begin{cases} \dot{x}_1^{(1)} = x_2^{(1)} \\ \dot{x}_2^{(1)} = \mu^{(1)}\big(1 - (x_1^{(1)})^2\big)x_2^{(1)} - x_1^{(1)} - I(t) + K\big(x^{(N)} - 2x^{(1)} + x^{(2)}\big) \\ \\ \dot{x}_1^{(i)} = x_2^{(i)} \\ \dot{x}_2^{(i)} = \mu^{(i)}\big(1 - (x_1^{(i)})^2\big)x_2^{(i)} - x_1^{(i)} + K\big(x^{(i-1)} - 2x^{(i)} + x^{(i+1)}\big) \\ \quad i = 2, \ldots, N \end{cases} \tag{3.7}$$

Both the single and coupled oscillators systems are assumed to be subjected to random process noise and observation noise. Specifically, their dynamics are governed by a set of stochastic differential equations, and can be formulated in state-space form:

Process Equation: $\qquad\qquad\qquad \dot{\mathbf{x}}(t) = f(\mathbf{x}(t), I(t)) + \mathbf{\Gamma} \qquad\qquad$ (3.8)

Measurement Equation: $\qquad\qquad\qquad \mathbf{z}_k = h(\mathbf{x}_k) + \mathbf{w}_k \qquad\qquad$ (3.9)

where $\mathbf{x}(t) \in \mathbb{R}^n$, ($n = 2$ for the single oscillator system, $n = 2N$ for the coupled oscillators system) is the state vector at time t, $I(t)$ is the external periodic input, $\mathbf{z}_k \in \mathbb{R}^d$ ($d = 1$ for the single oscillator system, $d < N$ for the coupled oscillators system) is the measurement at discrete time t_k, $f : \mathbb{R}^n \times \mathbb{R} \to \mathbb{R}^n$ is the drift coefficient, $h : \mathbb{R}^n \times \mathbb{R} \to \mathbb{R}^d$ is the measurement function, $\mathbf{\Gamma} \in \mathbb{R}^n$ and $\mathbf{w}_k \in \mathbb{R}^d$ are vectors of random Gaussian noise with zero mean and covariance Q and R respectively.

The observations collected from this system are the oscillators positions. For the single forced oscillator case, noisy observations of the oscillator position x_1 are collected. Whereas for the heterogeneous network of oscillators only a subset of oscillators positions $x_1^{(j)}, j \in d < N$ serves as observations. Fig. 3.1 shows the behavior of a single noisy Van der Pol oscillator variables for the presented input with damping constant $\mu = 2$. The model was simulated for $50sec$ with sampling rate $dt = 0.1sec$.
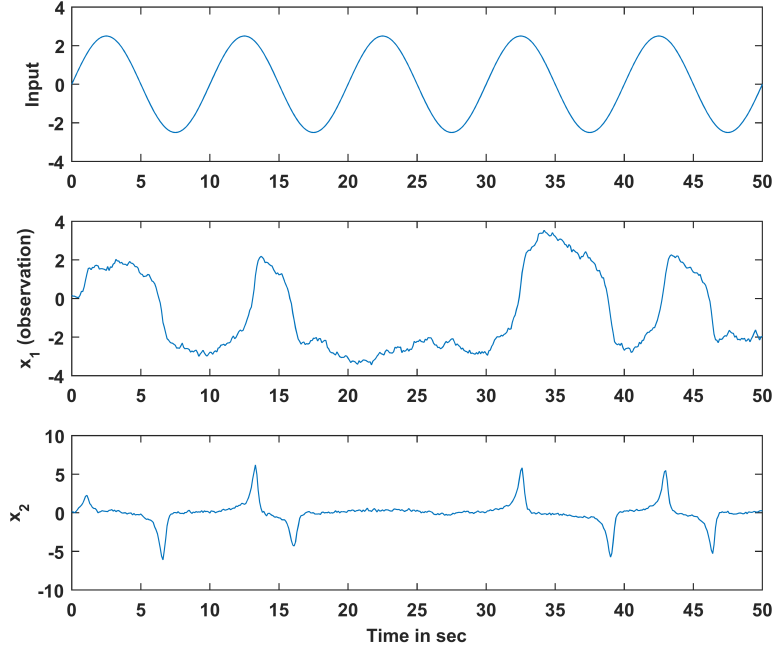
Figure 3.1: Single noisy Van der Pol oscillator variables for a given input (top plot).

3.2 Double Well

Another system to be considered is the double-well potential model that represents a dissipative system with bimodal variability [30]. The model has a single state and is driven by a periodic input:

$$\dot{x} = \frac{ax}{1 + x^2} - \frac{x}{16} + \frac{I(t)}{4} = f(x, I) \tag{3.10}$$

where $I(t) = A\sin(wt)$ is the input and a is a constant parameter.

When subjected to noise, the above dynamics are transformed to stochastic differential equation governing the system evolution. By further assuming that only a set of noisy discrete observations are available, a hybrid state-space representation of this system ensues, as follows:

Process Equation: $$\dot{x}(t) = f(x(t), I) + \Gamma \tag{3.11}$$
Measurement Equation: $$z_k = h(x_k) + w_k \tag{3.12}$$

where $\Gamma \in \mathbb{R}$ and $w_k \in \mathbb{R}$ are random Gaussian noise with zero mean and variance Q and R respectively. In the measurement equation, $z_k \in \mathbb{R}$ is the measurement at discrete time t_k and $h : \mathbb{R} \times \mathbb{R} \to \mathbb{R}$, $h(x_k) = \frac{x_k^2}{4}$ is the measurement function having a quadratic form which makes this system a challenging inversion problem.
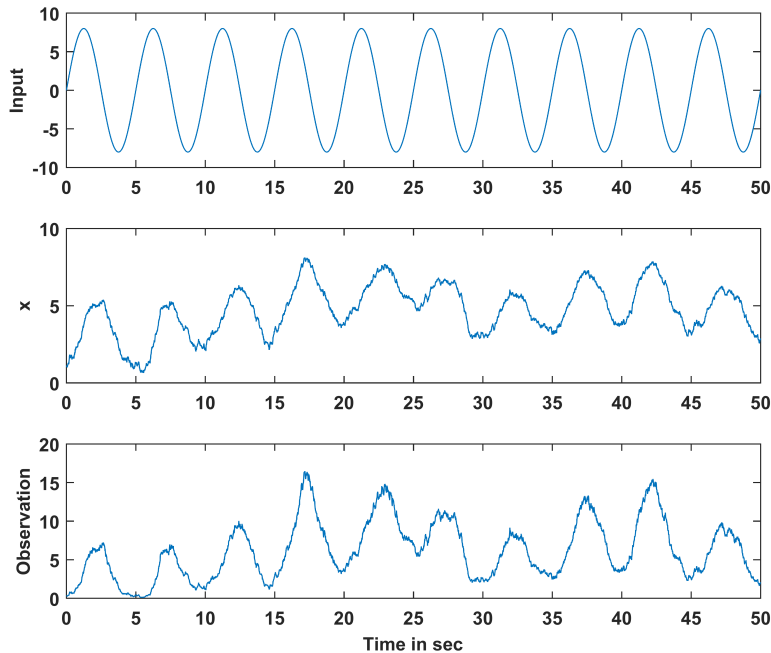
Figure 3.2: Double well behavior for the presented input (top plot).

Fig. 3.2 shows the behavior of a noisy double well system for the presented input with constant parameter $a = 2$. The model was simulated for $50sec$ with sampling rate $dt = 0.1sec$.

3.3 Conductance-Based Neuronal Model

3.3.1 Simple Area Neuronal Model

We will adopt a simplified neuronal network based on Morris–Lecar model. The network consists of a single neuronal population driven by an external excitatory input. The neuronal population has a self-inhibition connection in order to balance the total excitation from the external input (Fig. 3.4). The dynamics of the neuronal membrane potential are given by the following stochastic differential equation [65]:

$$C\dot{V} \quad = \quad g_L(V_L - V) + g_I(V_I - V) + I + \Gamma_V \qquad (3.13)$$

Where C is the membrane capacitance, V is the membrane potential, I is the external excitatory input current, Γ_V is Gaussian noise, g_I represents the inhibitory conductance, V_L, and V_I are the reversal potentials, and V_R is the threshold potential.

40
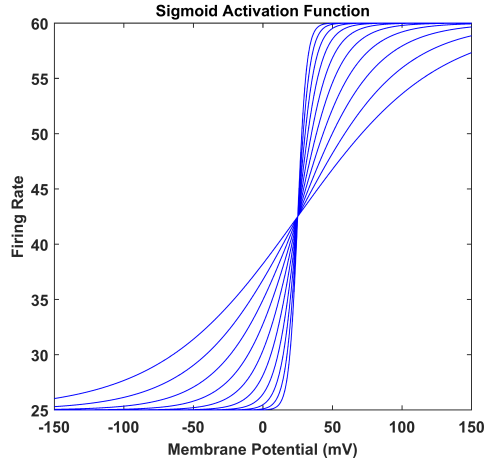
Figure 3.3: Sigmoid activation function for different values of α, as α increases the function becomes highly nonlinear.

The inhibitory conductance can also be described by stochastic differential equation whose dynamics depend on the pre-synaptic input ς and a characteristic rate constant κ [66]:

$$\dot{g}_I = \kappa(\varsigma - g_I + \tilde{g}_I) + \Gamma_I \tag{3.14}$$

$$\varsigma_I = \gamma\sigma(V - V_R) \tag{3.15}$$

Where the pre-synaptic input to the neuronal population, denoted by ς, is the firing rate in that population times a coupling parameter γ, $\tilde{g}_I$ is the mean (static) inhibitory conductances, Γ_I is Gaussian noise, and $\sigma(.)$ is a sigmoid activation function that transforms the post-synaptic potential to firing rate and is given by [67]:

$$\sigma(V - V_R) = \frac{1}{1 + e^{-\alpha(V - V_R)}} \tag{3.16}$$

Where V_R is a threshold potential, and α is a constant that determines the slope (voltage sensitivity) of the activation function (Fig. 3.3).

The stochastic differential equations describing the simple neuronal area can be formulated in state-space model of the form:

Process Equation: $$\dot{\mathbf{x}}(t) = f(\mathbf{x}(t), I) + \mathbf{\Gamma} \tag{3.17}$$

Measurement Equation: $$z_k = h(\mathbf{x}_k) + w_k \tag{3.18}$$

Where $\mathbf{x}(t) \in \mathbb{R}^n$ is the state vector of the dynamic system at time t, I is the exogenous input, $z_k \in \mathbb{R}^d$ is the measurement at discrete time t_k, $f : \mathbb{R}^n \times \mathbb{R} \to \mathbb{R}^n$ is the drift coefficient, $h : \mathbb{R}^n \times \mathbb{R} \to \mathbb{R}^d$ is the measurement function, $\mathbf{\Gamma} \in \mathbb{R}^n$ and $w_k \in \mathbb{R}^d$ are vectors of random Gaussian noise with zero mean and covariance Q and R respectively.

41
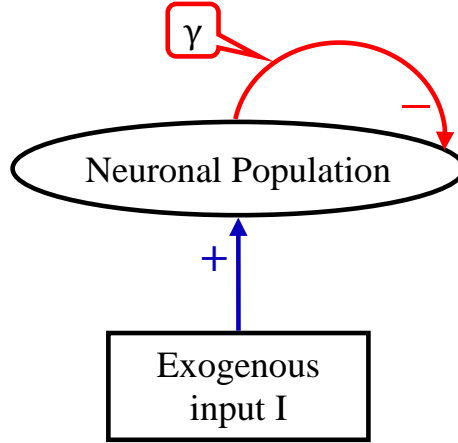
Figure 3.4: Simple neuronal model: a single self-inhibitory neuronal population driven by excitatory external input.

The state vector $\mathbf{x}$ comprises the membrane potential and the inhibitory conductance, and $f(.)$ is a vector that comprises the equations of motion of each state:

$$\mathbf{x} = \begin{bmatrix} V & g_I \end{bmatrix}^T$$

$$f(\mathbf{x}(t), I) = \begin{bmatrix} \frac{1}{C}\left[g_L(V_L - V) + g_I(V_I - V) + I\right] \\ \kappa[\gamma\sigma(V - V_R) - g_I + \tilde{g}_I] \end{bmatrix}$$

The measurement equation function $h(x_k)$ depends on the membrane potentials V:

$$h(\mathbf{x}_k) = V$$

3.3.2 Multi-Area Neuronal Model

Single Area Model Description

As a basic building block of single area, we employ a simplified Morris–Lecar model to a describe the neuronal dynamics of different layers of a cortical column. A cortical column is a vertical structure and hypothesized to represent a basic functional unit of sensory processing, which contains densely connected neurons that are stacked throughout the cortical depth into anatomically distinct layers and that share similar response properties [57]. Herein, a cortical column is summarized to consist of of three primary layers (Fig. 3.5) namely:

- Granular layer that containing excitatory spiny stellate cells.

- Supra-granular layer containing inhibitory interneurons.

42
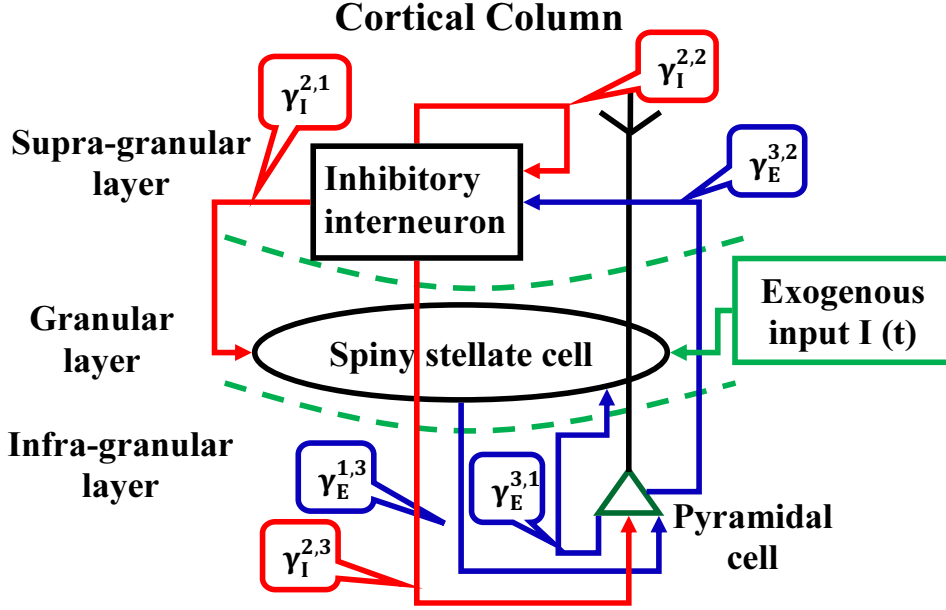
Figure 3.5: Cortical column architecture segregated into three layers. Intrinsic connections between layers are illustrated with arrows: red arrows are inhibitory, and blue arrows are excitatory.

- Infra-granular layer consisting of excitatory pyramidal cells.

The dynamics of the membrane potential are formulated as a parallel RC circuit where capacitive synaptic current flow balances the sum of all currents across the membrane [65]. The governing dynamics are given by the following stochastic differential equations:

$$C\dot{V} = g_L(V_L - V) + g_E(V_E - V) + g_I(V_I - V) + I + \Gamma_V \qquad (3.19)$$

where C is the membrane capacitance, V is the membrane potential, I is the input current, Γ_X is Gaussian noise, and the currents across the membrane are as follows (see Table 3.1):

- $g_E(V_E - V)$: is the excitatory sodium (Na^+) current with conductance g_E and reversal potential V_E.

- $g_I(V_I - V)$: is the inhibitory chloride (Cl^-) current with conductance g_I and reversal potential V_I.

- $g_L(V_L - V)$: is the potassium (K^+) leak current with conductance g_L and reversal potential V_L.

To simulate in vivo-like fluctuations in the background activity, the conductances are customarily described by stochastic differential equations whose dynamics

depend on the pre-synaptic input ς_l and a characteristic rate constant κ_l ($l = E, I$):

$$\dot{g}_l = \kappa_l(\varsigma_l - g_l + \tilde{g}_l) + \Gamma_l \tag{3.20}$$

where $\tilde{g}_l$ ($l = E, I$) are the mean (static) excitatory and inhibitory conductances, and Γ_l is Gaussian noise.

In turn the synaptic coupling of a given neuron is dictated by the pre-synaptic input $\varsigma_l^{(i)}$, as the product of the firing rate in another neuron j and a coupling parameter $\gamma^{(j,i)}$ [66]:

$$\varsigma_l^{(i)} = \gamma_l^{j,i}\sigma(V^{(j)} - V_R), \qquad l = E, I \tag{3.21}$$

where $\sigma(.)$ is a sigmoid activation function that transforms the post-synaptic potential of neuron j to firing rate, and is given by [67]:

$$\sigma(V^{(j)} - V_R) = \frac{1}{1 + e^{(-\alpha(V^{(j)} - V_R)}} \tag{3.22}$$

where V_R a a threshold potential, and α is a constant that determines the slope (voltage sensitivity) of the activation function.

The above model described above is adopted here to describe the stochastic dynamics of interacting populations in a cortical column. Thus, for each layer $i = 1, 2, 3$ representing Granular, Supra-granular, and Infra-granular respectively:

$$
\begin{aligned}
C\dot{V}^{(i)} &= g_L(V_L - V^{(i)}) + g_E^{(i)}(V_E - V^{(i)}) + g_I^{(i)}(V_I - V^{(i)}) + I + \Gamma_V^{(i)} & (3.23)\\
\dot{g}_E^{(i)} &= \kappa_E(\varsigma_E^{(i)} - g_E^{(i)} + \tilde{g}_E) + \Gamma_E^{(i)} & (3.24)\\
\dot{g}_I^{(i)} &= \kappa_I(\varsigma_I^{(i)} - g_I^{(i)} + \tilde{g}_I) + \Gamma_I^{(i)} & (3.25)\\
\varsigma_l^{(i)} &= \gamma_l^{(j,i)}\sigma(V^{(j)} - V_R), \qquad l = E, I & (3.26)
\end{aligned}
$$

where the input I is assumed to excite only the granular (input) layer.

These stochastic differential equations can be formulated in state-space model of the form:

$$\dot{\mathbf{x}}(t) = f(\mathbf{x}(t), I) + \mathbf{\Gamma} \tag{3.27}$$

Where the state vector $\mathbf{x}$ comprises the membrane potentials, the excitatory and inhibitory conductances, and $f(.)$ is a vector that comprises the equations of motion of each state:

$$\mathbf{x} = [\; V^{(1)} \quad g_I^{(1)} \quad g_E^{(1)} \quad V^{(2)} \quad g_I^{(2)} \quad g_E^{(2)} \quad V^{(3)} \quad g_I^{(3)} \quad g_E^{(3)} \;]^T$$

$$f(\mathbf{x}(t), I) = \begin{bmatrix} \frac{1}{C}[g_L(V_L - V^{(1)}) + g_E^{(1)}(V_E - V^{(1)}) + g_I^{(1)}(V_I - V^{(1)}) + I] \\ \kappa_I(\gamma_I^{(2,1)}\sigma(V^{(2)} - V_R) - g_I^{(1)} + \tilde{g}_I) \\ \kappa_E(\gamma_E^{(3,1)}\sigma(V^{(3)} - V_R) - g_E^{(1)} + \tilde{g}_E) \\ \frac{1}{C}[g_L(V_L - V^{(2)}) + g_E^{(2)}(V_E - V^{(2)}) + g_I^{(2)}(V_I - V^{(2)})] \\ \kappa_I(\gamma_I^{(2,2)}\sigma(V^{(2)} - V_R) - g_I^{(2)} + \tilde{g}_I) \\ \kappa_E(\gamma_E^{(3,2)}\sigma(V^{(3)} - V_R) - g_E^{(2)} + \tilde{g}_E) \\ \frac{1}{C}[g_L(V_L - V^{(3)}) + g_E^{(3)}(V_E - V^{(3)}) + g_I^{(3)}(V_I - V^{(3)})] \\ \kappa_I(\gamma_I^{(2,3)}\sigma(V^{(2)} - V_R) - g_I^{(3)} + \tilde{g}_I) \\ \kappa_E(\gamma_E^{(1,3)}\sigma(V^{(1)} - V_R) - g_E^{(3)} + \tilde{g}_E) \end{bmatrix}$$

Table 3.1: Conductance-Based neuronal model parameters.

Parameter	Interpretation	Value	Unit
$V^{(i)}$	Membrane potential, $i = 1, 2, 3$ for granular, supra-granular, and infra-granular respectively	—	mV
V_L	potassium (K^+) reversal potential	-70	mV
V_E	sodium (Na^+) reversal potential	60	mV
V_I	chloride (Cl^-) reversal potential	-90	mV
V_R	Threshold potential	-40	mV
C	Membrane capacitance	10	μF
I	Input current at the granular layer	—	μA
g_L	Conductance of potassium leak current	1	mS
$g_E^{(i)}$	Excitatory sodium current conductance, $i = 1, 2, 3$ for granular, supra-granular, and infra-granular respectively	—	mS
$\tilde{g}_E$	Mean excitatory sodium current conductance	0.2	mS
$g_I^{(i)}$	Inhibitory chloride current conductance, $i = 1, 2, 3$ for granular, supra-granular, and infra-granular respectively	—	mS
$\tilde{g}_I$	Mean inhibitory chloride current conductance	0.5	mS

κ_E	Sodium diffusion rate constant (opening of sodium channels)	0.25	s^{-1}
κ_I	Chloride diffusion rate constant (opening of chloride channels)	0.0625	s^{-1}
α	Constant that controls the voltage sensitivity of the activation function	0.56	—
$\gamma_I^{(2,1)}$	Inhibitory connection strength from supra-granular to granular layers	0.7	—
$\gamma_I^{(2,3)}$	Inhibitory connection strength from supra-granular to infra-granular layers	2	—
$\gamma_I^{(2,2)}$	Inhibitory connection strength within the supra-granular layer	0.25	—
$\gamma_E^{(3,1)}$	Excitatory connection strength from infra-granular to granular layers	0.5	—
$\gamma_E^{(3,2)}$	Excitatory connection strength from infra-granular to supra-granular layers	1	—
$\gamma_E^{(1,3)}$	Excitatory connection strength from granular to infra-granular layers	1	—

A qualitative description of the model dynamics is as follows: an exogenous input arrives at the granular layer and excites the spiny stellate cells, and that in turn sends post-synaptic excitation to pyramidal neurons located in the infra-granular layer. The activated pyramidal cells send a feedback signal to both granular and supra-granular layers, where the inhibitory interneurons in supra-granular layer tend to inhibit both granular and infra-granular cells as well as the interneurons themselves. Moreover, each layer is affected by the background activity resultant from their respective noisy excitatory and inhibitory conductances. The activity of infra-granular layer is considered as the main output in a cortical column [68]. Thus, this layer will serve as an output layer in which its activity is observed and serve as measurement in the Kalman setup.

To illustrate the basic network dynamics, we examined the neuronal responses of different layers (shown in Fig. 3.6) with the application of afferent input (The exogenous input consisted of random DC currents applied for time windows of length 200 ms) by integrating the equations aforementioned for one second.

Figure 3.6: Cortical model activity for all states at different layers for the exogenous input shown in the top left panel.

Multi-Area Model

To extend the single area model to represent multiple interacting areas, salient long range inter-areal connections and an extended state-space representation will be described. We assume that the long-range connections between two areas are made by the excitatory connection from the infra-granular pyramidal cells in a given area to those residing in another area. We proposed a network consisted of four areas having a ring configuration, in which each area is receiving an excitatory input at its infra-granular level from the infra-granular activity of its adjacent area (Fig. 3.7). The long-range connections are summarized by an

47
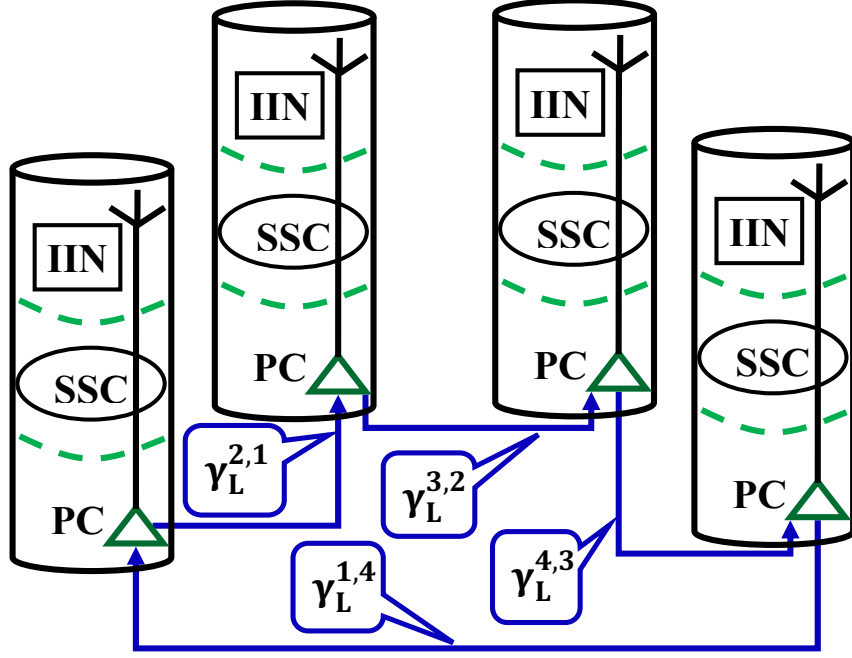
Figure 3.7: Network of four areas in a ring configuration. PC: pyramidal cells, SSC: spiny stellate cells, IIN: inhibitory interneurons.

excitatory coupling parameter $\gamma_L^{(i,j)}$ from area i to area j. Thus, in addition to local columnar inputs, the infra-granular layer in area i receives an additional pre-synaptic input, through the excitatory conductances, originating from the adjacent area j:

$$(\dot{g}_E^{(3)})^{(i)} = \kappa_E(\varsigma_L^{(i,j)} + (\varsigma_E^{(1)})^{(i)} - (g_E^{(3)})^{(i)} + \tilde{g}_E) + \Gamma_E^{(3)} \tag{3.28}$$

Where $(\varsigma_E^{(1)})^{(i)}$ is the pre-synaptic input from the respective granular layer, $\varsigma_L^{(i,j)}$ is the pre-synaptic input from infra-granular layer in area j:

$$\varsigma_L^{(i,j)} = \gamma_L^{(i,j)}\sigma[(V^{(3)})^{(j)} - V_R] \tag{3.29}$$

Where $(V^{(3)})^{(j)}$ is the membrane potential of infra-granular cells in area j.

As before, the stochastic differential equations describing the neuronal multi area model can be formulated in state-space as follows:

Process Equation: $\qquad\qquad\qquad\qquad \dot{\mathbf{x}}(t) = f(\mathbf{x}(t), I) + \mathbf{\Gamma} \qquad\qquad (3.30)$

Measurement Equation: $\qquad\qquad\qquad z_k = h(\mathbf{x}_k) + w_k \qquad\qquad\qquad (3.31)$

Where $\mathbf{x}(t) \in \mathbb{R}^n$ is the state vector of the dynamic system at time t, I is the exogenous input, $z_k \in \mathbb{R}^d$ is the measurement at discrete time t_k, $f : \mathbb{R}^n \times \mathbb{R} \to \mathbb{R}^n$ is the drift coefficient, $h : \mathbb{R}^n \times \mathbb{R} \to \mathbb{R}^d$ is the measurement function, $\mathbf{\Gamma} \in \mathbb{R}^n$ and

$w_k \in \mathbb{R}^d$ are vectors of random Gaussian noise with zero mean and covariance Q and R respectively. The state vector $\mathbf{x}$ comprises the membrane potentials, the excitatory and inhibitory conductances for all four areas, and $f(.)$ is a vector that comprises the equations of motion of each state:

$$\mathbf{x} = \left[\begin{array}{cccc} \mathbf{x}^{(1)} & \mathbf{x}^{(2)} & \mathbf{x}^{(3)} & \mathbf{x}^{(4)} \end{array} \right]^T$$

$$\mathbf{x}^{(i)} = \left[(V^{(1)})^{(i)} \ (g_I^{(1)})^{(i)} \ (g_E^{(1)})^{(i)} \ (V^{(2)})^{(i)} \ (g_I^{(2)})^{(i)} \ (g_E^{(2)})^{(i)} \ (V^{(3)})^{(i)} \cdots \right.$$

$$\left. (g_I^{(3)})^{(i)} \ (g_E^{(3)})^{(i)} \right]^T$$

Where the superscript i correspond to area $i = 1, 2, 3, 4$.

$$f(\mathbf{x}(t), I) = \left[\begin{array}{cccc} f^{(1)}(\mathbf{x}(t), I) & f^{(2)}(\mathbf{x}(t), I) & f^{(3)}(\mathbf{x}(t), I) & f^{(4)}(\mathbf{x}(t), I) \end{array} \right]$$

$$f^{(i)}(\mathbf{x}(t), I) =$$

$$\begin{bmatrix} \frac{1}{C}\{g_L[V_L - (V^{(1)})^{(i)}] + (g_E^{(1)})^{(i)}[V_E - (V^{(1)})^{(i)}] + (g_I^{(1)})^{(i)}[V_I - (V^{(1)})^{(i)}] + I\} \\[6pt] \kappa_I\{\gamma_I^{(2,1)}\sigma[(V^{(2)})^{(i)} - V_R] - (g_I^{(1)})^{(i)} + \tilde{g}_I\} \\[6pt] \kappa_E\{\gamma_E^{(3,1)}\sigma[(V^{(3)})^{(i)} - V_R] - (g_E^{(1)})^{(i)} + \tilde{g}_E\} \\[6pt] \frac{1}{C}\{g_L[V_L - (V^{(2)})^{(i)}] + (g_E^{(2)})^{(i)}[V_E - (V^{(2)})^{(i)}] + (g_I^{(2)})^{(i)}[V_I - (V^{(2)})^{(i)}]\} \\[6pt] \kappa_I\{\gamma_I^{(2,2)}\sigma[(V^{(2)})^{(i)} - V_R] - (g_I^{(2)})^{(i)} + \tilde{g}_I\} \\[6pt] \kappa_E\{\gamma_E^{(3,2)}\sigma[(V^{(3)})^{(i)} - V_R] - (g_E^{(2)})^{(i)} + \tilde{g}_E\} \\[6pt] \frac{1}{C}\{g_L[V_L - (V^{(3)})^{(i)}] + (g_E^{(3)})^{(i)}[V_E - (V^{(3)})^{(i)}] + (g_I^{(3)})^{(i)}[V_I - (V^{(3)})^{(i)}]\} \\[6pt] \kappa_I\{\gamma_I^{(2,3)}\sigma[(V^{(2)})^{(i)} - V_R] - (g_I^{(3)})^{(i)} + \tilde{g}_I\} \\[6pt] \kappa_E\{\gamma_L^{(i,j)}\sigma[(V^{(3)})^{(j)} - V_R] + \gamma_E^{(1,3)}\sigma[(V^{(1)})^{(i)} - V_R] - (g_E^{(3)})^{(i)} + \tilde{g}_E\} \end{bmatrix}$$

Where $f^{(i)}(\mathbf{x}(t), I)$ is the vector of equations of motion for each area $i = 1, 2, 3, 4$, and $\gamma_L^{(i,j)}\sigma[(V^{(3)})^{(j)} - V_R]$ is the pre-synaptic input from area $j = 4, 1, 2, 3$ to area $i = 1, 2, 3, 4$.

The measurement equation function $h(x_k)$ depends on the infra-granular layer membrane potentials $(V^{(3)})^{(i)}$, where $i = 1, \ldots, 4$ denotes neuronal areas. The output of this network is considered to be the mean value of all infra-granular membrane potentials of all areas. This output is regarded as a simplified approx-

imation of local field potential (LFP) measurement [69]:

$$h(\mathbf{x}_k) = \frac{1}{n} \sum_{i=1}^{n_p} (V^{(3)})^{(i)} \tag{3.32}$$

Where $n_p = 4$ represents the total number of areas in the network.

To illustrate the network dynamics, we examined the responses of different layers in all four neuronal areas (shown in Fig. 3.8) and observed the resultant LFP of this network with the application of afferent input (The exogenous input consisted of random DC currents applied for time windows of length 200 ms) by integrating the equations aforementioned for one second.

3.4 Jansen Model

Single Area Model Description

The Jansen model was originally introduced as a model for a cortical column in order to emulate the EEG activity of a cortical area [70]. This model consists of three sub-populations corresponding to spiny stellate input cells (granular layer), deep pyramidal output cells (infra-granular layer) and inhibitory inter-neurons (supra-granular layer).

The dynamics in each layer are based on two operators: The first is a transformation of the incoming average density of pre-synaptic input ($u(t)$) to that layer into an average post-synaptic membrane potential ($v(t)$). This operator is modeled as a convolution between the incoming input and a parameterized impulse response $h(t)$:

$$v(t) = h_l(t) * u(t) \tag{3.33}$$
$$h_l(t) = H_l \kappa_l t \exp(-t\kappa_l) \qquad l = E, I \tag{3.34}$$

Where $h_l, l = E, I$ represents the excitatory (E) and inhibitory (I) impulse responses and are parameterized by H_l and κ_l. The parameter H_E and H_I tune the maximum amplitude of post-synaptic membrane potential, and κ_E and κ_I are lumped representations of the sum of the reciprocal of the time constants of passive membrane and all other spatially distributed delays in the dendritic network [70].

Whereas, the second operator is a transformation of the average membrane potential of the population into the average firing rate of action potentials. This transformation is assumed to be instantaneous and is described by the sigmoid function:

$$S(v) = \frac{1}{1 + \exp(-\rho_1(v - \rho_2))} - \frac{1}{1 + \exp(\rho_1 \rho_2)} \tag{3.35}$$
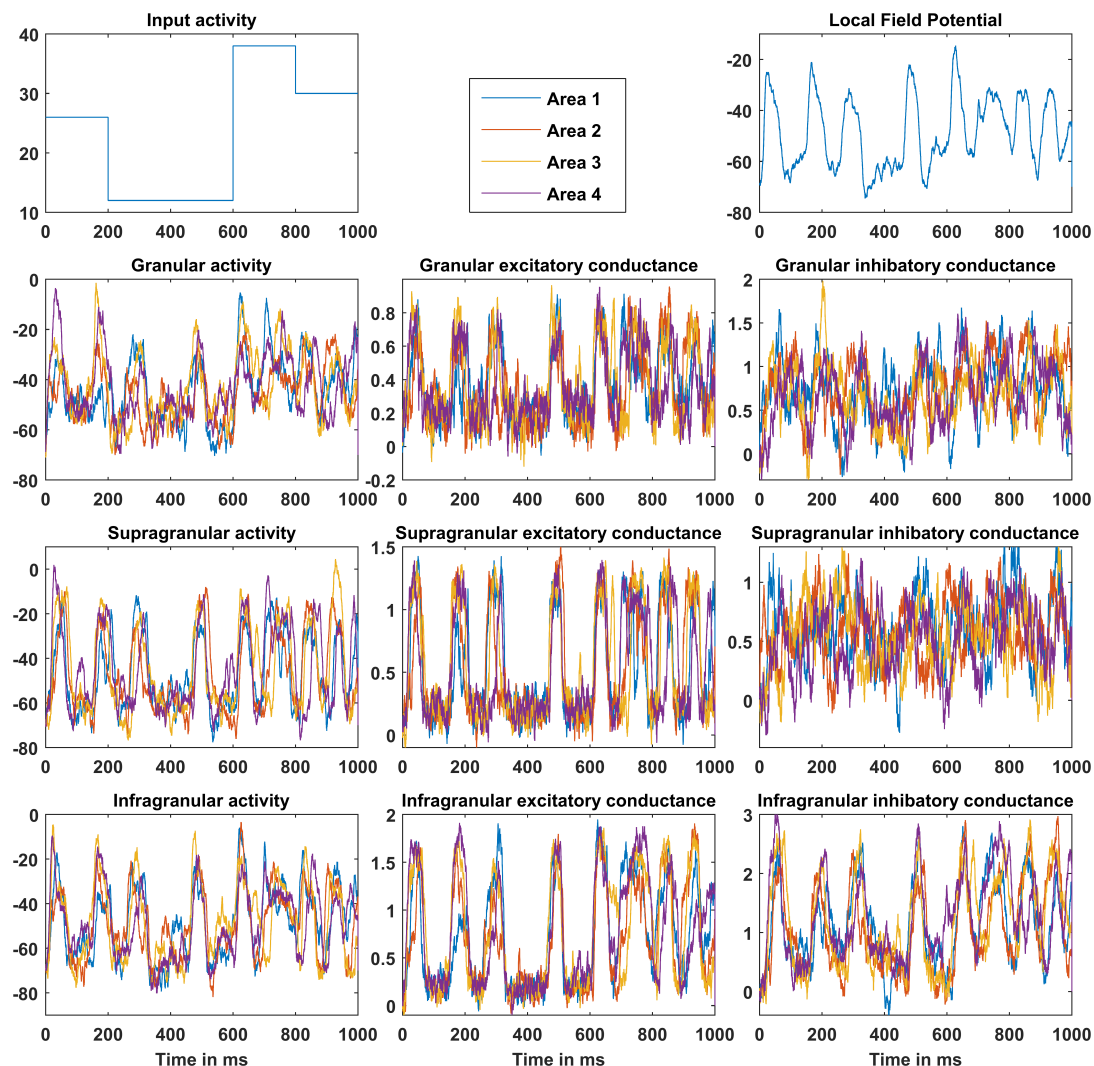
Figure 3.8: Multi-area model activity for all states at different layers for the exogenous input shown in the top left panel. The observed LFP signal (computed as the mean of infra-granular activity in all areas) is shown in the top right panel

Where ρ_1 and ρ_2 are parameters that determine the shape (e.g. voltage sensitivity) and position of the sigmoid function [71].

The convolution function in equation (3.34) can be formulated as a second-order differential equation of the form:

$$\ddot{v}(t) = H_l \kappa_l u(t) - 2\kappa_l \dot{v}(t) - \kappa_l^2 v(t) \qquad l = E, I \qquad (3.36)$$

51

Which in turn can be decomposed in state-space form:

$$\dot{v}(t) = i(t) \tag{3.37}$$

$$\dot{i}(t) = H_l \kappa_l u(t) - 2\kappa_l i(t) - \kappa_l^2 v(t) \qquad l = E, I \tag{3.38}$$

We will consider a cortical column that is composed of three layers:

- Granular layer: consists of excitatory spiny stellate cells.
- Supra-granular layer: consists of inhibitory interneurons.
- Infra-granular layer: consists of excitatory pyramidal cells.

The interactions between these layers in a cortical column depend on coupling parameters γ_i which control the strength of intrinsic connections and the total number of synapses expressed by each subpopulation [72]. The granular layer receives excitatory input from the infra-granular layer via a coupling parameter γ_1 as well as from exogenous input ($I(t)$) coming to the cortical column. The pyramidal cells in infra-granular layer are driven by excitatory spiny stellate cells in the granular layer mediated by coupling parameter γ_2, and inhibitory input from the inter-neurons in supra-granular layer mediated through coupling parameter γ_4. The inhibitory inter-neurons in supra-granular layer receives inputs from the excitatory pyramidal cells in the infra-granular layer mediated by the coupling parameter γ_3 as well as from recurrent connections from the inhibitory population itself, by the inhibitory–inhibitory coupling parameter γ_5 (Fig. 3.9). The model parameters are listed in Table 3.2. The dynamics of these interactions are governed by the model given in equations (3.38) and (3.38):

1. Supra-granular layer:

$$\dot{v}_4 = i_4 \tag{3.39}$$

$$\dot{i}_4 = H_E \kappa_E \gamma_3 S(v_6) - 2\kappa_E i_4 - \kappa_E^2 v_4 \tag{3.40}$$

$$\dot{v}_5 = i_5 \tag{3.41}$$

$$\dot{i}_5 = H_I \kappa_I \gamma_5 S(v_7) - 2\kappa_I i_5 - \kappa_I^2 v_5 \tag{3.42}$$

$$\dot{v}_7 = i_4 - i_5 \tag{3.43}$$

2. Granular layer:

$$\dot{v}_1 = i_1 \tag{3.44}$$

$$\dot{i}_1 = H_E \kappa_E (\gamma_1 S(v_6) + I) - 2\kappa_E i_1 - \kappa_E^2 v_1 \tag{3.45}$$

3. Infra-granular layer:

$$\dot{v}_2 = i_2 \tag{3.46}$$

$$\dot{i}_2 = H_E \kappa_E \gamma_2 S(v_1) - 2\kappa_E i_2 - \kappa_E^2 v_2 \tag{3.47}$$

$$\dot{v}_3 = i_3 \tag{3.48}$$

$$\dot{i}_3 = H_I \kappa_I \gamma_4 S(v_7) - 2\kappa_I i_3 - \kappa_I^2 v_3 \tag{3.49}$$

$$\dot{v}_6 = i_2 - i_3 \tag{3.50}$$
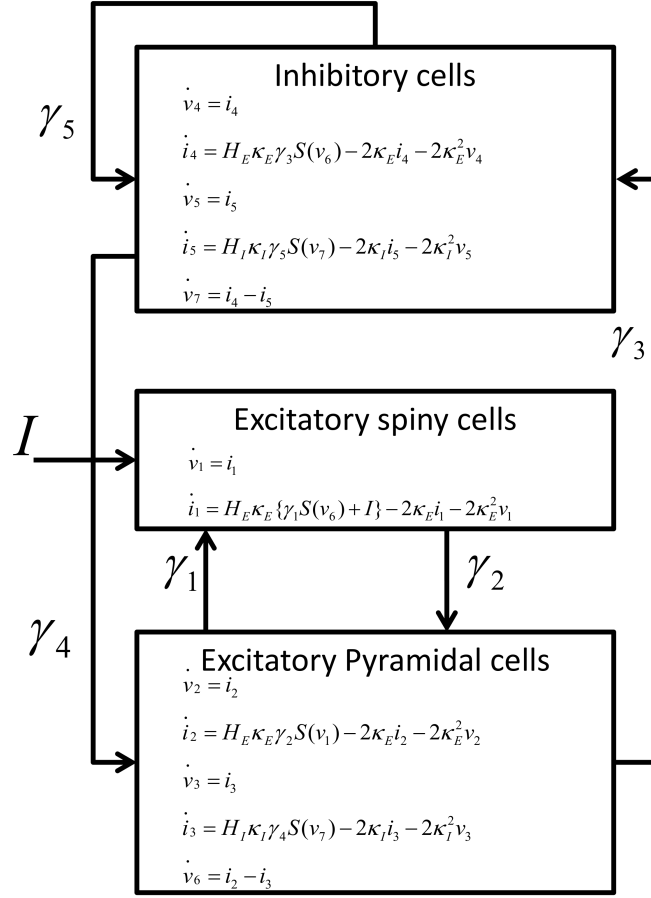
Figure 3.9: Jansen model for a single area, where $S(.)$ is a sigmoid functions, $\gamma_1, \ldots, \gamma_5$ are the coupling parameters between layers and I is the exogenous input.

The model described above will be adopted to describe the stochastic dynamics of interacting layers in a cortical column. These differential equations can be formulated in state-space model of the form:

$$\dot{\mathbf{x}} = f(\mathbf{x}, I) + \mathbf{\Gamma} \tag{3.51}$$

Where $\mathbf{\Gamma}$ is a vector of random Gaussian noise, $\mathbf{x}$ is the state vector that comprises the neuronal states of the cortical column, and $f(.)$ is a vector that comprises the equations of motion of each state:

$$\mathbf{x} = \begin{bmatrix} v_4 & i_4 & v_5 & i_5 & v_7 & v_1 & i_1 & v_2 & i_2 & v_3 & i_3 & v_6 \end{bmatrix}^T$$

Table 3.2: Jansen model parameters.

Parameter	Interpretation	Value	Unit
H_E	Maximum amplitude of excitatory post-synaptic potential	3.25	mV
H_I	Maximum amplitude of inhibitory post-synaptic potential	28	mV
$\kappa_E = 1/\tau_E$	Excitatory rate constant	1/10	ms^{-1}
$\kappa_I = 1/\tau_I$	Inhibitory rate constant	1/20	ms^{-1}
γ_1	Average number of synaptic contacts to granular layer cells	135	–
$\gamma_2 = 0.8\gamma_1$	Average number of synaptic contacts to infra-granular layer excitatory cells	108	–
$\gamma_3 = 0.25\gamma_1$	Average number of synaptic contacts to supra-granular layer inhibitory inter-neurons	33.75	–
$\gamma_4 = 0.25\gamma_1$	Average number of synaptic contacts to infra-granular layer inhibitory cells	33.75	–
$\gamma_5 = 0.01\gamma_1$	Average number of synaptic contacts to supra-granular layer inhibitory–inhibitory inter-neurons	1.35	–

$$
f(\mathbf{x}, I) =
\begin{bmatrix}
i_4 \\
H_E \kappa_E \gamma_3 S(v_6) - 2\kappa_E i_4 - \kappa_E^2 v_4 \\
i_5 \\
H_I \kappa_I \gamma_5 S(v_7) - 2\kappa_I i_5 - \kappa_I^2 v_5 \\
i_4 - i_5 \\
i_1 \\
H_E \kappa_E (\gamma_1 S(v_6) + I) - 2\kappa_E i_1 - \kappa_E^2 v_1 \\
i_2 \\
H_E \kappa_E \gamma_2 S(v_1) - 2\kappa_E i_2 - \kappa_E^2 v_2 \\
i_3 \\
H_I \kappa_I \gamma_4 S(v_7) - 2\kappa_I i_3 - \kappa_I^2 v_3 \\
i_2 - i_3
\end{bmatrix}
$$

Fig. 3.10 shows neuronal responses of different layers with the application of afferent input (The exogenous input consisted of random DC currents applied for time windows of length 200 ms) by integrating the equations aforementioned for one second.
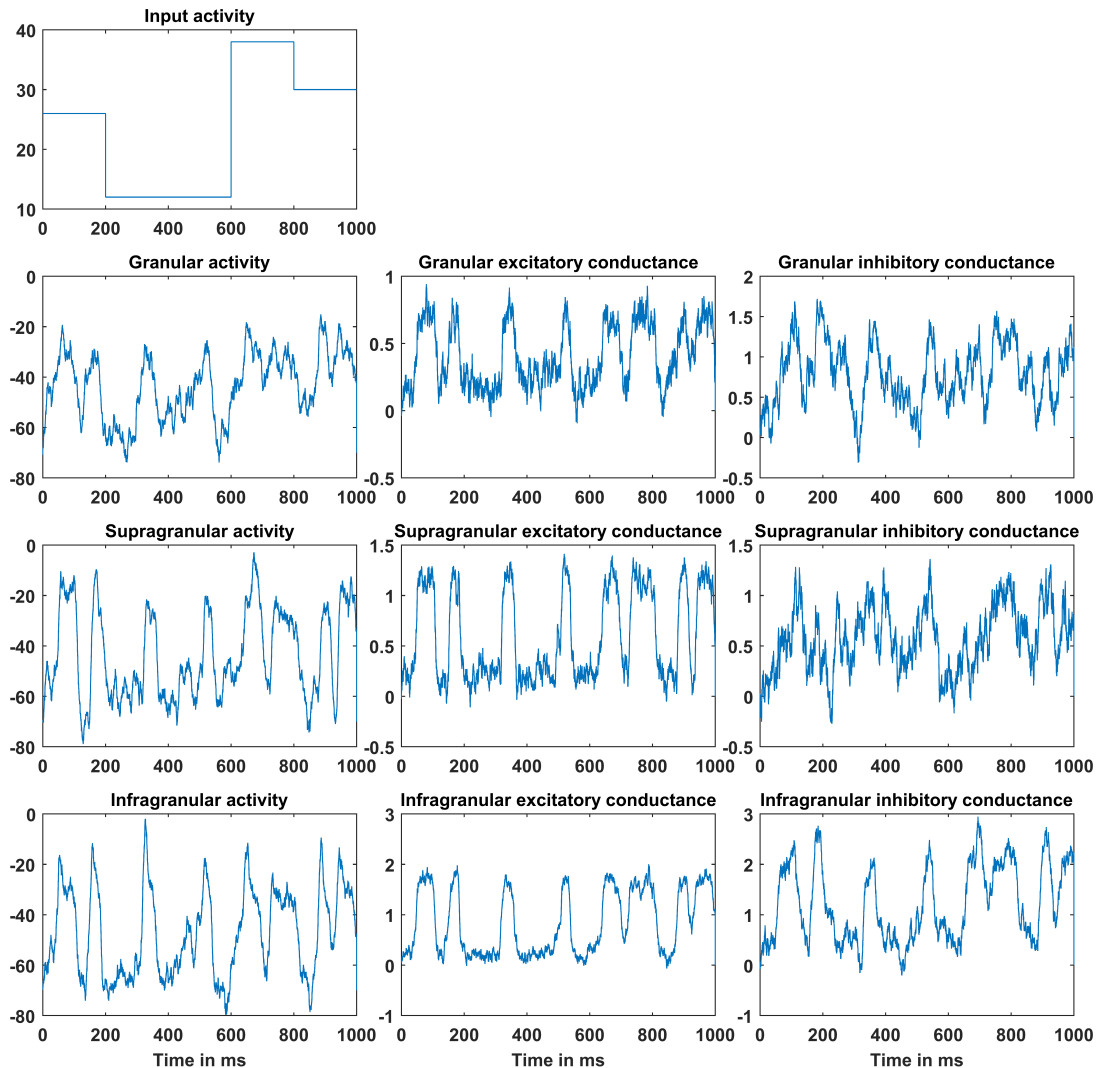
Multi-Area Model

In this section, the single area model is extended to represent multiple interacting areas. We define the long-range connections between two areas to be made by an excitatory connection from the infra-granular pyramidal cells in a given area to cells residing in the granular layer of another area.

We proposed a network consisted of three areas, in which each area is receiving an excitatory input at its granular level from the infra-granular layer of another area. The strength of such excitatory activity is defined by a connectivity parameter $\gamma_L^{(i,j)}$ (long-range coupling parameter from area i to area j) (Fig. 3.11).

Thus, for multi-area model, the granular layer in area i receives an additional

55
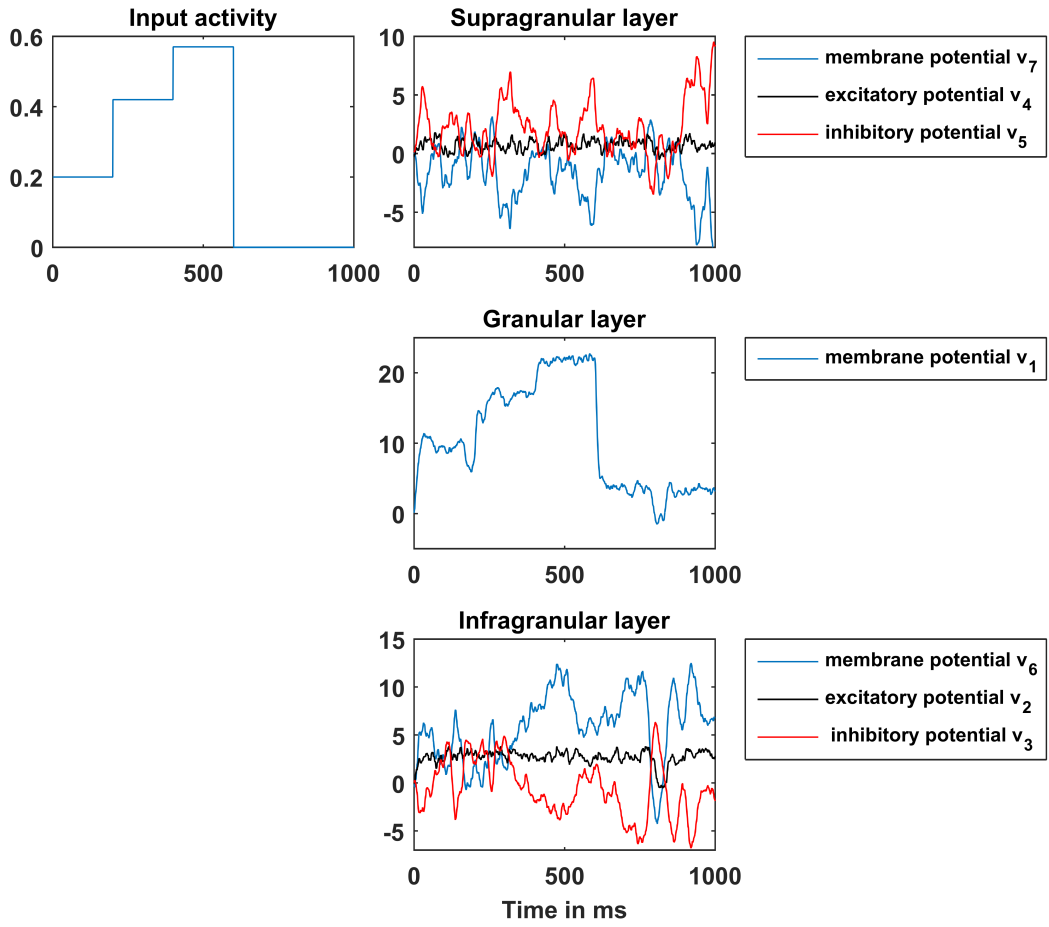
Figure 3.10: Jansen model activity for all membrane potentials, excitatory and inhibitory potentials at different layers for the exogenous input shown in the top left panel.

pre-synaptic input originated from area j:

$$\dot{v}_1^{(i)} \;\; = \;\; i_1^{(i)} \tag{3.52}$$

$$\dot{i}_1^{(i)} \;\; = \;\; H_E \kappa_E \left\{ \left(\gamma_1 S(v_6^{(i)}) + I + \sum_{j=1}^{3} [\gamma_L^{(i,j)} S(v_6^{(j)})] \right) \right\} - 2\kappa_E i_1^{(i)} - \kappa_E^2 v_1^{(i)} \tag{3.53}$$

Where $v_6^{(j)}$ is the membrane potential of infra-granular cells in area j.

The stochastic differential equations describing the neuronal areas can be formulated in state-space model of the form:

Process Equation: $\qquad\qquad\qquad\qquad \dot{\mathbf{x}}(t) = f(\mathbf{x}(t), I) + \mathbf{\Gamma}$ $\qquad\qquad$ (3.54)

Measurement Equation: $\qquad\qquad\qquad\qquad z_k = h(\mathbf{x}_k) + w_k$ $\qquad\qquad$ (3.55)

56
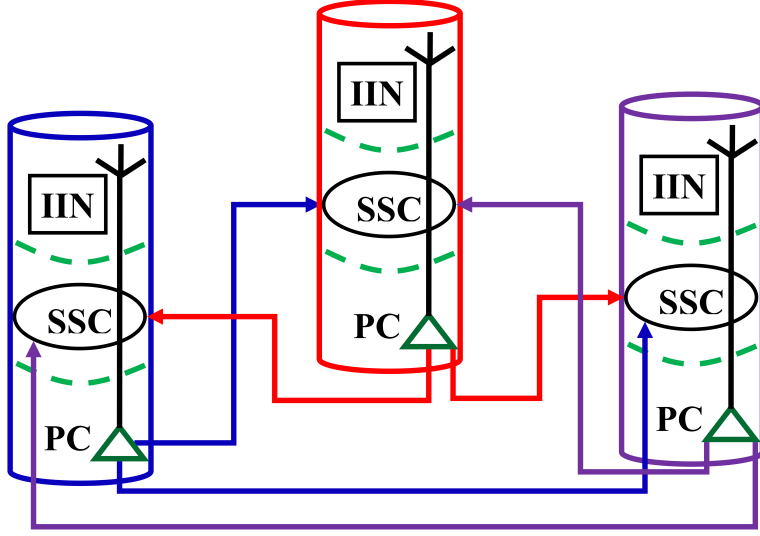
Figure 3.11: Network of three areas with all possible long-range coupling connections between them. PC: pyramidal cells, SSC: spiny stellate cells, IIN: inhibitory interneurons.

Where $\mathbf{x}(t) \in \mathbb{R}^n$ is the state vector of the dynamic system at time t, I is the exogenous input, $z_k \in \mathbb{R}^d$ is the measurement at discrete time k, $f : \mathbb{R}^n \times \mathbb{R} \to \mathbb{R}^n$ is the drift coefficient, $h : \mathbb{R}^n \times \mathbb{R} \to \mathbb{R}^d$ is the measurement function, $\boldsymbol{\Gamma} \in \mathbb{R}^n$ and $w_k \in \mathbb{R}^d$ are vectors of random Gaussian noise with zero mean and covariance Q and R respectively.

The state vector $\mathbf{x}$ comprises the membrane potentials, the excitatory and inhibitory currents for all three areas, and $f(.)$ is a vector that comprises the equations of motion of each state:

$$\mathbf{x} = \begin{bmatrix} \mathbf{x}^{(1)} & \mathbf{x}^{(2)} & \mathbf{x}^{(3)} \end{bmatrix}^T$$

$$\mathbf{x}^{(i)} = \begin{bmatrix} v_4^{(i)} & i_4^{(i)} & v_5^{(i)} & i_5^{(i)} & v_7^{(i)} & v_1^{(i)} & i_1^{(i)} & v_2^{(i)} & i_2^{(i)} & v_3^{(i)} & i_3^{(i)} & v_6^{(i)} \end{bmatrix}^T$$

57

Where the superscript i correspond to area $i = 1, 2, 3$.

$$f(\mathbf{x}(t), I) = \begin{bmatrix} f^{(1)}(\mathbf{x}(t), I) \\ f^{(2)}(\mathbf{x}(t), I) \\ f^{(3)}(\mathbf{x}(t), I) \end{bmatrix}$$

$$f^{(i)}(\mathbf{x}(t), I) = \begin{bmatrix} i_4^{(i)} \\ H_E \kappa_E \gamma_3 S(v_6^{(i)}) - 2\kappa_E i_4^{(i)} - \kappa_E^2 v_4^{(i)} \\ i_5^{(i)} \\ H_I \kappa_I \gamma_5 S(v_7^{(i)}) - 2\kappa_I i_5^{(i)} - \kappa_I^2 v_5^{(i)} \\ i_4^{(i)} - i_5^{(i)} \\ i_1^{(i)} \\ H_E \kappa_E [\gamma_1 S(v_6^{(i)}) + I + \sum_{j=1}^{3} [\gamma_L^{(i,j)} S(v_6^{(j)})]] - 2\kappa_E i_1^{(i)} - \kappa_E^2 v_1^{(i)} \\ i_2^{(i)} \\ H_E \kappa_E \gamma_2 S(v_1^{(i)}) - 2\kappa_E i_2^{(i)} - \kappa_E^2 v_2^{(i)} \\ i_3^{(i)} \\ H_I \kappa_I \gamma_4 S(v_7^{(i)}) - 2\kappa_I i_3^{(i)} - \kappa_I^2 v_3^{(i)} \\ i_2^{(i)} - i_3^{(i)} \end{bmatrix}$$

Where $f^{(i)}(\mathbf{x}(t), I)$ is the vector of equations of motion for each area $i = 1, 2, 3$.

The measurement equation function $h(x_k)$ depends on the infra-granular layer membrane potentials $v_6^{(i)}$, where $i = 1, \ldots, 3$ denotes neuronal areas. The observations from this network are assumed to be the infra-granular membrane potentials of all areas:

$$h(\mathbf{x}_k) = \begin{bmatrix} v_6^{(1)} \\ v_6^{(2)} \\ v_6^{(3)} \end{bmatrix}$$

3.5 Hemodynamic Model

We introduce the mathematical description of the hemodynamic model that relates input neuronal activity (NA) (u) to measured BOLD signals [34, 73, 74]. The model is based on four physiological state variables: vasodilatory signal (s), cerebral blood flow (CBF) (f), cerebral blood volume (CBV) (v), and deoxyhemoglobin content (dHb) (q). The hemodynamic model is given by:

$$\dot{s} = u - \kappa s - \gamma(f - 1) \tag{3.56}$$

$$\dot{f} = s \tag{3.57}$$

$$\tau\dot{v} = f - v^{\frac{1}{\alpha}} \tag{3.58}$$

$$\tau\dot{q} = \frac{E(f, \rho)f}{\rho} - \frac{q}{v}v^{\frac{1}{\alpha}} \tag{3.59}$$

The vasodilatory signal (s) is a linear function of NA input (u) (expressed as firing rate of a given neuronal population) and is subject to auto-regulatory feedback by CBF (f). The rate of change in CBV (v) is the difference of blood inflow (CBF) and blood outflow (which is function of CBV) from the venous compartment, and the rate of change in dHb (q) is the delivered deoxyhemoglobin into the venous compartment minus that expelled (blood outflow ($v^{1/\alpha}$) times deoxyhemoglobin concentration (q/v). Where κ is the rate constant of signal decay, γ is the rate constant of feedback regulation, u is the input NA, τ is the hemodynamic transit time (average time needed for the blood to traverse the venous compartment), α is the stiffness or Grubbs exponent, $E(f, \rho) = 1 - (1 - \rho)^{1/f}$ is the oxygen extraction function, and ρ is the resting oxygen extraction fraction. The hemodynamic model parameters are listed in Table 3.3.

Table 3.3: Hemodynamic model parameters.

Parameter	Physiologic Interpretation	Value	Unit
κ	Rate of signal decay	0.65	sec^{-1}
γ	Rate of feedback regulation	0.38	sec^{-1}
α	Grubbs exponent	0.32	—
τ	Hemodynamic transit time	0.98	sec
ρ	Resting oxygen extraction fraction	0.34	—

The hemodynamic model can be generalized by incorporating an additive noise

process, and thus the model can be formulated by the following stochastic differential equations system:

$$\dot{\mathbf{x}} = F(\mathbf{x}, u) + \mathbf{\Gamma} \tag{3.60}$$

Where $\mathbf{\Gamma}$ is a Gaussian noise vector, the hemodynamic state vector $\mathbf{x}$ and the model functions $F(\mathbf{x}, u)$ are as follow:

$$\mathbf{x} = \begin{bmatrix} s & f & v & q \end{bmatrix}^T$$

$$F(\mathbf{x}, u) = \begin{bmatrix} u - \kappa s - \gamma(f - 1) \\ s \\ \frac{1}{\tau}[f - v^{\frac{1}{\alpha}}] \\ \frac{1}{\tau}\left[\frac{E(f,\rho)f}{\rho} - \frac{q}{v}v^{\frac{1}{\alpha}}\right] \end{bmatrix}$$

The observation BOLD signal is a nonlinear function of CBV (v), dHb (q) and the resting blood volume fraction (V_0):

$$z = V_0[k_1(1 - q) + k_2(1 - \frac{q}{v}) + k_3(1 - v)] \tag{3.61}$$

$$k_1 = 7\rho, \qquad k_2 = 2, \qquad k_3 = 2\rho - 0.2$$

The stochastic differential equations describing the hemodynamic model can be formulated in state-space model of the form:

Process Equation: $\qquad\qquad\qquad \dot{\mathbf{x}}(t) = F(\mathbf{x}(t), u) + \Gamma \qquad$ (3.62)

Measurement Equation: $\qquad\qquad\qquad z_k = h(\mathbf{x}_k) + w_k \qquad$ (3.63)

Where $\mathbf{x}(t) \in \mathbb{R}^n$ is the state of the dynamic system at time t, u is the NA input, $z_k \in \mathbb{R}^d$ is the measurement at discrete time k, $F : \mathbb{R}^n \times \mathbb{R} \to \mathbb{R}^n$ is the process function, $h : \mathbb{R}^n \times \mathbb{R} \to \mathbb{R}^d$ is the measurement function, $\Gamma \in \mathbb{R}^n$ and $w_k \in \mathbb{R}^d$ are vectors of random Gaussian noise with zero mean and covariance Q and R respectively. The state vector x includes the hemodynamic model variables, the process equation function $F(.)$ is a vector that comprises the equations of motion of each state, and the measurement equation function $h(x_k)$ is the observation BOLD signal.

Fig. 3.12 shows the behavior of hemodynamic variables for the presented neural activity input (u). The model was simulated for 200 s with sampling rate $dt = 0.1sec$ without adding noise to the system.
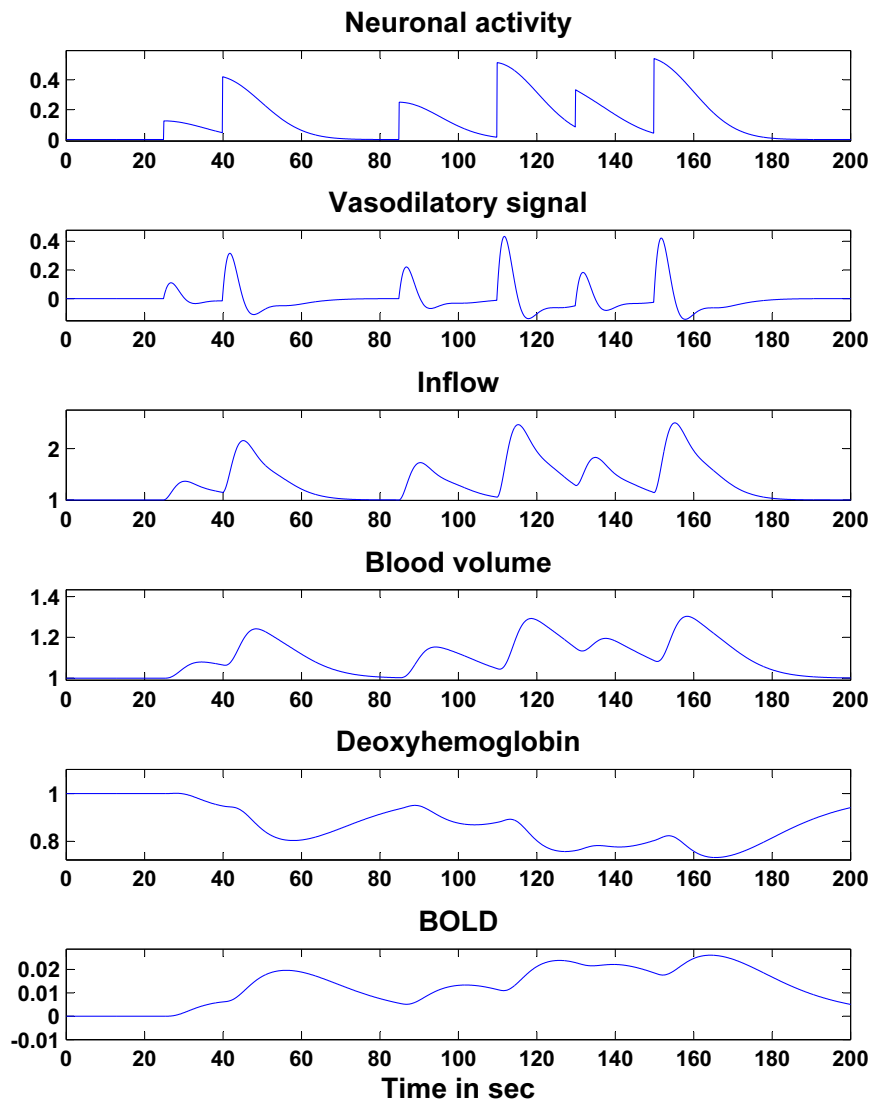
Figure 3.12: Noiseless BOLD signal and the dynamics of the hemodynamic variables for a given neuronal activity input (top plot).

61

Chapter 4

Optimal Input Design for Kalman-based Estimation of Nonlinear Dynamical System Models

In this chapter, we present an adaptive approach for joint input design and parametric identification of nonlinear system models. By integrating techniques from Adaptive Design Optimization (ADO) and square-root Cubature Kalman filtering (SCKF), we aim to introduce an efficient identification algorithm that selects in single experimental trials those system inputs that cause the output trajectory to be maximally informative about the nonlinear system model parameters. We demonstrate the algorithm performance in several simulated scenarios that are derived from benchmark nonlinear problems (Double well and Van der Pol oscillators) as well as from nonlinear stochastic neuronal models of electric potential generation.

4.1   Problem Definition and Setup

We consider the identification of dynamic models of biological processes for which repeated experimental manipulations are time consuming, costly, or impractical due to the nonstationarity of *in vivo* operating conditions. The temporal dynamics of a large class of such processes can be described by nonlinear stochastic nonhomogeneous differential equations, and are therefore amenable to state space reformulations that separate the dynamical character of the system from the measurement or observation method utilized (equations (3.1) and (3.2)). For

a prescribed state-space model structure, and for a given set of discrete observations (e.g. equations (4.1) and (4.2)), it is desired to conduct single experimental runs and to employ estimation techniques that allow (a) the recovery of accurate estimates of the hidden state variables (often directly related to one or more internal physiological quantities), and (b) the identification of unknown (but deterministic) parameters of the model structure.

At the estimation level, we seek the employment of a Bayesian estimator that minimizes the covariance of the prediction error for hidden states based on discrete and noisy observations. We assume that both the process and measurement equations are affected by noise processes that are Markovian in nature and Gaussian distributed. This allows the use of of a Kalman filter for state predictions. At the model identification level, parameters are searched for as the mean of additional states that follow a random walk process. Again, a Kalman filter setup allows finding the augmented state vector (hidden states and parameters) that minimize the one step prediction error.

Finally, at the experimental level, we assume that the system's exogenous or driving input(s) can be manipulated over an operational range. It is therefore desired to provide a time sequence of inputs over a single experimental trial that maximize the accuracy of the obtained estimates. In a simulated set of experiments, we seek to employ adaptive design optimization (ADO) techniques to provide, based on current Kalman estimates of the system model, designed inputs that, when applied over future time windows, produce the most informative measurements about the hidden states and the unknown parameters.

4.1.1   State estimation using Cubature Kalman filters

Given the state-space formulation of a dynamical system:

Process Equation:
$$\dot{\mathbf{x}}(t) = f(\mathbf{x}(t), I) + \mathbf{\Gamma} \tag{4.1}$$
Measurement Equation:
$$z_k = h(\mathbf{x}_k) + w_k \tag{4.2}$$

The stochastic differential equation (SDE) represented in the process equation (4.1) is in continuous time, we can discretize the SDE using Local Linearization (LL) method as described in section (2.3); this will transform the state-space model to a pair of difference equations in order to apply the CKF.

The discrete state-space model becomes:

Process Equation:
$$\mathbf{x}_k = f_d(\mathbf{x}_{k-1}, I) + \mathbf{v}_{k-1} \tag{4.3}$$
Measurement Equation:
$$z_k = h(\mathbf{x}_k) + w_k \tag{4.4}$$

Where $v_{k-1} \in \mathbb{R}^n$ is a vector of random Gaussian noise with zero mean and covariance V_{k-1}, $w_k \in \mathbb{R}^d$ is a vector of random Gaussian noise with zero mean and covariance R_k, and z_k is the discrete noisy observation at discrete time k.

Since the Kalman filtering approach estimates the hidden state vector, we will augment the hidden state vector to include the presumed dynamics of the unknown parameter vector $\boldsymbol{\theta}$ ("augmented" states). The augmented state vector is composed of (a) model hidden states, (b) unknown parameter vector:

$$\mathbf{x}_k^{\text{aug}} = \begin{bmatrix} \mathbf{x}_k & \boldsymbol{\theta} \end{bmatrix}^T$$

The augmented discrete nonlinear process equation $f_d^{\text{aug}}(\mathbf{x}_{k-1}, I)$ is the discrete version of $f^{\text{aug}}(\mathbf{x}(t), I)$

$$f^{\text{aug}}(\mathbf{x}(t), I) = \begin{bmatrix} f(\mathbf{x}(t), I) \\ f_{\boldsymbol{\theta}}(\mathbf{x}(t)) \end{bmatrix}$$

Where $f_\theta(\mathbf{x}(t))$ describes the dynamics of the unknown parameters which are assumed to follow a random walk, thus, $f_{\boldsymbol{\theta}}(\mathbf{x})$ is just vector of zeros.

$$\dot{\boldsymbol{\theta}} = \boldsymbol{\Gamma}_\theta \tag{4.5}$$

Input specification using Adaptive Design Optimization

We will adopt a method commonly used to find the optimal exogenous input I^* that produces the most informative observations about the unknowns of a given model [39, 40]. Under the hypothesis that the measurements have additive zero-mean Gaussian noise with a diagonal covariance matrix, the practical identifiability of model unknown parameters has been noted to improve through the maximization of the Fisher information matrix (FIM) [40].

In formulating the optimization problem, it is necessary to define a scalar cost function which depends on the FIM. Among several candidates, we herein adopt the T-Optimality criterion under which I^* is computed by solving the following problem:

$$\underset{I}{\operatorname{argmax}} \quad \operatorname{trace}(FIM)$$
$$\text{subject to} \quad I_{min} \leq I \leq I_{max} \tag{4.6}$$

Given the state-space model in equations (4.3) and (4.4), the elements of the Fisher information matrix are combinations of partial derivatives of the system response variables with respect to the model parameters. The FIM elements and

sensitivities are obtained by solving the so-called sensitivity equations [75]. The FIM is determined by the following equation:

$$FIM = \sum_{k=1}^{N} \sum_{l=1}^{n_z} \left(\frac{\partial z_{l,k}}{\partial \boldsymbol{\theta}}\right)^T R^{-1} \left(\frac{\partial z_{l,k}}{\partial \boldsymbol{\theta}}\right) \tag{4.7}$$

Where N is the total number of available measurements points, R is the covariance matrix of the measurement noise, and the sensitivities $\partial z_{l,k}/\partial \boldsymbol{\theta}$ are the partial derivatives of the lth observation $z_{l,k}$ at discrete time k ($l = 1 \ldots n_z$) with respect to unknown parameters vector $\boldsymbol{\theta} \in \mathbb{R}^{n_\theta}$ and they are solutions of:

$$\begin{cases} \dfrac{d}{dt}\left(\dfrac{\partial \mathbf{x}}{\partial \theta_j}\right) = \sum_{i=1}^{n} \left\{\dfrac{\partial f}{\partial x_i}\dfrac{\partial x_i}{\partial \theta_j}\right\} + \dfrac{\partial f}{\partial \theta_j} \\[4mm] \dfrac{\partial z_{l,k}}{\partial \theta_j} = \sum_{i=1}^{n} \left\{\dfrac{\partial h_l}{\partial x_i}\dfrac{\partial x_i}{\partial \theta_j}\right\} + \dfrac{\partial h_l}{\partial \theta_j} \qquad l = 1 \ldots n_z \end{cases} \tag{4.8}$$

Where n is the total number of states, and θ_j ($j = 1 \ldots n_\theta$) refers to unknown parameters.

Typically, optimal experiment design is a sequential process whereby, at each time stage and using the current estimates of the parameters, a new optimal experiment is identified and conducted. The loop of planning an optimal experiment based on previous results and conducting a new experiment has to be repeated several times, until satisfactory results are achieved.

We proposed an iterative method which consists of finding the optimal input for the next time-stage based on parameters estimated using the Kalman filter at the current stage and by solving the optimization problem in equation (4.6) using brute-force approach (in which all possible solutions are calculated and and the optimal solution is selected) with the analytical solution of the partial derivatives. The proposed iterative method is detailed next.

4.1.2 Framework of Optimal Input Design and Kalman Filter Estimation (OID-SCKF)

The time-line of an experiment (simulation) is divided into time-stages of equal length[1]. Each stage of the proposed sequential method is composed of N samples (e.g. 500 ms time window for the neural modeling scenario). For a given stage s, starting at a time $k = s * N$, the algorithm designs for the optimal input

---

[1]inequality or uniformity of the length of time stages does not affect the procedure described
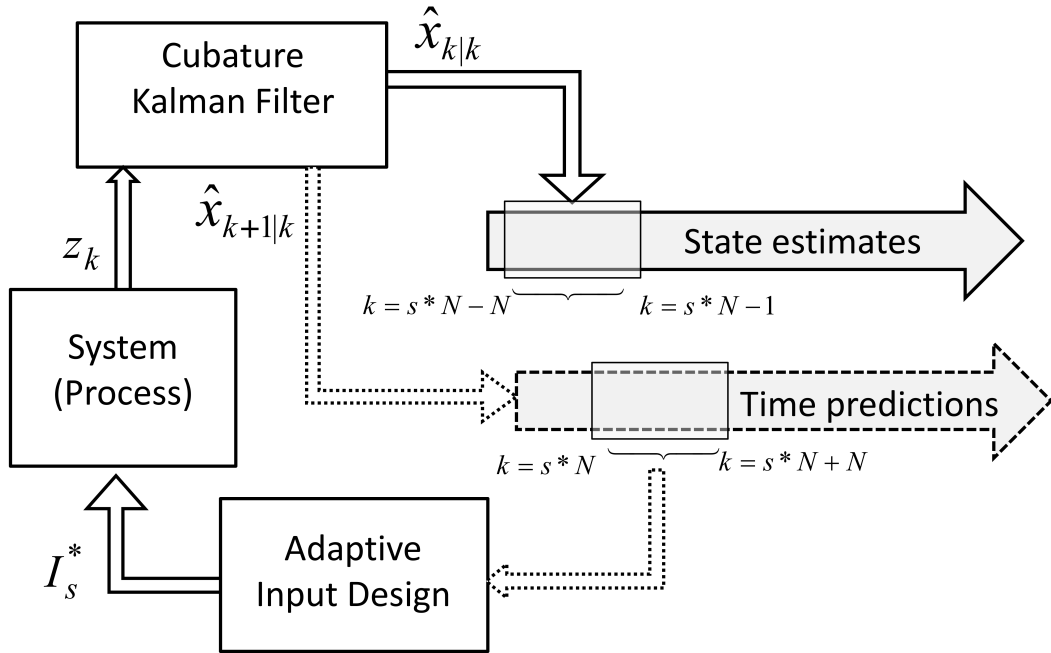
Figure 4.1: Schematic of the proposed OID-SCKF algorithm.

for the next time stage $k = s * N, \ldots, N + s * N$ (total of N samples). This requires evaluating the sensitivity functions (equation (4.7)) that depend on the values of the states and the parameters which are obviously unknown for that next stage. Accordingly, predictions of these unknown states and parameters are first obtained by evaluating the time-update step of the SCKF over the horizon $k = s * N$ to $k = N + s * N$ prior to input design. This procedure is repeated for different input values in $[I_{min}, I_{max}]$ interval until the optimizer has found a maximum.

Thereafter, this optimized input is applied to the system generating measurements data for the next stage, during which the SCKF is applied to provide estimates of the states and the parameters for the s ($k = s*N-N, \ldots, s*N-1$) time window. Fig. 4.1 shows a diagram of basic elements and processes of the proposed algorithm and Algorithm (1) shows the the pseudo-code for the proposed OID-SCKF method.

4.1.3   Performance assessment

To aid in the quantitative assessment of the introduced OID-SCKF algorithm against estimation with no input design, we use performance terms similar to those used in control and input tracking applications. This is particularly useful since we are concerned with single trial experiments. Starting from arbitrary ini-

---

Algorithm 1 Framework for the sequential optimal design and SCKF estimation

---

1: Initialization: Set initial states and parameters values $\hat{x}_0$ and the square-root of process and measurement noise covariances: $S_{R,0}$ and $S_{V,0}$.

2: Define: the input space $I_s \in [I_{min}, I_{max}]$

3: Define: the time-stages for fixed inputs, $s = 1, \ldots, S$.

4: $s = 1$ ▷ initialization time-stage or window

5: Define a random initial input I_1.

6: **for** $k = 0$ to N **do**

7:     Simulate model and collect measurements z_k

8:     Apply SCKF and get the states and parameters estimates $\hat{x}_k$

9: **end for**

10: **for** $s = 2$ to S **do**   ▷ design stages

11:     **function** DESIGN INPUT($s, \hat{x}_k, S_{k|k}$)   ▷ Find the optimal input I_s^* given the states and parameters estimates $\hat{x}_k$ and their corresponding square-root error covariance $S_{K|K}$ where $k = N + (s-1) * N - 1$ (i.e. the last time step from previous time window)

12:         **for** $k = s * N$ to $K = N + s * N$ **do**

13:             Apply the time update of SCKF to get uncorrected estimates $\hat{x}_{k|k-1}$

14:             Evaluate the sensitivity functions given $\hat{x}_{k|k-1}$

15:             Evaluate the FIM and its trace $\text{trace}(FIM(I_s))$

16:         **end for**

17:         $I_s^* = \max \text{trace}(FIM(I_s))$

18:     **end function**

19:     **function** APPLY AND ESTIMATE(s, I_s^*)

20:         **for** $k = s * N$ to $K = N + s * N$ **do**

21:             Simulate model and collect measurements z_k for stage s

22:             Apply SCKF and get the states and parameters estimates $\hat{x}_k$ for stage s

23:         **end for**

24:     **end function**

25: **end for**

---

tial conditions for the estimate of an unknown parameter, we set out to determine the speed of the approach of this estimate to the true value of that parameter and its confinement around that true value for the remainder of the experiment. Accordingly, we utilize (i) Rise time, which is defined as the time required for the estimate to rise from 10% to 90% of its steady-state value, and (ii) settling time is defined as the time required for the estimate to get within 2% of its steady-state value. Finally, statistical assessment of these values is conducted over a set of repeated simulations to reduce the effect of randomness in process and observation noise.

4.2 Results

In this section, we will present estimation results based on the optimal input design for square root Cubature Kalman filter (OID-SCKF) algorithm and compare them with those estimated based on random (not designed) inputs.

4.2.1 Van der Pol System

The Van der Pol oscillator has two states $\mathbf{x} = [x_1 \ x_2]^T$ (oscillator position and velocity) in addition to one unknown damping parameter which is set here to $\mu = 3$ (See section 3.1). For the single oscillator as well as the coupled oscillator networks considered next, the exogenous driving input is assumed to be of periodic nature $I(t) = A\sin(wt), w = 0.2\pi$ rad/sec. Furthermore, the input amplitude A falls within a finite set of quantized levels $A \in [0, 0.1, 0.2, \ldots, 3]$. Two types of inputs are considered: a randomly selected sequence of amplitudes, henceforth denoted by "random input", and a sequence of amplitudes that would be designed online based on the suggested algorithm, denoted by "designed input".

Single Oscillator

The output of the oscillator is considered to be a noisy discrete measurement of its position x_1. In the Kalman setup, the state vector is augmented as $\mathbf{x^a} = [x_1 \ x_2 \ \mu]^T$. The proposed OID-SCKF method is applied for a simulation length of 300 seconds with sampling interval $dt = 0.1$ seconds. The design stages or time windows were of length 25 sec whereby a designed (optimal) or random input is applied over that stage with fixed amplitude. For statistical assessment of the algorithm performance, a total of 50 independent Monte Carlo runs were made.

The estimate of the damping parameter μ is shown in Fig. 4.2 where the means and 95% confidence intervals (shaded region) under designed and random inputs. The figure qualitatively demonstrates that, under designed input estimate (left graph) converges faster to its final value when compared to the random input (right graph). Under designed input, the final mean value (solid blue line) is also closer to the true parameter value (red line) when compared to the random input case (solid green line). In addition, the standard error in the average value (95 % interval) is tighter under the designed input case (shaded blue region) indicating a higher confidence in the estimate than the random case (shaded green region). A more quantitative assessment of these observations will be included in subsequent larger simulations.

Figure 4.2: Estimated damping parameter μ (blue and green traces) in terms of their mean (solid lines) and a 95% confidence interval (shaded regions), and the true parameter (red trace). Left: under designed optimal inputs. Right: Under random inputs.

Network of Coupled Oscillators

Three Oscillators:

A ring network of three non-identical oscillators ($N = 3$) with coupling parameter $K = 1.3$ and damping parameters $\boldsymbol{\mu} = [\mu^{(1)} \ \mu^{(2)} \ \mu^{(3)}]^T = [3 \ 2 \ 1]^T$ is considered (Fig. 4.3).

In this scenario, the external periodic input is assumed to drive the first oscillator only. We also consider the two cases of randomly or optimally designed inputs. It is assumed that two noisy observation signals, corresponding to the positions $x_1^{(1)}$ and $x_1^{(3)}$ of the first and third oscillators, are available. It is here desired to estimate the augmented state vector which includes six states $\mathbf{x} = [x_1^{(i)} \ x_2^{(i)}]^T, i = 1, \ldots, 3$ in addition to three unknown damping parameters $\boldsymbol{\mu}$.

The OID-SCKF method is applied for a simulation length of 500 seconds with sampling interval $dt = 0.1$ sec whereby a designed (optimal) or random input is applied for 25 *sec* time windows. For statistical assessment, a total of 50 independent Monte Carlo runs were made.

Fig. 4.4 shows the means and 95% confidence intervals of the estimated damping parameters $\boldsymbol{\mu}$ under designed and random inputs. Similar results to that of the single oscillator case, as will be presented quantitatively next. Specifically, the summarized statistics about the estimated damping parameters and their rate

69
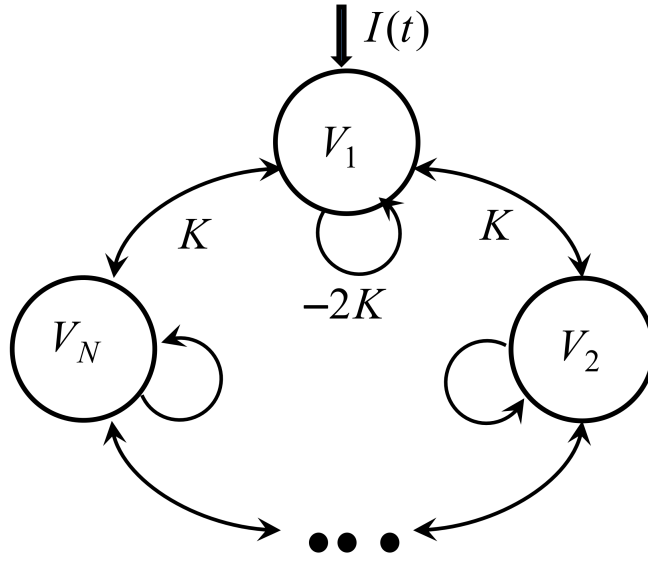
Figure 4.3: Ring configuration of N Van der Pol oscillators. Each Oscillator has two states: position and velocity. Damping factors are unknown parameters of the model

of convergence are listed in Table 4.1. When compared with SCKF estimation with random inputs, it is seen that the OID-SCKF method achieved, for all three parameters, (a) mean values that are closer to their corresponding true values, (b) attained a smaller variance and hence tighter confidence intervals around the final value across the 50 simulations, and (c) faster convergence rates– as assessed by the smaller rise time values and the settling time (see section 4.1.3).

Table 4.1: Statistics of the estimated damping parameters for three coupled non-identical oscillators averaged over 50 Monte Carlo runs under optimal and random inputs.

	Parameter	Mean	Standard deviation	Rise Time (in sec)	Settling Time (in sec)
Optimal Input	$\mu^1 = 3$	2.91	0.065	70.6	119.1
	$\mu^2 = 2$	1.68	0.09	82.6	153.8
	$\mu^3 = 1$	1.007	0.036	66.8	141.4
Random Input	$\mu^1 = 3$	2.9	0.065	72.4	125.6
	$\mu^2 = 2$	1.67	0.101	117.2	197.1

	$\mu^3 = 1$	0.98	0.034	55.2	112.1
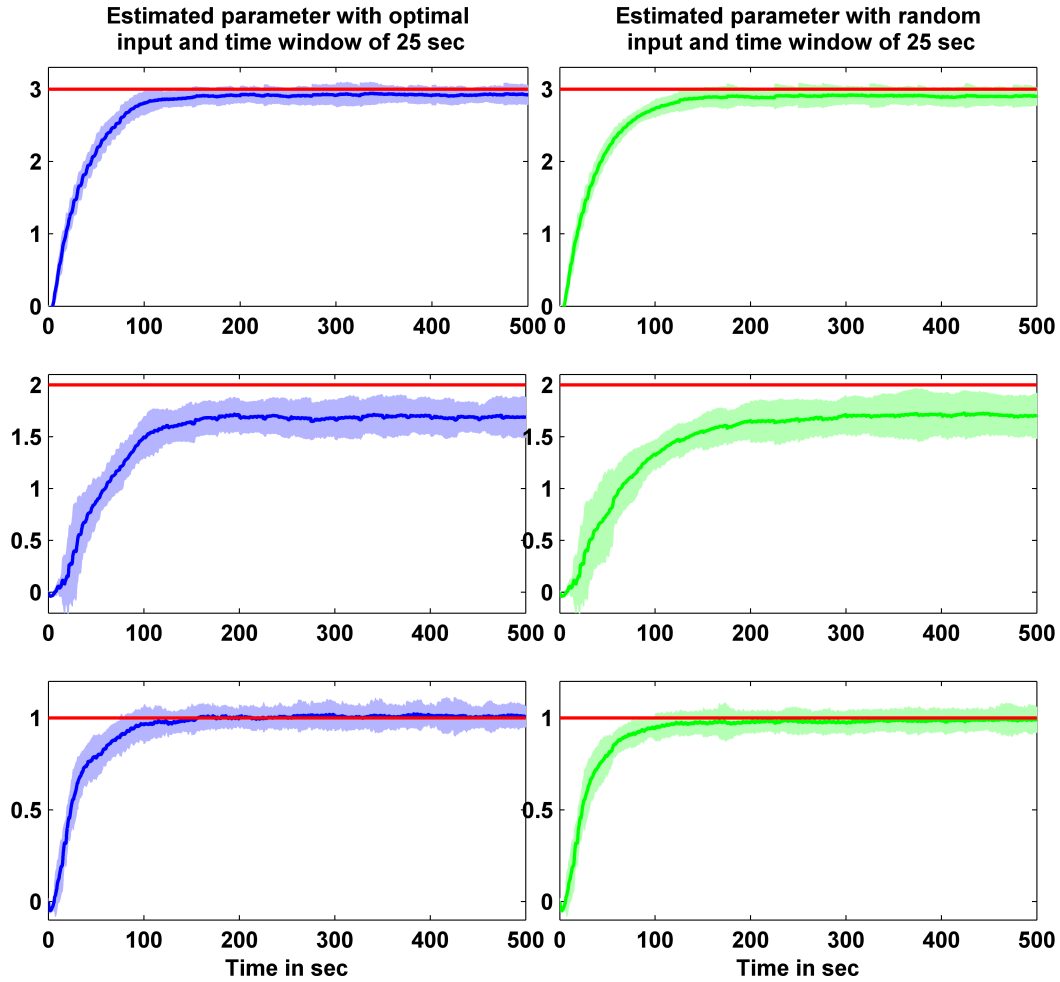
Figure 4.4: Estimated damping parameters $\boldsymbol{\mu} = [3;\ 2;\ 1]$ (blue and green traces) in terms of their mean (solid lines) and a 95% confidence interval (shaded regions), and the true parameter (red trace). Left: under designed optimal inputs. Right: Under random inputs.

Five Oscillators:

A ring network of five non-identical oscillators ($N = 5$) with coupling parameter $K = 1.3$ and damping parameters $\boldsymbol{\mu} = [3\ 2\ 1\ 1\ 3]^T$ is considered. This system has ten states in addition to five unknown damping parameters $\boldsymbol{\mu}$. The external periodic input is assumed to drive the first oscillator only and can be either a random or a designed input. The augmented state vector of fifteen quantities is

71

now to be estimated from three noisy observation signals corresponding to the positions $x_1^{(1)}$, $x_1^{(3)}$ and $x_1^{(5)}$ of the first, third, and fifth oscillators.

The proposed method is applied for a simulation length of 500 seconds with sampling interval $dt = 0.1$ whereby a designed or random input is applied for time stages or windows of 25 sec. A total of 50 independent Monte Carlo runs were made. Fig. 4.5 shows the means and 95% confidence intervals of the estimated damping parameters $\boldsymbol{\mu} = [\mu^{(2)}; \ \mu^{(4)}]$ (of the oscillators whose positions are not observed) under designed and random inputs. The figures show that, unlike the designed input case, there are considerable variations in the random input scenario (wider confidence tube, right graphs). While the estimates under designed input remains close to the corresponding true values, the random input scenario exhibits a slow divergence of the mean of $\mu^{(4)}$ estimate from its true value of 1.0. The summarized statistics as listed in Table 4.2 show predominantly more accurate estimates, smaller variances and faster approach towards final values for the designed input.

Table 4.2: Statistics of the estimated damping parameters for five coupled non-identical oscillators averaged over 50 Monte Carlo runs under optimal and random inputs.

	Parameter	Mean	Standard deviation	Rise Time (in sec)	Settling Time (in sec)
Optimal Input	$\mu^1 = 3$	2.88	0.075	42	85
	$\mu^2 = 2$	1.96	0.12	87.1	125.1
	$\mu^3 = 1$	1.04	0.058	19.3	36.7
	$\mu^4 = 1$	1.1	0.093	73.6	145.9
	$\mu^5 = 3$	2.92	0.061	38	72.7
Random Input	$\mu^1 = 3$	2.9	0.076	41.7	76.4
	$\mu^2 = 2$	1.92	0.18	138.4	200.1
	$\mu^3 = 1$	1.08	0.058	21.3	45
	$\mu^4 = 1$	1.14	0.14	117.2	320
	$\mu^5 = 3$	2.94	0.067	37.3	90.3
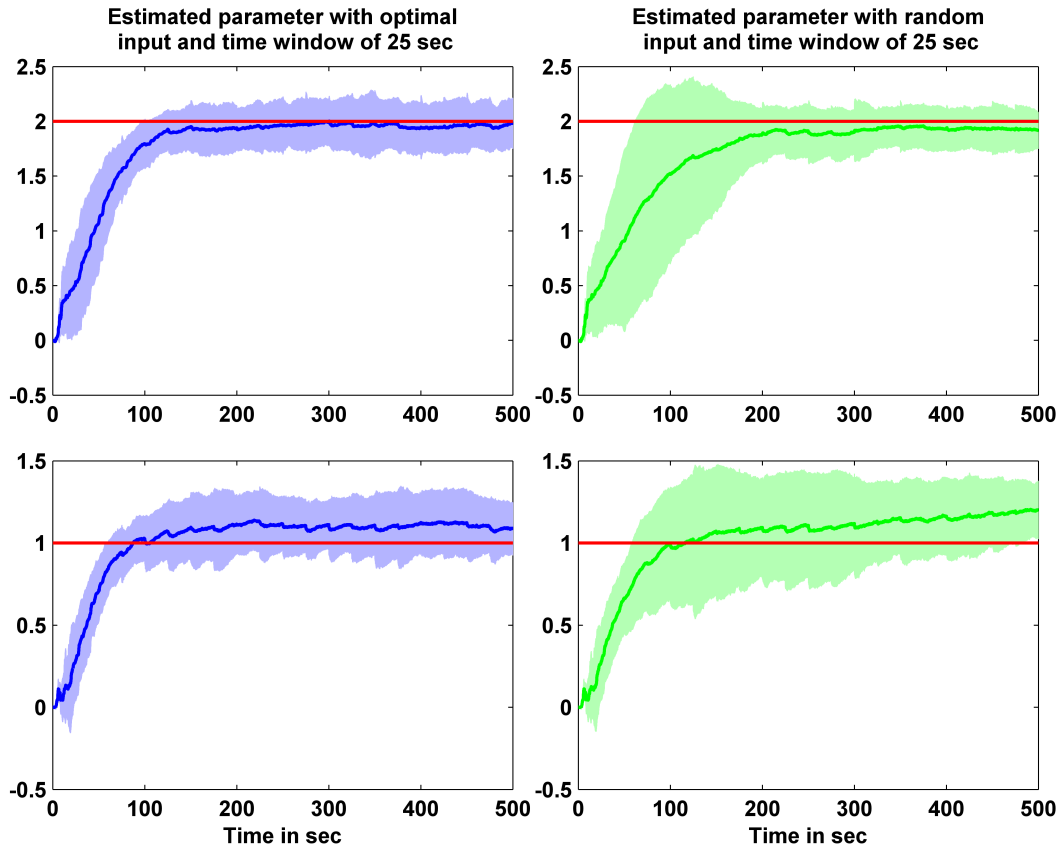
Figure 4.5: Estimation of damping parameters $\boldsymbol{\mu} = [2;\ 1]$ for oscillators $i = 2$, and 4 in a five-oscillator network. Note that the states of these oscillators are not measured. Shown are the means of the estimates (solid lines), their 95% confidence interval (shaded regions), and the true parameter (red traces). Left: under designed optimal inputs (blue traces). Right: Under random inputs (green traces).

4.2.2   Double Well

This system has one states x in addition to one unknown free parameter $a = 2$ (See section 3.2). The external periodic input $I(t) = A\sin(wt), w = 0.08\pi$ rad/sec, with the amplitude A being considered as a variable $A \in [2.5, 3, 3.5, \ldots, 17.5]$ and was selected either randomly or optimally designed over time stages. The augmented state vector had two quantities to be estimated from one noisy observation signal x.

The proposed method is applied for a simulation length of 500 seconds with sampling interval $dt = 0.1$ seconds whereby a designed (optimal) or random input is applied for 50 *sec* time windows. For statistical assessment, a total of 50

Estimated parameter with optimal input and time window of 50 sec

Estimated parameter with random input and time window of 50 sec
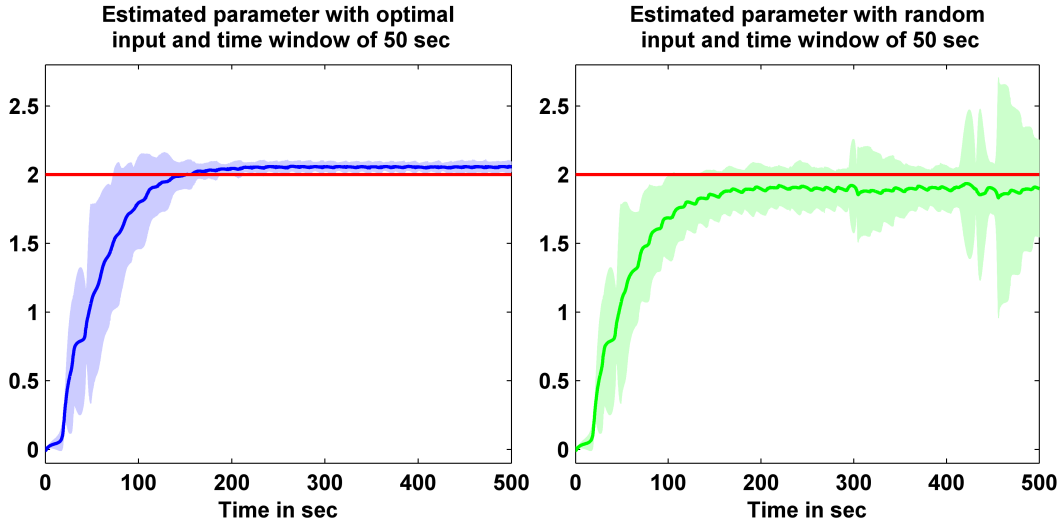
Figure 4.6: Estimated parameters a (blue and green traces) in terms of their mean (solid lines) and a 95% confidence interval (shaded regions), and the true parameter (red trace). Left: under designed optimal inputs. Right: Under random inputs.

independent Monte Carlo runs were made.

Fig. 4.6 shows the mean and 95% confidence intervals of the estimated parameter a under designed and random inputs. It is noted here that, in addition to faster approaching the steady state value and more accurate means, the designed input exhibited here a considerably more consistent estimation as time progresses as is demonstrated by a narrower confidence interval. This is in contrast to the random input case where high variability across trials become more prominent later in the procedure (green shaded region in right graph).

4.2.3 Conductance-Based Neuronal Model

We consider a four area network connected in a ring, non reciprocal configuration (see section 3.3.2). Each area is composed of three layers with a total of 9 hidden internal states including the membrane potential, excitatory and inhibitory conductances for each layer with local field potential (LFP) as observations proportional to the membrane potential of the infra-granular layer. A schematic of the OID-SCKF algorithm for neural estimation is shown in figure 4.7.

Two neural network models of increasing complexity were utilized. For the first scenario, we consider a homogeneous connectivity pattern, that is, connection strengths between the all areas are the same, and hence induce one unknown parameter to be augmented with all hidden states in the estimation scheme.
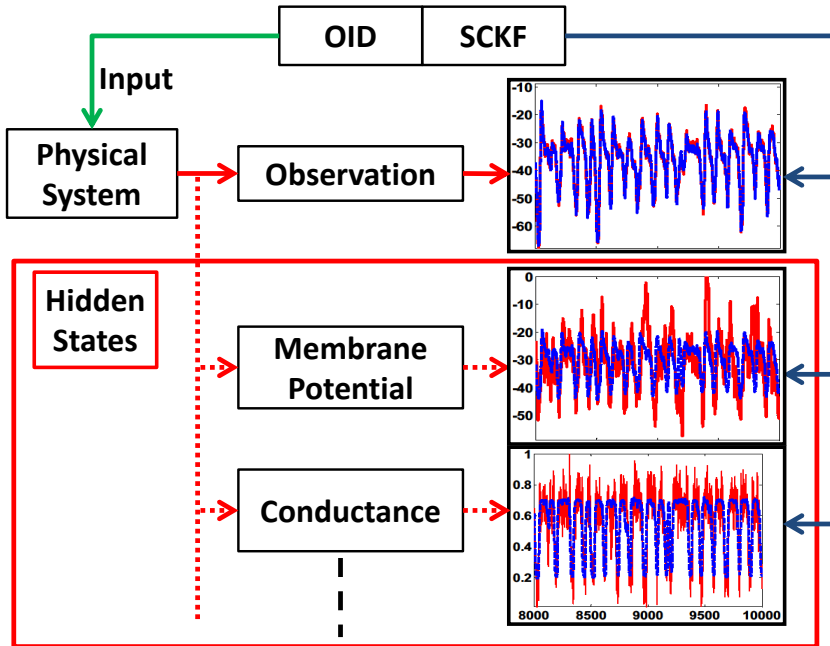
Figure 4.7: Basic elements of the neuronal model estimation. OID design an input for the system from which we collect the observations, whereas the SCKF provides estimates of the hidden states based on the collected observations. Blue traces are the estimated states and the red traces are the system's hidden states.

For the second scenario, a heterogeneous network is considered with varying connectivity strengths among the four areas, resulting in a total of four connection parameters to estimate within the augmented state vector.

First Scenario: homogenous connections

The augment state vector has a total of 36 hidden neural states in addition to one unknown parameter that are to be estimated from one noisy observation LFP signal corresponding to the mean infra-granular activity in all four areas. The proposed method is applied for a total simulation length of 10 seconds whereby a designed or random input are applied over time windows of 500 ms. A total of of 50 independent Monte Carlo runs were made for each case for statistical assessment. Fig. 4.8 shows the means and 95% confidence intervals of the estimated connectivity strength between areas under optimal inputs and random inputs. Over the 50 simulations, estimation under designed input (Left, blue traces) is noted to exhibit faster convergence, more accurate mean value and smaller variance when compared to that under random input (Right, green traces).

75
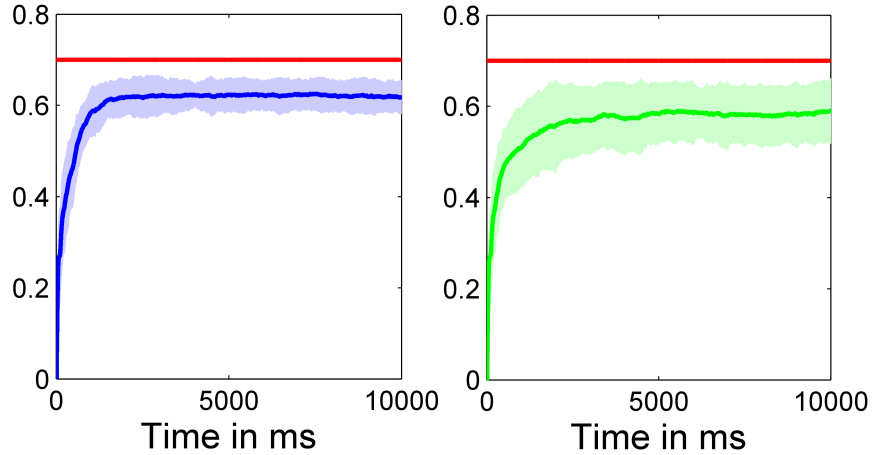
Figure 4.8: First scenario: Estimated connectivity parameter (blue and green traces) in terms of their mean (solid lines) and a 95% confidence interval (shaded regions), and the true parameter (red trace). Left: under designed optimal inputs. Right: under random inputs.

Second Scenario: Non homogenous connections

With four unknown connectivity parameters $\gamma_L = [\gamma_L^{(1,4)}; \gamma_L^{(4,3)}; \gamma_L^{(3,2)}; \gamma_L^{(2,1)}] = [1; 0.8; 0.7; 0.5]$, the augmented state vector had 40 quantities to be estimated. Under this heterogenous conditions, it was not possible to estimate the parameters from one LFP signal. A more relaxed condition was assumed on the the number of available observations. The proposed method is applied for a total simulation length of 4 seconds whereby a designed or random input are applied over time windows of 500 ms. A total of of 50 independent Monte Carlo runs were made for each case for statistical assessment.

Case a: Two LFP observations:

Two LFP signals corresponding to the average infra-granular activity in each two adjacent areas were considered as noisy observation signals for the SCKF. Fig. 4.9 shows the means and 95% confidence intervals of the estimated connectivity parameters between areas under optimal inputs and random inputs.The summarized statistics about the estimated connectivity strengths between areas and their rate of convergence are listed in Table 4.3. It is noted here that under the optimal input design, the estimated unknown connectivity parameters show more consistency indicated by the lower variance values and their rates of convergence are faster as determined by the rise and settling times.
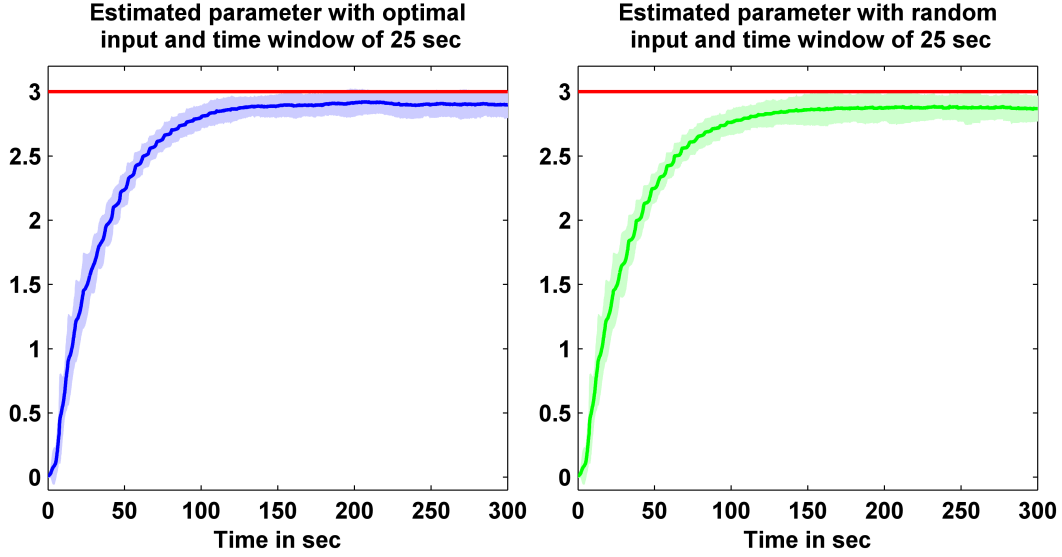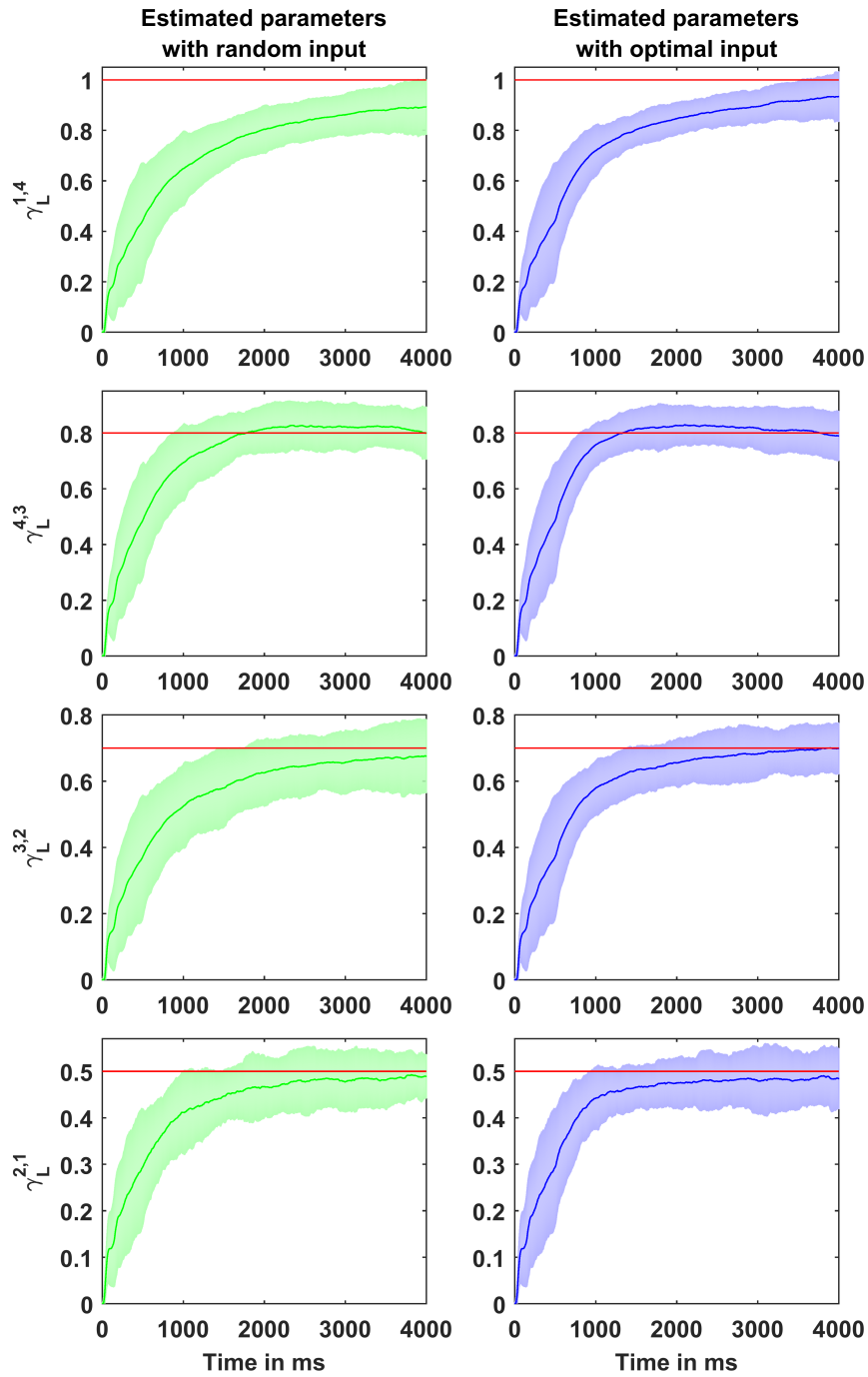
Figure 4.9: Second scenario: Case a: Two LFP observations: Estimated connectivity parameters (blue and green traces) in terms of their mean (solid lines) and a 95% confidence interval (shaded regions), and the true parameter (red trace). Left: under random inputs. Right: under designed optimal inputs.

Table 4.3: Statistics of the estimated parameters (connectivity strengths between areas) from two LFP observation signals averaged over 50 Monte Carlo runs under optimal and random inputs.

	Parameter	Mean	Standard deviation	Rise Time (in sec)	Settling Time (in sec)
Optimal Input	$\gamma_L^{1,4} = 1$	0.88	0.046	1.4	2.27
	$\gamma_L^{4,3} = 0.8$	0.81	0.046	0.86	1.33
	$\gamma_L^{3,2} = 0.7$	0.67	0.044	1.17	2.11
	$\gamma_L^{2,1} = 0.5$	0.47	0.034	0.88	1.73
Random Input	$\gamma_L^{1,4} = 1$	0.84	0.056	1.55	2.26
	$\gamma_L^{4,3} = 0.8$	0.81	0.052	1.19	1.76
	$\gamma_L^{3,2} = 0.7$	0.64	0.055	1.47	2.11
	$\gamma_L^{2,1} = 0.5$	0.47	0.036	1.21	1.97

Case b: Four LFP observations:

Four LFP signals corresponding to the infra-granular activity of each area were considered as observation signals for the SCKF. Fig. 4.10 shows the means and 95% confidence intervals of the estimated connectivity parameters between areas under optimal inputs and random inputs. The summarized statistics about the estimated connectivity strengths between areas and their rate of convergence are listed in Table 4.4. It is noted here that, when compared to estimation under random inputs, estimated unknown parameters under optimal inputs have comparable mean values but with tighter confidence intervals (smaller variances) across the 50 Monte Carlo runs and exhibit faster convergence rates towards final values.
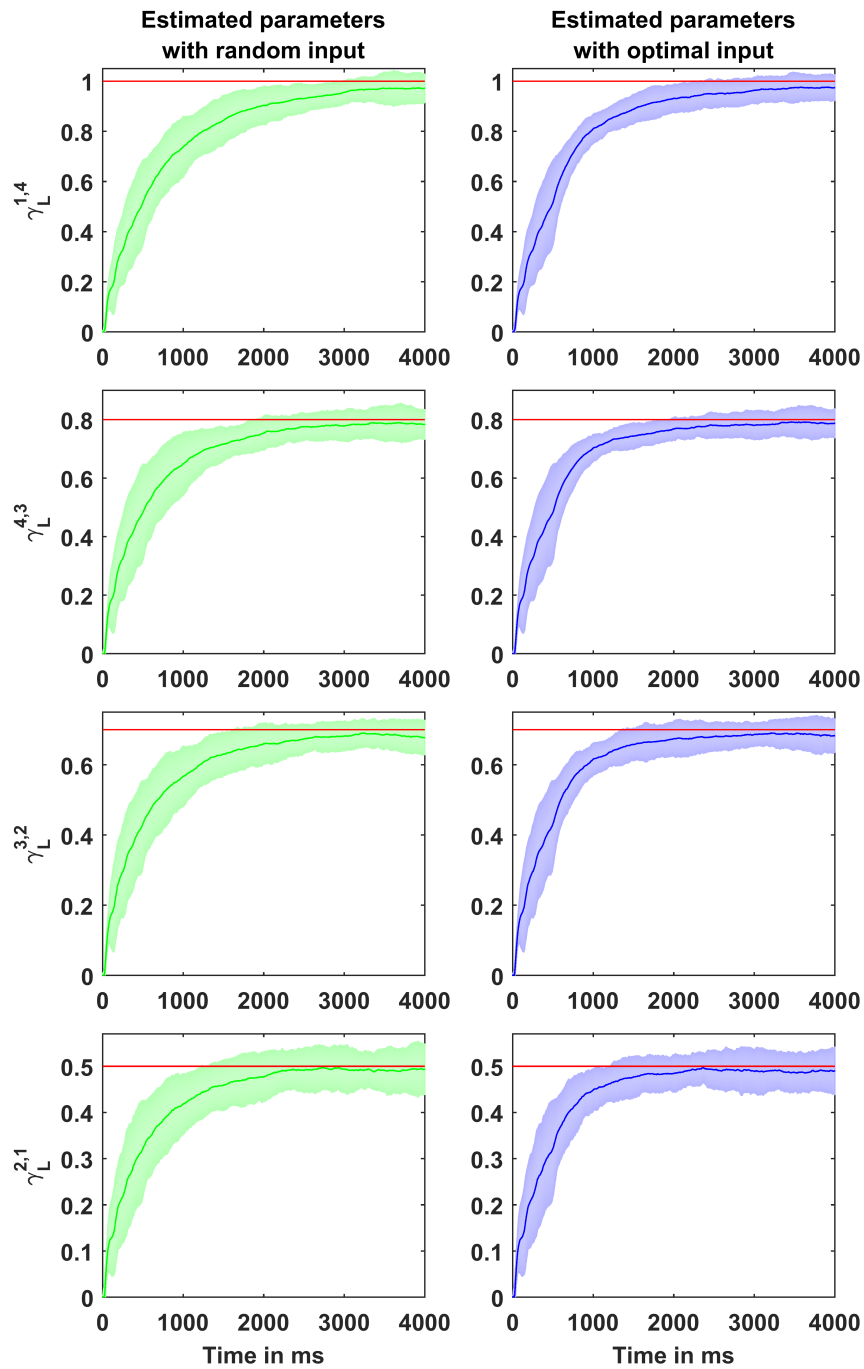
Figure 4.10: Second scenario: Case b: Four LFP observations: Estimated connectivity parameters (blue and green traces) in terms of their mean (solid lines) and a 95% confidence interval (shaded regions), and the true parameter (red trace). Left: under random inputs. Right: under designed optimal inputs.

Table 4.4: Statistics of the estimated parameters (connectivity strengths between areas) from four LFP observation signals averaged over 50 Monte Carlo runs under optimal and random inputs.

	Parameter	Mean	Standard deviation	Rise Time (in sec)	Settling Time (in sec)
Optimal Input	$\gamma_L^{1,4} = 1$	0.95	0.034	1.19	1.99
	$\gamma_L^{4,3} = 0.8$	0.77	0.029	0.94	1.85
	$\gamma_L^{3,2} = 0.7$	0.67	0.027	0.93	1.78
	$\gamma_L^{2,1} = 0.5$	0.48	0.025	0.86	1.55
Random Input	$\gamma_L^{1,4} = 1$	0.93	0.041	1.43	2.24
	$\gamma_L^{4,3} = 0.8$	0.77	0.037	1.19	2
	$\gamma_L^{3,2} = 0.7$	0.67	0.032	1.19	1.98
	$\gamma_L^{2,1} = 0.5$	0.48	0.029	1.15	2

4.3 Discussion

The presented approach in combining Kalman filtering with optimally designed inputs showed that, in principle, better convergence and higher estimation accuracy can be attained. The rates of such improvements, however, depends on the complexity of the inversion problem. For instance, for well-posed problems such as the single Van der Pol oscillator, the estimation accuracy and convergence under optimal inputs were close to but slightly better than those under random inputs (Fig. 4.2). Presumably, these comparable results are due to the well-posed nature of the inversion problem, that is the hidden states and unknown parameter are well observable from the available input/output data (for both random and optimal inputs).

For the three coupled non-identical Van der Pol oscillators (Fig. 4.4 and Table 4.1), the results show comparable estimation accuracy of the damping parameters of the oscillators whose positions are observed (oscillators $i = 1$ and 3) and better estimation accuracy under optimal inputs of the damping parameter of the oscillator whose position is not observed (oscillator $i = 2$). The same conclusion was drawn for the case of five coupled oscillators (Fig. 4.5 and Table 4.2) with estimation accuracy under optimal inputs being significantly better for unobserved oscillators (oscillators $i = 2$ and 4). For the Double Well system,

a challenging problem to invert due to its quadratic observation signal although it is a single state system, parameter estimation under optimal inputs was significantly better than those under random inputs case which showed high variability across trials as shown in Fig. 4.6.

The neuronal model results showed that the number of available observation signals has a great impact on the estimation problem. For one unknown connectivity parameter, one observation LFP signal is sufficient to identify the model correctly with improved accuracy under optimal inputs (Fig. 4.8). With four unknown connectivity parameters, one LFP signal was not enough for model identification (parameter estimates did not converge). For this case, at least two LFP signals were needed for proper convergence (Fig. 4.9 and Table 4.3) yet again with better accuracy under optimal inputs. As the number of available observations increases, parametric estimation improves in accuracy. This is concluded from the estimation results with four LFP observations (Fig. 4.10 and Table 4.4) which had closer mean values to true parameters, smaller variances across the 50 Monte Carlo simulations, and faster convergence when compared to estimation with two LFP observations. Once more, for this case, the estimation accuracy and convergence were better under optimal inputs than those under random inputs.

In conclusion, improved identification of models including those for neuronal activity generation from limited, yet carefully designed observations has large potential gains in the general modeling field as well as the field of computational neuroscience and other areas of biophysical modeling. Yet, these gains in estimation accuracy pose heavy computational load making this procedure intractable for on-line applications, an issue that we will address later on by proposing an alternative procedure to significantly reduce the computational needs for designing experiments suitable for on-line applications.

Chapter 5

Optimal Design of Process Noise Covariance in Nonlinear Kalman Filters

In a Kalman framework, an a priori statistical knowledge about all the above Gaussian noise processes, namely their covariance matrices, is necessary for correct performance. These covariances are referred to as the filter tuning parameters and need to be determined by the designer for proper performance of the filter. This manual tuning is often time consuming since performance is assessed post estimation and the direction and magnitude of change in tuning parameters is left to the tweaking skills of a modeler, a challenging endeavor that becomes considerably more complicated in nonlinear systems setups.

It is therefore highly desirable to automate this tuning procedure to both aid in estimation convergence and produce more confident estimates of the augmented states. Earlier efforts on this topic include [4, 76].

In this chapter, we propose an approach whereby the tuning parameters of the Kalman filter are optimally designed based on sensitivity analysis of the underlying system. We demonstrate this method on a benchmark hemodynamic model where driving neuronal activity input (NA) is unknown (input deconvolution). Using state augmentation in the Kalmak setup, NA input is assumed to follow a random walk process whose tuning parameter (covariance of this process) is designed using an Adaptive Design Optimization (ADO) method within the forward pass of the Cubature Kalman filter. A final backward pass of the CKF (namely the Cubature Kalman Smoother, CKS) demonstrates superior performance of the proposed solution to the tedious manual iterative, and approximate tuning.

5.1 Problem Definition and Setup

Given the discrete state-space form of the hemodynamic model :

Process Equation: $\qquad\qquad\qquad \mathbf{x}_k = F_d(\mathbf{x}_{k-1}, u) + \mathbf{v}_{k-1}$ $\hfill$ (5.1)

Measurement Equation: $\qquad\qquad\quad z_k = h(\mathbf{x}_k) + w_k$ $\hfill$ (5.2)

Where $v_{k-1} \in \mathbb{R}^n$ is a vector of random Gaussian noise with zero mean and covariance V_{k-1}, $w_k \in \mathbb{R}^d$ is a vector of random Gaussian noise with zero mean and covariance R_k, and z_k is the discrete noisy observation BOLD signal at discrete time k.

The problem at hand is defined as recovering unobserved hemodynamic variables and estimating unknown NA input from observed BOLD signal (input deconvolution) (see section 3.5). In order to solve this problem, we will utilized the square-root Cubature Kalman Filter (SCKF) (see section 2.3) as an estimation tool for the model in state-space form. Accordingly, the unknown input is estimated as an augmented state variable which is assumed to follow be a random walk dynamic process in the SCKF setup. This leads to a parameter tuning problem, tuning the covariance of random walk process which is unknown and can highly affect the stability and accuracy of the filter estimates. The tuning parameter is achieved using the ADO method so as to search for those optimal covariance values that produce the most informative measurements about the unknown input. Moreover, since the assumed unknown NA input is a time varying variable, a backward smoothing pass using square-root Cubature Kalman Smoother (SCKS) is applied after the forward SCKF pass in order to improve input estimation (SCKS algorithm is listed in section 2.3.4).

The augmented state vector includes (a) the hemodynamic model states and (b) the unknown NA input.

$$\mathbf{x}_k^{\text{aug}} = \begin{bmatrix} \mathbf{x}_k & u \end{bmatrix}^T$$

The augmented discrete nonlinear process equation $F_d^{\text{aug}}(\mathbf{x}_{k-1}, u)$ is the discrete version of $F^{\text{aug}}(\mathbf{x}(t), u)$

$$F^{\text{aug}}(\mathbf{x}(t), u) = \begin{bmatrix} F(\mathbf{x}(t), u) \\ F_u(\mathbf{x}(t)) \end{bmatrix}$$

Where $F_u(\mathbf{x}(t))$ describes the dynamics of the unknown NA input as a random walk process:

$$\dot{u} = \Gamma_u \qquad\qquad \text{(continuous time representation)} \qquad (5.3)$$

$$u_{k-1} = u_{k-1} + v_{u_{k-1}} \qquad\qquad \text{(discrete time representation)} \qquad (5.4)$$

Where $v_{u_{k-1}}$ is random Gaussian noise with zero mean and covariance $Q_{u_{k-1}}$.

5.1.1 Optimal Covariance Design Problem

For optimal covariance design, we will rely on an approach used for optimal input design ([39, 40]), but *instead of searching for the optimal input we will search for the optimal covariance* that will produce most informative observations about the unknown NA input. The optimization problem is formulated through the maximization of a scalar function of the Fisher information matrix (FIM). Here, the optimal covariance Q_u^* is computed by solving the following optimization problem:

$$
\begin{aligned}
Q_u^* &= \operatorname*{argmax}_{Q_u} \text{ trace}(FIM) \\
\text{subject to} \quad & Q_{u_{min}} \leq Q_u \leq Q_{u_{max}}
\end{aligned}
\tag{5.5}
$$

Given the state-space model in equations (5.1) and (5.1), the elements of the Fisher information matrix are combinations of partial derivatives of the system response variables with respect to the unknown NA input u. The FIM elements and sensitivities are obtained by solving the sensitivity equations. The FIM is determined by the following equation:

$$
FIM = \sum_{k=1}^{N} \left(\frac{\partial z_k}{\partial u}\right)^T R^{-1}\left(\frac{\partial z_k}{\partial u}\right)
\tag{5.6}
$$

Where N is the total number of available measurements points, R is the covariance matrix of the measurement noise, and the sensitivities $\partial z_k/\partial u$ are the partial derivatives of the observation z_k at discrete time k with respect to unknown input $u \in \mathbb{R}$ and they are solutions of:

$$
\begin{cases}
\dfrac{d}{dt}\left(\dfrac{\partial \mathbf{x}}{\partial u}\right) = \displaystyle\sum_{i=1}^{n}\left\{\dfrac{\partial F}{\partial x_i}\,\dfrac{\partial x_i}{\partial u}\right\} + \dfrac{\partial F}{\partial u} \\[2em]
\dfrac{\partial z_k}{\partial u} = \displaystyle\sum_{i=1}^{n}\left\{\dfrac{\partial h}{\partial x_i}\,\dfrac{\partial x_i}{\partial u}\right\} + \dfrac{\partial h}{\partial u}
\end{cases}
\tag{5.7}
$$

Where n is the total number of states, and u refers to unknown NA input.

5.1.2 Framework of Optimal Covariance Design and Kalman Filter Estimation (OCD-SCKF)

For each time step, a new input covariance was designed and used for the next time step of the SCKF. In designing the input covariance, we solved the optimization problem using brute-force approach (in which all possible solutions are calculated and and the optimal solution is selected) with the analytical solution
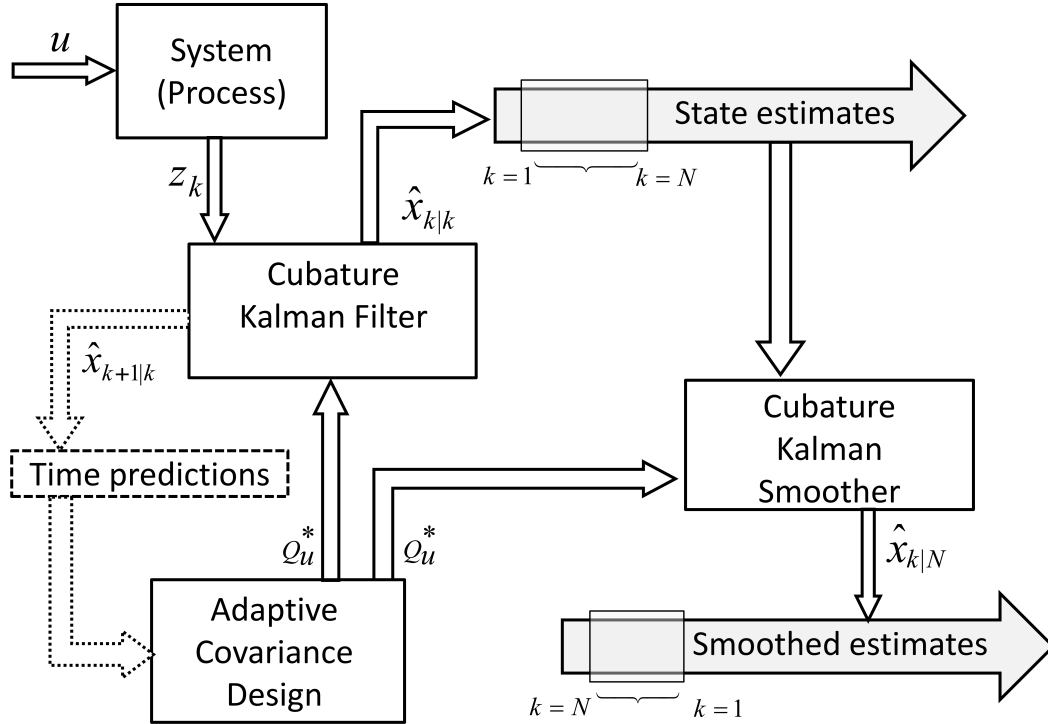
Figure 5.1: Schematic of the proposed OCD-SCKF algorithm.

of the partial derivatives. This is done by solving for the sensitivity functions in equation (5.7) and their corresponding FIM for the input covariance space $[Q_{u_{min}}, Q_{u_{max}}]$ based on current state vector estimates $\hat{\mathbf{x}}_k$ and its corresponding error covariance S_{kk} and their predicted evolution for the next time step (using the time update step of the SCKF).

Since we are estimating an unknown input, the designed covariance values at each cycle of the forward SCKF run were stored in order to be used in the backward smoothing run (SCKS). Fig. 5.1 shows a diagram of basic elements and processes of the proposed algorithm.

5.2 Results

In this section, we will present estimation results based on optimally designed input covariance and compare them with those estimated based on fixed covariance.

The proposed method is applied for a simulation length of 200 seconds for which the observation BOLD signals were generated with sampling interval $dt = 0.1$ and then re-sampled at $dt = 0.5$ (sampling rate at which the Kalman Filter

is applied). The search range for Q_u is $Q_{u_{min}} = 0.01$ and $Q_{u_{max}} = 0.06$. The estimation accuracy of unknown NA input under optimal covariance design is compared with that under fixed input covariance. For statistical assessment, a total of 50 independent Monte Carlo runs were made. The estimation accuracy is computed in terms of the Mean Square Error and its variance:

$$MSE \;=\; \frac{1}{MK} \sum_{m=1}^{M} \sum_{k=1}^{K} \frac{\left(u_k^{\text{real}} - \hat{u}_{k,m}\right)^2}{\left(\max(u^{\text{real}}) - \min(u^{\text{real}})\right)^2} \tag{5.8}$$

Where K is the length of the total simulation time vector, M is the Monte Carlo runs, u_k^{real} the true input at time k, $\hat{u}_{k,m}$ is the estimated input at time k in the mth Monte Carlo run, and $(\max(u^{\text{real}}) - \min(u^{\text{real}}))^2$ is a normalizing factor.
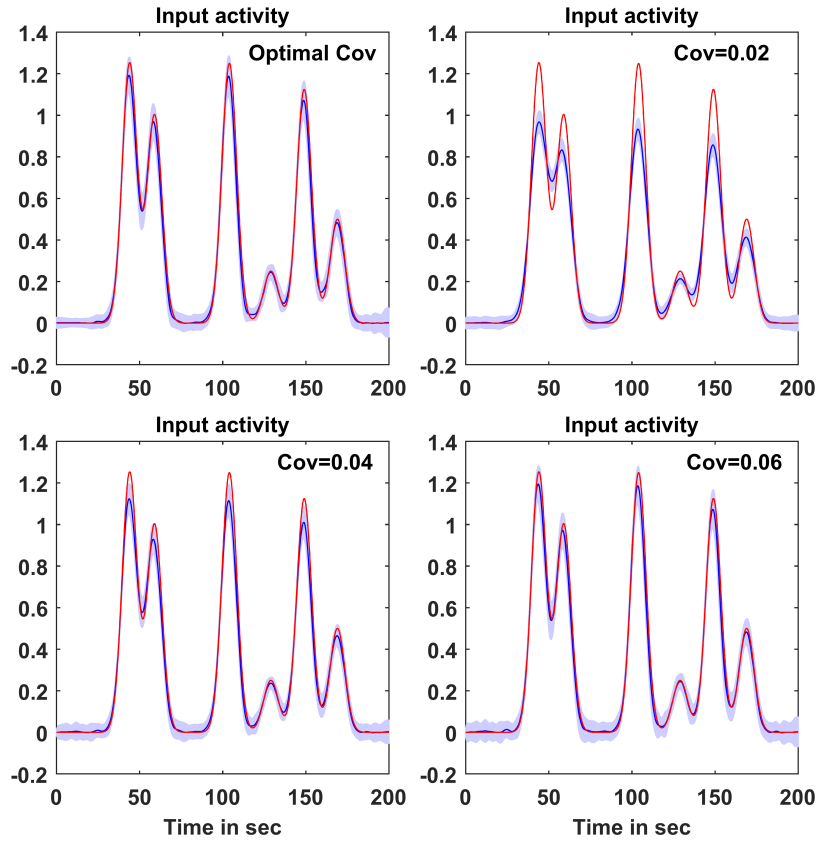
Figure 5.2: Estimated NA inputs in terms of their mean (solid lines) and a 95% confidence interval (shaded regions), and the true NA input (red trace). Top left: under designed input covariance. The rest of sub-figures are under fixed input covariance, top right: Cov = 0.02, bottom left: Cov = 0.04, bottom right: Cov = 0.06.

Fig. 5.2 shows the means and 95% confidence intervals of the estimated unknown

NA input under designed and fixed input covariance. The summarized statistics about estimation accuracy are listed in Table 5.1 where the term "deviation counts" refers to the number of times at which the Kalman filter diverges out of total 50 Monte Carlo runs. From Fig. 5.2 we can see that optimally designed covariance provided better input estimates in terms of their mean as compared to low and intermediate fixed covariance values (Cov = 0.02 and Cov = 0.04) and this also can be inferred from Table 5.1 where the MSE score for the optimal case was lower than those of the fixed covariance cases. It is also noted that for high fixed covariance value case (Cov = 0.06), the accuracy of the estimated input was comparable to that of the optimal case (almost similar MSE values between these two cases), but for the fixed covariance case (Cov = 0.06) the filter failed twice out of 50 Monte Carlo runs and it scored higher variance value (this is shown in Fig. 5.3 as fixed covariance case (Cov = 0.06) has a wider confidence interval around the mean as compared to the optimal covariance case).

Table 5.1: Statistics of the estimated NA inputs averaged over 50 Monte Carlo runs under optimal and fixed input covariance.

Covariance Value	Mean Square Error (MSE)	Variance of MSE	Deviation counts
Q_u^*	0.0015	$0.9e^{-3}$	0
$Q_u = 0.02$	0.0058	$0.36e^{-3}$	0
$Q_u = 0.04$	0.002	$0.69e^{-3}$	0
$Q_u = 0.06$	0.0016	$1e^{-3}$	2
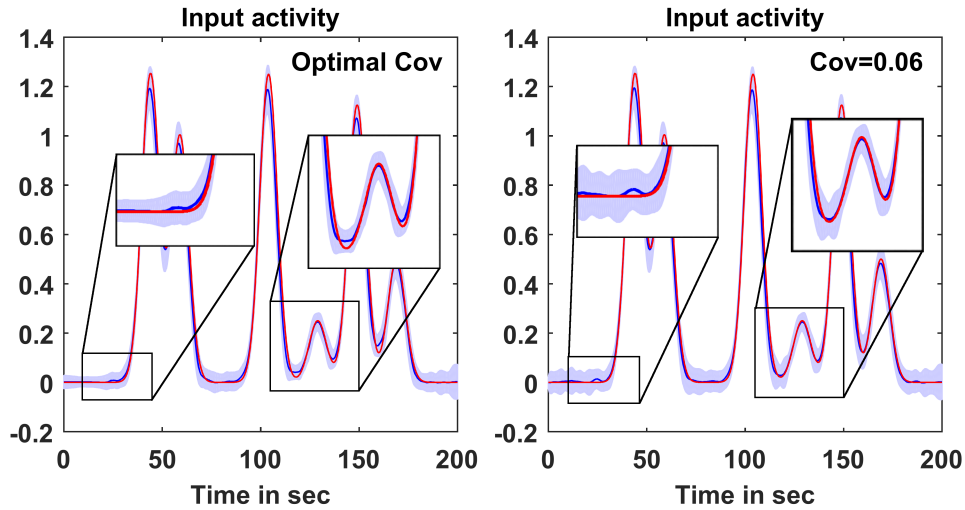
Figure 5.3: Accuracy in terms of confidence intervals. Left: under designed input covariance. Right: fixed input covariance Cov = 0.06.

5.3 Discussion

In this chapter, we proposed a procedure to optimally design the tuning parameter (the covariance of the unknown input which follows a random walk process) of the Kalman filter based on sensitivity analysis of the model (solving for the sensitivity functions and the FIM). We demonstrated this procedure on a hemodynamic model where driving neuronal activity input (NA) is unknown (input deconvolution).

The proposed approach is demonstrated to produce more confident estimates and better convergence without the need of an iterative tuning process from the designer, as seen in Fig. 5.2 and Table 5.1, optimally designed covariance provided better input estimates in terms of their mean as compared to low and intermediate fixed covariance values (Cov = 0.02 and Cov = 0.04). Moreover, optimally designed covariance showed better estimation accuracy when compared to the best manually tuned input covariance case (Cov = 0.06) which scored higher variance value (wider confidence interval around the mean as shown in Fig. 5.3) and more importantly the filter failed twice out of 50 Monte Carlo runs for this case whereas for the optimal case the filter remained stable throughout all Monte Carlo simulations.

It is worth to mention that this procedure is aimed for off-line model estimation, that is model identification using Klaman filters from already collected input/output data. Thus, the computational complexity associated with designing

the tuning parameters of the Kalman filter does not pose any serious limitations and this procedure may provide a solution to the tedious manual iterative, and approximate tuning.

Chapter 6

Dual Kalman Filter Setup for Input Design and Estimation of Nonlinear Dynamical System Models

In chapter 4, we have introduced the OID-SCKF method for optimal input design using ADO method and showed that optimally designed inputs produce more informative input/output data about the model unknowns and better Kalman performance in terms of estimation accuracy of unknown model states and parameters. However, this was accomplished with the cost of higher computational burden exerted by solving the optimization problem associated with ADO method to find the optimal input that produces the most informative output about the model unknowns. Since the optimization problem of the OID part is non-convex and nonlinear, the computational complexity tied with finding an optimal input makes the proposed OID-SCKF method unsuitable for on-line applications.

In this chapter, we will introduce a new method based on a dual Kalman filters setup which will circumvent the computational demands for solving for the optimal input. The main idea is to "transform" the optimization problem into a Kalman filter setup which will "estimate" a sub-optimal input that achieves informative observations about unknown parameters and hidden states. In doing so, by transforming and setting up the optimization problem in a Kalman filter setup, this will discard the optimization problem along with its computational burden and hence drastically reduces the computational needs to design an input.

6.1 Problem Definition and Setup

We consider experiment design paradigms suitable for on-line applications in which inputs are designed to generate informative observations that aid in improving estimation accuracy of the hidden state variables and unknown parameters of the model structure. We propose a method based on two Kalman filters aimed to circumvent solving a non-convex and nonlinear optimization problem associated with the introduced OID-SCKF method.

The proposed Dual Kalman setup consists of two SCKF filters with different sampling times, (i) the first SCKF filter, operating at a sampling rate Δt_1 as same as the collected observations from conducted experiments, will estimate hidden states and unknown parameters given input/output data, and (ii) the second SCKF filter, operating at a sampling rate Δt_2 much higher than that of the first filter Δt_1 (the time-line of an experiment (simulation) is divided into time windows or stages of equal length Δt_2), is aimed to provide designed inputs based on current estimates of the system model states and parameters provided from the first SCKF filter.

In what follows, we will describe in details the setup for the Dual Kalman filters for a given dynamical system formulated in state-space form as:

Process Equation: $$\dot{\mathbf{x}}(t) = f(\mathbf{x}(t), I) + \mathbf{\Gamma} \tag{6.1}$$
Measurement Equation: $$z_k = h(\mathbf{x}_k) + w_k \tag{6.2}$$

6.1.1 First Kalman filter setup

The first SCKF is aimed to estimate model states and unknown parameters, the role of this filter is exactly the same as the one described in section 4.1.1.

Given the state-space model as defined in equations (6.1) and (6.2), we will augment the hidden state vector to include the presumed dynamics of the unknown parameter vector $\boldsymbol{\theta}$. The augmented state vector is composed of (a) model hidden states, (b) unknown parameter vector:

$$\mathbf{x}_1(t) = [\ \mathbf{x}(t) \quad \boldsymbol{\theta}\ ]^T$$

The resultant state-space formulation for the first SCKF is defined as:

Process Equation: $$\dot{\mathbf{x}}_1(t) = f_1(\mathbf{x}_1(t), I) + \mathbf{\Gamma}_1 \tag{6.3}$$
Measurement Equation: $$z_{1_k} = h_1(\mathbf{x}_{1_k}) + w_{1_k} \tag{6.4}$$

Where $\mathbf{x}_1(t) \in \mathbb{R}^{n_1}$ is the augmented state vector of the system at time t (n_1 is the size of the augmented state vector for the first SCKF), I is the exogenous

input, $z_{1_k} \in \mathbb{R}^{d_1}$ is the measurement at discrete time k (d_1 is the size of the measurement vector for the first SCKF), $f_1 : \mathbb{R}^{n_1} \times \mathbb{R} \to \mathbb{R}^{n_1}$ is the drift coefficient, $h_1 : \mathbb{R}^{n_1} \times \mathbb{R} \to \mathbb{R}^{d_1}$ is the measurement function, $\mathbf{\Gamma}_1 \in \mathbb{R}^{n_1}$ and $w_{1_k} \in \mathbb{R}^{d_1}$ are vectors of random Gaussian noise with zero mean and covariance Q_1 and R_1 respectively.

The stochastic differential equation (SDE) represented in the process equation (6.3) is in continuous time, we can discretize the SDE using Local Linearization (LL) method as described in section (2.3); this will transform the state-space model to a pair of difference equations in order to apply the SCKF.

The discrete state-space model becomes:

Process Equation: $$\mathbf{x}_{1_k} = f_{1,d}(\mathbf{x}_{1_{k-1}}, I) + \mathbf{v}_{1_{k-1}} \tag{6.5}$$

Measurement Equation: $$z_{1_k} = h_1(\mathbf{x}_{1_k}) + w_{1_k} \tag{6.6}$$

Where $v_{1_{k-1}} \in \mathbb{R}^{n_1}$ is a vector of random Gaussian noise with zero mean and covariance $V_{1_{k-1}}$, $w_{1_k} \in \mathbb{R}^{d_1}$ is a vector of random Gaussian noise with zero mean and covariance R_{1_k}, and z_{1_k} is the discrete noisy observation at discrete time k.

Where the discrete nonlinear process equation $f_{1,d}(\mathbf{x}_{1_{k-1}}, I)$ is the discrete version of $f_1(\mathbf{x}_1(t), I)$:

$$f_1(\mathbf{x}_1(t), I) = \begin{bmatrix} f(\mathbf{x}_1(t), I) \\ f_{\boldsymbol{\theta}}(\mathbf{x}_1(t)) \end{bmatrix}$$

Where $f_\theta(\mathbf{x}(t))$ describes the dynamics of the unknown parameters which are assumed to follow a random walk:

$$\dot{\boldsymbol{\theta}} = \mathbf{\Gamma}_\theta \tag{6.7}$$

6.1.2 Second Kalman filter setup

The second SCKF filter is aimed to design the exogenous excitatory input to the system for future time windows based on current estimates of the system model states and parameters provided from the first SCKF filter.

As described in section 4.1.1, the OID part is based on an optimization problem defined as maximizing a scalar function of the Fisher information matrix (FIM) over the input space $[I_{min}, I_{max}]$, where the optimal input I^* is computed by solving the following optimization problem:

$$\begin{aligned} &\underset{I}{\text{argmax}} && \text{trace}(FIM) \\ &\text{subject to} && I_{min} \leq I \leq I_{max} \end{aligned} \tag{6.8}$$

The basic idea of the dual Kalman filters is to transform the optimization problem in equation (6.8) into a Kalman filter setup in order to circumvent the computational burden of solving this optimization problem. We propose to do so by setting the second SCKF to estimate the exogenous input I that achieves FIM values higher than the current FIM values that are computed from current model states and parameters provided from the first SCKF filter. In other words, the second SCKF will update the current exogenous input I towards a more informative input estimates that generates observations with higher FIM values. The second SCKF will update the input every $\Delta t_2 \gg \Delta t_1$ where Δt_2 is the size of the time window during which the first SCKF is applied and model states and unknown parameters are estimated with the updated input is being applied to the system and observations are collected with sampling time Δt_1. In what follows we will describe the setup of the second SCKF in details.

The purpose of the second SCKF is to update the exogenous input I based on current model estimates from the first SCKF. the state-space formulation for this filter in discrete time is given by:

Process Equation: $\qquad\qquad \mathbf{x}_{2_k} = f_{2,d}(\mathbf{x}_{1_{k-1}}, \mathbf{x}_{2_{k-1}}) + \mathbf{v}_{2_{k-1}}$ $\qquad\qquad$ (6.9)

Measurement Equation: $\qquad\qquad z_{2_k} = h_2(\mathbf{x}_{1_k}) + w_{2_k}$ $\qquad\qquad\qquad$ (6.10)

Where $\mathbf{x}_{1_k} \in \mathbb{R}^{n_1}$ is the augmented state vector of the dynamic system at time k (n_1 is the size of the augmented state vector for the first SCKF), $\mathbf{x}_{2_k} \in \mathbb{R}^{n_2}$ is the augmented state vector of the second SCKF at time k (n_2 is the size of the augmented state vector for the second SCKF), $z_{2_k} \in \mathbb{R}^{d_2}$ is the measurement for the second filter at discrete time k (d_2 is the size of the measurement vector for the second SCKF), $f_2 : \mathbb{R}^{n_2} \times \mathbb{R} \to \mathbb{R}^{n_2}$ is the drift coefficient, $h_2 : \mathbb{R}^{n_2} \times \mathbb{R} \to \mathbb{R}^{d_2}$ is the measurement function for the second filter, $\mathbf{v}_{2_{k-1}} \in \mathbb{R}^{n_2}$ and $w_{2_k} \in \mathbb{R}^{d_2}$ are vectors of random Gaussian noise with zero mean and covariance Q_2 and R_2 respectively. The state vector for the second SCKF in discrete time is defined as:

$$\mathbf{x}_{2_k} = \begin{bmatrix} \mathbf{x}_k & \boldsymbol{\theta}_k & I_k \end{bmatrix}^T$$

Or equivalently as function of the augmented state vector of the first SCKF:

$$\mathbf{x}_{2_k} = \begin{bmatrix} \mathbf{x}_{1_k} & I_k \end{bmatrix}^T$$

The measurement equation function $h_2(\mathbf{x}_{1_k})$ is a function of the FIM of the model computed based on current estimates of model states (i.e. model states and parameters provided from the first SCKF filter $\mathbf{x}_{1_k}$):

$$h_2(\mathbf{x}_{1_k}) = FIM(\mathbf{x}_{1_k}) + \delta \qquad\qquad (6.11)$$

93

Where $FIM(\mathbf{x}_{1_k})$ is the FIM computed at the end of a given time window after the first SCKF has completed estimation of the model states $\mathbf{x}_1$, and δ is a small fraction of $FIM(\mathbf{x}_{1_k})$ to make the measurement of the second SCKF (z_{2_k}) updates the input towards higher values of the current FIM.

$$\delta = 0.05 \; FIM(\mathbf{x}_{1_k}) \tag{6.12}$$

Thus, the measurements of the second CKF are computed to drive the state vector $\mathbf{x}_2$ to be updated towards a higher FIM values.

Given the state-space model (6.1) and (6.1), the Fisher information matrix elements are combinations of partial derivatives of the system response variables with respect to the model parameters. The FIM elements and sensitivities are obtained by solving the sensitivity equations [75]. The following equation is set to compute the FIM values at the end of the time window at time k:

$$FIM \;\; = \sum_{l=1}^{d_1} \left(\frac{\partial z_{1_{l,k}}}{\partial \boldsymbol{\theta}}\right)^T R_1^{-1} \left(\frac{\partial z_{1_{l,k}}}{\partial \boldsymbol{\theta}}\right) \tag{6.13}$$

Where R_1 is the covariance matrix of the measurement noise of the first SCKF, and the sensitivities $\partial z_{1_{l,k}}/\partial \boldsymbol{\theta}$ are solutions of:

$$\begin{cases} \dfrac{d}{dt}\left(\dfrac{\partial \mathbf{x}_1}{\partial \theta_j}\right) = \displaystyle\sum_{i=1}^{n_1} \left\{\dfrac{\partial f_1}{\partial x_{1_i}} \dfrac{\partial x_{1_i}}{\partial \theta_j}\right\} + \dfrac{\partial f_1}{\partial \theta_j} \\[4mm] \quad \dfrac{\partial z_{l,k}}{\partial \theta_j} = \displaystyle\sum_{i=1}^{n_1} \left\{\dfrac{\partial h_{1,l}}{\partial x_{1_i}} \dfrac{\partial x_{1_i}}{\partial \theta_j}\right\} + \dfrac{\partial h_{1,l}}{\partial \theta_j} \qquad l = 1 \dots d_1 \end{cases} \tag{6.14}$$

Where n_1 is the total number of states of the first SCKF, and θ_j $(j = 1 \dots n_\theta)$ refers to unknown parameters.

In this setup, we are computing the FIM (equation (6.13)) as a single value at the end of the time window (not as summation over the entire time window), thus, we are looking at the FIM when the system reaches its steady state (assuming that the time window or Δt_2 is large enough). Hence, we are interested in finding the model states that achieve the higher FIM value at steady state (or at the end of the time window). For that, we have defined the second SCKF to estimate the model states that achieve a higher FIM value at steady state. Thus, the equations of motion of model states ($\mathbf{x}$) are defined as random walk processes in $f_{2,d}(.)$ in order to be updated towards the higher FIM value, and the equation of motion of the exogenous input I is based on the steady state solution of process equation (6.1) (that is at $\dot{\mathbf{x}} = 0$). Thus, the equation of motion that governs the dynamics of the input in the second SCKF are defined as:

$$\dot{I} = f_I(\mathbf{x}(t)) + \mathbf{\Gamma}_\theta \qquad (6.15)$$

$$f_I(\mathbf{x}(t)) = f^{-1}(\mathbf{x}(t), I)\Big|_{\dot{\mathbf{x}}(t)=0} \qquad (6.16)$$

In other words, the second SCKF is designed to find the model states that achieve better FIM value at steady state, and from these estimated model states the exogenous input for the next time window is estimated.

The equations of motion for the second SCKF are defined in $f_{2,d}(.)$ for the state vector $\mathbf{x}_2$ as follows:

$$f_{2_d}(\mathbf{x}_{1_{k-1}}, \mathbf{x}_{2_{k-1}}) = \begin{bmatrix} \mathbf{x}_{k-1} \\ \boldsymbol{\theta}_{k-1} \\ f_{I,d}(\mathbf{x}_{k-1}) \end{bmatrix}$$

Where $f_{I,d}(\mathbf{x}_{k-1})$ is the discrete version of $f_I(\mathbf{x}(t))$ defined in equation (6.16).

6.1.3 Framework of the Dual Kalman filters

The Dual Kalman filters are defined to estimate hidden states ($\mathbf{x}$) and model unknown parameters ($\boldsymbol{\theta}$), in addition to designing the input that produces more informative observations. The first SCKF is aimed to estimate the model variables, whereas the second filter is aimed to design the input. The two filters have different sampling times, the first SCKF (model estimation) has a sampling time Δt_1 dictated by the sampling rate of collected noisy observations, whereas the second SCKF (input design) has a sampling time $\Delta t_2 \gg \Delta t_1$ defined as the time window or stage s during which the designed input is applied to system. Starting from an initial input, observations are collected and the first SCKF is applied to provide model estimates. At the end of each time window or stage s: (a) The FIM values are computed given current model states $\mathbf{x}$ and unknown parameters $\boldsymbol{\theta}$ estimates from the first SCKF, which will serve as measurements for the second SCKF. (b) As for the second SCKF, the model states and unknown parameters in state vector $\mathbf{x}_2$ are initialized by current estimates of $\mathbf{x}$ and $\boldsymbol{\theta}$, and based on FIM measurements, the second SCKF will predict the model variables ($\mathbf{x}$ and $\boldsymbol{\theta}$ which follows random walk processes) along with the input (I whose dynamics are governed by the inverse of process equation at steady state) that produce better FIM values and update the state vector $\mathbf{x}_2$ ($\mathbf{x}$, $\boldsymbol{\theta}$ and I) towards targeted better FIM values. From the second SCKF state vector $\mathbf{x}_2$, the input I is the
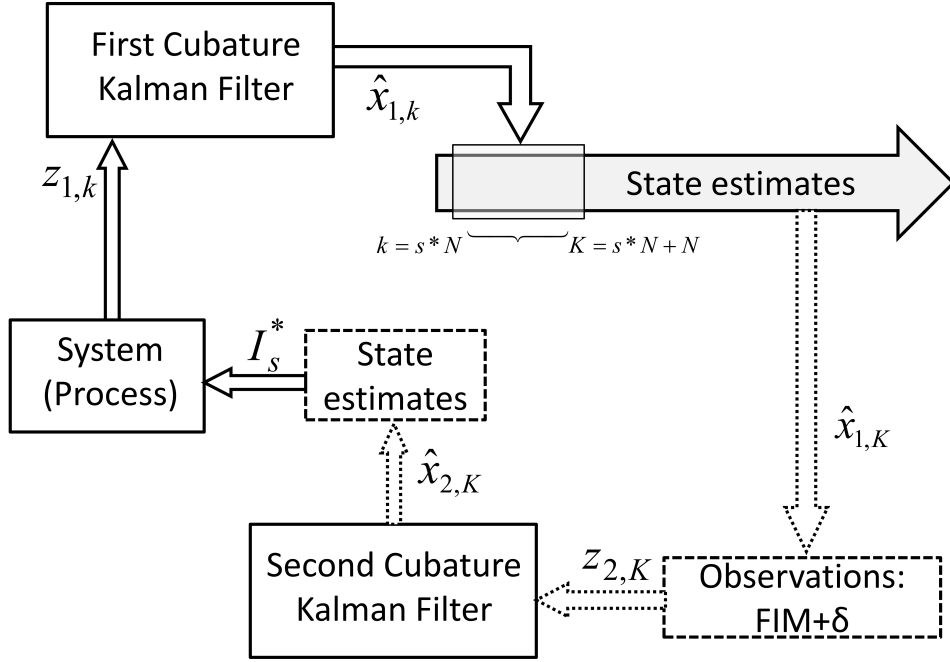
Figure 6.1: Basic elements of the proposed Dual Kalman filters. The first SCKF provides estimates of the hidden states and parameters based on the collected noisy observations from the system, and supply the observations for the second SCKF. The second SCKF provides the designed input to the system based on the FIM observations and model estimates from the first SCKF.

only variable of interest (the updated $\mathbf{x}$ and $\boldsymbol{\theta}$ in the state vector $\mathbf{x}_2$ are discarded at the end of the second SCKF cycle, since these variables are estimated and updated by the first SCKF from the available system dynamics and observations). The designed (updated) input I at the end of the second SCKF cycle will be supplied to the system for the next stage $s + 1$.

Fig. 6.1 shows a diagram of basic elements and processes of the proposed Dual Falman filters and Algorithm (2) shows the the pseudo-code for the proposed OID-SCKF method.

6.1.4 Performance assessment

The quantitative assessment of the introduced Dual Kalman method against estimation under other input design methods (e.g. OID-SCKF algorithm and random inputs) is carried out with performance assessment tools such as "Rise time" and "Settling time" as defined in section 4.1.3. Moreover, we utilize "Computation time" defined as the time required to apply a given algorithm to conduct a single simulation run. Finally, statistical assessment of these values is conducted over

Algorithm 2 Framework for the Dual Kalman filters estimation problem

1: Initialization: Set initial states and parameters values $\hat{x}_1(0)$ $\hat{x}_2(0)$ and the square-root of process and measurement noise covariances: $S_{R_1,0}$, $S_{V_1,0}$, $S_{R_2,0}$ and $S_{V_2,0}$.

2: Define the input space $[I_{min}, I_{max}]$.

3: **for** $s = 0$ to S **do**   ▷ % for each stage s or time window Δt_2 %

4:     **if** $s = 0$ **then**   ▷ % First stage or time window%

5:         Define a random initial input I_0.

6:     **else**

7:         Define the designed input from the state vector $\hat{x}_2(s)$ of the second Kalman $I_s = \hat{x}_2(s)$.

8:     **end if**

9:     **for** $k = s * N$ to $K = N + s * N$ **do**

10:         Simulate model and collect measurements z_{1_k}

11:         Apply first Kalman filter and get the states and parameters estimates $\hat{x}_1(k)$

12:     **end for**

13:     Evaluate the FIM given $\hat{x}_1(K)$.

14:     Set the observations for the second Kalman $h_2(\mathbf{x}_1(K)) = FIM(\mathbf{x}_1(K)) + \delta$.

15:     Initialize the state vector for the second Kalman filter given the state vector of the first Kalman filter. That is by setting $\hat{x}_2(s) = \hat{x}_1(K)$ with their corresponding the corresponding error covariance matrix.

16:     Apply the second Kalman filter and get the input estimates from the corrected state vector $\hat{x}_2(s + 1)$ for stage $s + 1$.

17: **end for**

a set of repeated simulations to reduce the effect of randomness in process and observation noise.

6.2 Results

In this section, we will present estimation results based on designed inputs using Dual Kalman method and compare them with (i) those estimated based on random (not designed) inputs and (ii) those estimated based on optimal input design using OID-SCKF method.

6.2.1 Van der Pol System

The Van der Pol oscillator has two states $\mathbf{x} = [x_1 \ x_2]^T$ (oscillator position and velocity) in addition to one unknown damping parameter which is set here to $\mu = 3$
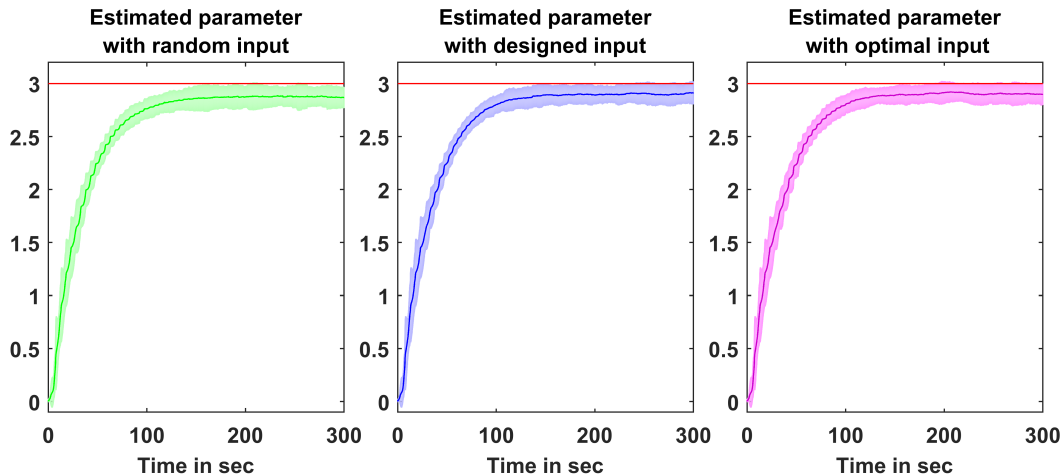
Figure 6.2: Estimated damping parameter μ (green, blue and purple traces) in terms of their mean (solid lines) and a 95% confidence interval (shaded regions), and the true parameter (red trace). Left: Under random input. Middle: under designed (Dual Kalman) input. Right: Under optimal (OID-SCKF) input.

(See section 3.1). For the single oscillator as well as the coupled oscillator networks considered next, the exogenous driving input is assumed to be of periodic nature $I(t) = A\sin(wt)$, $w = 0.2\pi$ rad/sec. Furthermore, the input amplitude A falls within a finite set of quantized levels $A \in [0, 0.1, 0.2, \dots, 3]$. Three types of inputs are considered: (i) a randomly selected sequence of amplitudes, henceforth denoted by "random input", (ii) a sequence of amplitudes that would be designed based on Dual Kalman algorithm, denoted by "designed input", and (iii) a sequence of amplitudes that would be designed based on OID-SCKF algorithm, denoted by "optimal input".

Single Oscillator

The output of the oscillator is considered to be a noisy discrete measurement of its position x_1. In the Kalman setup, the state vector is augmented as $\mathbf{x^a} = [x_1 \ x_2 \ \mu]^T$.

The proposed Dual Kalman method is applied for a simulation length of 300 seconds with sampling interval $\Delta t_1 = 0.1$ sec. The design stages or time windows were of length $\Delta t_2 = 25$ sec whereby a designed input is applied over that stage with fixed amplitude. The same applies for the random and optimal input cases where the SCKF is applied for 300 seconds with sampling interval $\Delta t_1 = 0.1$ sec and with time window of length $\Delta t_2 = 25$ sec whereby a random or optimal (OID-SCKF method) input is applied. For statistical assessment, a total of 50 independent Monte Carlo runs were made. The estimate of the damping param-

98

eter μ is shown in Fig. 6.2 where the means and 95% confidence intervals (shaded region) under designed (Dual Kalman), random, and optimal (OID-SCKF) inputs. The summarized statistics about the estimated damping parameters and their rate of convergence are listed in Table 6.1. From Table 6.1 we can see that all three methods achieved comparable mean values, however, when compared with SCKF estimation with random inputs and with OID-SCKF method, the Dual Kalman method (a) attained a smaller variance than both methods (optimal and random inputs) and hence tighter confidence intervals around the final value across the 50 simulations, (b) faster convergence rates than the random inputs case but slower than OID-SCKF method, and (c) in terms of computation times, the Dual Kalman method was much more efficient than the OID-SCKF method in designing informative inputs as the time needed to simulate a single run was much lower than OID-SCKF method and close to that of random inputs method.

Table 6.1: Statistics of the estimated damping parameter for single Van der Pol oscillator averaged over 50 Monte Carlo runs.

	Parameter	Mean	Standard deviation	Rise Time (sec)	Settling Time (sec)	Computation Time (sec)
Optimal Input	μ	2.9	0.055	64.7	110.1	84.2
Designed Input	μ	2.89	0.054	65.2	110.9	3.2
Random Input	μ	2.87	0.059	65.5	117.4	3

Network of Three Coupled Oscillators

A ring network of three non-identical oscillators ($N = 3$) with coupling parameter $K = 1.3$ and damping parameters $\boldsymbol{\mu} = [\mu^{(1)} \ \mu^{(2)} \ \mu^{(3)}]^T = [3 \ 2 \ 1]^T$ is considered.

In this scenario, the external periodic input is assumed to drive the first oscillator only. We also consider the three cases of designed (Dual Kalman), randomly, or optimally (OID-SCKF) designed inputs. It is assumed that two noisy observation signals, corresponding to the positions $x_1^{(1)}$ and $x_1^{(3)}$ of the first and third oscillators, are available. It is here desired to estimate the augmented state vector which includes six states $\mathbf{x} = [x_1^{(i)} \ x_2^{(i)}]^T, i = 1, \ldots, 3$ in addition to three

unknown damping parameters $\boldsymbol{\mu}$.

The Dual Kalman method is applied for a simulation length of 500 seconds with sampling interval $\Delta t_1 = 0.1$ sec where a designed input is applied for $\Delta t_2 = 25$ sec time window. The same applies for the random and optimal (OID-SCKF) input cases. For statistical assessment, a total of 50 independent Monte Carlo runs were made.
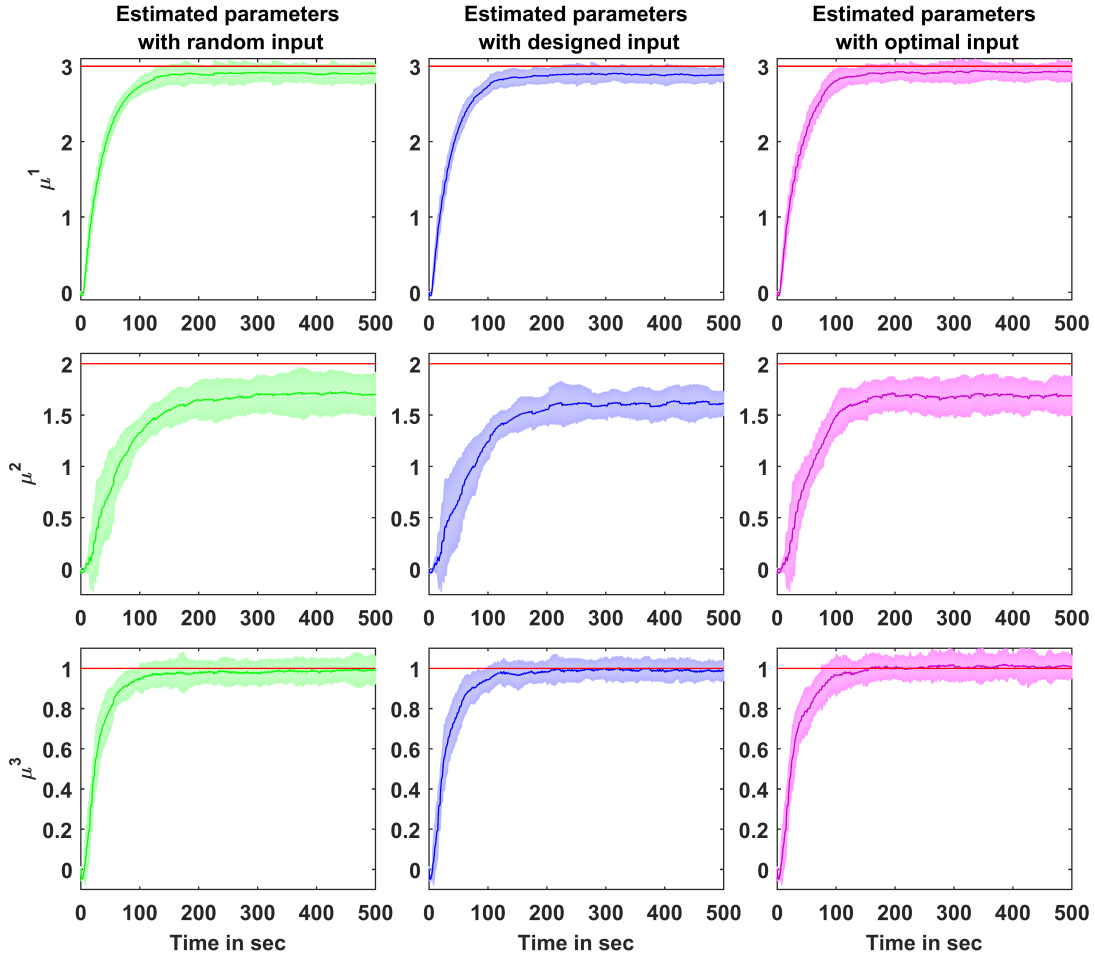
Figure 6.3: Estimated damping parameters $\boldsymbol{\mu} = [3;\ 2;\ 1]$ in terms of their mean (solid lines) and a 95% confidence interval (shaded regions), and the true parameters (red traces). Left: Under random input. Middle: under designed input. Right: Under optimal input.

Fig. 6.3 shows the means and 95% confidence intervals of the estimated damping parameters $\boldsymbol{\mu}$ under designed, random, and optimal inputs. The summarized statistics about the estimated damping parameters and their rate of convergence are listed in Table 6.2. For this scenario, the Dual Kalman method did slightly

worse (for the second damping parameter $\mu^{(2)}$) than the random and optimal cased in terms of the mean values of estimated parameter but for damping parameter $\mu^{(1)}$ and $\mu^{(3)}$ the mean values under designed inputs were comparable with those estimated under random and optimal inputs. However, this method showed smaller variance values (tighter confidence intervals) around the final mean values across the 50 simulations. Similar results to that of the single oscillator case, the computation times per simulation run were considerably slower for the Dual Kalman method as compared with the OID-SCKF method.

Table 6.2: Statistics of the estimated damping parameters for three coupled non-identical oscillators averaged over 50 Monte Carlo runs.

	Parameter	Mean	Standard deviation	Rise Time (sec)	Settling Time (sec)	Computation Time (sec)
Optimal Input	μ^1	2.91	0.065	70.6	119.1	129.1
	μ^2	1.68	0.09	82.6	153.8	
	μ^3	1.007	0.036	66.8	141.4	
Designed Input	μ^1	2.88	0.057	70.6	121.2	17.3
	μ^2	1.59	0.08	114.1	203.2	
	μ^3	0.98	0.03	59.7	111.3	
Random Input	μ^1	2.9	0.065	72.4	125.6	16.4
	μ^2	1.67	0.101	117.2	197.1	
	μ^3	0.98	0.034	55.2	112.1	

6.2.2   Double Well

This system has one states x in addition to one unknown free parameter $a = 2$ (See section 3.2). The external periodic input $I(t) = A\sin(wt), w = 0.08\pi$ rad/sec, with the amplitude A being considered as a variable $A \in [2.5, 3, 3.5, \ldots, 17.5]$ and was selected either by design (Dual Kalman), randomly, or optimally (OID-SCKF) designed over time stages. The augmented state vector had two quantities to be estimated from one noisy observation signal x.

The proposed method is applied for a simulation length of 500 seconds with
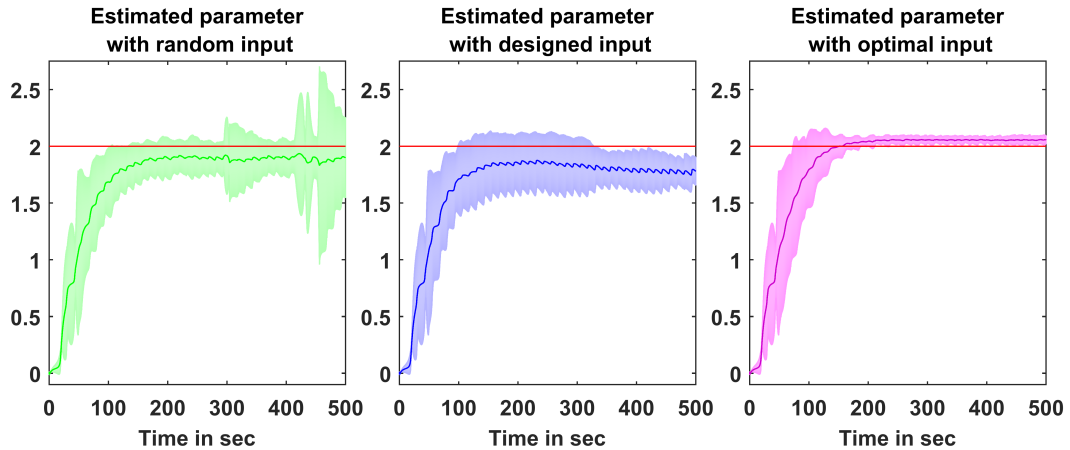
Figure 6.4: Estimated parameter a (green, blue and purple traces) in terms of their mean (solid lines) and a 95% confidence interval (shaded regions), and the true parameter (red trace). Left: Under random input. Middle: under designed input. Right: Under optimal input.

sampling interval $\Delta t_1 = 0.1$ sec whereby a designed (Dual Kalman), random, or optimal (OID-SCKF) input is applied for $\Delta t_2 = 50$ sec time windows. For statistical assessment, a total of 50 independent Monte Carlo runs were made.

Fig. 6.4 shows the mean and 95% confidence intervals of the estimated parameter a under under designed, random, and optimal inputs. The summarized statistics about the estimated damping parameters and their rate of convergence are listed in Table 6.3. Similar to the three Van der Pol oscillators results, the Dual Kalman method scored lower estimation mean value across the 50 simulations, however, the estimated parameter demonstrated more consistency as time progresses particularly toward the end of simulation time (> 300 sec) as compared to the random input case which showed higher variability (jumps in the green shaded region at times > 300 sec).

Table 6.3: Statistics of the estimated parameter a for the double well averaged over 50 Monte Carlo runs.

	Parameter	Mean	Standard deviation	Rise Time (sec)	Settling Time (sec)	Computation Time (sec)
Optimal Input	a	2.05	0.06	88.4	158.9	115

Designed Input	a	1.81	0.12	73	129.8	3.4
Random Input	a	1.89	0.13	85.3	144.3	3.3

6.2.3 Conductance-Based Neuronal Model

Simple Neuronal Model

We consider a simple neuronal model consisted of one self-inhibited neuronal population driven by an exogenous excitatory input, for which the coupling parameter γ is considered unknown (See section 3.3.1). The proposed method was applied for a simulation length of 7.5 seconds with sampling interval $\Delta t_1 = 0.1$ ms whereby a designed (Dual Kalman), random, or optimal (OID-SCKF) input is applied for a time window $\Delta t_2 = 500$ ms. For statistical assessment, a total of 50 independent Monte Carlo runs were made.

The model had one hidden state (inhibitory conductance g_I) in addition to one unknown parameter (coupling parameter γ). The resultant augmented state vector had two quantities to be estimated from one noisy observation (membrane potential V) sampled at $\Delta t_1 = 0.1$ ms. Fig. 6.5 shows the means and 95% con-
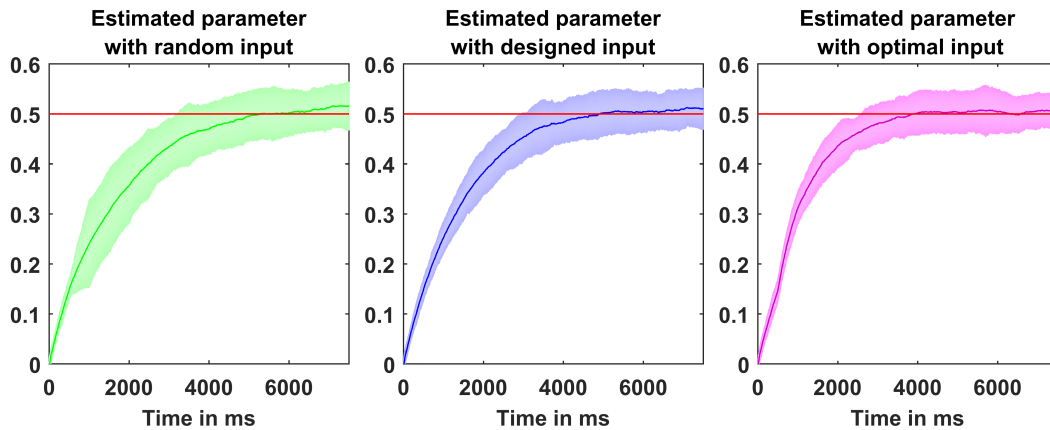
Figure 6.5: Estimated coupling parameter γ in terms of its mean (solid lines) and a 95% confidence interval (shaded regions), and the true parameter (red trace). Left: Under random input. Middle: under designed input. Right: Under optimal input

fidence intervals of the estimated coupling parameter γ under designed inputs,

random inputs, and optimal inputs. The summarized statistics about the estimated coupling parameter γ (under designed, random , and optimal inputs) and their rate of convergence are listed in Table 6.4. From Table 6.4, we can see that estimation accuracy in terms of the mean and variance across the 50 simulations for the Dual Kalman method were better than that of the random inputs case. This is also valid in terms of convergence rates. As compared to the optimal inputs (OID-SCKF), the Dual Kalman method did worse in terms of mean, variance, and convergence rates, however, the Dual Kalman method was substantially more efficient than the OID-SCKF method in designing informative inputs as the time needed to simulate a single run was much lower than OID-SCKF method and close to that of random inputs method.

Table 6.4: Statistics of the estimated coupling parameter γ for the neuronal model averaged over 50 Monte Carlo runs.

	Parameter	Mean	Standard deviation	Rise Time (sec)	Settling Time (sec)	Computation Time (sec)
Optimal Input	γ	0.5	0.018	2.12	3.43	1476.4
Designed Input	γ	0.49	0.02	2.7	4	58.9
Random Input	γ	0.48	0.026	2.96	4.32	58.4

Multi-Area Neuronal Model

We consider a four area network connected in a ring, non reciprocal configuration (see section 3.3.2). Each area is composed of three layers with a total of 9 hidden internal states including the membrane potential, excitatory and inhibitory conductances for each layer with local field potential (LFP) as observations proportional to the membrane potential of the infra-granular layer. we consider a heterogeneous network with varying connectivity strengths among the four areas, resulting in a total of four connection parameters to estimate within the augmented state vector.

The model had 36 hidden states in addition to four unknown parameters $\gamma_L = [\gamma_L^{(1,4)}; \gamma_L^{(4,3)}; \gamma_L^{(3,2)}; \gamma_L^{(2,1)}] = [1; 0.8; 0.7; 0.9]$, the augmented state vector had 40 quantities to be estimated. Under this heterogenous conditions, four LFP sig-

nals corresponding to the infra-granular activity of each area were considered as observation signals for the SCKF.

For this scenario, each neuronal area is considered to be excited by a distinct external input. That is this network has four external inputs to be designed or selected randomly, the input vector defined as $\mathbf{I} = [I_{(1)}; I_{(2)}; I_{(3)}; I_{(4)}]$ where $I_{(i)}$ ($i = 1, \ldots, 4$) is the input that excites area i and defined over the input space $I_{(i)} \in [I_{min}, I_{max}] = [25, 60]$.

Since the OID-SCKF method is carried out by solving the optimization problem in equation (6.8) using brute-force approach (see section 4.1.1), applying the OID-SCKF method for this scenario is infeasible due to the size of input space over the input vector $\mathbf{I}$ as a single run would take days to solve the optimization problem associated with OID-SCKF method (since we are using brute-force technique to search for a solution). Hence, for this scenario, we consider applying the Dual Kalman method for a simulation length of 6 seconds with sampling interval $\Delta t_1 = 0.1$ ms whereby a designed is applied for a time window $\Delta t_2 = 500$ ms. The Dual Kalman method is compared with the case where random inputs are applied under the same simulation conditions. For statistical assessment, a total of 50 independent Monte Carlo runs were made.

Fig. 6.6 shows the means and 95% confidence intervals of the estimated coupling parameters $\gamma_L^{(i,j)}$ under designed inputs and random inputs. The summarized statistics about the estimated connection strengths between the areas $\gamma_L^{(i,j)}$ (under designed and random inputs) and their rate of convergence are listed in Table 6.5. When compared with SCKF estimation with random inputs, it is seen that the Dual Kalman method achieved, for all four parameters, (a) mean values that are closer to their corresponding true values, (b) attained a smaller variance and hence tighter confidence intervals around the final value across the 50 simulations, and (c) faster convergence rates. Moreover, the computation load for the Dual Kalman method was comparable with the random inputs case, whereas, the OID-SCKF method was impractical to simulate due to the computational power needed to find an optimal input vector $\mathbf{I}$ for this scenario.

105

Table 6.5: Statistics of the estimated connectivity parameters $\gamma_L^{(i,j)}$ for the multi-area neuronal model averaged over 50 Monte Carlo runs.

	Parameter	Mean	Standard deviation	Rise Time (sec)	Settling Time (sec)	Computation Time (sec)
Designed Input	$\gamma_L^{1,4}$	0.98	0.023	1.09	2.1	139.3
	$\gamma_L^{4,3}$	0.79	0.022	0.99	1.82	
	$\gamma_L^{3,2}$	0.68	0.023	0.98	1.77	
	$\gamma_L^{2,1}$	0.88	0.024	1.08	2.06	
Random Input	$\gamma_L^{1,4}$	0.97	0.026	1.27	2.28	127.3
	$\gamma_L^{4,3}$	0.78	0.025	1.09	2.05	
	$\gamma_L^{3,2}$	0.68	0.026	1.07	2.07	
	$\gamma_L^{2,1}$	0.87	0.029	1.24	2.13	
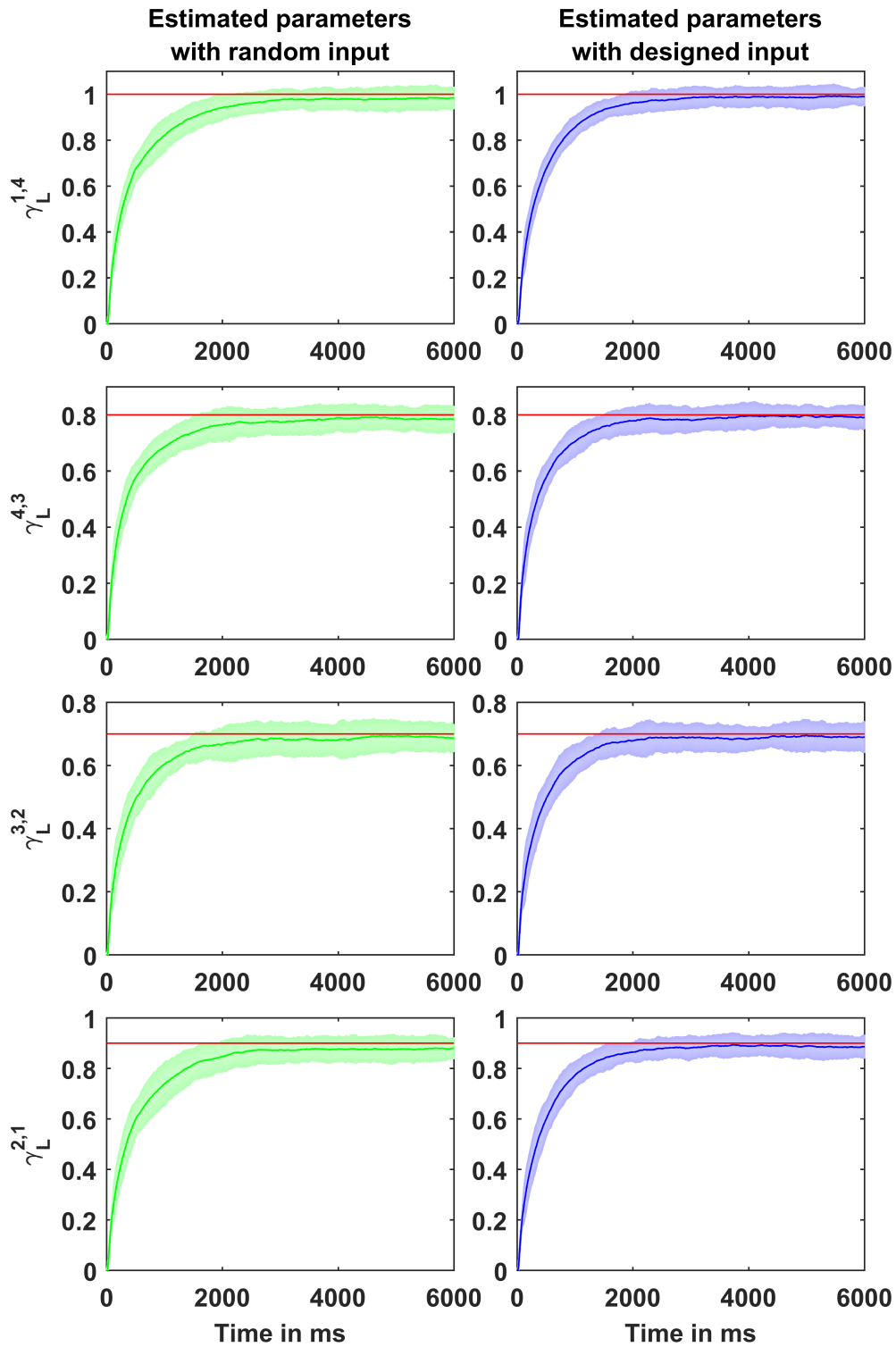
Figure 6.6: Estimated connectivity parameters $\gamma_L^{(i,j)}$ in terms of their mean (solid lines) and a 95% confidence interval (shaded regions), and the true parameter (red trace). Left: Under random input. Right: under designed input.

6.3 Discussion

The proposed Dual Kalman filters method aimed to design sub-optimal inputs that achieve informative observations about unknown parameters and hidden states by "transforming" the optimization problem associated with OID-SCKF (that solves for the optimal inputs) into a Kalman filter setup. The proposed setup discarded the optimization problem along with its computational burden and drastically reduced the computational needs to design an input.

The presented Dual Kalman approach showed that, in principle, better convergence and higher estimation accuracy can be attained when compared to random inputs cases. When compared to optimal inputs (OID-SCKF method), the Dual Kalman method showed comparable convergence and estimation accuracy, and more importantly, substantially more efficient than the OID-SCKF method in terms of computational time needed in designing informative inputs.

For the Van der Pol oscillator, the overall performance of estimation accuracy was comparable under different input specification methods (Dual Kalman, OID-SCKF, or random) with slight improvement for the OID-SCKF method over the other two methods (Figs. 6.2 and 6.3, Tables 6.1 and 6.2), noting that the estimated parameters under Dual Kalman method showed tighter confidence intervals (smaller variance values) around the mean values across Monte Carlo simulations.

Same conclusions are also drawn for the Double Well system in terms of superior estimation accuracy under optimal inputs (OID-SCKF). When comparing the Dual Klaman method estimation with that under random inputs, the former showed more consistency as time progresses particularly toward the end of simulation time and faster convergence rates, whereas the latter showed higher inconsistency across the Monte Carlo runs (Fig. 6.4 and Table 6.3).

Investigation of the Dual Kalman method for the simulated neuronal model demonstrated the immense gain in computational power against the OID-SCKF method in designing informative inputs while maintaining the out-performance in estimation accuracy over the random inputs case. For the single area model (Fig. 6.5 and Table 6.4), the Dual Kalman method, as compared to the random inputs case, performed better in terms of the estimated means and their corresponding variances, as well as scored faster convergence rates. For the multi-area neuronal model, we considered four neuronal areas each having its distinct input (four areas and four inputs) which made the input space fairly large (each input is defined over the input space $I_{(i)} \in [I_{min}, I_{max}] = [25, 60]$). Thus, this made the application of OID-SCKF method for this scenario infeasible as a single run would take days to solve the optimization problem associated with this method (since we are using brute-force technique to search for a solution). However, applying

the Dual Kalman method did not pose additional computational demands when compared to the random inputs case (Table 6.5 shows comparable computation time per run between Dual Klaman and random inputs cases). Moreover, the Dual Kalman method achieved (a) better mean values that are closer to their corresponding true values, (b) attained a smaller variance and hence tighter confidence intervals around the final value across the 50 simulations, and (c) faster convergence rates.

In conclusion, we have shown that the proposed Dual Kalman method, in principle, can achieve better convergence and higher estimation accuracy when compared to random inputs cases without posing any serious additional computational needs. Yet, when compared the OID-SCKF method, the proposed procedure showed comparable estimation accuracy while significantly reduces the computational demands. Since the Kalman filter is theoretically an on-line algorithm, the proposed method could be suitable for designing experiments for on-line applications.

Chapter 7

Model Selection for Identification of Functional Connectivity based on Input Design

In the previous chapters, we focused on introducing techniques to improve model parameters estimation for which we always assumed that the structure of the mathematical model describing the studied system is known. For the cases where the structure of the system under investigation is unknown, one will resort to statistical procedures called "model discrimination" or "model selection" techniques to decide from a pool of competing model candidates, on the basis of available observation data, which model is the most appropriate.

In this chapter, we will address the problem where the model structure of the underlying system is unknown. Given a whole bank of model candidates $\mathcal{M}_m, m = 1, \ldots, M$ which represent competing model hypotheses of the investigated system, where each model $\mathcal{M}_m, m = 1, \ldots, M$ has p_m unknown parameters $\boldsymbol{\theta}(\mathcal{M}_m)$ to be estimated from measurement data, we aim to incorporate ADO technique to design experiments to improve model fitting (parameter estimation) and model selection (identifying most plausible model structure). We will demonstrate the proposed method for a multi-neuronal-area model based on Jansen model for cortical activity (section 3.4).

7.1 Problem Definition and Setup

Given the state-space formulation of multi-area Jansen model:

Process Equation:
$$\dot{\mathbf{x}}(t) = f(\mathbf{x}(t), I) + \mathbf{\Gamma} \tag{7.1}$$

Measurement Equation:
$$\mathbf{z}_k = h(\mathbf{x}_k) + w_k \tag{7.2}$$

Where $\mathbf{x}(t) \in \mathbb{R}^n$ is the state vector of the dynamic system at time t (n is the total number of states in all considered neuronal areas) , I is the exogenous input, $\mathbf{z}_k \in \mathbb{R}^d$ is the measurement at discrete time k (d is the size of measurement vector), $f : \mathbb{R}^n \times \mathbb{R} \to \mathbb{R}^n$ is the drift coefficient, $h : \mathbb{R}^n \times \mathbb{R} \to \mathbb{R}^d$ is the measurement function, $\mathbf{\Gamma} \in \mathbb{R}^n$ and $w_k \in \mathbb{R}^d$ are vectors of random Gaussian noise with zero mean and covariance Q and R respectively.

We consider a network consisted of three areas, in which each area is receiving an excitatory input at its granular level from the infra-granular layer of another area. The strength of such excitatory activity is defined by a connectivity parameter $\gamma_L^{(i,j)}$ (long-range coupling parameter from area i to area j) (see section 3.4). These connectivity parameters $\gamma_L^{(i,j)}$ define the architecture of the neuronal network and they can be expressed in matrix form to simplify model representation:

$$\mathbf{\gamma}_L = \begin{bmatrix} \gamma_L^{(1,1)} & \gamma_L^{(1,2)} & \gamma_L^{(1,3)} \\ \gamma_L^{(2,1)} & \gamma_L^{(2,2)} & \gamma_L^{(2,3)} \\ \gamma_L^{(3,1)} & \gamma_L^{(3,2)} & \gamma_L^{(3,3)} \end{bmatrix}$$

This is also referred to as the "connectivity matrix" where the rows denote area i and the columns denote area j.

It is assumed that the structure of the multi-area network is unknown. That is, we are assuming that the number and the values of long-range connectivity parameters $\gamma_L^{(i,j)}$ are unknown. In order to identify the true structure of the network, a pool of $\mathcal{M}$ model structure candidates will be suggested, each model $\mathcal{M}_m, m = 1, \ldots, M$ has p_m unknown connectivity parameters $\gamma_L^{(i,j)}$ which need to be estimated. The proposed model candidates are defined by connectivity matrices, that is, for each model candidate $\mathcal{M}_m, m = 1, \ldots, M$ we define a particular connectivity matrix $\mathbf{\gamma}_{L,m}$. Model candidates differ from each other by the number (p_m) of assumed unknown connectivity parameters $\gamma_L^{(i,j)}$. The goal is to identify the most plausible model structure through statistical model selection procedure.

One can incorporate ADO method to design experiments to improve model fitting (parameter estimation) and model selection (identifying most plausible model structure).

A straight-forward (yet inefficient) implementation of ADO would consist of a two-phase procedure: In the first phase, for each model candidate $\mathcal{M}_m, m = 1, \ldots, M$, the optimal input could be designed to identify the unknown parameters for model $\mathcal{M}_m$ (OED is repeated M times to estimate unknown parameters for each model candidate). In the second phase, after the parameters of each model have been estimated, the input could be designed for discriminating the competing models. This procedure, however, is very time consuming and will not be suitable for applications in which experiments are costly, their repetition is impractical, and/or are time-consuming.

We propose a method that does not require repeated experiments in which model fitting (parameters estimation) and model assessment (model selection) are done in a single phase procedure. The method is a sequential algorithm in which at each stage the input is designed to produce the most informative observations about unknown parameters of the *current* most plausible model. Model assessment is carried out by computing the posterior probability of a model $\Pi(\mathcal{M}_m|\mathbf{z}_k)$ (at time k) among all model candidates and given a set of collected observations, using Bayesian approaches to model selection [77, 78, 79, 80]:

$$\Pi(\mathcal{M}_m|\mathbf{z}_k) = \frac{p(\mathbf{z}_k|\mathcal{M}_m)\Pi(\mathcal{M}_m|\mathbf{z}_{k-1})}{\sum\limits_{m=1}^{M} p(\mathbf{z}_k|\mathcal{M}_m)\Pi(\mathcal{M}_m|\mathbf{z}_{k-1})} \tag{7.3}$$

Where $p(\mathbf{z}_k|\mathcal{M}_m)$ is the likelihood probability density function (PDF), and $\Pi(\mathcal{M}_m|\mathbf{z}_{k-1})$ is the prior probability of model $\mathcal{M}_m$.

For any model candidate $\mathcal{M}_m$, the likelihood function $p(\mathbf{z}_k|\mathcal{M}_m)$ can be computed from estimated model states and parameters at time k assuming that the likelihood function is normally distributed [79, 81]:

$$p(\mathbf{z}_k|\mathcal{M}_m) \approx \frac{1}{(2\pi)^{d/2}(\det\Sigma_k)^{1/2}} \exp(-\frac{1}{2}\mathbf{r}_k^T\Sigma_k^{-1}\mathbf{r}_k) \tag{7.4}$$

Where r is the residual error between the observed measurements and the estimated measurements (computed from the Kalman update step, see section 2.3 equation (2.43)) at time k:

$$\mathbf{r}_k = \mathbf{z}_k - \hat{\mathbf{z}}_k \tag{7.5}$$

And $\Sigma_k = S_{\mathcal{Z}\mathcal{Z},k}^T S_{\mathcal{Z}\mathcal{Z},k}$ is the corresponding error covariance matrix (computed from the Kalman update step, see section 2.3 equation (2.44)).

We proposed an iterative method which consists of performing model assessment (computing $\Pi(\mathcal{M}_m|\mathbf{z}_k), m = 1, \ldots, M$ from equation (7.3)) at each time instant k based on states and parameters estimated using the Kalman filter. At the end of each stage, an input is designed for the next stage to maximize parameters

identifiability of the most plausible model (by maximizing the FIM of the most plausible model):

$$\underset{I}{\arg\max} \quad \text{trace}(FIM_{m^*})$$
$$\text{subject to} \quad I_{min} \leq I \leq I_{max} \tag{7.6}$$

Where FIM_{m^*} is the Fisher information matrix of model candidate m having the highest model probability $\Pi(\mathcal{M}_m|\mathbf{z}_k)$ value.

7.1.1 Framework of Model Selection based on Input Design

The time-line of an experiment (simulation) is divided into time-stages of equal length. Each stage of the proposed method is composed of N samples. For a given stage s, starting at a time $k = s * N$ up to $k = s * N + N$, the algorithm computes model probabilities $\Pi(\mathcal{M}_m|\mathbf{z}_k), m = 1, \ldots, M$ (equation (7.3)) at each time instant k based on estimated states and parameters $(\hat{\mathbf{x}}_{m,k}, \hat{\boldsymbol{\theta}}_{m,k})$ of each model candidate $\mathcal{M}_m$. At the end of stage s (i.e. at $k = s * N + N$), the algorithm designs an input for the next stage $s + 1$ using OID-SCKF method or Dual Kalman method based on the most plausible ($\mathcal{M}_{m^*}$) model estimated states and parameters $(\hat{\mathbf{x}}_{m^*,k}, \hat{\boldsymbol{\theta}}_{m^*,k})$.

Thereafter, this designed input is applied to the system generating measurements data for the next stage, during which the SCKF is applied to provide estimates of the states and the parameters $(\hat{\mathbf{x}}_{m,k}, \hat{\boldsymbol{\theta}}_{m,k})$ for each model candidate $\mathcal{M}_m, m = 1, \ldots, M$ and performing model assessment (equation (7.3)). Fig. 7.1 shows a diagram of basic elements and processes of the proposed algorithm and Algorithm (3) shows the the pseudo-code for the proposed method.

7.1.2 Performance assessment

As in previous chapters, the quantitative assessment of the introduced method of simultaneous model selection and parameter estimation is carried out with performance assessment tools "Rise time" and "Settling time" as defined in section 4.1.3 to quantify estimation performance under designed (Dual Kalman), random, and optimal (OID-SCKF) inputs.

7.2 Results

In this section, we will present estimation and model assessment results based on optimally designed inputs using OID-SCKF method (introduced in chapter 4)
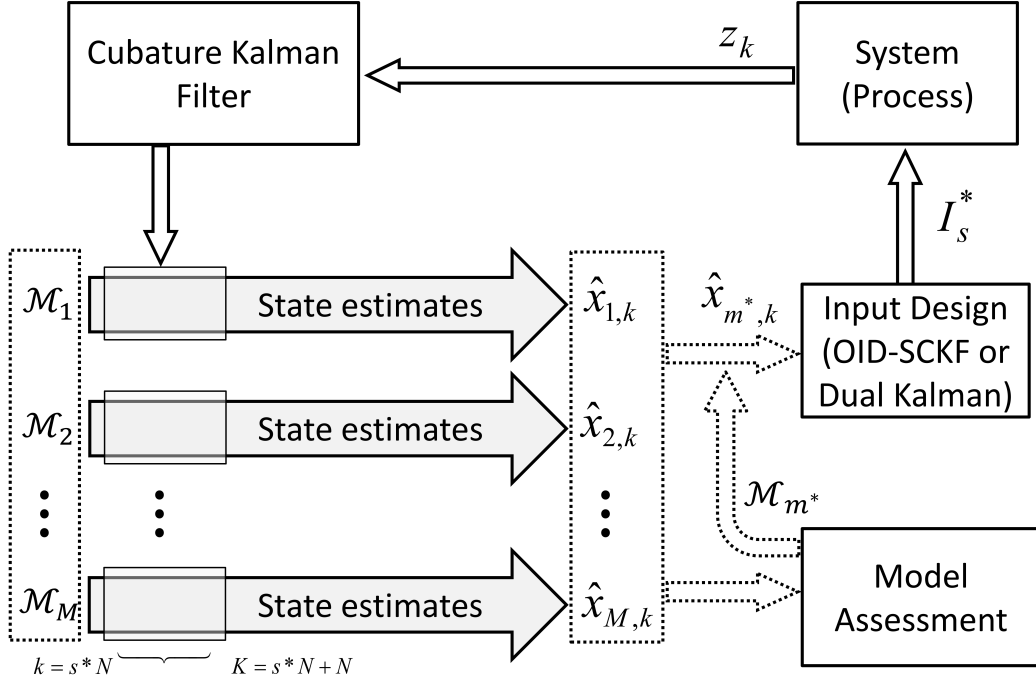
Figure 7.1: Schematic of the proposed model selection algorithm.

and compare them with those based on random inputs, as well as those based on designed inputs using the Dual Kalman method (see chapter chapter:Dual).

We propose a network of three neuronal areas (as described in section 3.4) for which the long-range connectivity parameters $\gamma_L^{(i,j)}$ defining the architecture of the neuronal network are given as:

$$
\boldsymbol{\gamma}_{L,\text{true}} = \begin{bmatrix} 0 & 40 & 30 \\ 30 & 0 & 50 \\ 60 & 0 & 0 \end{bmatrix}
$$

Where $\boldsymbol{\gamma}_{L,\text{true}}$ represents the true model structure of the system under investigation.

For the problem at hand, the architecture of the network is considered unknown. Thus, we suggest three candidate models defined by connectivity matrices and apply our proposed method of model assessment and input design (design an exogenous excitatory input I that drive all three neuronal areas) to estimate connectivity matrices of model candidates and to select the most plausible model structure.

The first model $\mathcal{M}_1$ is defined to have three unknown connectivity parameters

114

Algorithm 3 Framework for model selection and input design

1: Initialization: Set initial states and parameters values $\hat{x}_1(0)$ $\hat{x}_2(0)$ and the square-root of process and measurement noise covariances: $S_{R_1,0}$, $S_{V_1,0}$, $S_{R_2,0}$ and $S_{V_2,0}$.

2: Define the input space $[I_{min}, I_{max}]$.

3: Initialization: $\Pi(\mathcal{M}_1|\mathbf{z}_0) = \Pi(\mathcal{M}_2|\mathbf{z}_0) = \ldots = \Pi(\mathcal{M}_M|\mathbf{z}_0) = 1/M$

4: **for** $s = 0$ to S **do**   ▷ % for each stage s %

5:     **if** $s = 0$ **then**   ▷ % First stage or time window%

6:        Define a random initial input I_0.

7:     **else**

8:        **function** DESIGN INPUT$(s,\hat{x}_{m^*,k},m^*)$ ▷ % Using OID-SCKF method or Dual Kalman method %

9:          $I_s^* = \max \text{trace}(FIM_{m^*})$

10:       **end function**

11:     **end if**

12:     **for** $k = s * N$ to $K = N + s * N$ **do**

13:        Simulate model and collect measurements z_k

14:        Apply SCKFr and get the states and parameters estimates $\hat{x}_{m,k}$ for each model candidate $\mathcal{M}_m, m = 1, \ldots, M$

15:        Update model probabilities $\Pi(\mathcal{M}_m|\mathbf{z}_k), m = 1, \ldots, M$ by performing model assessment using equation (7.3)

16:     **end for**

17:     Identify the most plausible model $\mathcal{M}_{m^*}$: $m^* = \max \Pi(\mathcal{M}_m|\mathbf{z}_k), m = 1, \ldots, M$

18: **end for**

(under-parametrized model structure):

$$\boldsymbol{\gamma}_{L,1} = \begin{bmatrix} 0 & \gamma_L^{(1,2)} & \gamma_L^{(1,3)} \\ 0 & 0 & 0 \\ \gamma_L^{(3,1)} & 0 & 0 \end{bmatrix}$$

The second model $\mathcal{M}_2$ is defined to have five unknown connectivity parameters (true model structure):

$$\boldsymbol{\gamma}_{L,2} = \begin{bmatrix} 0 & \gamma_L^{(1,2)} & \gamma_L^{(1,3)} \\ \gamma_L^{(2,1)} & 0 & \gamma_L^{(2,3)} \\ \gamma_L^{(3,1)} & 0 & 0 \end{bmatrix}$$

The third model $\mathcal{M}_3$ is defined to have seven unknown connectivity parameters

115

(over-parametrized model structure):

$$
\boldsymbol{\gamma}_{L,3} =
\begin{bmatrix}
0 & \gamma_L^{(1,2)} & \gamma_L^{(1,3)} \\
\gamma_L^{(2,1)} & 0 & \gamma_L^{(2,3)} \\
\gamma_L^{(3,1)} & \gamma_L^{(3,2)} & \gamma_L^{(3,3)}
\end{bmatrix}
$$

Each model candidate $\mathcal{M}_m, m = 1, \ldots, 3$ had 36 hidden states (membrane potentials, excitatory and inhibitory currents) in addition to p_m unknown parameters, resulting in a total of $36 + p_m$ quantities to be estimated within the augmented state vector for each model candidate from three noisy observations (infragranular membrane potentials $v_6^{(i)}$, $i = 1, \ldots, 3$).

The proposed method was applied for a simulation length of 4 seconds with sampling interval $\Delta t_1 = 0.2$ ms whereby a designed (Dual Kalman method), random, or optimal (OID-SCKF method) input is applied for a time window of length $\Delta t_2 = 500$ ms. The input space over which the exogenous input I was designed (or selected randomly) was defined over $I \in [I_{min}, I_{max}] = [0.1, 0.45]$. For statistical assessment, a total of 25 independent Monte Carlo runs were made. The summarized statistics about model selection (under designed, random and optimal inputs) are listed in Table 7.1, which shows that the Dual Kalman (designed input) and OID-SCKF (optimal input) methods identified the true model ($\mathcal{M}_2$) 25 times out of 25, whereas random inputs selection method failed to identify the true model structure once out of 25 runs and selected the over-parameterized model $\mathcal{M}_3$.

Table 7.1: Statistics of model selection over 25 Monte Carlo runs.

	$\mathcal{M}_1$	$\mathcal{M}_2$	$\mathcal{M}_3$
Designed Input	0/25	25/25	0/25
Random Input	0/25	24/25	1/25
Optimal Input	0/25	25/25	0/25

Figs. 7.2, 7.3, and 7.4 show the means and 95% confidence intervals of the estimated connectivity parameters $\gamma_L^{(i,j)}$ under designed (Dual Kalman), random, and optimal (OID-SCKF) inputs for the first $\mathcal{M}_1$, second $\mathcal{M}_2$, and third $\mathcal{M}_3$ models respectively. The summarized statistics about the estimated connectivity

116

parameters between areas $\gamma_L^{(i,j)}$ (under designed, random, and optimal inputs) and their rate of convergence are listed in Tables 7.2, 7.3, and 7.4 for $\mathcal{M}_1$, $\mathcal{M}_2$, and $\mathcal{M}_3$ respectively.

By examining estimation results for $\mathcal{M}_1$ listed in Table 7.2, we can see that estimated parameters under optimal inputs (OID-SCKF) were closest to true values in terms of mean values across 25 runs, whereas Dual Kalman method (designed input) scored faster convergence rates (smaller rise and settling times) and tighter confidence intervals around the final value across the 25 simulations.

Table 7.3 list estimation statistics for model $\mathcal{M}_2$ (representing the true structure of the simulated system) which was correctly identified by the Dual Kalman (designed inputs) and OID-SCKF (optimal inputs) methods as the true system structure 100 % rate out of the total 25 simulations. Once more, the OID-SCKF method (optimal inputs) showed superior estimation accuracy in terms of the mean values across simulations. In terms of scored variance values across 25 simulations, the Dual Kalman did better than The OID-SCKF, however, from Fig. 7.3 we can see that the standard error in the average value (95 % interval) under optimal input case (shaded purple region) becomes tighter towards the end of simulation time as noted in Fig. 7.3 for $\gamma_L^{2,1}$ (first column), $\gamma_L^{3,1}$ (second column), and $\gamma_L^{2,3}$ (last column) for the optimal inputs case (shaded purple region) for procedure time> 2.5 sec. Estimation under random inputs case showed wider confidence intervals around the mean values and slower convergence rates as indicated in Table 7.3 and shown in Fig. 7.3 (first row, green shaded regions).

As for model $\mathcal{M}_3$ (the over-parametrized model), some estimated parameters showed high variability across trials and failed to converge properly to a given value (marked by $**$ in Table 7.4). This is clearly evident in Fig 7.4 where the parameters $\gamma_L^{3,1}$ (second column), $\gamma_L^{3,2}$ (third column), and $\gamma_L^{3,3}$ (last column) exhibit wide confidence intervals (green, blue, and purple shaded regions) around the mean values (green, blue, and purple solid lines). It is worthwhile to mention that the two additional parameters $\gamma_L^{3,2}$ and $\gamma_L^{3,3}$ (true parameter value of 0) that add to the actual model structure have affected the convergence of $\gamma_L^{3,1}$ (true parameter value of 60) and one might conclude by solely examining these estimation results without referring to model selection procedures that this model is over-parametrized due to the high variability of some parameters across multiple runs.

Table 7.2: Statistics of the estimated connectivity parameters $\gamma_L^{(i,j)}$ for the first model $\mathcal{M}_1$ averaged over 25 Monte Carlo runs.

	Parameter	Mean	Standard deviation	Rise Time (sec)	Settling Time (sec)
Designed Input	$\gamma_L^{3,1}$	59.3	0.92	0.8	1.57
	$\gamma_L^{1,2}$	38.1	1.2	0.9	2.1
	$\gamma_L^{1,3}$	31.2	1.12	0.44	0.68
Random Input	$\gamma_L^{3,1}$	59.2	1.32	0.86	1.73
	$\gamma_L^{1,2}$	38.5	1.25	1	2.14
	$\gamma_L^{1,3}$	31	1.27	0.44	0.68
Optimal Input	$\gamma_L^{3,1}$	59.7	0.87	0.86	1.76
	$\gamma_L^{1,2}$	38.8	1.32	1	2.09
	$\gamma_L^{1,3}$	30.8	1.23	0.45	0.67

Table 7.3: Statistics of the estimated connectivity parameters $\gamma_L^{(i,j)}$ for the first model $\mathcal{M}_2$ averaged over 25 Monte Carlo runs.

	Parameter	Mean	Standard deviation	Rise Time (sec)	Settling Time (sec)
Designed Input	$\gamma_L^{2,1}$	32.2	1.76	0.38	0.56
	$\gamma_L^{3,1}$	59.3	0.92	0.8	1.57
	$\gamma_L^{1,2}$	38.1	1.19	0.9	2.15
	$\gamma_L^{1,3}$	31.2	1.12	0.44	0.67
	$\gamma_L^{2,3}$	47.4	1.85	1.37	2.49
Random Input	$\gamma_L^{2,1}$	32.3	2.13	0.38	0.57
	$\gamma_L^{3,1}$	59.2	1.32	0.86	1.73
	$\gamma_L^{1,2}$	38.5	1.24	1	2.14
	$\gamma_L^{1,3}$	31	1.27	0.44	0.68
	$\gamma_L^{2,3}$	47.4	2.3	1.28	2.51

	Parameter	Mean	Standard deviation	Rise Time (sec)	Settling Time (sec)
Optimal Input	$\gamma_L^{2,1}$	31.2	1.54	0.37	0.52
	$\gamma_L^{3,1}$	59.7	0.87	0.86	1.76
	$\gamma_L^{1,2}$	38.8	1.32	1	2.09
	$\gamma_L^{1,3}$	30.8	1.23	0.45	0.66
	$\gamma_L^{2,3}$	48.6	1.51	1.29	2.29

Table 7.4: Statistics of the estimated connectivity parameters $\gamma_L^{(i,j)}$ for the first model $\mathcal{M}_3$ averaged over 25 Monte Carlo runs.
Convergence rates marked by $**$ denote parameters that showed high variability across Monte Carlo runs.

	Parameter	Mean	Standard deviation	Rise Time (sec)	Settling Time (sec)
Designed Input	$\gamma_L^{2,1}$	32.2	1.76	0.38	0.56
	$\gamma_L^{3,1}$	44	6.5	$**$	$**$
	$\gamma_L^{1,2}$	38.1	1.18	0.9	2.15
	$\gamma_L^{3,2}$	9.2	5	$**$	$**$
	$\gamma_L^{1,3}$	31.2	1.11	0.44	0.68
	$\gamma_L^{2,3}$	47.3	1.85	1.37	2.49
	$\gamma_L^{3,3}$	6.3	5.1	$**$	$**$
Random Input	$\gamma_L^{2,1}$	32.3	2.13	0.38	0.57
	$\gamma_L^{3,1}$	45.6	8	$**$	$**$
	$\gamma_L^{1,2}$	38.5	1.24	1	2.14
	$\gamma_L^{3,2}$	7.6	5.3	$**$	$**$
	$\gamma_L^{1,3}$	31	1.27	0.44	0.68
	$\gamma_L^{2,3}$	47.4	2.3	1.28	2.51
	$\gamma_L^{3,3}$	5.9	5.5	$**$	$**$
Optimal Input	$\gamma_L^{2,1}$	31.2	1.55	0.37	0.52
	$\gamma_L^{3,1}$	51.08	6.3	$**$	$**$
	$\gamma_L^{1,2}$	38.8	1.32	1	2.09

$\gamma_L^{3,3}$	5.7	4.8	**	**
$\gamma_L^{1,3}$	30.8	1.23	0.45	0.67
$\gamma_L^{2,3}$	48.6	1.51	1.29	2.29
$\gamma_L^{3,3}$	1.8	3.2	**	**
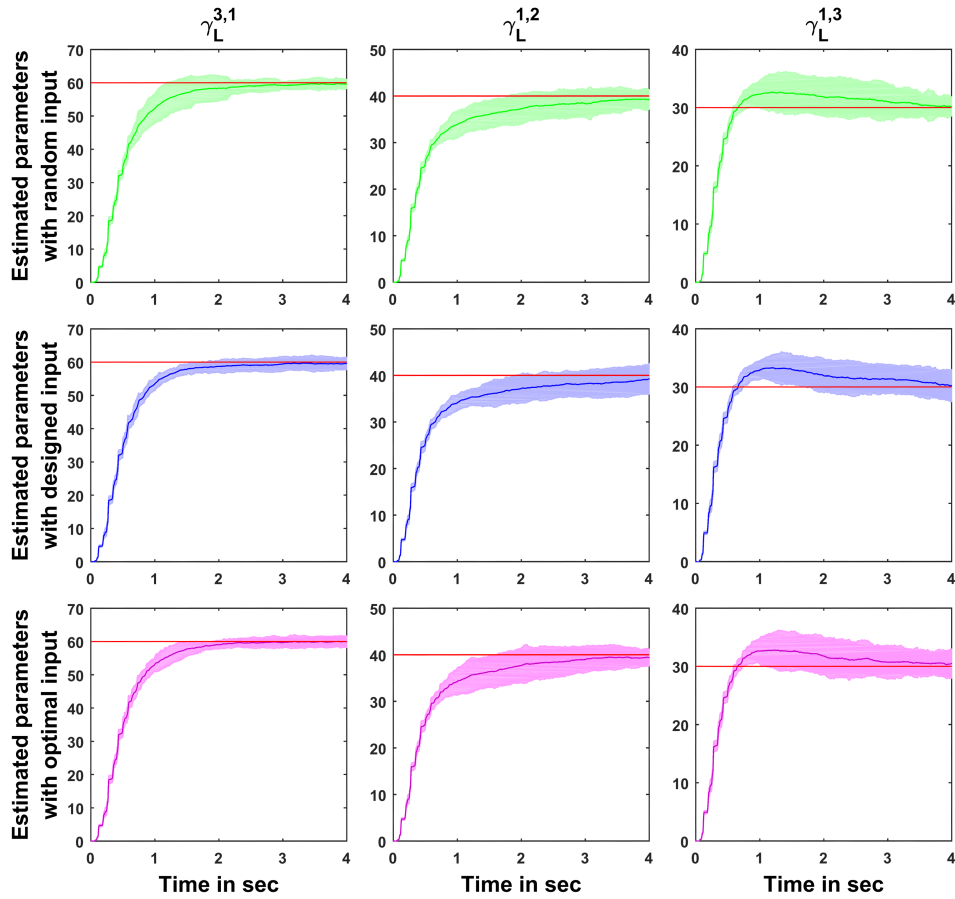
Figure 7.2: Estimated connectivity parameters $\gamma_L^{(i,j)}$ for the first model $\mathcal{M}_1$ in terms of their means (solid lines) and a 95% confidence interval (shaded regions), and the true parameter (red trace). Top: Under random input. Middle: under designed input. Bottom: Under optimal input.
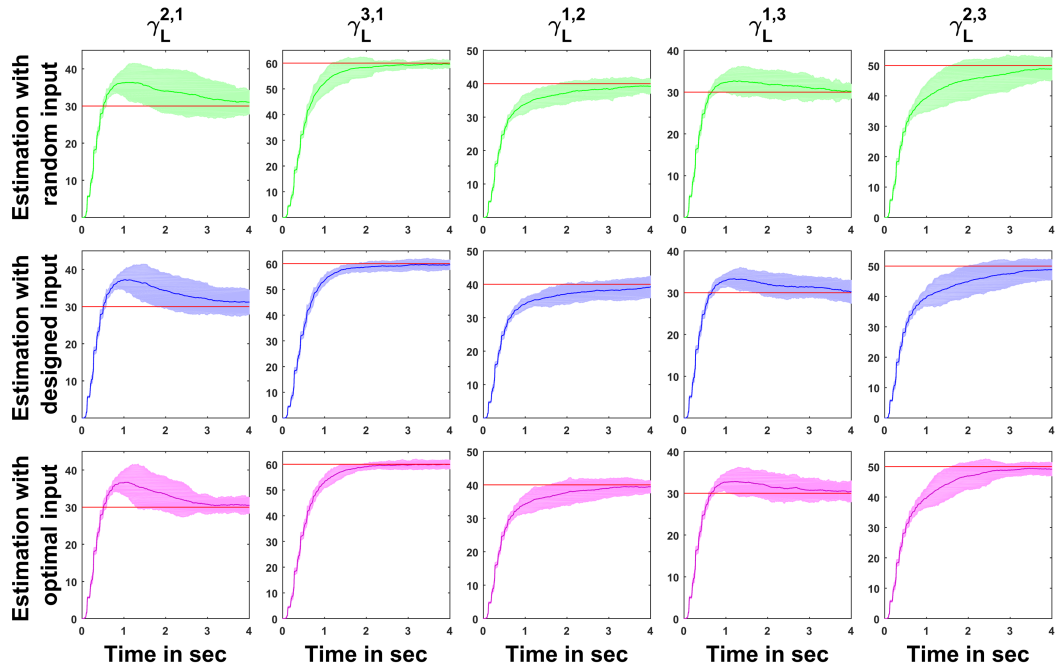
Figure 7.3: Estimated connectivity parameters $\gamma_L^{(i,j)}$ for the first model $\mathcal{M}_2$ in terms of their means (solid lines) and a 95% confidence interval (shaded regions), and the true parameter (red trace). Top: Under random input. Middle: under designed input. Bottom: Under optimal input.
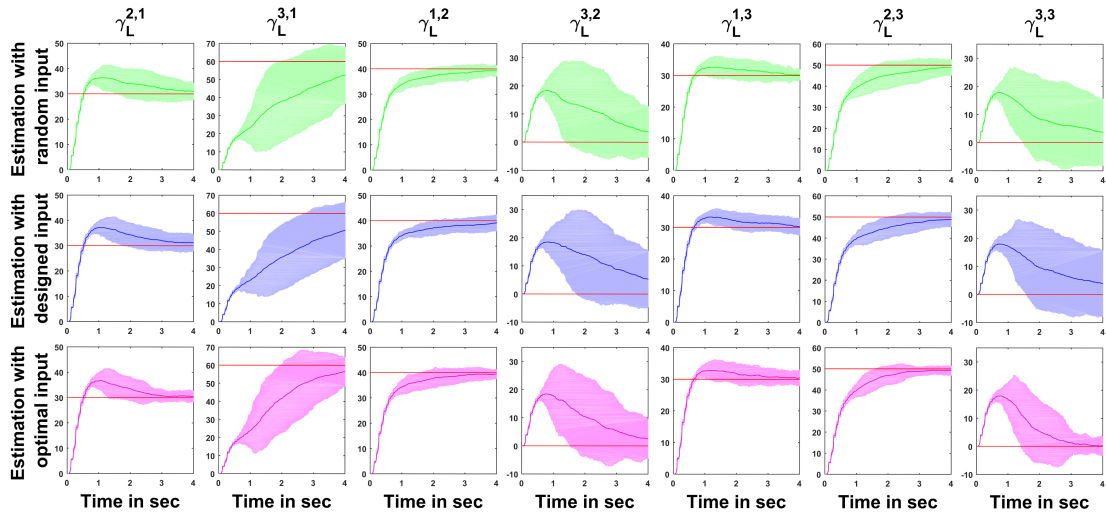
Figure 7.4: Estimated connectivity parameters $\gamma_L^{(i,j)}$ for the first model $\mathcal{M}_3$ in terms of their means (solid lines) and a 95% confidence interval (shaded regions), and the true parameter (red trace). Top: Under random input. Middle: under designed input. Bottom: Under optimal input.

7.3 Discussion

In this chapter, We addressed the problem of model assessment within the framework of input design where we proposed a method that does not require repeated experiments in which model fitting (parameters estimation) and model assessment (model selection) are done in a single phase procedure. Given a pool of model candidates $\mathcal{M}$ which represent competing model hypotheses of the investigated system, input design is employed to produce the most informative observations about unknown parameters of the *current* most plausible model. Model assessment is carried out by computing the posterior probability of a model $\Pi(\mathcal{M}_m|\mathbf{z}_k)$ (at time k) among all model candidates and given a set of collected observations, using Bayesian approaches to model selection. We demonstrated the proposed method for a multi-neuronal-area model based on Jansen model for cortical activity.

Given three candidate models defined by connectivity matrices (under-parametrized, true, and over-parameterized model structures), the proposed method of model assessment and input design was applied to estimate connectivity matrices of model candidates and to select the most plausible model structure. For the input design part, the procedure was conducted with inputs generated based on optimally designed inputs using OID-SCKF method, on random inputs, and on designed inputs using the Dual Kalman method. The investigated multi-area neuronal model was assumed to consist of three neuronal areas driven by the same input. The single input assumption was used to keep the input-space as compact as possible in order to simulate the proposed method with the OID-SCKF method in a reasonable time.

In terms of model assessment accuracy (Table 7.1), the proposed procedure when combined with either OID-SCKF (optimal inputs) or the Dual Kalman (designed inputs) had 100 % correct selection rate. Whereas, when combined with random inputs, the procedure failed to identify the true model structure once out of 25 simulation runs.

In terms of estimation accuracy (Figs. 7.2, 7.3, and 7.4), and Tables 7.2, 7.3, 7.4) the reported results are in line with those observed in chapter 6; parameter estimations with the OID-SCKF method showed the best accuracy and were comparable with those obtained with the Dual Kalman method, however, these gains in estimation accuracy came at the cost of additional computational demands for the OID-SCKF method. When compared with estimation under random inputs, the Dual Kalman method performed better in terms of estimation accuracy and convergence rates.

It is worth to mention that this single phase procedure when incorporated with the Dual Kalman method could be appropriate for on-line applications in which

one can benefit from the simultaneous model assessment tools along with designed experiments that produce informative outcomes about model unknowns.

Chapter 8

Estimation of Effective Connectivity in The Visual Cortex During a Picture-Naming Task

There are three different patterns of brain connectivity that exist between distinct anatomically segregated brain regions. The first is formed by structural or anatomical links such as fiber pathways between distant cortical areas, these are refereed to as "Structural connectivity" [82]. Another pattern type is referred to as "Functional connectivity" which is defined as the temporal dependency of neuronal activation patterns of anatomically separated brain regions [82]. It reflects statistical dependencies between distinct and distant brain regions and can be quantified with statistical measures, such as correlations, coherence, transfer entropy, or phase locking [82, 83]. lastly, "Effective connectivity" which may be viewed as the union of structural and functional connectivity, as it describes the influence one cortical region exerts upon another, thus reflecting causal interactions between activated brain regions [82]. It can be quantified by time series causality measures such as Granger causality or by specification of parameterized models to test hypotheses concerning coupling architectures between different brain regions [29, 84].

In this chapter, we address Kalman-based estimation of effective connectivity between cortical areas residing in the visual cortex from experimental data. The experimental data[1] are recorded with dense-EEG system (256 electrodes) from subjects while performing a cognitive task, namely the Picture-Naming task.

---

[1]Made available by Prof. Fabrice Wendling, Reaserch Director at Inserm 1099 - Signal and Image Processing Laboratory - University of Rennes 1

From recorded EEG data, *source localization* techniques are applied to solve the *inverse EEG problem* in order to estimate the the location and strengths of electric current sources, generated by macro-columns of pyramidal cells lying in the cortical mantle, that generate the observed scalp EEG electric potentials. The inverse-problem is solved based on anatomical segmentation of structural MRI images to obtain the time series of reconstructed sources corresponding to 148 cortical regions (for the detailed data acquisition procedures and inverse-problem solution, the reader is advised to refer to [85, 86]. For our application, the cortical areas of interest are chosen from the visual cortex, namely the primary visual cortex (V1) and the secondary visual cortex (V2) from both left and right hemispheres. The cortical areas are modeled with the multi-neuronal-area Jansen model for cortical activity (section 3.4). We aim to estimate the effective connectivity between these areas based on Cubature Kalamn filter and Cubature Kalman smoother as detailed in next sections, as we describe data collection and source localization procedures.

8.1 Picture Naming Task

As in [86], the research group at University of Rennes performed the cognitive task as follow: Twenty one right-handed healthy volunteers (11 women: mean age 28 year; min: 19, max: 40 and 10 men: mean age 23 years; min: 19, max: 33), with no neurological disease, were involved in the study. Participants were asked to name at a normal speed 148 displayed pictures on a screen. The images were selected from a database of 400 pictures and were used during session about eight minutes. All pictures were shown as black drawings on a white background. Order of presentation was randomized across participants. Naming latencies were determined as the time between picture onset and the beginning of vocalization recorded by the system. Oral responses were recorded and then analyzed to set the voice onset time. A typical trial started with the appearance of an image during 3 seconds followed by a jittered inter-stimulus interval of 2 or 3 seconds randomly. Most responses were given while the image was still present on the screen. Errors in naming were discarded for the subsequent analysis [86]. The task structure is illustrated in Fig. 8.1.

8.2 Data

The brain activity was recorded using dense-EEG, 256 electrodes. The main feature of this system is the large coverage of the subject's head by surface electrodes allowing for the improved analysis of the intracerebral activity from noninvasive
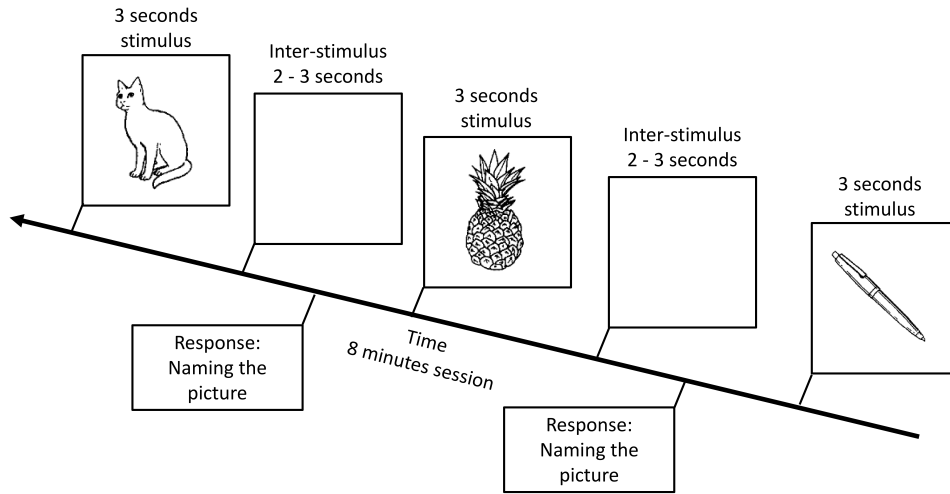
Figure 8.1: Picture-naming paradigm: Picture-naming task. Each picture was presented for 3 seconds interval during which the participants were required to name (response) the stimulus appearing on the computer screen. Picture stimuli were separated by 2 or 3 seconds intervals.

scalp measurements, as compared with 32- to 128-electrodes standard systems. EEG signals were collected with a 1 kHz sampling frequency and band-pass filtered between 3 and 45 kHz [86].

8.3 Source Localization

According to the linear discrete equivalent current dipole model, EEG signals $s(k)$ measured from q channels can be expressed as linear combinations of p time-varying current dipole sources $d(k)$:

$$S = G.D + e \tag{8.1}$$

Where S is a $q \times T$ matrix containing data measurements at different times from different channels $s(j, k)$, $j = 1, \ldots, q$; $k = 1, \ldots, T$, D is $p \times T$ matrix of dipole moments at different time instants at different dipole positions $d(i, k)$, $i = 1, \ldots, p$; $k = 1, \ldots, T$, e is an additive noise, and the gain matrix G ($q \times p$) is often referred to as the "lead-field" matrix and it describes the current flow for a given electrode through each dipole position [87].

The inverse problem consists in finding an estimate $\hat{D}$ of the dipolar source parameters (typically, the position, orientation and magnitude), given the EEG measurement matrix S and the gain matrix G. This matrix can be computed

from a multiple layer head model (volume conductor) and from the EEG electrodes' positions on the scalp. For instance, the Boundary Element Method is a numerical method classically used in the case of realistic head models [86].

As this problem is ill-posed ($p \gg q$), physical and mathematical constraints have to be added to obtain a unique solution among the many solutions that minimize the residual term in the fitting of measured EEG signals. Using segmented MRI data, the source distribution can be constrained to a field of current dipoles homogeneously distributed over the cortex, and normal to the cortical surface [86].

Technically, in the source model, it is assumed that EEG signals are generated by macro-columns of pyramidal cells lying in the cortical mantle and aligned orthogonally with respect to its surface. Thus, the electrical contribution of each macro-column to scalp electrodes can be represented by a current dipole located at the center of gravity of each triangle of the 3-dimensional mesh and oriented normally to the triangle surface. Using this source space, the weighted Minimum Norm Estimate (wMNE) method only estimates the moment of dipole sources. The wMNE compensates for the tendency of classical MNE to favor weak and surface sources. This is done by introducing a weighting matrix W_S [85, 86]:

$$\hat{D}_{\text{wMNE}} = (G^T W_S G + \lambda I_e)^{-1} G^T W_S S \tag{8.2}$$

Where matrix W_S adjusts the properties of the solution by reducing the bias inherent to MNE solutions, W_S is a diagonal matrix built from matrix G with non-zero terms inversely proportional to the norm of the lead field vectors. The value of λ is computed relatively to the signal to noise ratio for each signal computed as the ration between the post-stimuli period to the pre-stimulus (200 ms), and I_e is the identity matrix.

8.4   Problem Definition

Given the estimated current dipole sources $\hat{D}$ for the 148 cortical regions from observed EEG data, we selected those that correspond to cortical areas residing in the visual cortex, namely the primary visual cortex (V1) and the secondary visual cortex (V2) from both left and right hemispheres (Fig. 8.2). The cortical areas are modeled with the multi-neuronal-area Jansen model for cortical activity (section 3.4).

Given the state-space formulation of multi-area Jansen model:

Process Equation:	$\dot{\mathbf{x}}(t) = f(\mathbf{x}(t), \mathbf{I}) + \mathbf{\Gamma}$	(8.3)
Measurement Equation:	$\mathbf{z}_k = h(\mathbf{x}_k) + w_k$	(8.4)
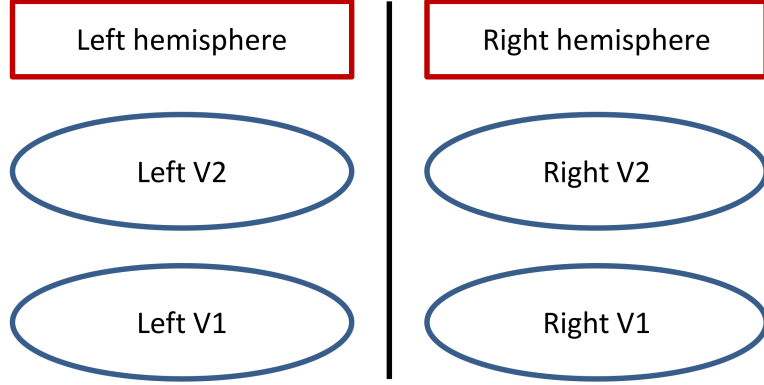
Figure 8.2: Cortical areas of interest.

Where $\mathbf{x}(t) \in \mathbb{R}^n$ is the state vector of the dynamic system at time t (n is the total number of states in all considered neuronal areas) , $\mathbf{I}$ is the exogenous input, $\mathbf{z}_k \in \mathbb{R}^d$ is the measurement at discrete time k (d is the size of measurement vector), $f : \mathbb{R}^n \times \mathbb{R} \rightarrow \mathbb{R}^n$ is the drift coefficient, $h : \mathbb{R}^n \times \mathbb{R} \rightarrow \mathbb{R}^d$ is the measurement function, $\mathbf{\Gamma} \in \mathbb{R}^n$ and $w_k \in \mathbb{R}^d$ are vectors of random Gaussian noise with zero mean and covariance Q and R respectively.

The current dipole measurements $\mathbf{z}_k$ (from the estimated current dipole sources $\hat{D}$) are related to model states through the measurement function $h(x_k)$ which relates the current dipole source ($\mathbf{z}_k$) to membrane potentials. A common method that relates a current source (ι) to potential (Φ) in a homogeneous conductor is given by [88, 89]:

$$\Phi(r) = \frac{\iota}{4\pi\sigma r} \tag{8.5}$$

Where ι is a point current source, $\Phi(r)$ is the potential at distance r, and σ is the medium conductivity. Thus, given that we are assuming that the activity of infra-granular layer is considered as the main output in a cortical area [68]. The measurement function $h(x_k)$ depends on the infra-granular layer membrane potentials $v_6^{(i)}$, where $i = 1, \ldots, 4$ denotes cortical areas, and it is given by:

$$h(\mathbf{x}_k) = \begin{bmatrix} 4\pi\sigma r \; v_6^{(1)} \\ 4\pi\sigma r \; v_6^{(2)} \\ 4\pi\sigma r \; v_6^{(3)} \\ 4\pi\sigma r \; v_6^{(4)} \end{bmatrix}$$

Where $r = 1.2$ - 1.5 mm is the distance from the cortical surface to infra-granular layer pyramidal cells, and $\sigma = 0.3$ - 0.4 S/m is the cortical grey matter conductivity. -

We consider a network consisted of four cortical areas (V1 and V2 from both hemispheres), in which each area is receiving an excitatory input at its granular level from the infra-granular layer of another area. The strength of such excitatory activity is defined by a connectivity parameter $\gamma_L^{(i,j)}$ (long-range coupling parameter from area i to area j) (see section 3.4). These connectivity parameters $\gamma_L^{(i,j)}$ define the architecture of the neuronal network and they can be expressed as "connectivity matrix":

$$\boldsymbol{\gamma}_L = \begin{bmatrix} \gamma_L^{(1,1)} & \cdots & \gamma_L^{(1,4)} \\ \vdots & \vdots & \vdots \\ \gamma_L^{(4,1)} & \cdots & \gamma_L^{(4,4)} \end{bmatrix}$$

Where the rows denote area i and the columns denote area j.

The problem at hand is defined to estimate the effective connectivity $(\gamma_L^{(i,j)})$ between the cortical areas using Cubature Kalman filter and smoother (SCKF and SCKS) as an estimation tool and under the assumption that the cortical areas are modeled by the Jansen model. In addition to estimating the unknown effective (inter-areas) connectivity, we will estimate intra-area connectivity $(\gamma_1, \ldots, \gamma_5)$ and the unknown inputs $\mathbf{I}$ which considered to account for the total unmodeled afferent excitation originated from other cortical areas. We assumed that all areas have similar intra-area connections and that these connections are assumed to be as a fraction of one constant, C, where $\gamma_1 = C, \gamma_2 = 0.8C, \gamma_3 = 0.25C, \gamma_4 = 0.25C, \gamma_5 = 0.01C$ (see section 3.4 and Table 3.2). In order to keep the number of unknowns as low as possible, we assumed that V1 areas in the left and right hemispheres share the same input, and left and right V2 areas share the same input.

In this application, we considered as an estimation procedure applying the SCKF forward pass (see section 2.3.3) followed by SCKS backward pass (see section 2.3.4) to obtain smoothed estimates (since we are dealing with unknown inputs to cortical areas). Since the initial conditions of this system are unknown, this procedure was iterated five times as in [30] in order to estimate the initial conditions and improve parameters estimates.

8.5   Problem Setup

We consider two scenarios (models $\mathcal{M}_1$ and $\mathcal{M}_2$) with reciprocal connections (in order to keep the number of unknowns as low as possible) that differ in the number of assumed inter-areas connections.

8.5.1 First Scenario

For model $\mathcal{M}_1$, the assumed inter-areas connectivity is shown in Fig. 8.3 with reciprocal connections as represented in the connectivity matrix $\boldsymbol{\gamma}_L$:

$$
\boldsymbol{\gamma}_L = \begin{bmatrix} \gamma_L^{(1,1)} & \gamma_L^{(1,2)} & \gamma_L^{(1,3)} & \gamma_L^{(1,4)} \\ \gamma_L^{(2,1)} & \gamma_L^{(2,2)} & \gamma_L^{(2,3)} & \gamma_L^{(2,4)} \\ \gamma_L^{(3,1)} & \gamma_L^{(3,2)} & \gamma_L^{(3,3)} & \gamma_L^{(3,4)} \\ \gamma_L^{(4,1)} & \gamma_L^{(4,2)} & \gamma_L^{(4,3)} & \gamma_L^{(4,4)} \end{bmatrix} = \begin{bmatrix} 0 & G_3 & G_1 & G_5 \\ G_3 & 0 & G_5 & G_1 \\ G_2 & G_4 & 0 & G_3 \\ G_4 & G_2 & G_3 & 0 \end{bmatrix}
$$

Where the assumed reciprocal connections are:

$$
\begin{aligned}
G_1 &= \gamma_L^{(1,3)} = \gamma_L^{(2,4)} \\
G_2 &= \gamma_L^{(3,1)} = \gamma_L^{(4,2)} \\
G_3 &= \gamma_L^{(1,2)} = \gamma_L^{(2,1)} = \gamma_L^{(3,4)} = \gamma_L^{(4,3)} \\
G_4 &= \gamma_L^{(3,2)} = \gamma_L^{(4,1)} \\
G_5 &= \gamma_L^{(1,4)} = \gamma_L^{(2,3)}
\end{aligned}
$$
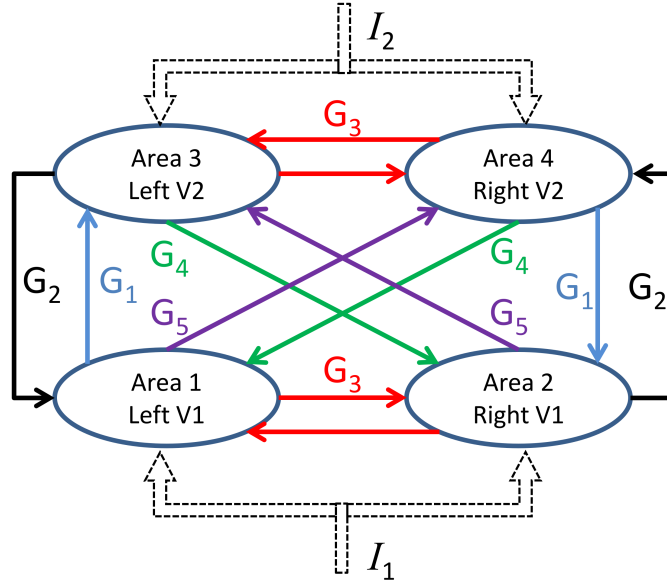
Figure 8.3: First scenario: model $\mathcal{M}_1$ inter-areas connections. Blue arrows: G_1, black arrows: G_2, red arrows: G_3, green arrows: G_4, purple arrows: G_5.
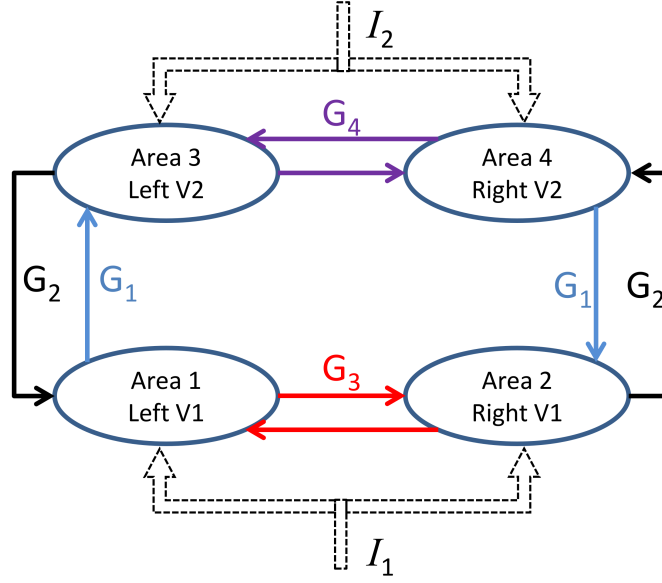
Figure 8.4: Second scenario: model $\mathcal{M}_2$ inter-areas connections. Blue arrows: G_1, black arrows: G_2, red arrows: G_3, purple arrows: G_4.

8.5.2 Second Scenario

Fig. 8.4 shows inter-areas connectivity between cortical areas for model $\mathcal{M}_2$, the connectivity matrix $\boldsymbol{\gamma}_L$ is defined as:

$$\boldsymbol{\gamma}_L = \begin{bmatrix} \gamma_L^{(1,1)} & \gamma_L^{(1,2)} & \gamma_L^{(1,3)} & \gamma_L^{(1,4)} \\ \gamma_L^{(2,1)} & \gamma_L^{(2,2)} & \gamma_L^{(2,3)} & \gamma_L^{(2,4)} \\ \gamma_L^{(3,1)} & \gamma_L^{(3,2)} & \gamma_L^{(3,3)} & \gamma_L^{(3,4)} \\ \gamma_L^{(4,1)} & \gamma_L^{(4,2)} & \gamma_L^{(4,3)} & \gamma_L^{(4,4)} \end{bmatrix} = \begin{bmatrix} 0 & G_3 & G_1 & 0 \\ G_3 & 0 & 0 & G_1 \\ G_2 & 0 & 0 & G_4 \\ 0 & G_2 & G_4 & 0 \end{bmatrix}$$

Where the assumed reciprocal connections are:

$$G_1 = \gamma_L^{(1,3)} = \gamma_L^{(2,4)}$$
$$G_2 = \gamma_L^{(3,1)} = \gamma_L^{(4,2)}$$
$$G_3 = \gamma_L^{(1,2)} = \gamma_L^{(2,1)}$$
$$G_4 = \gamma_L^{(3,4)} = \gamma_L^{(4,3)}$$

8.6 Results

The available dataset consisted of the estimated current dipole sources $\hat{D}$ over 820 ms sampled at $dt = 1$ ms for 148 cortical regions from observed EEG data

collected from one subject during Picture-Naming task. The task was repeated over 60 trials.

In this section, we will present estimation results based on repeated SCKF-SCKS algorithm of effective connectivity between primary and secondary visual cortices (V1 and V2) from left and right hemispheres.

8.6.1 First scenario

The augmented state vector has a total of 56 states and is composed of: 48 hidden neuronal states (Jansen model states for all four areas), six unknown model parameters corresponding to one unknown intra-area connection (parameter C) and five inter-areas connections (parameters $G_1, \ldots, G_5$), and two unknown inputs (I_1 and I_2), to be estimated from four current dipole observations.

Fig. 8.5 shows the box-plots of the estimated effective connections across 60 trials for the first scenario.
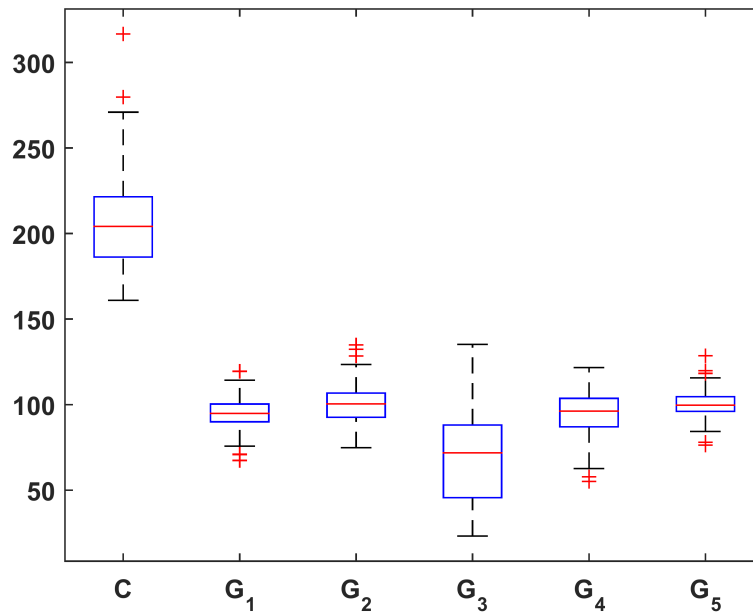
Figure 8.5: First scenario: Box-plots of the estimated intra-area connectivity variable C and the estimated effective (inter-areas) connections $G_1, \ldots, G_5$ over 60 trials. Each box-plot is based on 60 data trials. The horizontal red lines inside the boxes are the medians, The boxes contain 50% of the trials where the lower and upper edges of each box are the 25th and 75th percentiles, the "whiskers" above and below the box indicate the range of the samples (the locations of minimum and maximum sample data points that are not considered outliers), and the red plus signs are the outliers.

8.6.2 Second scenario

The augmented state vector has a total of 55 states and is composed of: 48 hidden neuronal states (Jansen model states for all four areas), five unknown model parameters corresponding to one unknown intra-area connection (parameter C) and five inter-areas connections (parameters $G_1, \ldots, G_4$), and two unknown inputs (I_1 and I_2), to be estimated from four current dipole observations.

The box-plots of the estimated effective connections across 60 trials for the second scenario are shown in Fig. 8.6.
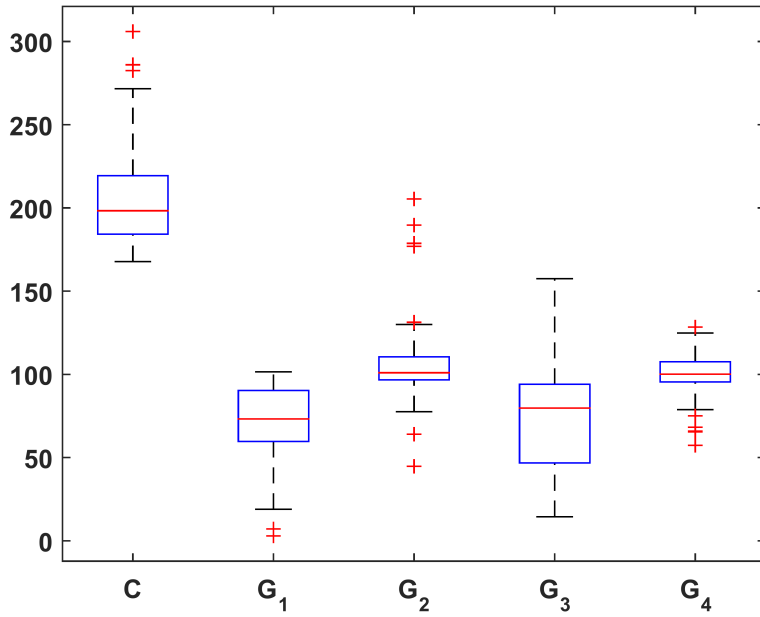
Figure 8.6: Second scenario: Box-plots of the estimated intra-area connectivity variable C and the estimated effective (inter-areas) connections $G_1, \ldots, G_4$ over 60 trials.

8.6.3 Model Selection

Model assessment is carried out by computing the posterior probability of a model $\Pi(\mathcal{M}_m | \mathbf{z}_k)$ (at time k) among proposed model candidates and given a set of collected observations, using Bayesian approaches to model selection [77, 78, 79, 80]:

$$\Pi(\mathcal{M}_m | \mathbf{z}_k) = \frac{p(\mathbf{z}_k | \mathcal{M}_m)\Pi(\mathcal{M}_m | \mathbf{z}_{k-1})}{\sum\limits_{m=1}^{M} p(\mathbf{z}_k | \mathcal{M}_m)\Pi(\mathcal{M}_m | \mathbf{z}_{k-1})} \tag{8.6}$$

Where $p(\mathbf{z}_k|\mathcal{M}_m)$ is the likelihood probability density function (PDF), and $\Pi(\mathcal{M}_m|\mathbf{z}_{k-1})$ is the prior probability of model $\mathcal{M}_m$.

For model candidates $\mathcal{M}_1$ and $\mathcal{M}_2$, the likelihood function $p(\mathbf{z}_k|\mathcal{M}_m), m = 1, 2$ is computed from estimated model states and parameters at time k assuming that the likelihood function is normally distributed [79, 81]:

$$p(\mathbf{z}_k|\mathcal{M}_m) \approx \frac{1}{(2\pi)^{d/2}(\det\Sigma_k)^{1/2}} \exp(-\frac{1}{2}\mathbf{r}_k^T\Sigma_k^{-1}\mathbf{r}_k) \tag{8.7}$$

Where r is the residual error between the observed measurements and the estimated measurements (computed from the Kalman update step, see section 2.3 equation (2.43)) at time k:

$$\mathbf{r}_k = \mathbf{z}_k - \hat{\mathbf{z}}_k \tag{8.8}$$

And $\Sigma_k = S_{\mathcal{Z}\mathcal{Z},k}^T S_{\mathcal{Z}\mathcal{Z},k}$ is the corresponding error covariance matrix (computed from the Kalman update step, see section 2.3 equation (2.44)).

The summarized statistics about model selection are listed in table 8.1, which shows that $(\mathcal{M}_2)$ 25 times out of 25,

Table 8.1: Statistics of model selection over 60 trials.

	$\mathcal{M}_1$	$\mathcal{M}_2$
Selection Rate	26/60	34/60

8.7   Discussion

In this chapter, we addressed estimation of effective connectivity between cortical areas residing in the visual cortex from experimental data. The cortical areas of interest were chosen from the visual cortex, namely the primary visual cortex (V1) and the secondary visual cortex (V2) from both left and right hemispheres and were modeled with the multi-neuronal-area Jansen model for cortical activity. The estimation procedure was based on repeated SCKF-SCKS algorithm with current dipole sources $\hat{D}$ sering as observations estimated from observed EEG data (by solving the EEG inverse-problem) collected from one subject during Picture-Naming task (overall of 60 trials). We considered two models ($\mathcal{M}_1$ and $\mathcal{M}_2$) with reciprocal connections that differ in the number of assumed inter-areas connections. Furthermore, model assessment was performed and carried out using Bayesian approaches to model selection in order to statistically choose the best fitting model of experimental data.

In terms of estimation accuracy (Figs. 8.5 and 8.6), the estimated parameters for the first scenario $\mathcal{M}_1$ showed more consistency across trials than those for the second scenario $\mathcal{M}_2$. This is interpreted from the tighter box-plots of estimated parameters (C, G_1, G_2, G_3, and G_4) for $\mathcal{M}_1$ (Fig. 8.5). The parameter G_3 (assumed connection V1-to-V1 in the first model, assumed connection V1-to-V1 and V2-to-V2 in the second model) showed higher variability across trials for both models (wider box-plot).

In terms of model assessment (Table 8.1), $\mathcal{M}_1$ was chosen as the best model 34 times out of 60 (56.66% selection rate), and $\mathcal{M}_2$ was selected 26 times out of 60 (43.33% selection rate).

The reported results suggest a moderate tendency towards $\mathcal{M}_1$, however, further propositions of model candidates with non-reciprocal connections are highly required, specifically, non-reciprocal V1-to-V1 and V2-to-V2 connections as well as cross hemisphere V1-to-V2 connections might present clearer insight of the connectivity structure between these cortical areas.

Chapter 9

Improving Estimation Accuracy with Hybrid Cubature Kalman Filtering

Representations of physiological processes, such as neural systems, often admit state-space models that are of the continuous-discrete hybrid types (continuous-time process dynamics and discrete time measurements). For estimation of these systems, therefore, the hybrid Continuous-Discrete Cubature Kalman Filter (CD-CKF), introduced as an extension of the CKF for mixed systems, seems to be more natural. The CD-CKF discretizes the continuous process equation in SDE form using the Itô-Taylor expansion of order 1.5 and transforms it to stochastic difference equation in discrete time. This transformation will result in a state-space model with both process and measurement equations expressed in stochastic difference equations in discrete time.

In the chapter, we address the accuracy of state and parameter estimation using CKF and CD-CKF techniques in the context of neural state estimation from EEG and fMRI recordings as specific examples of physiological dynamical system modeling. Starting with nonlinear state-space simulation models, we elaborate estimation performance while varying conditions related to (i) the observation sampling frequency, (ii) the observation signal-to-noise ratio and (iii) the structure of the additive noise process underlying the state dynamics. In particular, we aim to highlight those situations where an added benefit can be obtained by explicitly employing a hybrid filtering (CD-CKF).

We pay specific attention to the effect of the sampling interval of the observations principally because it relates to the inherent time constants (speed of dynamics) of the underlying continuous processes and hence constrains the modelers ability to recover detailed dynamics from observations obtained using a given

recording modality. We also compare the accuracy of the CD-CKF and CKF techniques in estimating the neural activity and parameters for simulated neural models in cases where the observation signal-to-noise ratio are decreased, and/or the Gaussian process noise assumptions are violated. Low signal to noise ratios are common for modalities that record electrical potentials at a location distant from the source (depth electrodes, scalp EEG) due to spatial filtering (smearing ($\sim$0.5 cm^2) and activity aggregation across numerous neural subtypes (leading to unmodeled signal components). Finally, and since Kalman-based techniques invariably assume that process noise is of Gaussian nature (for a continuous time, the derivative of the state is driven by a Wiener process), we aim to assess, using Monte-Carlo simulations, the performance of both CKF and CD-CKF when noise structures violate Gaussianity. In neural estimation, non-Gaussian noise models are common. Examples include the additive noise in synaptic dynamics (approximating in vivo conductance fluctuations) that has specific structures (OrnsteinUhlenbeck process [90]), and the afferent neural activity impinging onto a given population, that has been reported to possess an un-symmetric tailed distribution [91, 92, 93, 94, 95, 96].

9.1   Problem Definition

Given the state-space model of a given nonlinear dynamical system in continuous-discrete form:

Process Equation: $$\dot{\mathbf{x}}(t) = \mathbf{f}(\mathbf{x}(t), t) + \sqrt{\mathbf{Q}}\mathbf{\Gamma} \tag{9.1}$$

Measurement Equation: $$\mathbf{z}_k = \mathbf{h}(\mathbf{x}_k, k) + \mathbf{w}_k \tag{9.2}$$

Where $\mathbf{x}(t) \in \mathbb{R}^n$ is the state of the dynamic system at time t, $z_k \in \mathbb{R}^d$ is the measurement at discrete time instance k, $\mathbf{f} : \mathbb{R}^n \times \mathbb{R} \to \mathbb{R}^n$ is the drift coefficient, $\mathbf{h} : \mathbb{R}^n \times \mathbb{R} \to \mathbb{R}^d$ is the measurement function, $\mathbf{\Gamma} \in \mathbb{R}^n$ is a Gaussian noise process assumed to be independent of states and measurement noise, $Q \in \mathbb{R}^{n \times n}$ is the diffusion coefficient, $\mathbf{w}_k \in \mathbb{R}^d$ is a vector of random Gaussian measurement noise with zero mean and covariance R_k.

We seek to compare the estimation accuracy between CKF and CD-CKF techniques (sections 2.3 and 2.4). Starting with nonlinear state-space simulation models, we elaborate estimation performance while varying conditions related to (i) the observation sampling frequency, (ii) the observation signal-to-noise ratio (SNR) and (iii) the structure of the additive noise process underlying the state dynamics. In particular, we aim to highlight those situations where an added benefit can be obtained by explicitly employing a hybrid filtering (CD-CKF).

In order to apply the CKF, the continuous-discrete state-space model in equations (9.1) and (9.2) is transformed to a pair of stochastic difference equations by

discretizing the continuous-time SDE process equation (equation (9.1)) using the LL method (as described in section 2.3). Whereas, the formulation of the CD-CKF is inherently accounting for the continuous-time process equation. States and parameters estimation are carried out with square-root versions of both CKF and CD-CKF (sections 2.3.3 and 2.4.2) since they have improved numerical accuracy.

9.2 Simulation Data

9.2.1 Conductance-Based Neuronal Model

We consider a single neuronal area modeled with conductance-based neuronal model (see section 3.3.2). The neuronal area is composed of three layers with a total of 9 hidden internal states including the membrane potential, excitatory and inhibitory conductances with the membrane potential of the infra-granular layer is considered as observations.

We address estimation performance of Kalman filters (CKF and CD-CKF) while varying simulation conditions related to:

- Observation sampling frequency: Measurements collection from this model is carried out by simulating the system with low sampling interval $\Delta t = 0.01$ ms, then they are re-sampled at different high sampling intervals $dt = 0.1, 0.5, 1, 2, 4, 8$ ms.

- Observation signal-to-noise ratio (SNR): Measurement data was generated by this model with different levels of background noise. A total of eight cases were taken into consideration to simulate conditions for a range of SNR (Table 9.1). The SNR is defined as:

$$\text{SNR}_{\text{dB}} = 10 \log_{10} \left(\frac{P_{\text{signal}}}{P_{\text{noise}}} \right) = 10 \log_{10} \left(\frac{E[V_{\text{signal}}^2]}{\sigma_{\text{noise}}^2} \right) \tag{9.3}$$

Where P is the average power, $E[V_{\text{signal}}^2]$ is the mean squared value of output amplitude, and σ_{noise}^2 is the variance of the noise.

Table 9.1: SNR values in dB over the observation signal (membrane potential of infra-granular layer).

Case	1	2	3	4	5	6	7	8
SNR (dB)	4	7	8	9	11	12	14	18

- Structure of the additive noise process: Different noise processes other than the Gaussian process are considered to affect the dynamics of the system, as described in the subsequent subsections.

Additive White Noise

For the case where the assumed additive noise has a Gaussian distribution, applying the Itô-Taylor expansion of order 1.5 to the process equation over the time interval $(t, t + \Delta t)$ yields [3]:

$$\mathbf{x}_{k+1} = \mathbf{f}_d(\mathbf{x}_k, k) + \sqrt{\mathbf{Q}}\mathbf{w} + (\mathbb{L}f(\mathbf{x}_k, k))\mathbf{y} \tag{9.4}$$

Where:

$$\mathbf{f}_d(\mathbf{x}_k, k) = \mathbf{x}_k + \Delta t\mathbf{f}(\mathbf{x}_k, k) + \frac{1}{2}\Delta t^2 \mathbb{L}_0\mathbf{f}(\mathbf{x}_k, k) \tag{9.5}$$

$\mathbb{L}_0$ and $\mathbb{L}$ are two differential operators defined as:

$$\mathbb{L}_0 = \frac{\partial}{\partial t} + \sum_{i=1}^{n} f_i \frac{\partial}{\partial x_i} + \frac{1}{2}\sum_{j=1}^{n}\sum_{p=1}^{n}\sum_{q=1}^{n}\sqrt{Q}_{pj}\sqrt{Q}_{qj}\frac{\partial^2}{\partial x_p \partial x_q}$$

Where f_i denotes the ith element of function vector $\mathbf{f}$.

And the term $\mathbb{L}\mathbf{f}$ denotes a square matrix with its $(i, j)^{\text{th}}$ element being $\mathbb{L}_j f_i$, $(i, j = 1, \ldots, n)$:

$$\mathbb{L}_j f_i = \sum_{p=1}^{n}\sqrt{Q}_{pj}\frac{\partial f_i}{\partial x_p}$$

$(\mathbf{w}, \mathbf{y})$ is a pair of correlated n-dimensional Gaussian random variables, which can be generated from a pair of independent n-dimensional standard Gaussian random variables $(\mathbf{u}_1, \mathbf{u}_2)$ as follows:

$$\mathbf{w} = \sqrt{\Delta t}\mathbf{u}_1$$

$$\mathbf{y} = \frac{1}{2}\Delta t^{3/2}(\mathbf{u}_1 + \frac{\mathbf{u}_2}{\sqrt{3}})$$

Accordingly, the correlated Gaussian random variables $(\mathbf{w}, \mathbf{y})$ have the following three covariance matrices (with $\mathbf{I}_n$ being the identity matrix of size $n \times n$):

$$E[\mathbf{w}\mathbf{w}^T] = \Delta t\mathbf{I}_n$$

$$E[\mathbf{w}\mathbf{y}^T] = \frac{1}{2}\Delta t^2\mathbf{I}_n$$

$$E[\mathbf{y}\mathbf{y}^T] = \frac{1}{3}\Delta t^3\mathbf{I}_n$$

The model is simulated by integrating the state-space model (equations (9.1) and (9.2)) using IT-1.5 discretization method for SDE as described above, and observations $\mathbf{z}_k$ were collected with sampling interval Δt by applying equation (9.2).

Additive Colored Noise

We will describe the process model for the case where the additive noise is colored noise. The SDE process equation is formulated as:

$$\dot{\mathbf{x}}(t) = \mathbf{f}(\mathbf{x}(t), t) + \mathbf{\Psi} \tag{9.6}$$

Where $\mathbf{\Psi}$ is filtered white noise.

In order to be able to simulate this model with colored noise using the IT-1.5 discretization method for SDE, we augmented the state vector to include the colored noise as state variables driven by white noise. The augmented state vector becomes:

$$\mathbf{x}^{\text{aug}} = \begin{bmatrix} \mathbf{x} & \mathbf{\Psi} \end{bmatrix}^T$$

Using the augmented vector notation, the process equation is defined as:

$$\dot{\mathbf{x}}^{\text{aug}}(t) = \mathbf{f}^{\text{aug}}(\mathbf{x}^{\text{aug}}(t), t) + \sqrt{\mathbf{\Theta}}\mathbf{\Gamma} \tag{9.7}$$

$$\begin{bmatrix} \dot{\mathbf{x}} \\ \dot{\mathbf{\Psi}} \end{bmatrix} = \begin{bmatrix} \mathbf{f}(\mathbf{x}(t), t) + \mathbf{\Psi} \\ \mathbf{f}_{\mathbf{\Psi}}(t) \end{bmatrix} + \sqrt{\mathbf{\Theta}}\mathbf{\Gamma} \tag{9.8}$$

Where

$$\mathbf{f}_{\mathbf{\Psi}}(t) = -\frac{1}{\alpha}\mathbf{\Psi} \tag{9.9}$$

$$\mathbf{\Theta} = \begin{bmatrix} \mathbf{0} & \mathbf{0} \\ \mathbf{0} & \frac{1}{\alpha^2}\mathbf{Q} \end{bmatrix} \tag{9.10}$$

And $\mathbf{Q}$ is the covariance matrix of the white noise process driving the colored noise vector $\mathbf{\Psi}$, and α is a constant that determines the cutoff frequency of the colored noise.

The aforementioned reformulation of the process equation allows the expression of affected model states with additive colored noise in terms of a white noise process. By augmenting the state vector with additional variables $\mathbf{\Psi}$ and setting the process function $\mathbf{f}^{\text{aug}}$ to act as a low-pass filter of the white noise process for variables $\mathbf{\Psi}$, and then adding these variables $\mathbf{\Psi}$ to the states without the model

sates being directly affected by the white noise process. The state-space model for the additive colored noise case becomes:

Process Equation:
$$\dot{\mathbf{x}}^{\mathrm{aug}}(t) = \mathbf{f}^{\mathrm{aug}}(\mathbf{x}^{\mathrm{aug}}(t), t) + \sqrt{\mathbf{\Theta}}\mathbf{\Gamma} \qquad (9.11)$$

Measurement Equation:
$$\mathbf{z}_k = \mathbf{h}(\mathbf{x}_k^{\mathrm{aug}}, k) + \mathbf{w}_k \qquad (9.12)$$

Where $\mathbf{x}^{\mathrm{aug}}(t) \in \mathbb{R}^{2n}$ is the state of the dynamic system at time t, $z_k \in \mathbb{R}^d$ is the measurement at discrete time instance k, $\mathbf{f}^{\mathrm{aug}} : \mathbb{R}^{2n} \times \mathbb{R} \to \mathbb{R}^{2n}$ is the drift coefficient, $\mathbf{h} : \mathbb{R}^{2n} \times \mathbb{R} \to \mathbb{R}^d$ is the measurement function, $\mathbf{\Gamma} \in \mathbb{R}^{2n}$ is a Gaussian noise process assumed to be independent of states and measurement noise, $\mathbf{\Theta} \in \mathbb{R}^{2n \times 2n}$ is the diffusion coefficient, $\mathbf{w}_k \in \mathbb{R}^d$ is a vector of random Gaussian measurement noise with zero mean and covariance R_k.

Now, as the state-space model is generally reformulated as a system driven by additive Gaussian noise, the model is simulated by integrating the state-space model (equations (9.11) and (9.12)) using IT-1.5 discretization method for SDE as same as in section 9.2.1, and observations $\mathbf{z}_k$ were collected with sampling interval Δt by applying equation (9.12).

Other Types of Noise Processes

In order to examine the effect of Gaussianity assumption for the noise structure in neural model on the performance of Kalman filter in estimating neuronal hidden states, we assumed that the actual continuous system could be driven by different types of noise processes whereas these processes are assumed to be a Wiener process in the Kalman setup. The system will be examined under the following noise types:

- Poisson process.

- Exponential process.

- Gamma process.

- Low frequency noise.

The simulation of a given model driven by Poisson, Exponential and Gamma noise processes is carried out under the assumption that these noise processes are the resultant discrete processes after the discretization of the continuous process equation; that is we are assuming that by discretizing the process equation we do not have any prior knowledge about what kind of original continuous noise process could produce these discrete noise processes. Hence, in order to simulate such system driven by these noise types, the continuous system will be discretized with the LL method and the noise process will be added as a discrete process to

the discrete dynamics. Thus, given the continuous time dynamics of the system without the noise term:

$$\dot{\mathbf{x}}(t) = \mathbf{f}(\mathbf{x}(t)) \qquad (9.13)$$

The discrete version of this ODE system by the LL method is given by [97]:

$$\mathbf{x}_k \approx \mathbf{x}_{k-1} + \mathcal{J}_{k-1}^{-1}[e^{(\mathcal{J}_{k-1}\Delta t)} - I_e]\mathbf{f}(\mathbf{x}_{k-1}) \qquad (9.14)$$

Where $\mathcal{J}_k$ is the Jacobian of $\mathbf{f}$ at discrete time k and Δt is the time interval between samples, and I_e is the identity matrix.

Given this discrete version of the continuous system dynamics, we can add the noise from a discrete process to get a process equation with additive noise as follow:

$$\mathbf{x}_k = \mathbf{x}_{k-1} + \mathcal{J}_{k-1}^{-1}[e^{(\mathcal{J}_{k-1}\Delta t)} - I_e]\mathbf{f}(\mathbf{x}_{k-1}, k-1) + \boldsymbol{\Omega} \qquad (9.15)$$

Where $\boldsymbol{\Omega}$ represents a discrete Poisson, Exponential or Gamma process.

The state-space representation in discrete time for these cases is:

Process Equation: $\qquad \mathbf{x}_k = \mathbf{x}_{k-1} + \mathcal{J}_{k-1}^{-1}[e^{(\mathcal{J}_{k-1}\Delta t)} - I_e]\mathbf{f}(\mathbf{x}_{k-1}) + \boldsymbol{\Omega} \qquad (9.16)$

Measurement Equation: $\qquad \mathbf{z}_k = \mathbf{h}(\mathbf{x}_k, k) + \mathbf{w}_k \qquad (9.17)$

Where $\mathbf{x}_k \in \mathbb{R}^n$ is the state vector of the dynamic system at discrete time time k, $z_k \in \mathbb{R}^d$ is the measurement at discrete time instance k, $h : \mathbb{R}^n \times \mathbb{R} \to \mathbb{R}^d$ is the measurement function, $\boldsymbol{\Omega} \in \mathbb{R}^n$ is a discrete noise process, $w_k \in \mathbb{R}^d$ is a vector of random Gaussian noise.

The model is simulated by integrating the state-space model (equations (9.16) and (9.17)) as described above for the cases where the system is assumed to be driven by Poisson, Exponential and Gamma noise processes. Observations $\mathbf{z}_k$ were collected with sampling interval Δt by applying equation (9.17).

In addition, we will consider the case where the system is driven by very slow varying noise which is considered as filtered white noise. This model will be simulated in the same manner as the colored noise case was simulated (see section 9.2.1) but by varying the constant α in the covariance matrix $\boldsymbol{\Theta}$ in order to produce noise process having frequency components in the range of 1–5 Hz. This type of slow noise is aimed to test the performance of Klaman filters for situations in which the frequency components of the noise are mainly focused in the operational band of the system (the 1–5 Hz band is the frequency range of the system output of the conductance-based neuronal model).

9.2.2 Hemodynamic Model

In simulating the hemodynamic model (see section 3.5), the continuous time dynamics are assumed to be driven by Wiener noise processes. The neural activity

took the shape of Gaussian-bump functions with different amplitudes. The IT-1.5 discretization method with a simulation time step of $\Delta t = 0.1$ sec was adopted to generate the continuous observation BOLD signal, which was then artificially re-sampled at the repeat time (TR = 1 sec). The states, observation, and inputs to the model are assumed to be driven by random noise having precisions similar to those reported in [30].

The blind deconvolution procedure was applied for two scenarios: (a) only the input is unknown, and (b) the input as well as two model parameters (rate of signal decay κ and rate of feedback regulation λ) are unknown.

For the estimation problem, linear interpolations between successive samples were obtained at uniform time steps ($dt = 0.2, 0.5$ sec) and are utilized as effective discrete-time observations. Subsequent estimation consisted of a forward pass using the square-root CKF and square-root CD-CKF then a backward smoothing pass (namely SCKS and SCD-CKS). Since the unknown quantities are the input (first scenario) as well as two parameters (second scenario), the backward pass is necessary to improve on the estimates of the forward pass, as reported in [30]. Furthermore, estimation of unknown parameters (second scenario) was constrained to specific intervals (rate of signal decay $\kappa \in [0.6 - 0.9]$ and rate of feedback regulation $\lambda \in [0.3 - 0.5]$) and were initialized randomly within these intervals and sampled from uniform distributions.

9.3 Performance assessment

The performance of CKF and CD-CKF was evaluated as the accumulative mean square error (MSE) of all normalized states over a total of 100 Monte-Carlo simulations. For a state vector $\mathbf{x} \in \mathbb{R}^n$, the MSE is defined as:

$$MSE \; = \frac{1}{nMK} \sum_{m=1}^{M} \sum_{k=1}^{K} \sum_{i=1}^{n} \frac{\left(x_{i,k}^{\text{real}} - \hat{x}_{i,k,m}\right)^2}{\left(\max(x_i^{\text{real}}) - \min(x_i^{\text{real}})\right)^2} \qquad (9.18)$$

Where K is the length of the total simulation time vector, M is the total number of Monte Carlo runs, n is the size of the state vector $\mathbf{x}$, $x_{i,k}^{\text{real}}$ is the true i^{th} state at time k, $\hat{x}_{i,k,m}$ is the estimated i^{th} state at time k in the mth Monte Carlo run, and $\left(\max(x_i^{\text{real}}) - \min(x_i^{\text{real}})\right)^2$ is a normalizing factor and it is defined as the square of the difference between the maximum and minimum true values of the ith state. This factor is introduced in order to make all states magnitude in $[0, 1]$ range.

Another assessment quantity for performance evaluation is the squared error (SE) ratio between the two filters. For a state vector $\mathbf{x} \in \mathbb{R}^n$, The SE ratio for the

$m^{\text{th}}, (m = 1, \ldots, M)$ Monte Carlo run (R^m) is defined as follow:

$$\mathrm{R}^m = \frac{(\mathrm{SE}^m)^{\text{CD-CKF}}}{(\mathrm{SE}^m)^{\text{CKF}}}, \qquad m = 1, \ldots, M \tag{9.19}$$

Where the squared error (SE) of each filter is defined as:

$$\mathrm{SE}^m = \frac{1}{nK} \sum_{k=1}^{K} \sum_{i=1}^{n} \frac{\left(x_{i,k}^{\text{real}} - \hat{x}_{i,k,m}\right)^2}{\left(\max(x_i^{\text{real}}) - \min(x_i^{\text{real}})\right)^2} \tag{9.20}$$

Where K is the length of the total simulation time vector, , n is the size of the state vector $\mathbf{x}$, $x_{i,k}^{\text{real}}$ is the true i^{th} state at time k, $\hat{x}_{i,k,m}$ is the estimated i^{th} state at time k in the mth Monte Carlo run, and $\left(\max(x_i^{\text{real}}) - \min(x_i^{\text{real}})\right)^2$ is a normalizing factor.

Finally, a deviation analysis to examine the *inaccuracy rates* of each filter by introducing *probability of inaccuracy metric* that will be used as a measure of the *inaccuracy* of a given filter. The filer is said to be inaccurate when the normalized error between estimated and real states exceeds 20%. The probability of inaccuracy (PI) measure is regarded as the probability of the obtaining an inaccurate state estimate, that is, the estimated states being 20% far from the true states. It can further be considered as the total fraction of time when the estimated states were 20% far away from the true states. The probability of inaccuracy (PI) measure is defined as:

$$\mathrm{PI} = \frac{1}{nMK} \sum_{m=1}^{M} \sum_{k=1}^{K} \sum_{i=1}^{n} U\left[\left(\frac{x_{i,k}^{\text{real}} - \hat{x}_{i,k,m}}{x_i^{\text{real}}}\right)^2 > \beta^2\right] \tag{9.21}$$

Where K is the length of the total simulation time vector, M is the total number of Monte Carlo runs, n is the size of the state vector $\mathbf{x}$, $x_{i,k}^{\text{real}}$ is the true i^{th} state at time k, $\hat{x}_{i,k,m}$ is the estimated i^{th} state at time k in the mth Monte Carlo run, $\beta = 0.2$ is the accuracy threshold, and the function $U[.]$ is the Heaviside function defined as:

$$U\left[s^2 > \beta^2\right] = \begin{cases} 0 & \text{if } s^2 < \beta^2 \\ 1 & \text{if } s^2 \geqslant \beta^2 \end{cases} \tag{9.22}$$

9.4   Results

9.4.1   Single Area Conductance-Based Neuronal Model

The single neuronal area model has a total of 9 hidden states including the membrane potential, excitatory and inhibitory conductances to be estimated from

noisy observations considered as the membrane potential of the infra-granular layer. The model was simulated with different levels of background noise (total of eight SNR cases as in Table 9.1)for a simulation length of 200 ms with sampling interval $\Delta t = 0.01$ ms using IT-1.5 discretization method as described above. For each SNR case, measurement data were collected with sampling interval Δt and then were re-sampled at different sampling time steps $dt = 0.1, 0.5, 1, 2, 4, 8$ ms, in order to examine the effect of decreasing the sampling rate on the estimation error.

The square-root CKF and square-root CD-CKF filters were applied, in which the *measurement update* for the observations in both filtering cases is obviously dictated by the assumed sampling rate. For the CKF, the *time update* occurs in concurrence with the measurements every dt millisecond (see section 2.3.3). For the CD-CKF, however, the *time update* occurs every δ milliseconds where each sampling interval dt is divided into m steps of length δ, where $\delta = dtm$ (m is taken to equal 5) (see section 2.4.2).

The performance of both filters was evaluated for different noise scenarios (6 cases, white, colored, Poisson, Exponential, Gamma, and Low frequency noise), several sampling rates (6 different dt cases), and signal-to-noise ratios (8 SNR cases). We will consider in detail two main noise scenarios (white and colored noise).

White Noise Case

The continuous time system is assumed to be driven by a Wiener noise process for different SNRs. For the purpose of simulation, a time step of $\Delta t = 0.01$ ms was adopted in IT-1.5 discretization method in order to generate measurement data. The output data of the simulation were then artificially re-sampled at different sampling rates ($dt = 0.1, 0.5, 1, 2, 4, 8$ ms) and made available as measurement data for the two filters.

Fig. 9.1 shows the MSE values averaged over 100 Monte-Carlo runs of CD-CKF and CKF for different SNRs at different sampling rates. From the figure, it is clear that the CD-CKF outperformed the CKF for all cases. For a given SNR, both filters showed improved convergence to true underlying processes as the sampling rate decreases. However, for a given sampling rate, the CD-CKF scored smaller MSE values than those of the CKF.

In order to statistically examine how better the CD-CKF performed than the CKF, Fig. 9.2 shows the box-plots at different sampling rates of CD-CKF squared error to CKF squared error ratio (the squared error ratio R is computed as described in section 9.3). Each box-plot refers to ratios computed for a given SNR at a given sampling rate for the 100 Monte-Carlo runs. As seen in Fig. 9.2,

Figure 9.1: Performance of CD-CKF and CKF under white noise. MSE values averaged over 100 Monte-Carlo runs of CD-CKF and CKF for different SNRs and different sampling rates where the underlying system is perturbed by additive white noise.

the median ratio was consistently greater than one for all simulations. Seen in terms of the length of sampling time step dt, it is noted that the CD-CKF to CKF ratio is highest for very small time step ($dt = 0.1$ ms) and large time steps ($dt = 4 - 8$ ms). At intermediate time step, ($dt = 1 - 2$ ms), the ratio is nearly unity (performance is comparable) only for very low SNR (4 dB). In terms of the SNR variation, it is noted that the ratio was the highest for all SNR levels at very small time steps ($dt = 0.$ ms, or frequent measurements). An increase in the SNR value generally improves the ratio for smaller time steps (both in median value and overall spread but not at wider time steps ($dt = 4 - 8$ ms), where the ratio does not increase in neither median nor overall spread with large SNR).

The system is again simulated using the IT-1.5 (as described in section 9.2.1) with $\Delta t = 0.01$ ms to produce observations which then were re-sampled at different sampling rates for the application of filters and the MSE values averaged over 100 Monte-Carlo runs for both filters under different SNRs and sampling rates were computed and shown in Fig. 9.3.

146

Figure 9.2: Distribution of squared error ratios of 100 Monte-Carlo runs for different sampling rates and different SNRs for the additive white noise case. Each box plot is based on 100 data samples. The horizontal red lines inside the boxes are the medians, The boxes contain 50% of the samples where the lower and upper edges of each box are the 25th and 75th percentiles, and the "whiskers" above and below the box indicate the range of the samples (the locations of minimum and maximum sample data points that are not considered outliers).

It is noted here that these results are in line with those observed in the white noise case; the CD-CKF performed better than the CKF with an improvement of performance with decreasing sampling times for both filters. Fig. 9.4 shows the box-plots of squared error ratio for different SNRs and sampling times for the 100 Monte-Carlo runs. When compared to the white noise case, dependence
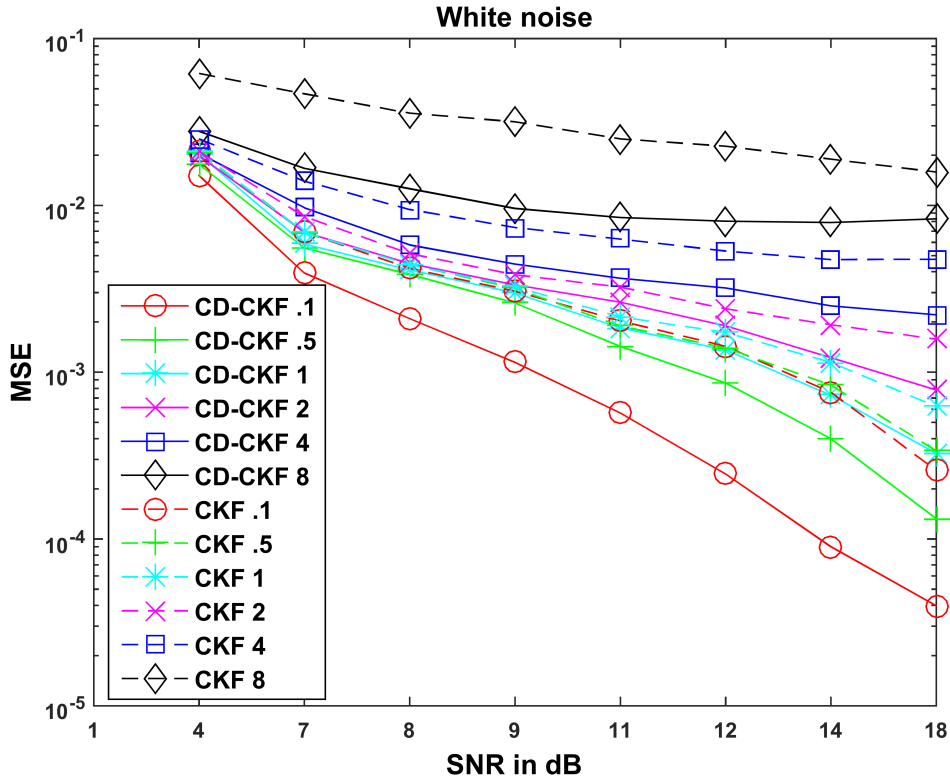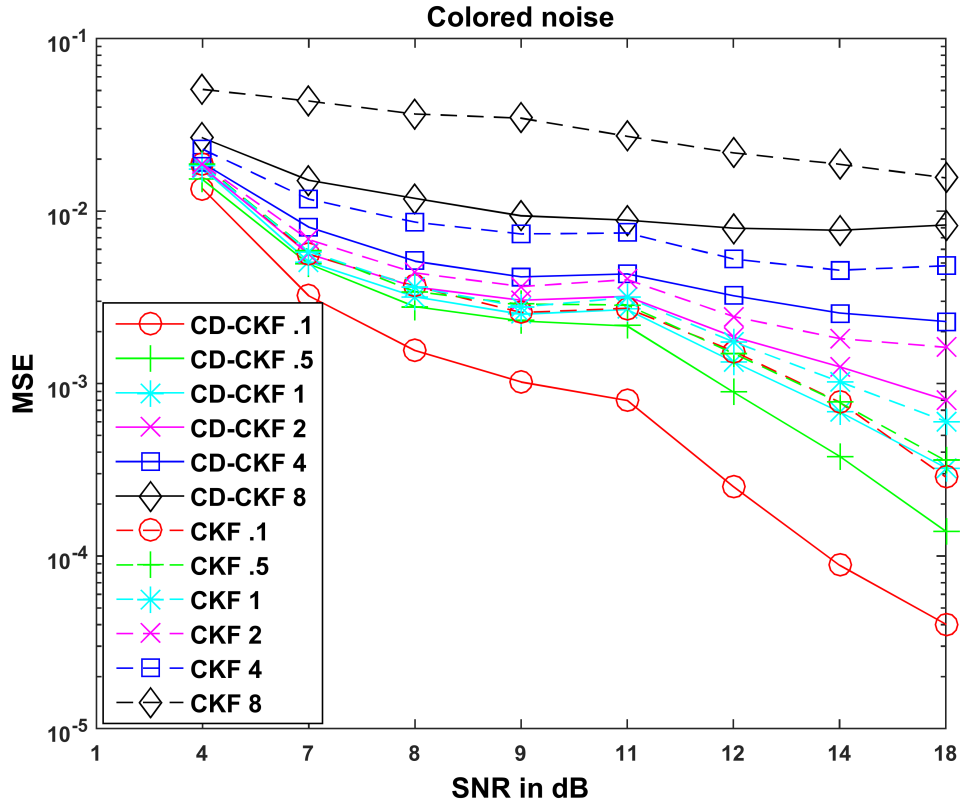
Figure 9.3: Performance of CD-CKF and CKF under colored noise. MSE values averaged over 100 Monte-Carlo runs of CD-CKF and CKF for different SNRs and different sampling rates where the underlying system is perturbed by additive colored noise.

of the ratio on time steps and SNR in the colored noise case follows a similar pattern (Figs 9.2 and 9.4): The ratio is highest at the two opposite ends of the sampling rate ($dt = 0.1$ ms $and dt = 8$ ms), and the performance improves with increasing SNR particularly at intermediate step lengths ($dt = 1 - 2$ ms) but not at large time steps ($dt = 8$ ms). Notably, however, the actual value of the ratio was higher (CD-CKF was better) for low SNR in the colored noise case of all sampling intervals. That is, it is apparent that the CD-CKF is more resilient to additive colored-noise particularly under large noise components.

Effect of the Simulation Method

The continuous time simulations of the system were performed using IT-1.5 discretization methods. Therefore, and since the CD-CKF uses the IT-1.5 method to discretize the continuous process equation while the CKF uses the local linearization scheme (LL), a legitimate concern is whether the improvement in re-
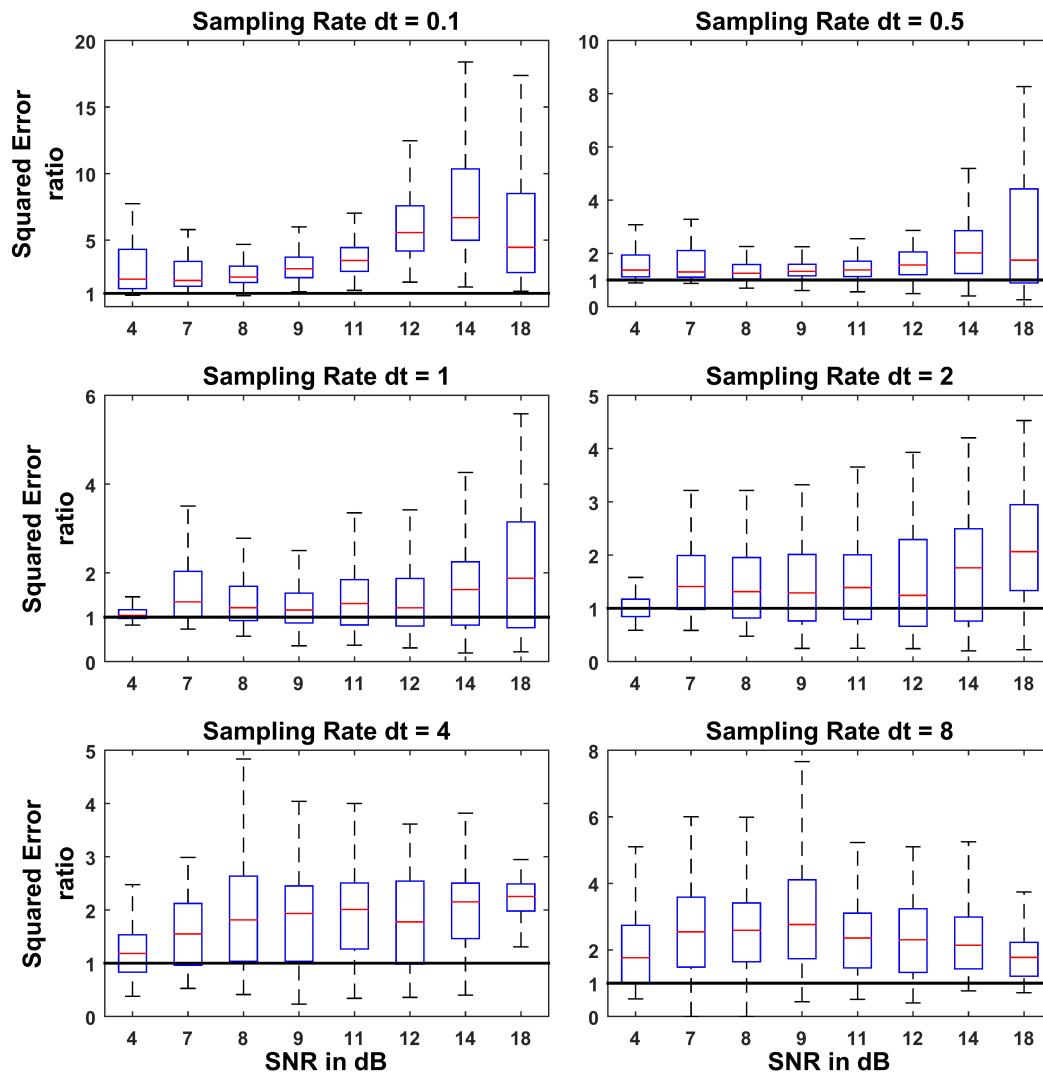
148
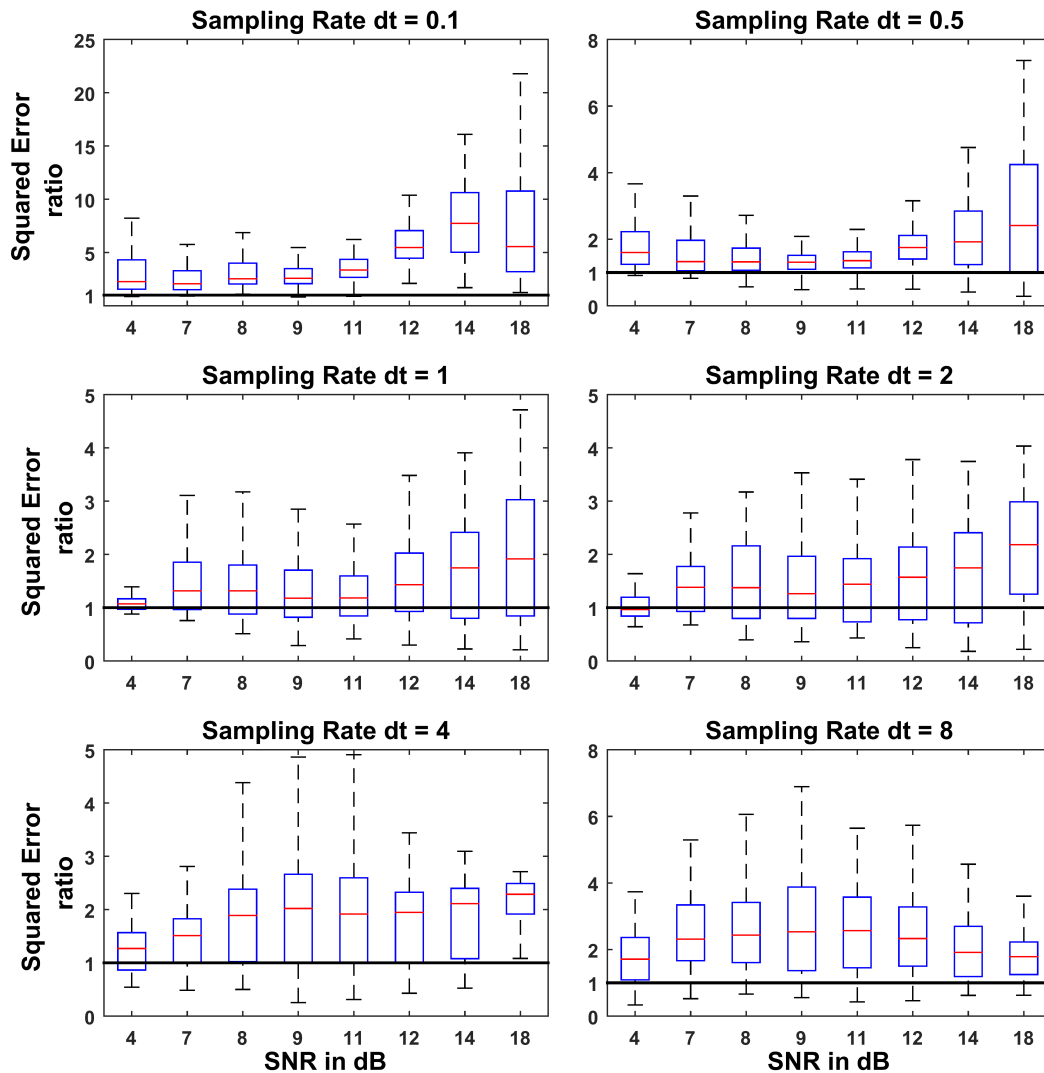
Figure 9.4: Distribution of squared error ratios of 100 Monte-Carlo runs for different sampling rates and different SNRs for the additive colored noise case.

sults obtained with CD-CKF is simply caused by the matching discretization techniques in CD-CKF and system simulation.

We therefore repeated the estimation problem for both scenarios with the observations obtained by simulating the system using the LL discretization method. The MSE values averaged over 100 Monte-Carlo runs of both filters for additive white and colored noise in this case are shown in Fig. 9.5. We can see that CD-CKF still performed better than the CKF and hence the simulation method has no effect on the relative performance of both filters.
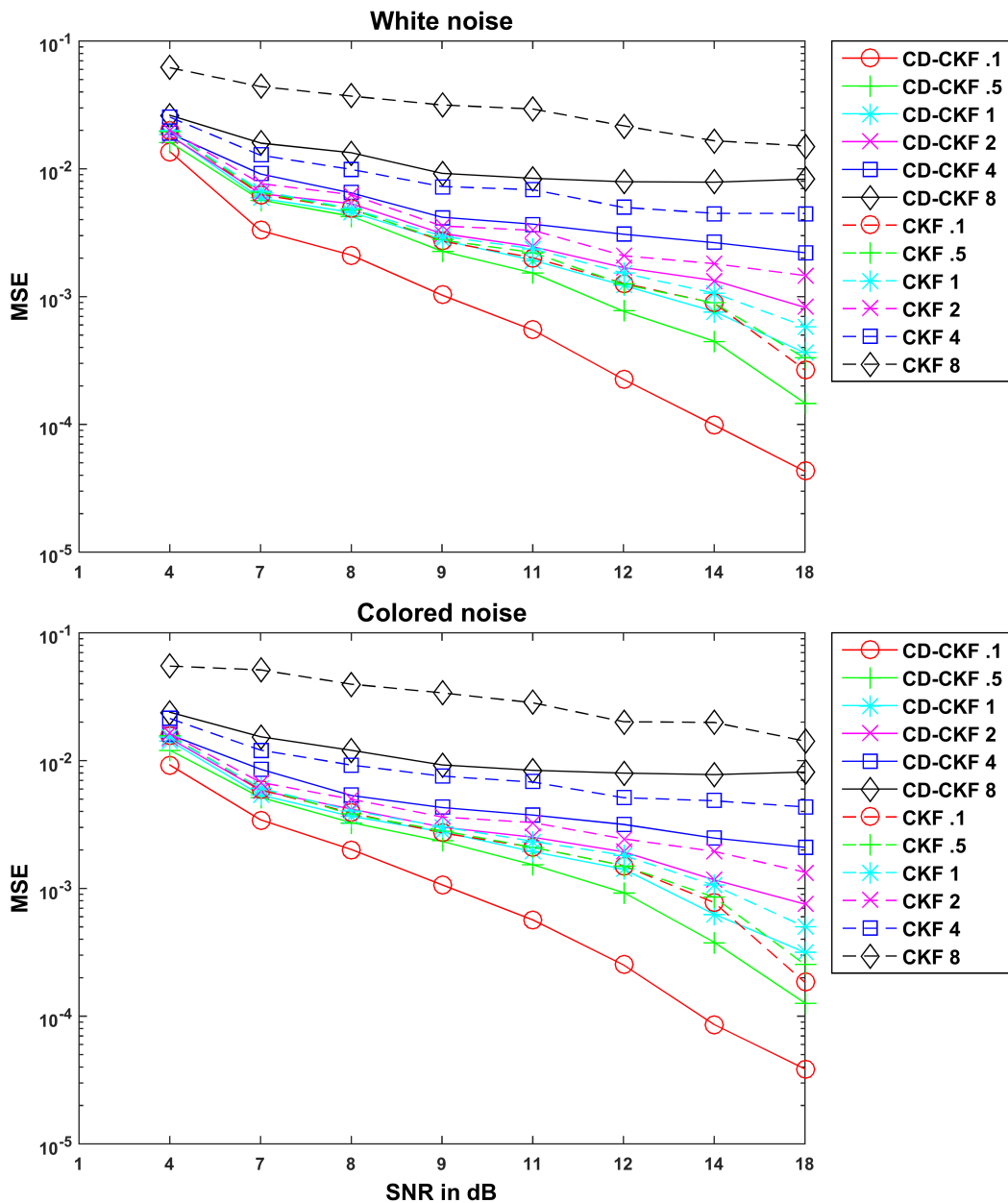
Figure 9.5: Performance of CD-CKF and CKF with the observations obtained by simulating the system using the LL discretization method. MSE of CD-CKF and CKF for different SNRs and different sampling rates where the underlying system is perturbed by additive white noise (top) and colored noise (bottom).

Other types of noise processes

In the Kalman estimation framework, the additive noise is assumed to be derived from a Wiener process. To address the sensitivity of the obtained results on

this assumption, we examine in this section the performance of CD-CKF and CKF under the assumption that the actual continuous time system is driven by other forms of additive noise processes. Here, the continuous system is discretized with the LL method and the noise process is added as a discrete process to the discrete dynamics in the same manner that we have simulated the system with additive white noise case. (Note here that the correspondence of discrete white noise to a continuous Wiener process is a well-known phenomenon. The discrete non-white processes as incorporated here, however, are assumed to correspond to other continuous processes that are generally unknown and are intended solely to study the robustness of the Kalman filtering techniques). In particular, the performance of the two filters is examined under discrete-time noise derived from (i) Poisson, (ii) Exponential, and (iii) Gamma distributions. A final noise case to be considered is that of (iv) additive very slowly varying noise that is concentrated in the frequency range of the observed signals. Specifically, noise is modeled as filtered white noise having frequency components of $1 - 5$ Hz which is in the frequency range of the measured membrane potential.

Performance of the CD-CKF:

The PI measure (as introduced in section 9.3) of the CD-CKF filter for white noise case is listed in Table 9.2. The values are the percentage out of 100 Monte-Carlo runs of the time where the estimated states were 20% away from the true states. From Table 9.2 it is noted that the total fraction of time (PI) is decreasing with increasing SNR. That is, the states will wander off for shorter periods of time from the true value as the SNR is increased. In terms of the sampling time dt, and for a given SNR, this measure is decreasing with dt, that is, the CD-CKF will produce more accurate estimates more often (longer periods of time) with smaller sampling rates.

The CD-CKF performance when the whiteness assumption is violated was also evaluated and shown in Fig. 9.6. Here, the error ratio PI_{noise}/PI_{white} was computed for different time steps and multiple SNRs to quantify the deterioration in performance. It is seen that this ratio was closest to unity for additive colored noise while it was largest for additive low frequency noise. Importantly, Poisson-type noise, a common approximation of background input in neuronal networks, showed mild performance deviation from that of white noise. At small time steps $(dt = 0.1 - 1$ ms$)$, the computed ratio is (very) high since the CD-CKF under white noise performance was significantly better than the CD-CKF performance under other noise types. This distinction becomes less obvious for larger time steps$(dt \geqslant 2$ ms$)$, particularly with increasing SNR. Hence, the CD-CKF performance was most sensitive to whiteness assumption for small time steps and is least sensitive to this assumption at large time steps and high SNR values.

151

Table 9.2: Probability rates of CD-CKF filter for white noise. Each number denotes the percentage out of 100 Monte-Carlo simulations of the time where the estimated states were 20% away from the true states

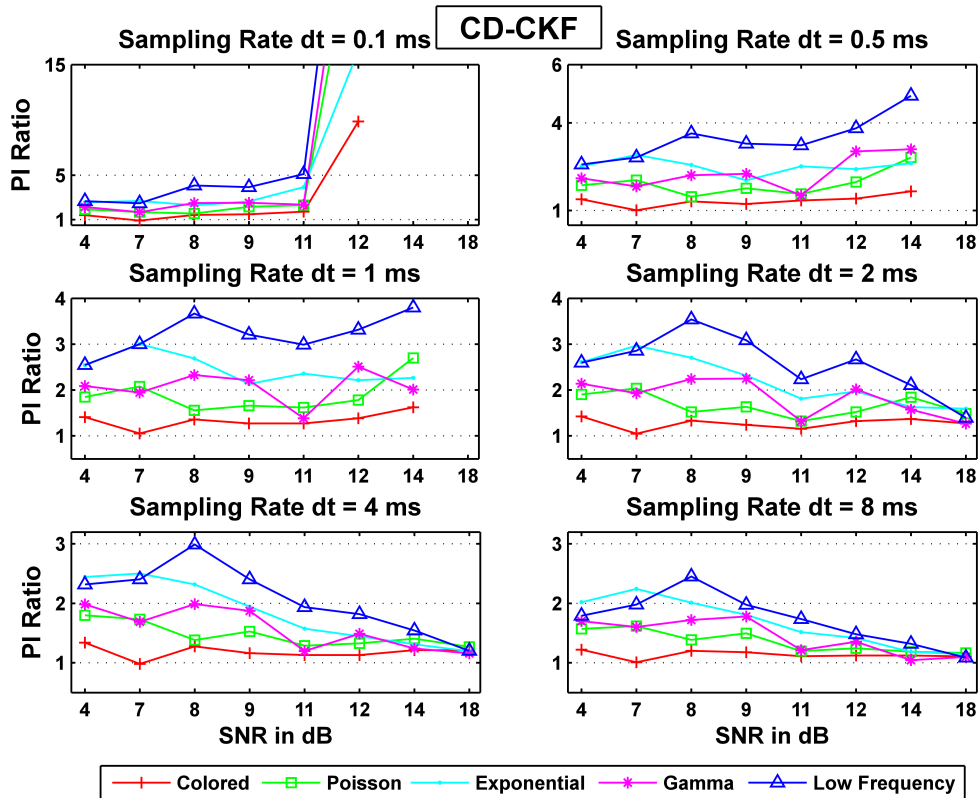|		CD-CKF Probability measure PI: White noise case					
		dt in ms					
		0.1	0.5	1	2	4	8
SNR in dB	4	6.67	7.69	7.75	7.53	8.06	11.61
	7	2.37	3.33	3.51	3.77	4.79	6.64
	8	1.37	2.43	2.52	2.84	3.69	4.94
	9	0.68	1.76	2	2.28	3.23	4.03
	11	0.19	0.92	1.18	1.86	2.79	3.68
	12	0.003	0.46	0.75	1.28	2.45	3.47
	14	0	0.08	0.23	0.78	1.87	3.37
	18	0	0	0	0.45	1.63	3.26

Figure 9.6: Probability ratios PI_{noise}/PI_{white} for CD-CKF for different sampling intervals and noise structures.

Performance of the CKF:

The analysis of the CKF performance for different additive noise cases has also been conducted and results are summarized in Table 9.3, and Fig. 9.7. In Fig. 9.7, it is again seen that colored noise had the closest performance to white while low frequency noise was the farthest from satisfying the whiteness assumption. Importantly, Fig. 9.7 show that quality of the CKF estimates mildly deteriorate from white noise to other noise types as the SNR increase at low sampling rates ($dt = 0.1$ ms), unlike the performance sensitivity shown for the CD-CKF at small time. Furthermore, the CKF performance becomes largely independent of the noise structure at large sampling rates ($dt = 8$ ms).

Table 9.3: Probability rates of CKF filter for white noise. Each number denotes the percentage out of 100 Monte-Carlo simulations of the time where the estimated states were 20% away from the true states

		CKF Probability measure PI: White noise case					
		dt in ms					
		0.1	0.5	1	2	4	8
SNR in dB	4	7.98	7.82	7.74	7.76	10.8	24.49
	7	3.77	3.71	3.57	3.95	7.06	21.49
	8	2.63	2.62	2.59	2.68	5.29	17.63
	9	2.1	2.16	2.15	2.29	4.67	14.72
	11	1.35	1.28	1.43	1.94	4.23	12.66
	12	0.9	0.9	1.01	1.34	3.46	11.61
	14	0.35	0.44	0.64	1.03	3.27	10.54
	18	0.02	0.04	0.17	0.67	3.43	9.28

Comparison of CD-CKF and CKF:

For a simple and concise comparative assessment of the performance of CD-CKF and CKF for different noise types, the probability rates for each scenario are plotted after being normalized by the worst probability PI_0 value of the CD-CKF with white noise case (which were obtained for lowest SNR = 4 dB and largest time step ($dt = 8$ ms).

Figs. 9.8 and 9.9 show the normalized probability rates for the CD-CKF and the CKF respectively. Here again, we notice that while both filters improve their performance as the SNR increase, the CD-CKF has a sharper SNR-related improvement (faster slop decline) for a given time step and all noise types tested. Furthermore, the CD-CKF performance improved steadily with smaller time steps
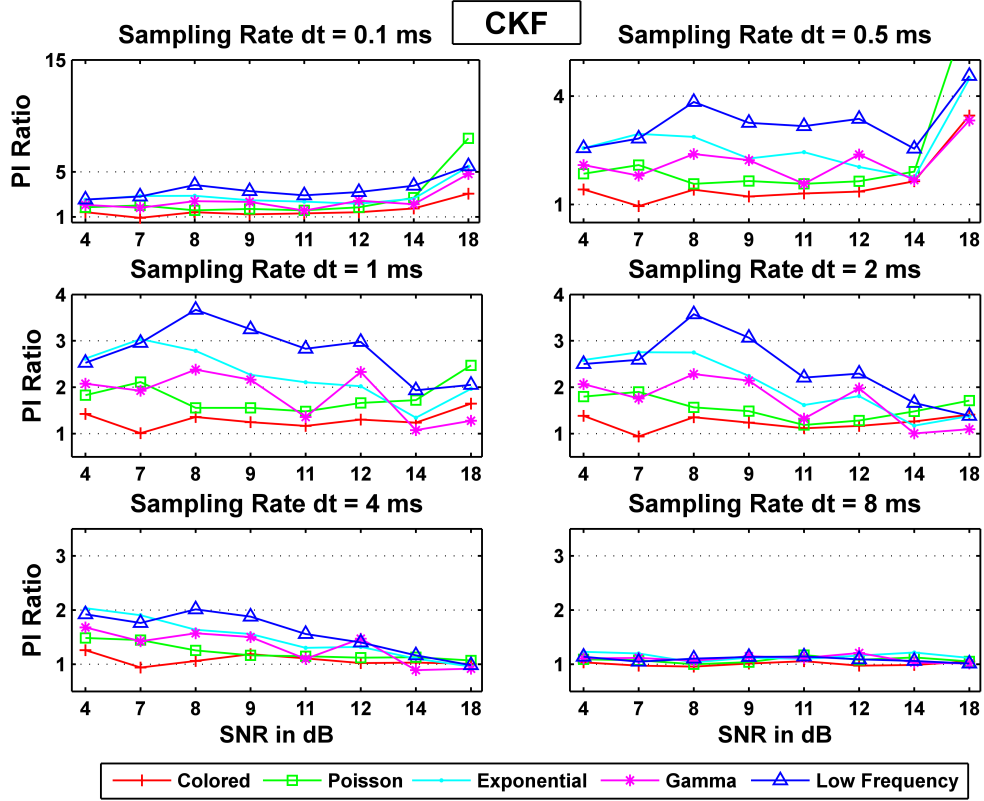
Figure 9.7: Probability ratios $\mathrm{PI}_{\mathrm{noise}}/\mathrm{PI}_{\mathrm{white}}$ for CKF estimation.

while the CKF performance remains essentially unchanged as the sampling time steps decrease below $dt = 1$ ms.

To examine the performance improvement of the CD-CKF over the CKF, we computed the ratios of the values obtained for CKF over those of CD-CKF for the probability measure PI, that is:

$$\mathrm{Ratio}_{i,j,l} = \left(\frac{\mathrm{PI}_{i,j}^{\mathrm{CKF}}}{\mathrm{PI}_{i,j}^{\mathrm{CD\text{-}CKF}}} \right)_l \tag{9.23}$$

Where l denotes the noise type, i for SNR value, and j denotes the sampling rate dt value. Fig 9.10 shows the ratios of the probability of inaccuracy (PI) measure of the CKF values to that of the CD-CKF values. We can see that the CD-CKF quality of estimates are better (ratio > 1) for most cases tested.

First, for large sampling intervals ($dt = 8$ ms), the CD-CKF is nearly twice more accurate for Gaussian noise (white, colored) with the CKF performance improving as the SNR increases (slope of ratio decreases). The CD-CKF is also significantly more accurate under other noise types (Poisson, Exponential, low frequency) with the CKF performance lagging behind that of the CD-CKF as

154
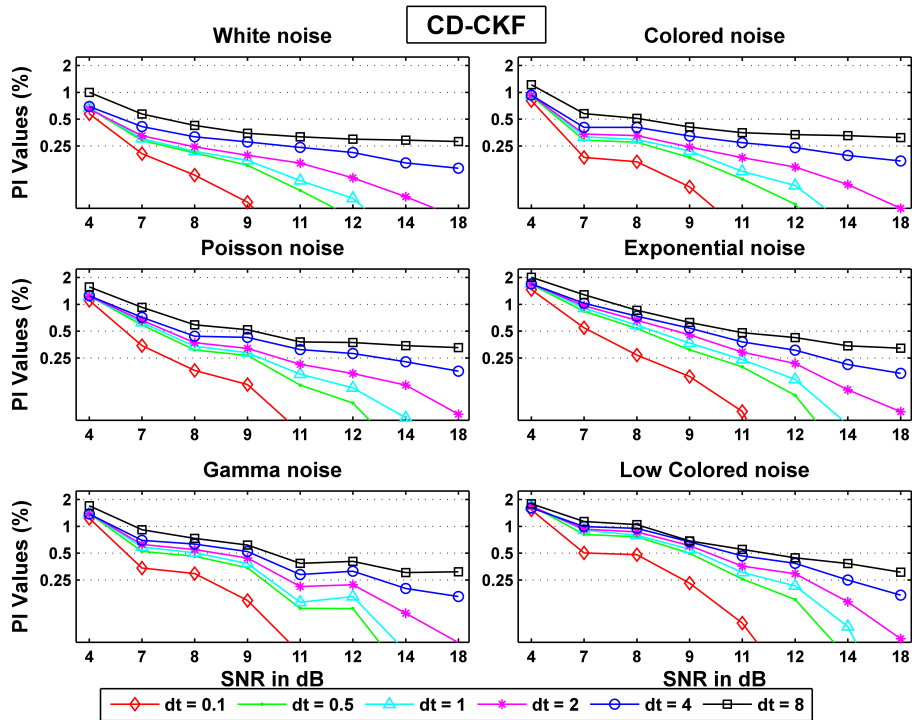
Figure 9.8: Normalized probability rates for the CD-CKF.

the SNR increases (slope of ratio increases). Second, for small sampling intervals ($dt = 0.1, 0.5$ and 1 ms), the CD-CKF performance improves at a much higher rate compared to that of the CKF as the SNR increases, regardless of the noise structure assumed. Finally, for intermediate sampling step ($dt = 2 - 4$ ms), the CD-CKF performance is comparable to that of the CKF for a wide SNR range and is only significantly better for the largest SNR tested (18 dB).
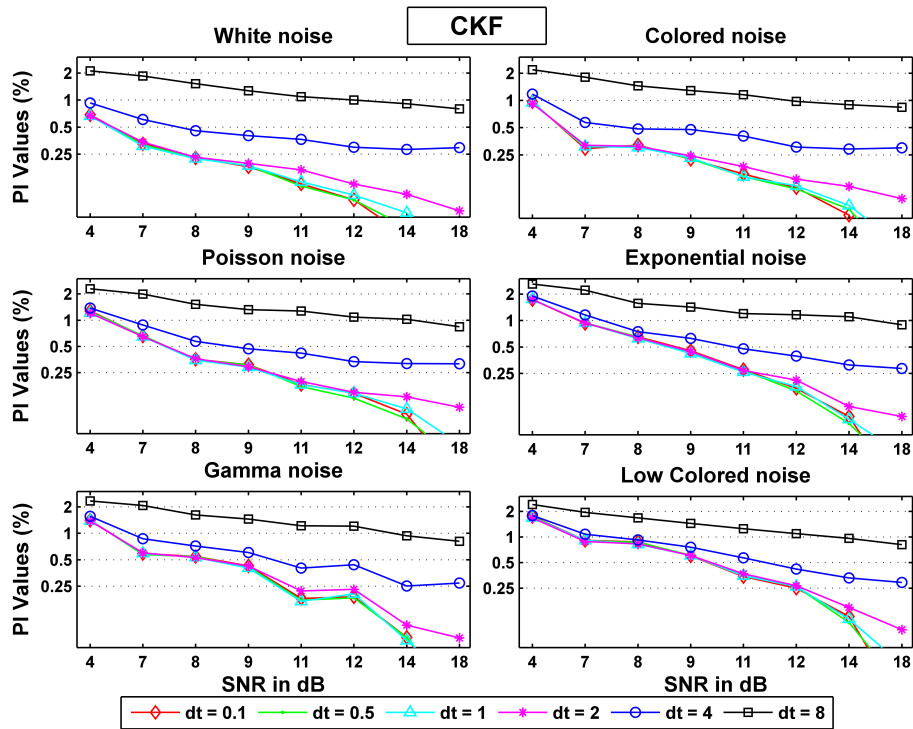
Figure 9.9: Normalized probability rates for the CKF.
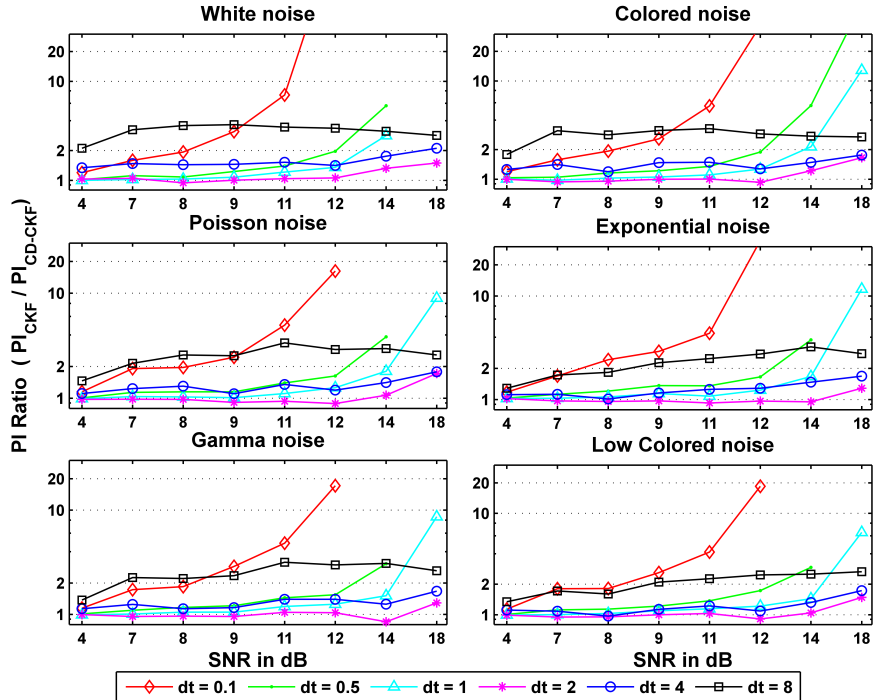
Figure 9.10: Ratios of the performance index PI of the CKF to that the CD-CKF values for different process noise structures and observation noise levels.

9.4.2 Hemodynamic Model

The performance of CKF and the hybrid CD-CKF in performing blind input deconvolution was tested under two scenarios of first unknown neural activity (NA) input and, second unknown NA inputs and model parameters (see Methods section). Fig. 9.11-A shows the simulated BOLD signals (red trace) and estimated BOLD signal (overlapping blue trace) for both filters under the first scenario (unknown NA input) for two time steps ($dt = 0.2, 0.5$ sec). The corresponding estimated NA input, which was obtained after a smoothed backward pass of both filters (Cubature smoother), is shown in Fig. 9.11-B (red trace: true input, blue trace: estimated input). It is noted here that the CKF produced inaccurate estimates of the input at larger time steps (Fig. 9.11-B1 and Fig. 9.11B3, bottom). More importantly, it is seen that the CKF was unable to accurately localize the time of occurrence of the NA input (input timing) for both time steps (Fig. 9.11-B1 and enlarged plots in Fig. 9.11-B3). On the other hand, the CD-CKF is shown to produce more robust estimates of both the magnitude and input timing dynamics for the two sampling times ($dt = 0.2, 0.5$ sec) (Fig. 9.11-B2 and enlarged plots in Fig. 9.11-B4). Finally, Fig. 9.11-C shows the estimates of one hidden state, the vasodilatory signal (s), which exhibits similar performance limitations of the CKF (in terms of signal shape and timing inaccuracy) when compared to the CD-CKF.

The estimation accuracy for the second scenario (unknown NA input and unknown model parameters) is shown in Fig. 9.12. Again, it is seen that while the BOLD signal is fitted properly with both CKF and CD-CKF, the timing accuracy of the input (Fig. 9.12-B) and hidden states (Fig. 9.12-C) continues to be better for the hybrid filter under the two time steps ($dt = 0.2, 0.5$ sec). The average value of the two parameters estimates show performance of the two filters (Fig. 9.12-A3 and Fig. 9.12-A4). To gain more understanding, the normalized MSE values obtained for both CD-CKF and CKF are averaged over 100 Monte-Carlo runs of the two scenarios at different sampling rates are given in Table 9.4. A clear superior performance of the CD-CKF is seen in all the cases for the input, state and parameter estimates.
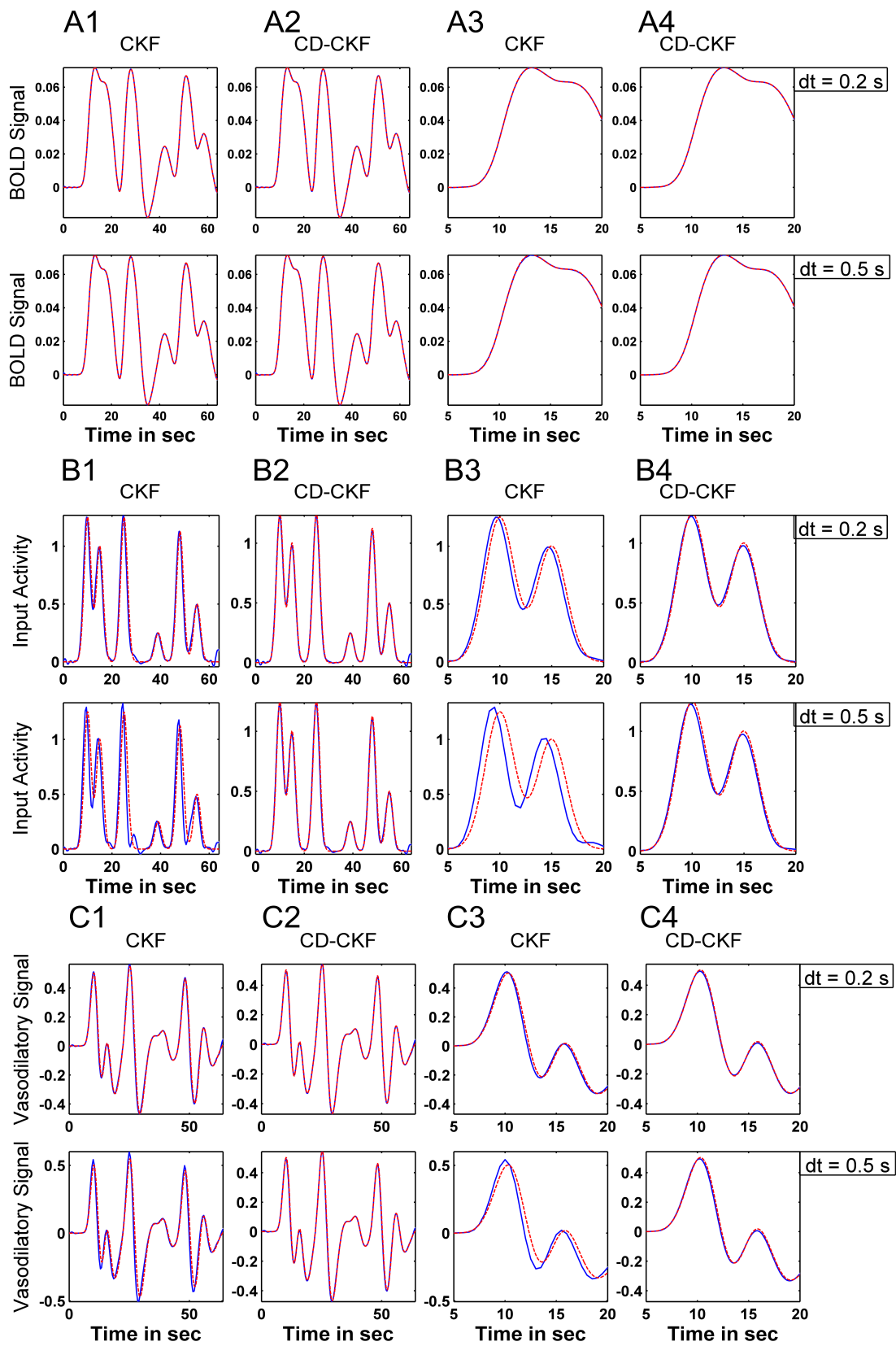
Figure 9.11: *(previous page)* Performance of the square-root CKF and square-root CD-CKF (with backward smoothers) for estimating hemodynamic states from simulated BOLD signals under unknown NA inputs. A: BOLD signal and its CKF (left) and CD-CKF (right) estimates for sample interval $dt = 0.2$, and 0.5 sec (top and lower rows, respectively). In all figures, simulated signals are in red and estimates in blue. Shaded blue regions correspond to 95% confidence intervals (100 simulations) which are extremely tight around the mean value. B: NA input for CKF (B1) and CD-CKF (B2), which are enlarged in B3, B4 respectively. C: vasodilatory signal for different time $dt = 0.2$, and 0.5 sec.

Table 9.4: Normalized MSE values averaged over 100 Monte-Carlo runs of the Hemodynamic estimation for both CKF and CD-CKF filters.

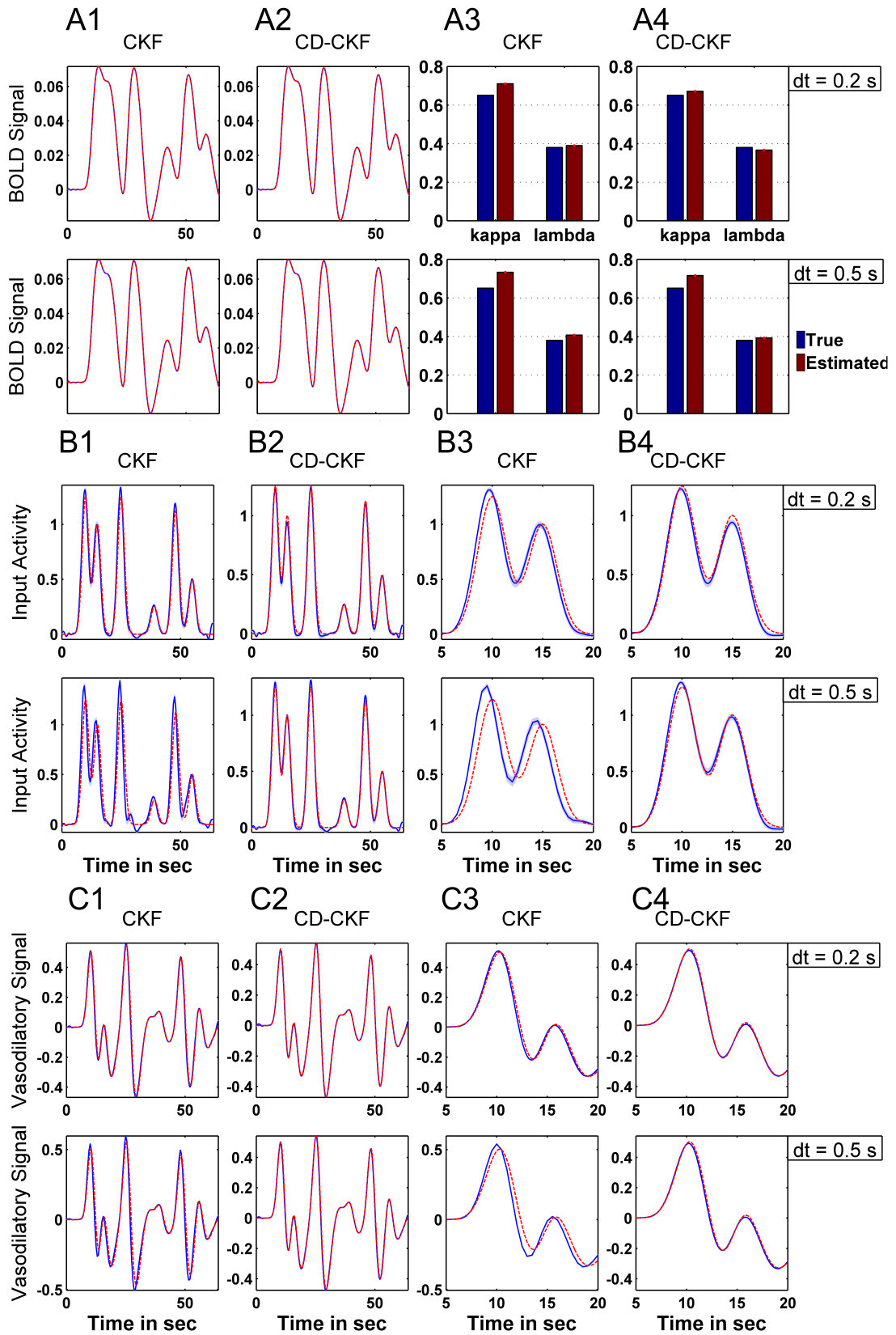|			dt in sec	
			0.5	0.2
First scenario	CKF	MSE of the states	14 e-4	1.8 e-4
		MSE of the input	169 e-4	31 e-4
	CD-CKF	MSE of the states	0.62 e-4	0.13 e-4
		MSE of the input	5.7 e-4	2.8 e-4
Second scenario	CKF	MSE of the states	13 e-4	1.8 e-4
		MSE of the input	148 e-4	29 e-4
		MSE of the parameters	109 e-4	48 e-4
	CD-CKF	MSE of the states	0.62 e-4	0.14 e- 4
		MSE of the input	6.04 e-4	7.7 e-4
		MSE of the parameters	58 e-4	14 e-4

Figure 9.12: *(previous page)* Performance of the square-root CKF and square-root CD-CKF (with backward smoothers) for estimating hemodynamic states from simulated BOLD signals under unknown NA inputs and two unknown parameters. A1-A2: BOLD signal and its CKF (left) and CD-CKF (right) estimates for sample interval $dt = 0.2$, and 0.5 sec (top and lower rows, respectively). A3-A4: Estimated parameters (rate of signal decay κ and rate of feedback regulation λ). B: NA input for CKF (B1) and CD-CKF (B2), which are enlarged in B3, B4 respectively. C: Estimated vasodilatory signal.

9.5 Discussion

In this chapter, we analyze the performance of two relatively novel nonlinear Bayesian estimation techniques, namely the discrete Cubature Kalman filter and the hybrid ContinuousDiscrete Cubature Kalman filter, that carry significant promise in efficiently and recursively estimating causal nonlinear models of hidden continuous random processes using a limited set of indirect observations. Examples of such processes are dispersed throughout biological phenomena, and are especially abundant and relevant in the field of Neuroscience. We here focus on the two problems of (a) estimating neural firing and intra-cortical conductances from direct real-time observations such as electric field potential (or EEG), and (b) estimating neural activity drive and hemodynamic parameters from indirect time-sampled observations such as BOLD signals (or fMRI).

Our results show that the explicit consideration of the continuous nature of the underlying biological process can (1) provide a significant improvement in the accuracy of the estimates and (2) allow for a wider range of noise processes that are commonly thought to adversely affect the applicability of Gaussian-based techniques such as the Kalman filter.

First, simulated noisy electric potential recordings were used to assess the accuracy of discrete and hybrid Kalman techniques in estimating the cortical neural firing rates as hidden realizations of the continuous time process that is governed by nonlinear dynamics and subjected to in vivo random noise. We have addressed, using multiple Monte-Carlo simulation runs, the accuracy of the hidden states obtained with the two tested Kalman filtering techniques under different assumptions on (i) the data sampling rate at which the observations are obtained, (ii) the signal-to-noise ratio in the observations, and (iii) the structure of the modeled process noise that additively affect the hidden process dynamics. The performance of a given filter was quantified in terms of the common mean square error (MSE) in the estimate (averaged over 100 Monte-Carlo simulations) and one devised measure of accuracy of the obtained estimates: the total fraction of time (PI) that an estimate is farther away than a threshold percentage (20%)

from the true states.

Second, simulated BOLD signal recordings were obtained to assess the ability of the two Kalman techniques in (i) deconvolving the input neural activity and (ii) estimating model parameters. We here focus on the superior ability of the hybrid filter (CD-CKF) in estimating the amplitude and, critically, the timing of the neural input.

We summarize our key findings as follows:

9.5.1 Performance of the Two Filters under Gaussian Process Noise:

For the two cases of white (independent) and colored (dependent) Gaussian noise structures (Figs. 9.1–9.4), state estimates that were obtained with either the CKF and CD-CKF techniques expectedly improved as the sampling time step size dt is decreased and the observation quality (SNR) is increased. In comparing the performance of both filters (in terms of MSE ratios over 100 simulations), the estimation accuracy for the cases of intermediate time step sizes ($dt = 12$ ms) was (i) comparable under low SNR level but (ii) higher for the CD-CKF under larger SNR levels. Importantly, the CD-CKF estimation accuracy was significantly higher in the simulated cases of both very small and very large time steps ($dt = 0.10.5$ms, $dt = 48$ ms, respectively) regardless of noise levels. The obtained results were consistent regardless whether the observations were obtained by simulating the system using the IT-1.5 or the LL discretization methods.

9.5.2 Effect of Observation Noise Level:

An improvement in the signal quality (higher SNR) expectedly resulted in an increase in the accuracy of the estimates for both filtering techniques. Still, the rate of increase was significantly larger when using the CD-CKF, particularly for lower SNR values. This result was consistent regardless of the noise structure and the sampling interval tested.

9.5.3 Effect of Sampling Time Step:

For all the noise structures tested, the state estimation accuracy (MSE) obtained when using the CKF and CD-CKF was generally comparable for intermediate step sizes ($dt = 2 - 4$ ms) particularly under low SNR levels (Figs. 9.6–9.10). At the largest sampling interval, the estimated obtained with CD-CKF were significantly better than those obtained with the CKF, regardless of the observation

noise levels and structure. Importantly, collecting even more frequent samples, or reducing the sampling interval below $dt = 1$ ms, resulted in a continuous improvement in the performance of the CD-CKF but no improvement in that of the CKF performance which exhibited a plateau in its accuracy.

9.5.4   Effect of Process Noise Structure:

The CD-CKF was more robust than the CKF against a wide range of additive noise structures that violated the Gaussianity assumption inherent to Kalman filtering techniques. The CD-CKF outperformed the CKF in all the cases of non-Gaussian additive noise considered. Furthermore, the CD-CKF performance at high SNR levels was less dependent on the actual noise structure and approached that of Gaussian noise, that is, the CD-CKF was able to utilize the decrease in observation uncertainty (noise power) to adaptively correct the state estimates. Among all the tested discrete random noise structures, low frequency noise constituted the most challenging structure for both filters, possibly since the power of this specific signal is more concentrated within the frequency range of the system output (leading to effective lower SNR levels). In the case of neural systems, this is a less likely scenario since the electric potential recordings (i.e. observations or output), are often noted to have lower frequency range compared to in-vivo fluctuations in the firing rate or synaptic conductances (i.e. hidden process noise).

Another important result is the ability of non-linear Kalman filtering techniques to overcome the limiting Gaussianity assumption on process noise structure in neural modeling. For the latter class of models, it is commonly assumed that the background noise impinging on local neural populations is the resultant of neuronal firing that is well approximated by a Poisson process. Current simulations demonstrated that the performance of both Kalman filters under Poisson process noise showed mild deterioration compared with that under Gaussian (white or colored) noise. In particular, the CD-CKF estimates under Poisson noise were very close to their counterparts under Gaussian noise and the quality of such estimates can be significantly improved by employing faster output sampling, a property that did not seem to hold for the CKF estimates.

9.5.5   Hemodynamic Model Estimation:

While both the CKF and CD-CKF were able to estimate the overall profile of a low-frequency neural activity driving the hemodynamic model, only the CD-CKF provided an accurate profile at increased time steps. Critically, only the CD-CKF with backward smoothing was able to provide an accurate time localiza-

tion of the neural input particularly since it explicitly accounts for the continuous dynamics over increasingly smaller interpolation steps of the low frequency observations. The ability to obtain accurate timing is of obvious importance to the whole series of studies that provide model-based estimates of the causal functional connectivity (directed information transfer) among brain areas using fMRI experiments [37, 83].

Chapter 10

Conclusion

In this dissertation, we addressed improving model fitting (states and parameters estimation) and model assessment (model selection) procedures in a Kalman-based framework by integrating techniques from Adaptive Design Optimization (ADO). We proposed identification algorithms that select in single experimental trials those system inputs that cause the output trajectory to be maximally informative about the nonlinear system model parameters. We showed that gains in estimation accuracy can be achieved using these algorithms in designing experiments/inputs when compared to those cases where no such designing is performed (i.e. randomized input application).

10.1 Contributions

The main contributions of this dissertation can be summarized as follows:

1. Proposing the OID-SCKF algorithm which is an adaptive approach for joint input design and parametric identification of nonlinear system models. When compared to estimation with Kalman filter with inputs being randomly selected, the proposed method in combining Kalman filtering with optimally designed inputs showed that, in principle, better convergence and higher estimation accuracy can be attained for a set of simulated scenarios that are derived from benchmark nonlinear problems as well as from nonlinear stochastic neuronal models. Yet, these gains in estimation accuracy posed heavy computational load making this procedure intractable for on-line applications.

2. Proposing the Dual Kalman filters method suitable for designing experiments for on-line applications. This method aimed to design sub-optimal inputs that achieve informative observations about unknown parameters

and hidden states by "transforming" the optimization problem associated with OID-SCKF (that solves for the optimal inputs) into a Kalman filter setup. The proposed setup discarded the optimization problem along with its computational burden and drastically reduced the computational needs to design an input. The presented Dual Kalman approach showed that better convergence and higher estimation accuracy can be attained when compared to estimation with random inputs. When compared to optimal inputs (OID-SCKF method), the Dual Kalman method showed comparable convergence and estimation accuracy, and more importantly, substantially more efficient than the OID-SCKF method in terms of computational time needed in designing informative inputs. Investigation of the Dual Kalman method for the simulated neuronal model demonstrated the immense gain in computational power against the OID-SCKF method in designing informative inputs while maintaining the out-performance in estimation accuracy over the random inputs case.

3. For off-line model fitting (states and parameters estimation) problems, we proposed a procedure to optimally design the tuning parameters of the Kalman filter based on sensitivity analysis of the model. The proposed approach is demonstrated on input deconvolution problem and showed to produce more confident estimates and better convergence without the need of an iterative tuning process from the designer.

4. Proposing an on-line single-phase procedure in which model fitting (parameters estimation) and model assessment (model selection) are carried out simultaneously using Bayesian approaches to model selection and by designing experiments that produce informative outcomes about model unknowns. This procedure demonstrated to accurately identify the true underlying model structure (and its unknown parameters) from a pool of model candidates having different levels of complexity. Moreover, this single-phase procedure when incorporated with the Dual Kalman method could be appropriate for on-line applications in which experiments are costly, their repetition is impractical, and/or are time-consuming.

10.2 Open Research Directions

As we have shown in chapter 9, implementing a hybrid Kalman filter (i.e. the CD-CKF) could (1) provide a significant improvement in the accuracy of the estimates and (2) allow for a wider range of noise processes that are commonly thought to adversely affect the applicability of Gaussian-based techniques such as the Kalman filter. Therefore, further investigations about the possible gains in estimation accuracy by implementing the hybrid Kalman filter within the proposed

algorithms instead of the CKF are highly needed especially when considering real life applications in which Gaussianity assumption on process noise structure in neural modeling might be violated.

As an experimental application, "Transcranial Current Stimulation" (tCS) with direct (tDCS) or alternating (tACS) current is emerging as a promising non-invasive brain stimulation technique for the treatment of neuropsychological disorders (including major depression, Parkinsons disease, and rehabilitation after stroke) as well as the study of human cognitive function. tCS can induce both immediate as well as long-lasting effects on brain electric activity by modulating cortical excitability in humans, albeit with limited understanding of the electrophysiological substrate underlying such modulation. Specifically, it remains unclear (i) how the applied currents delivered by tCS electrodes propagate and modify the ongoing neuronal population activities in the targeted areas, and (ii) which parameters of the stimulus (e.g. electrode location, current intensity, and duration) are key factors in achieving such neuronal activity modification.

The tCS might serve as an interesting technique for probing effective connectivity between brain areas along with the proposed procedures for model fitting (parameters estimation) and model assessment (model selection) with the Dual Kalman filters algorithm (which were aimed to be applicable for on-line applications). Such paradigms could involve designing (with the Dual Kalman algorithm) and applying current stimuli (tCS procedure) with EEG being used as an observation tool of brain activity from which effective connectivity between cortical areas under investigation are established as well as the most plausible effect of a given tCS stimulation on the underlying brain activity is highlighted.

Bibliography

[1] D. Schubert, R. Kötter, and J. F. Staiger, "Mapping functional connectivity in barrel-related columns reveals layer-and cell type-specific microcircuits," *Brain Structure and Function*, vol. 212, no. 2, pp. 107–119, 2007.

[2] M. S. Arulampalam, S. Maskell, N. Gordon, and T. Clapp, "A tutorial on particle filters for online nonlinear/non-gaussian bayesian tracking," *IEEE Transactions on signal processing*, vol. 50, no. 2, pp. 174–188, 2002.

[3] I. Arasaratnam, S. Haykin, and T. R. Hurd, "Cubature kalman filtering for continuous-discrete systems: theory and simulations," *Signal Processing, IEEE Transactions on*, vol. 58, no. 10, pp. 4977–4993, 2010.

[4] V. A. Bavdekar, A. P. Deshpande, and S. C. Patwardhan, "Identification of process and measurement noise covariance for state and parameter estimation using extended kalman filter," *Journal of Process control*, vol. 21, no. 4, pp. 585–601, 2011.

[5] H. W. Sorenson, *Kalman Filtering: Theory and Application*. IEEE Press, 1985.

[6] S. J. Julier and J. K. Uhlmann, "New extension of the kalman filter to nonlinear systems," in *AeroSense'97*, pp. 182–193, International Society for Optics and Photonics, 1997.

[7] R. Van Der Merwe and E. Wan, "The square-root unscented kalman filter for state and parameter-estimation," in *Acoustics, Speech, and Signal Processing, 2001. Proceedings.(ICASSP'01). 2001 IEEE International Conference on*, vol. 6, pp. 3461–3464, IEEE, 2001.

[8] M. Zheng, K. Ikeda, and T. Shimomura, "Estimation of continuous-time nonlinear systems by using the unscented kalman filter," in *SICE Annual Conference 2010, Proceedings of*, pp. 2192–2195, IEEE, 2010.

[9] I. Arasaratnam and S. Haykin, "Cubature kalman filters," *IEEE Trans. Autom. Control*, vol. 54, pp. 1254–1269, June 2009.

[10] A. López-Cuevas, B. Castillo-Toledo, L. Medina-Ceja, and C. Ventura-Mejía, "State and parameter estimation of a neural mass model from electrophysiological signals during the status epilepticus," *NeuroImage*, vol. 113, pp. 374–386, 2015.

[11] Y. Wei, G. Ullah, R. Parekh, J. Ziburkus, and S. J. Schiff, "Kalman filter tracking of intracellular neuronal voltage and current," in *Decision and Control and European Control Conference (CDC-ECC), 2011 50th IEEE Conference on*, pp. 5844–5849, IEEE, 2011.

[12] N. L. Hutcheson, K. R. Sreenivasan, G. Deshpande, M. A. Reid, J. Hadley, D. M. White, L. Ver Hoef, and A. C. Lahti, "Effective connectivity during episodic memory retrieval in schizophrenia participants before and after antipsychotic medication," *Human brain mapping*, vol. 36, no. 4, pp. 1442–1457, 2015.

[13] G. Lillacci and M. Khammash, "Parameter estimation and model selection in computational biology," *PLoS Comput Biol*, vol. 6, no. 3, p. e1000696, 2010.

[14] W. Jianlin, Z. Liqiang, and Y. Tao, "On-line estimation in fed-batch fermentation process using state space model and unscented kalman filter," *Chinese Journal of Chemical Engineering*, vol. 18, no. 2, pp. 258–264, 2010.

[15] E. Giraldo, A. den Dekker, and G. Castellanos-Dominguez, "Estimation of dynamic neural activity using a kalman filter approach based on physiological models," in *Engineering in Medicine and Biology Society (EMBC), 2010 Annual International Conference of the IEEE*, pp. 2914–2917, IEEE, 2010.

[16] S. M. Baker, C. H. Poskar, F. Schreiber, and B. H. Junker, "An improved constraint filtering technique for inferring hidden states and parameters of a biological model," *Bioinformatics*, vol. 29, no. 8, pp. 1052–1059, 2013.

[17] D. R. Freestone, P. Aram, M. Dewar, K. Scerri, D. B. Grayden, and V. Kadirkamanathan, "A data-driven framework for neural field modeling," *NeuroImage*, vol. 56, no. 3, pp. 1043–1058, 2011.

[18] M. Chong, R. Postoyan, D. Nešić, L. Kuhlmann, and A. Varsavsky, "Estimating the unmeasured membrane potential of neuronal populations from the EEG using a class of deterministic nonlinear filters," *Journal of neural engineering*, vol. 9, no. 2, p. 026001, 2012.

[19] M. Lankarany, W.-P. Zhu, M. Swamy, and T. Toyoizumi, "Trial-to-trial tracking of excitatory and inhibitory synaptic conductance using gaussian-mixture kalman filtering," *BMC Neuroscience*, vol. 14, no. Suppl 1, p. O2, 2013.

[20] A. Aarabi and B. He, "Seizure prediction in hippocampal and neocortical epilepsy using a model-based approach," *Clinical Neurophysiology*, vol. 125, no. 5, pp. 930–940, 2014.

[21] P. Gorzelic, S. Schiff, and A. Sinha, "Model-based rational feedback controller design for closed-loop deep brain stimulation of parkinson's disease," *Journal of neural engineering*, vol. 10, no. 2, p. 026016, 2013.

[22] G. Ullah and S. J. Schiff, "Assimilating seizure dynamics," *PLoS Comput Biol*, vol. 6, no. 5, p. e1000776, 2010.

[23] Z. Nahas, K. Al-Ali, H. Sawaya, A. Hamadeh, Z. Bazzi, M. Atoui, C. Ponton, and F. Karameh, "Functional connectivity focal electrically administered seizure therapy (FEAST) using high resolution EEG," in *Neuropsychopharmacology*, vol. 39, pp. S561–S561, NATURE PUBLISHING GROUP MACMILLAN BUILDING, 4 CRINAN ST, LONDON N1 9XW, ENGLAND, 2014.

[24] F. N. Karameh, M. Awada, F. Mourad, K. Zahed, I. C. Abou-Faycal, and Z. Nahas, "Modeling of neuronal population activation under electroconvulsive therapy.," in *BIOSIGNALS*, pp. 229–238, 2014.

[25] M. Sedigh-Sarvestani, S. J. Schiff, and B. J. Gluckman, "Reconstructing mammalian sleep dynamics with data assimilation," *PLoS Comput Biol*, vol. 8, no. 11, p. e1002788, 2012.

[26] J. Walters-Williams and Y. Li, "Comparison of extended and unscented kalman filters applied to EEG signals," in *Complex Medical Engineering (CME), 2010 IEEE/ICME International Conference on*, pp. 45–51, IEEE, 2010.

[27] A. Galka, O. Yamashita, T. Ozaki, R. Biscay, and P. Valdés-Sosa, "A solution to the dynamical inverse problem of EEG generation using spatiotemporal kalman filtering," *NeuroImage*, vol. 23, no. 2, pp. 435–453, 2004.

[28] L. Hamid, U. Aydin, C. Wolters, U. Stephani, M. Siniatchkin, and A. Galka, "MEG-EEG fusion by kalman filtering within a source analysis framework," in *Engineering in Medicine and Biology Society (EMBC), 2013 35th Annual International Conference of the IEEE*, pp. 4819–4822, IEEE, 2013.

[29] D. R. Freestone, P. J. Karoly, D. Nešić, P. Aram, M. J. Cook, and D. B. Grayden, "Estimation of effective connectivity via data-driven neural modeling," *Frontiers in neuroscience*, vol. 8, p. 383, 2014.

[30] M. Havlicek, K. J. Friston, J. Jan, M. Brazdil, and V. D. Calhoun, "Dynamic modeling of neuronal responses in fMRI using cubature kalman filtering," *Neuroimage*, vol. 56, no. 4, pp. 2109–2128, 2011.

[31] J. Toppi, F. Babiloni, G. Vecchiato, F. De Vico Fallani, D. Mattia, S. Salinari, T. Milde, L. Leistritz, H. Witte, and L. Astolfi, "Towards the time varying estimation of complex brain connectivity networks by means of a general linear kalman filter approach," in *Engineering in Medicine and Biology Society (EMBC), 2012 Annual International Conference of the IEEE*, pp. 6192–6195, IEEE, 2012.

[32] L. Sommerlade, M. Thiel, B. Platt, A. Plano, G. Riedel, C. Grebogi, W. Mader, M. Mader, J. Timmer, and B. Schelter, "Time-variant estimation of connectivity and kalmans filter," in *Methods in Brain Connectivity Inference through Multivariate Time Series Analysis* (K. Sameshima and L. A. Baccala, eds.), ch. 9, CRC press, 2014.

[33] M. M. Grant, D. White, J. Hadley, N. Hutcheson, R. Shelton, K. Sreenivasan, and G. Deshpande, "Early life trauma and directional brain connectivity within major depression," *Human brain mapping*, vol. 35, no. 9, pp. 4815–4826, 2014.

[34] K. J. Friston, L. Harrison, and W. Penny, "Dynamic causal modelling," *NeuroImage*, vol. 19, no. 4, pp. 1273–1302, 2003.

[35] O. David, S. J. Kiebel, L. M. Harrison, J. Mattout, J. M. Kilner, and K. J. Friston, "Dynamic causal modeling of evoked responses in EEG and MEG," *NeuroImage*, vol. 30, no. 4, pp. 1255–1272, 2006.

[36] S. J. Kiebel, M. I. Garrido, R. J. Moran, and K. J. Friston, "Dynamic causal modelling for EEG and MEG," *Cognitive neurodynamics*, vol. 2, no. 2, pp. 121–136, 2008.

[37] K. E. Stephan, L. Kasper, L. M. Harrison, J. Daunizeau, H. E. den Ouden, M. Breakspear, and K. J. Friston, "Nonlinear dynamic causal models for fMRI," *Neuroimage*, vol. 42, no. 2, pp. 649–662, 2008.

[38] C. Chen, S. J. Kiebel, and K. J. Friston, "Dynamic causal modelling of induced responses," *NeuroImage*, vol. 41, no. 4, pp. 1293–1312, 2008.

[39] E. Balsa-Canto, A. A. Alonso, and J. R. Banga, "Computational procedures for optimal experimental design in biological systems," *IET systems biology*, vol. 2, no. 4, pp. 163–172, 2008.

[40] J. R. Banga and E. Balsa-Canto, "Parameter estimation and optimal experimental design," *Essays in biochemistry*, vol. 45, pp. 195–210, 2008.

[41] D. Faller, U. Klingmüller, and J. Timmer, "Simulation methods for optimal experimental design in systems biology," *Simulation*, vol. 79, no. 12, pp. 717–725, 2003.

[42] C. Kreutz and J. Timmer, "Systems biology: experimental design," *FEBS journal*, vol. 276, no. 4, pp. 923–942, 2009.

[43] M. K. Transtrum and P. Qiu, "Optimal experiment selection for parameter estimation in biological differential equation models," *BMC bioinformatics*, vol. 13, no. 1, p. 1, 2012.

[44] M. Rodriguez-Fernandez, J. A. Egea, and J. R. Banga, "Novel metaheuristic for parameter estimation in nonlinear dynamic biological systems," *BMC bioinformatics*, vol. 7, no. 1, p. 1, 2006.

[45] J. Liepe, S. Filippi, M. Komorowski, and M. P. Stumpf, "Maximizing the information content of experiments in systems biology," *PLoS Comput Biol*, vol. 9, no. 1, p. e1002888, 2013.

[46] R. Schenkendorf, A. Kremling, and M. Mangold, "Optimal experimental design with the sigma point method," *IET systems biology*, vol. 3, no. 1, pp. 10–23, 2009.

[47] D. Telen, F. Logist, R. Quirynen, B. Houska, M. Diehl, and J. Impe, "Optimal experiment design for nonlinear dynamic (bio) chemical systems using sequential semidefinite programming," *AIChE Journal*, vol. 60, no. 5, pp. 1728–1739, 2014.

[48] L. Lu, "Optimal inputs and sensitivities for parameter estimation in bioreactors," *Journal of mathematical chemistry*, vol. 47, no. 3, pp. 1154–1176, 2010.

[49] M. Rodriguez-Fernandez, P. Mendes, and J. R. Banga, "A hybrid approach for efficient and robust parameter estimation in biochemical pathways," *Biosystems*, vol. 83, no. 2, pp. 248–265, 2006.

[50] C. DiMattina and K. Zhang, "Active data collection for efficient estimation and comparison of nonlinear neural models," *Neural computation*, vol. 23, no. 9, pp. 2242–2288, 2011.

[51] J. H. Huggins and L. Paninski, "Optimal experimental design for sampling voltage on dendritic trees in the low-SNR regime," *Journal of computational neuroscience*, vol. 32, no. 2, pp. 347–366, 2012.

[52] S. Bandara, J. P. Schlöder, R. Eils, H. G. Bock, and T. Meyer, "Optimal experimental design for parameter estimation of a cell signaling model," *PLoS Comput Biol*, vol. 5, no. 11, p. e1000558, 2009.

[53] N. A. van Riel, "Dynamic modelling and analysis of biochemical networks: mechanism-based models and model-based experiments," *Briefings in bioinformatics*, vol. 7, no. 4, pp. 364–374, 2006.

[54] A. G. Busetto, A. Hauser, G. Krummenacher, M. Sunnåker, S. Dimopoulos, C. S. Ong, J. Stelling, and J. M. Buhmann, "Near-optimal experimental design for model selection in systems biology," *Bioinformatics*, vol. 29, no. 20, pp. 2625–2632, 2013.

[55] D. R. Cavagnaro, J. I. Myung, M. A. Pitt, and J. V. Kujala, "Adaptive design optimization: A mutual information-based approach to model discrimination in cognitive science," *Neural computation*, vol. 22, no. 4, pp. 887–905, 2010.

[56] J. I. Myung and M. A. Pitt, "Optimal experimental design for model discrimination.," *Psychological review*, vol. 116, no. 3, p. 499, 2009.

[57] J. C. Horton, "Ocular integration in the human visual cortex," *Canadian Journal of Ophthalmology/Journal Canadien d'Ophtalmologie*, vol. 41, no. 5, pp. 584–593, 2006.

[58] R. B. Wells, "Cortical neurons and circuits: a tutorial introduction," *Unpublished paper, www. mrc. uidaho. edu*, 2005.

[59] C. Binnie and P. Prior, "Electroencephalography.," *Journal of Neurology, Neurosurgery & Psychiatry*, vol. 57, no. 11, pp. 1308–1319, 1994.

[60] J. Jimenez, I. Shoji, and T. Ozaki, "Simulation of stochastic differential equations through the local linearization method. a comparative study," *Journal of Statistical Physics*, vol. 94, no. 3-4, pp. 587–602, 1999.

[61] I. Arasaratnam and S. Haykin, "Cubature kalman smoothers," *Automatica*, vol. 47, no. 10, pp. 2245–2250, 2011.

[62] J. I. Myung, D. R. Cavagnaro, and M. A. Pitt, "A tutorial on adaptive design optimization," *Journal of mathematical psychology*, vol. 57, no. 3, pp. 53–67, 2013.

[63] M. A. Barron, D. Y. Medina, and I. Hilerio, "Collective behavior of a ring of van der pol oscillators under gaussian and random coupling schemes," *Open Journal of Applied Sciences*, vol. 2014, 2014.

[64] R. Yamapi, H. G. E. Kadji, and G. Filatrella, "Stability of the synchronization manifold in nearest neighbor nonidentical van der pol-like oscillators," *Nonlinear Dynamics*, vol. 61, no. 1-2, pp. 275–294, 2010.

[65] R. J. Moran, K. E. Stephan, R. J. Dolan, and K. J. Friston, "Consistent spectral predictors for dynamic causal models of steady state responses," *NeuroImage*, vol. 55, no. 4, pp. 1694–1708, 2011.

[66] A. C. Marreiros, S. J. Kiebel, J. Daunizeau, L. M. Harrison, and K. J. Friston, "Population dynamics under the laplace assumption," *Neuroimage*, vol. 44, no. 3, pp. 701–714, 2009.

[67] A. C. Marreiros, J. Daunizeau, S. J. Kiebel, and K. J. Friston, "Population dynamics: variance and the sigmoid activation function," *NeuroImage*, vol. 42, no. 1, pp. 147–157, 2008.

[68] C. De Kock, R. M. Bruno, H. Spors, and B. Sakmann, "Layer-and cell-type-specific suprathreshold stimulus representation in rat primary somatosensory cortex," *The Journal of physiology*, vol. 581, no. 1, pp. 139–154, 2007.

[69] M. Ursino and G.-E. La Cara, "Travelling waves and eeg patterns during epileptic seizure: analysis with an integrate-and-fire neural network," *Journal of theoretical biology*, vol. 242, no. 1, pp. 171–187, 2006.

[70] B. H. Jansen and V. G. Rit, "Electroencephalogram and visual evoked potential generation in a mathematical model of coupled cortical columns," *Biological cybernetics*, vol. 73, no. 4, pp. 357–366, 1995.

[71] R. J. Moran, S. J. Kiebel, K. Stephan, R. Reilly, J. Daunizeau, and K. J. Friston, "A neural mass model of spectral responses in electrophysiology," *NeuroImage*, vol. 37, no. 3, pp. 706–720, 2007.

[72] O. David, L. Harrison, and K. J. Friston, "Modelling event-related responses in the brain," *NeuroImage*, vol. 25, no. 3, pp. 756–770, 2005.

[73] K. J. Friston, A. Mechelli, R. Turner, and C. J. Price, "Nonlinear responses in fMRI: the balloon model, volterra kernels, and other hemodynamics," *NeuroImage*, vol. 12, no. 4, pp. 466–477, 2000.

[74] J. J. Riera, J. Watanabe, I. Kazuki, M. Naoki, E. Aubert, T. Ozaki, and R. Kawashima, "A state-space model of the hemodynamic approach: nonlinear filtering of BOLD signals," *NeuroImage*, vol. 21, no. 2, pp. 547–567, 2004.

[75] C. Jauberthie and E. Chanthery, "Optimal input design for a nonlinear dynamical uncertain aerospace system," *IFAC Proceedings Volumes*, vol. 46, no. 23, pp. 469–474, 2013.

[76] A. Tulsyan, B. Huang, R. B. Gopaluni, and J. F. Forbes, "On simultaneous on-line state and parameter estimation in non-linear state-space models," *Journal of Process Control*, vol. 23, no. 4, pp. 516–526, 2013.

[77] V. Vyshemirsky and M. A. Girolami, "Bayesian ranking of biochemical system models," *Bioinformatics*, vol. 24, no. 6, pp. 833–839, 2008.

[78] M. Sunnåker and J. Stelling, "Model extension and model selection," in *Uncertainty in Biology*, pp. 213–241, Springer, 2016.

[79] R. Schenkendorf and M. Mangold, "Online model selection approach based on unscented kalman filtering," *Journal of Process Control*, vol. 23, no. 1, pp. 44–57, 2013.

[80] E. Prudencio, P. Bauman, D. Faghihi, K. Ravi-Chandar, and J. Oden, "A computational framework for dynamic data-driven material damage control, based on bayesian inference and model selection," *International Journal for Numerical Methods in Engineering*, vol. 102, no. 3-4, pp. 379–403, 2015.

[81] R. King and E. D. Gilles, "Multiple filter methods for detection of hazardous states in an industrial plant," *AIChE journal*, vol. 36, no. 11, pp. 1697–1706, 1990.

[82] E. W. Lang, A. M. Tomé, I. R. Keck, J. Górriz-Sáez, and C. G. Puntonet, "Brain connectivity analysis: a short survey," *Computational intelligence and neuroscience*, vol. 2012, p. 8, 2012.

[83] K. J. Friston, "Functional and effective connectivity: a review," *Brain connectivity*, vol. 1, no. 1, pp. 13–36, 2011.

[84] P. Aram, D. R. Freestone, M. J. Cook, V. Kadirkamanathan, and D. Grayden, "Model-based estimation of intra-cortical connectivity using electrophysiological data," *NeuroImage*, vol. 118, pp. 563–575, 2015.

[85] M. Hassan, O. Dufor, I. Merlet, C. Berrou, and F. Wendling, "Eeg source connectivity analysis: from dense array recordings to brain networks," *PloS One*, vol. 9, no. 8, p. e105041, 2014.

[86] M. Hassan, P. Benquet, A. Biraben, C. Berrou, O. Dufor, and F. Wendling, "Dynamic reorganization of functional brain networks during picture naming," *Cortex*, vol. 73, pp. 276–288, 2015.

[87] R. Grech, T. Cassar, J. Muscat, K. P. Camilleri, S. G. Fabri, M. Zervakis, P. Xanthopoulos, V. Sakkalis, and B. Vanrumste, "Review on solving the inverse problem in EEG source analysis," *Journal of neuroengineering and rehabilitation*, vol. 5, no. 1, p. 1, 2008.

[88] C. Bédard, H. Kröger, and A. Destexhe, "Modeling extracellular field potentials and the frequency-filtering properties of extracellular space," *Biophysical journal*, vol. 86, no. 3, pp. 1829–1842, 2004.

[89] P. L. Nunez and R. Srinivasan, *Electric fields of the brain: the neurophysics of EEG*. Oxford University Press, USA, 2006.

[90] J.-M. Fellous, M. Rudolph, A. Destexhe, and T. J. Sejnowski, "Synaptic background noise controls the input/output characteristics of single cells in an in vitro model of in vivo activity," *Neuroscience*, vol. 122, no. 3, pp. 811–829, 2003.

[91] M. Rudolph and A. Destexhe, "The discharge variability of neocortical neurons during high-conductance states," *Neuroscience*, vol. 119, no. 3, pp. 855–873, 2003.

[92] M. N. Shadlen and W. T. Newsome, "The variable discharge of cortical neurons: implications for connectivity, computation, and information coding," *The Journal of neuroscience*, vol. 18, no. 10, pp. 3870–3896, 1998.

[93] M. Graupner and A. D. Reyes, "Synaptic input correlations leading to membrane potential decorrelation of spontaneous activity in cortex," *The Journal of Neuroscience*, vol. 33, no. 38, pp. 15075–15085, 2013.

[94] M. W. Levine, "The distribution of the intervals between neural impulses in the maintained discharges of retinal ganglion cells," *Biological cybernetics*, vol. 65, no. 6, pp. 459–467, 1991.

[95] D. Berger, K. Pribram, H. Wild, and C. Bridges, "An analysis of neural spike-train distributions: determinants of the response of visual cortex neurons to changes in orientation and spatial frequency," *Experimental brain research*, vol. 80, no. 1, pp. 129–134, 1990.

[96] L. Kostal and P. Lansky, "Similarity of interspike interval distributions and information gain in a stationary neuronal firing," *Biological cybernetics*, vol. 94, no. 2, pp. 157–167, 2006.

[97] J. Ramos, "Linearized methods for ordinary differential equations," *Applied mathematics and computation*, vol. 104, no. 2, pp. 109–129, 1999.